Aerodynamics and Heat Transfer Studies of Parameters Specific to the IGCC-Requirements: Endwall Contouring, Leading Edge Filleting and Blade Tip Ejection under Rotating Turbine Conditions

Final Report
October 01, 2009 to September 30, 2013

Prepared for

US-Department of Energy
National Energy Technology Laboratory

by
Dr. Meinhard T. Schobeiri, Project Director and PI,
Dr. Je-Chin Han, Co-PI

Reporting Period: October 01, 2013

DOE Award No. DE-FC26-FE0000753

TEXAS ENGINEERING EXPERIMENT STATION
Department of Mechanical Engineering
Texas A&M University
College Station, TX, 77843-3132
Phone: (979)845-0819
E-mail: tschobeiri@mengr.tamu.edu

DISCLAIMER

ABSTRACT

This report deals with the specific aerodynamics and heat transfer problematic inherent to high pressure (HP) turbine sections of IGCC-gas turbines. Issues of primary relevance to a turbine stage operating in an IGCC-environment are: (1) decreasing the strength of the secondary flow vortices at the hub and tip regions to reduce (a), the secondary flow losses and (b), the potential for end wall deposition, erosion and corrosion due to secondary flow driven migration of gas flow particles to the hub and tip regions, (2) providing a robust film cooling technology at the hub and that sustains high cooling effectiveness less sensitive to deposition, (3) investigating the impact of blade tip geometry on film cooling effectiveness. The document includes numerical and experimental investigations of above issues. The experimental investigations were performed in the three-stage multi-purpose turbine research facility at the Turbomachinery Performance and Flow Research Laboratory (TPFL), Texas A&M University. For the numerical investigations a commercial Navier-Stokes solver was utilized.

TABLE OF CONTENTS

1. EXECUTIVE SUMMARY

This report deals with the specific aerodynamics and heat transfer problematic inherent to high pressure (HP) turbine sections of IGCC-gas turbines as specified in the proposal. As defined in [1], issues of primary relevance to a turbine stage operating in an IGCC-environment are: (1) decreasing the strength of the secondary flow vortices at the hub and tip regions to reduce (a), the secondary flow losses and (b), the potential for end wall deposition, erosion and corrosion due to secondary flow driven migration of gas flow particles to the hub and tip regions, (2) providing a robust film cooling technology at the hub and that sustains high cooling effectiveness less sensitive to deposition, (3) investigating the impact of blade tip geometry on film cooling effectiveness. As seen, the accomplishments detailed in this report have gone far beyond those expected by achieving the objectives defined in [1]. The document includes numerical and experimental investigations.

The experimental investigations were performed in the three-stage multi-purpose turbine research facility at the Turbomachinery Performance and Flow Research Laboratory (TPFL), Texas A&M University. For the numerical investigations a commercial Navier-Stokes solver was utilized.

1) Decreasing the Strength of the Secondary Flow Vortices: Major efficiency improvement has been achieved by introducing a completely new endwall contouring technology. In contrast to the trial and error method presented in numerous papers, the new technology is based on the *controlled diffusion process* which is entirely physics based. The method utilizes a prescribed deceleration of the secondary flow velocity from pressure to suction surface. By defining a target pressure and constructing the non-axisymmetric endwall contouring, it was shown that the pressure difference between the blade pressure and the suction surface on the hub can be controlled by reducing the secondary flow and thus increasing the efficiency. This method can equally be applied to HP-, IP- or LP-turbines and compressors regardless of the load coefficient, flow coefficient and degree of reaction. It is strongly physics based, very straight forward and easy to use. The method was applied to the second rotor row of the TPFL-turbine. The contouring was cut into the rotor hub of the three-stage TPFL-research turbine using CNC-machining. Efficiency measurements show for the contoured rotor a maximum efficiency of 89.9% compared to the reference non-contoured case of $\eta_{t\text{-}s} = 88.86\%$. This is an efficiency increase of $\eta = 1.04\%$, which is almost double the value obtained from the numerical simulation of $\eta = 0.51\%$ presented in the report. This new method is particularly significant for applications to power generation steam turbines. The high-, intermediate and low pressure units (HP, IP, LP) consist of many stages, with HP- and IP-units. Contouring all rotor endwalls of these units will substantially increase the unit efficiency. For a 200MW HP-unit of 16 stages, we estimate an efficiency improvement close to 5%.

2) Robust Film Cooling at the Hub, Impact of Endwall Contouring: The new method of endwall contouring not only has improved the turbine aerodynamic efficiency but it also has substantially improved the film cooling effectiveness of the contoured endwall. The endwall portion of the first turbine stage is generally subjected to higher temperatures requiring a thorough cooling. To accomplish this, purge air is extracted

from the rotor internal cavity and is ejected through a circumferential slot onto the endwall of the first rotor row. To determine the impact of the endwall contouring on film cooling effectiveness, the new contouring technology was applied to the first rotor row. Performing an extensive RANS simulation by using the boundary conditions from the experiments, aerodynamics, performance and film cooling effectiveness studies were performed by varying the injection blowing ratio and turbine rotational speed. The film cooling experiments were carried out using pressure sensitive paint (PSP) measurement technique. Measurements were conducted for three coolant-to-mainstream mass flow ratios (MFR) of 0.5%, 1.0% and 1.5%. Film cooling data is also obtained for three rotational speeds, 3000 rpm (reference condition), 2550 rpm and 2400 rpm and they are compared with non-contoured endwall data. For 3000 rpm two more coolant to mainstream mass flow ratio of 0.75% and 1.25% are performed to have a better view of how film cooling effectiveness is changing. Comparing numerical and experimental results of the film cooling effectiveness investigations of the contoured case with the reference non-contoured case, clearly shows the improving effect of contouring on film cooling effectiveness for all cases investigated in this report.

3) Investigating the Impact of Blade Tip Geometry on Film Cooling Effectiveness: Detailed numerical and experimental investigations of film cooling effectiveness were conducted on the blade tips of the first rotor row pertaining to a three-stage research turbine. Four different blade tip ejection configurations were utilized to determine the impact of the hole arrangements on the film cooling effectiveness. Particular attention was paid to ensure a uniform pressure distribution within the small cavity inside the blade close to the blade tip. This required an extensive design iteration process implementing the results of solid mechanics design into the numerical simulation. The final configurations were manufactured and installed diametrically on the rotor hub to avoid rotor imbalance. The first configuration includes a pair of blades with radially arranged ejection holes positioned along the camber of the blade flat tip. The second configuration consists of a pair of blades with radially arranged holes embedded in the blade tip squealer. The third configuration has a flat tip but the ejection holes are arranged on the pressure side under given ejection angles. The fourth configuration has the same pressure side hole arrangements as the third configuration but the tip has squealer shape. Measurements were performed using pressure sensitive paint (PSP) technique. Three blowing ratios M = 0.75, 1.25 and 1.75 at three different rotational speeds of 3000 rpm (reference condition), 2550 rpm and 2000 rpm were utilized. In a parallel effort, extensive numerical investigations of the above configurations were performed to give a better view of flow behavior.

2. INTRODUCTION , BACKGROUND, OBJECTIVES

2.1 Introduction

Triggered by the energy crisis, limited resources of liquid fossil fuel, disposal of highly radioactive waste material from reactor operations and severe reactor accidents, more than three decades ago, the power generation industry particularly in the US and Germany started looking into an alternative old concept of gaseous fuel extraction from coal, the coal-based integrated coal gasification combined cycle (IGCC). The continuous increase of CO2-output leading to the alarming global warming, the abundance of coal as the primary energy source and the availability of necessary technology to extract clean hydrogen and syngas (HSG) with carbon capture, have re-attracted the interest of industry and government in re-introducing the IGCC concept. While the IGCC concept offers superior environmental performance as pointed out by Dennis and Harp [2], there are still technical issues to be solved. One of the issues inherently associated with HSG fuels that affects the efficiency and performance of the IGCC-gas turbine component, is the contamination of HSG with varying levels of impurities that cause corrosion, erosion, surface degradation and particle deposition on the turbine blade surface. Investigations by Wenglarz and Fox [3] indicate that an increase in gas temperature above the particulate melting point causes an increase in deposition rate. Accumulation of deposits on the blade hub section and the blade surface causes a deterioration of aerodynamic efficiency and heat transfer performance of the turbine unit. A multitude of pictures of turbine blades operating with heavy fuels show that the deposition is concentrated on the blade channel portions that is affected by secondary flow. This identifies the secondary flow as the triggering mechanism for the onset of deposition location. This circumstance suggests that reducing the onset and extent of the deposition requires some modification or reduction of the secondary flow.

The HP-turbine has, in contrast to LP-turbine, a relatively small aspect ratio, which causes major secondary flow regions close to the hub and tip. As a result, the secondary flow caused by a system of hub and tip vortices that induce drag forces resulting in an increase of secondary flow losses, as extensively discussed in the recently published book by Schobeiri [4]. Focusing on the secondary flow loss mechanisms, the fluid particles within the endwall boundary layers are exposed to a pitchwise pressure gradient in the blade channel. The particle moves pitchwise from the pressure side to the suction side, and generates a system of vortices. These vortices induce drag forces that are the cause of the secondary flow losses. In addition, their interaction with the main flow causes angle deviation inside and outside the blade channel, resulting in additional losses due to angle deviation. The nature of different flow losses is comprehensively treated in the classical work of Traupel [5]. Schobeiri [4] dedicated a full chapter of his book to the physics of loss generation and its calculation. Denton [6] summarized the loss mechanisms. Sieverding [7], and more recently, Langston [8] gave a comprehensive review on the secondary flow in axial turbine blade rows.

The secondary flow loss is almost inversely proportional to the aspect ratio [4]. Thus, in HP-turbines with small aspect ratios, the secondary flow loss of almost 40-50% is the major loss contributor. The secondary flow can be reduced by optimizing the following parameters:

1) 3-D Compound lean of the blade axis, bowed blades, already evidenced by own turbine design and its interstage measurements (see below).
2) Endwall contouring (proposed: to be confirmed in TPFL-rotating rig).
3) Modification of the leading edge near the endwalls (proposed: to be confirmed in TPFL-rotating rig).
4) Hub cooling mass flow injection to interact with the hub secondary flow (proposed).
5) Blade tip cooling ejection to reduce the tip secondary flow losses (proposed).

Secondary Flow, 3-D Compound Lean: One of the efficient methods of reducing the secondary flow zone is utilizing the compound lean blade design procedure that reduces the secondary losses by varying the lean angle (see for details Textbook by Schobeiri [4]). Using the streamline curvature method, optimizing the lean angle, and placing appropriate turbine profile from hub to tip, Schobeiri developed, designed and supervised the manufacturing of several high efficiency HP-rotor and have performed interstage loss and efficiency measurements. The effectiveness of the 3-D leaned design in suppressing the secondary flow is demonstrated in efficiency and performance studies by Schobeiri and his co-workers, among others [9] and [10]. These studies were performed in the Turbomachinery Performance and Flow Research Laboratory, TPFL, established by Dr. Schobeiri in 1997, with a three-stage high efficiency turbine with 3-D compound lean blades. A subsequent comparative study [11], using cylindrical blades with identical blade height, hub and tip diameter, and inlet conditions revealed a significant efficiency improvement of more than $\Delta\eta \approx 2\%$ for the rotor with 3-D compound lean blades compared to the one with cylindrical blades.

As detailed in [9] and [10], there is still a potential to further improve the efficiency by reducing the secondary flow and tip clearance losses. A glance at the contour plots of total pressure distributions explains the reason behind the efficiency improvement. Substantial reduction of secondary flow zone, clearly demonstrates the cause of efficiency improvement quantified in [4]. Despite this significant efficiency improvement, the results suggest that there is still a realistic potential to further improve the efficiency, as we discuss in the following.

Following the concept detailed in [9], [10], and [11], Abhari and his co-workers [12] performed similar investigations on two bladings. They reported that the compound-lean blading has a clear performance advantage of 1 to 1.5% in cascade efficiency over the cylindrical blading. Since the reduction of the secondary flow losses by utilizing the 3-D bowed blade design already evidenced in studies by Schobeiri and his co-workers, [9 and 10], the proposed research will be focused on further improving potentials of Endwall contouring, modification of the leading edge near the endwalls, and the blade tip ejection to reduce the tip secondary flow losses.

Endwall Contouring, Leading Edge Geometry: In recent years, numerous papers have been published that deal with the effect of endwall contouring and leading edge filleting. With a few exceptions of rotating rig investigations that deal with the endwall contouring of LP-turbines, most of the published studies are either numerically or experimentally performed in turbine cascades with steady inlet flow conditions. Numerical and experimental studies by [13], [14], [15], [16], [17], [18], [19], [20], [21] and [22] show a reduction of total pressure losses by as much as 50%.

Need for Turbine Rig Experimental Investigation: The above studies indicate that, based on the cascade loading, the endwall contouring positively influences the secondary flow reduction. However, the lack of the capability to consider the effects of rotation that encompasses rotor stator interaction, periodic unsteady wakes and their impact on the boundary layer transition of the following blade rows and the lack of centrifugal and Coriolis forces that are inherent to a rotating turbine, raises questions as to what extent these results are transferable to a rotating turbine environment. Recent comprehensive turbine rig experimental studies dealing with blade film cooling, blade channels and platform investigations at the TPFL, show major qualitative and quantitative differences between turbine rig and cascade results. In addition, as shown in [9] and [10], and confirmed by [18], a substantial increase in secondary flow losses is produced by operating at off-incidences caused by off-design rotational speeds. Because of the absence of rotating effects in stationary cascades discussed above, it seems highly unlikely that the stationary cascade investigation would produce any useful results for engine designer.

Considering the above facts, Schobeiri and Han [23] submitted a proposal to DOE with a detailed research program that focused entirely on rotating rig experiments with complementary rotating numerical simulation , where the existing three-stage turbine serves as the experimental platform. Details are discusses in 3.1 Objectives.

2.2 Background, Relation to the Present State of Knowledge

The following is a brief summary of the research work directly related to the proposed research and performed in by the PIs.

Turbine Rotor for Efficiency and Performance Research: To substantially increase the efficiency of HP-turbines, Siemens-Westinghouse (then Westinghouse) gave a major grant to Dr. Schobeiri in 1997 with the task to establish a multi-purpose research turbine facility for high resolution aerodynamics and performance measurements. In a record time of only eleven months, Dr. Schobeiri developed, designed, supervised the manufacturing and completed the shakedown of a state-of-the-art turbine research facility with a versatile three-stage research turbine as its core component. The research facilities are described in detail in study reported in [9], [10] and [12].

Rotating Turbine Blade Film Cooling Research at TPFL: The turbine rotor with 2D-Blades, was modified for measuring the turbine blade film-cooling effectiveness under rotating condition for a research contract with Solar Turbines (2001-2005). To measure the distribution of the film cooling effectiveness while the turbine is running, we used pressure sensitive paints (PSP). The PIs and their co-workers performed rotating blade film cooling investigations reported, among others in [24] and [25].

Rotating Turbine Hub Platform Film Cooling, Heat Transfer Research at TPFL: To successfully complete the research work for the UTSR, 7/1/03 – 12/31/06-project, Dr. Schobeiri designed a completely new and highly advanced three-stage turbine rotor with two independently controlled cooling loops that provides the necessary mass flows for cooling purposes, details are shown in several places in this report. This new turbine rotor exhibits the experimental platform of this research. The

new rotor provides the basic features to extract information relevant to gas turbine design communities. These features are (a) stator_rotor unsteady interaction, (b) blade and platform rotation, including the relative blade circulation and the exposure of the platform boundary layer to centrifugal and Coriolis forces, and (c) the flow acceleration. Except for the last feature (c), none of the above features can be simulated in a cascade investigation. Schobeiri and his co-workers [26] carried out the cooling effectiveness experiments on the rotor blade hub platform using the PSP technique. Particular attention was paid to the film cooling effectiveness from coolant leakage through the circumferential gap between the stationary and rotating components of the turbine. Film cooling effectiveness results were obtained at three rotational speeds of 2550 rpm, 2000 rpm and 1500 rpm with corresponding incidence angles of 23.2º, 43.4 º and 54.8 º. For each rotational speed, the mass flow ratio was varied from 0.5% to 2.0%. The study showed that film cooling effectiveness due to coolant injection from the stator-rotor gap increases with increasing of the coolant-to-mainstream mass flow ratio.

As a continuation of the previously published work involving stator-rotor gap purge cooling, the study reported in [27] investigates film cooling effectiveness on the first stage rotor platform due to coolant gas injection through nine discrete holes located downstream within the passage region. The study concludes that to optimize coolant usage, maintaining the stator-rotor gap injection mass flow ratio close to MFR=1% and increasing the number of holes on the platform without compromising the structural integrity is the way forward in providing proper film protection on the platform.

Rotating Turbine Hub Platform Heat Transfer Research at TPFL: Following the above film cooling experiments, heat transfer measurements were conducted using TPFL-designed and in house manufactured micro-heaters that were positioned diametrically on the blade channel hub. The heaters were connected via a slip ring to a power supply with variable power control. Detailed heat transfer coefficients measured on rotating hub platform at different rotational speeds are shown in [27] for different mass flow rations (MFR) and blowing ratio (M).

Unsteady Aerodynamics and Heat Transfer Research: HP-, LP- Turbine: Systematic fundamental research has been performed by Schobeiri and his co-researchers, dealing with turbulence, unsteady aerodynamics, unsteady boundary layer transition and heat transfer under unsteady wake flow conditions. NASA (1990-2005) and GE (1991-1993) sponsored research projects to investigate the effects of periodic unsteady wakes on boundary-layer flow transition and heat transfer in curved-wall channels with zero, positive, and negative pressure gradients. DOE-Advanced Gas Turbine Systems Research (1993-1996) and GE (1996-1997) sponsored a project to study the effects of periodic unsteady wakes on turbine blade boundary-layer transition and heat transfer, performance and trailing edge ejection optimization. These studies resulted in a number of technical publications among others [28], [29], [30], [31], [32], and [33], which constitutes the basis for the development of a new unsteady boundary layer transition implemented in many Navier-Stokes codes. LP-turbine unsteady aerodynamics research initiated by Schobeiri has been continuously supported by the NASA Glenn Research Center. This research has lead to numerous original publications, among others, [34], [35], [36], [37] and [38], that contribute to a full understanding of

LP-turbine boundary layer transition, separation and re-attachment. High resolution and detailed measurements using hot wire anemometry, pressure sensitive paints (PSP), liquid crystal, temperature sensitive paints (TSP) and surface mounted hot films are used to understand the flow behavior on the surface and in the boundary layer. In addition, pneumatic five and seven hole probes were used for measurement of flow total and static pressure as well as velocity components and angles.

Numerical Simulation: To critically evaluate the predictive capability of the commercially available RANS-based numerical methods, a comprehensive benchmark study on two different turbines was performed by Schobeiri and his co-workers [39]. It was shown, that in case of a three-stage high efficiency turbine with 3-D compound lean blades, the loss patterns due to decreased secondary flows in the hub and tip vicinity are predicted fairly well. Substantial differences between experiments and numerical simulations were observed in case of a turbine with high secondary flow at the hub. Despite the deficiency in quantitatively calculating the flow properties, it was also observed that the RANS based numerical methods can be used for parameter study. for design purposes.

2.3 Objectives of the Research

The objective of the research was to provide the gas turbine engine designer with a set of quantitative aerodynamics and film cooling effectiveness data which are essential for understanding the basic physics of the complex secondary flow, its influence on the efficiency and performance of gas turbines, and the impact of film cooling ejection arrangements on suppressing the detrimental effect of secondary flows. Endwall aerodynamics, film cooling experimental and the complementary numerical investigations were performed exclusively **under rotating condition**. The highly advanced three-stage turbine designed by Dr. Schobeiri for the past DOE-UTSR project (02-01-SR113, 7/1/03 – 12/31/06), has served as the experimental platform. Using the baseline configuration axisymmetric configuration, non-axisymmetric endwall was designed for endwall contouring.

3. CONTINUOUS DIFFUSION FOR ENDWALL CONTOURING DESIGN

3.1 Endwall Contouring

As discussed in chapter 2, numerous papers have been published that deal with reducing the secondary flow losses. In a recent paper Schobeiri and his co-workers [40] showed that by designing turbines with almost zero pressure difference over first 50% of the axial chord, the secondary flow can be eliminated. The combination of zero secondary flow and a moderate leading edge radius created a turbine blade that is insensitive with respect to an incidence change of ±30°. Investigations by Sauer and Wolf [41 , 42] and the subsequent study by Sauer et al. [21] have shown that the secondary flow losses of a turbine cascade could be reduced by modifying the leading edge profile of an inlet stator vane at the transition from the wall into the leading edge. Zess and Thole [17] performed both computational design and experimental validation of a fillet placed at the leading edge-endwall juncture of a guide vane to eliminate the horseshoe vortex. The fillet design effectively accelerated the incoming boundary layer thereby eliminate the horseshoe vortex. The results of this study also showed significant reductions in the turbulent kinetic energy levels and in the streamwise vorticity levels. Using leading edge bulbs, and a leading edge fillet Becz et al. [16] have shown that both the small bulb and fillet geometries each reduced area averaged total loss by 8%, while the large bulb exhibited a slight increase in total loss.

One of the measures to improve the turbine efficiency is the endwall contouring. Focusing on the impact of endwall contouring in the turbine efficiency, we present a physics based method which enables researchers and engineers to design endwall contours for any arbitrary blade type regardless of the blade loading, degree of reaction, stage load and flow coefficients. To emphasize the characteristic differences between the present method and those available in the literature, a brief review of existing research work is presented in the following.

Cascade Endwall: The papers discussed in this section represent a few among many that are dealing with the impact of endwall contouring on turbine endwall secondary flow. Experimental and numerical cascade flow study by Ingram et al. [43] showed the influence of end-wall profiling. The best end-wall profile tested has shown a 24% reduction in the secondary loss. Further investigations by Ingram et al. [44] designed a new ‘aggressive’ profiling of the end wall to produce a large reduction in loss possible. However, the experimental results, showed an increase of secondary flow loss. Saha and Acharya [45] combined two curves, one that varies in the streamwise direction while the other varies in the pitchwise direction. They created several contoured end-walls by varying the streamwise variation keeping the pitchwise curve constant. The results show that the contoured end-wall can reduce the secondary flow by decreasing radial pressure gradient.

Praisner et al. [46] studied the application of non-axisymmetric endwall contouring to mitigate the endwall losses of front- and aft loaded turbine blades. With flat endwalls, the front-loaded design showed significantly higher secondary losses than the aft-loaded and the reference conventional blades. To contour the endwall they used two-dimensional cubic splines in both the pitch- and stream-wise directions along the

endwall. The predicted loss reduction for the front loaded airfoil design was at 12% while the measured loss reduction was twice as high at 25%. The predicted and measured loss reductions for the reference blade were 4% and 10% respectively while a 5% row-loss reduction was predicted for the aft-loaded blade. The comparison between the CFD and experiments reveals that, while the CFD calculations predict the trends of flow modifications with endwall contouring, they lack a significant level of accuracy for individual flow features such as the passage vortex. Harvey et al. [47] and Hartland, et al. [48] modified the end wall for the large-scale, low-speed rotor profile in a linear cascade. The end wall surface was created by the product of two curves in axial and circumferential directions. The axial profile was defined by a B-spline curve through six control points. The first three terms in the Fourier series were used to produce the perturbations in the circumferential direction. They reported a measured net total loss reduction by 20% and the net secondary loss by 30%. The CFD losses show little change. The experimental data show mixed-out losses, where the reductions with the profiled end wall were 15% in net total loss and 34% in secondary loss.

Rotating Turbine: In contrast to the tremendous multitude of the cascade endwall papers, from which only a few have been discussed above, there are only a few investigations of the impact on endwall contouring in rotating turbines. Brennan et al. [49] redesigned the HP turbine of the Rolls-Royce Trent 500 engine with the application of non-axisymmetric end walls. The profiled end-wall shape was determined by six control stations which were fixed at specified axial distances along the mean camber line of the airfoil. The addition of profiling to the end-walls of the HP Turbine is predicted to reduce secondary loss by 0.24% of the NGV and by 0.16% for the Rotor. The total improvement in stage efficiency for the HP Turbine is therefore +0.4%.

Harvey et al. [50] redesigned the IP-turbine stager by applying non-axisymmetric end walls to both the vane and blade passages. They reported an improvement in the stage efficiency of 0.9 ± 0.4% at the design point. Germain et al. [51] studied the improvement of efficiency of a one-and-half stage high work axial flow turbine by non-axisymmetric endwall contouring. The endwalls have been designed using automatic numerical optimization by means of a Sequential Quadratic Programming (SQP) algorithm. Both hub and tip endwalls of the first stator as well as the hub endwall of the rotor were modified. The experimental results confirm the improvement of turbine efficiency, showing a total-total stage efficiency benefit of 1%±0.4%, while the improvement is underestimated by CFD. Snedden et al. [52, 53] utilized 5-hole probe measurements in a 1.5 stage low speed, model turbine in conjunction with computational fluid dynamics to gain a more detailed understanding of the influence of a generic endwall design. Results indicated a 0.4% improvement in total-total rotor and stage efficiency as a result of the application of the generic non-axisymmetric endwall contouring. However, at higher loading the rotor efficiency was reduced by 0.5%.

Considering this circumstance, extensive numerical simulations were performed to find an optimum method of endwall contouring to be applied to a three-stage turbine before an expensive hardware modification is performed for experimental verification.

3.2 Traditional Design Methods for Endwall Contouring

As extensively discussed in [54], the deficiencies in turbulence and transition models that cause major differences in efficiency calculations compared with the experiment, suggest that caution should be exercised, when interpreting numerical results. Therefore, the numerical results generated under these circumstances are of qualitative nature only. In performing parameter variations, however, the numerical simulation predicts the trends satisfactorily. For our turbine rig application shown in Figure 3.1, extensive verifications and possible rectifications of the existing methods were essential before producing hardware to be tested. This required extensive numerical studies to determine the impact of the above methods on the turbine rig flow field including pressure, velocity, vorticity, total pressure loss distributions and the turbine efficiency. We numerically simulated several cases. For each individual case several grids were generated to ensure the results were grid insensitive, Figure 3.2. By performing the grid sensitivity analysis, we refined the grid density until we achieved a constant efficiency for the entire turbine rig. This is imperative, whenever the efficiency verification is the most important outcome as is in this study. The efficiency convergence required for the rotor a mesh with over 2 million elements, 22 nodes at the wall region and 9 million elements for the entire model. For each single case a parallel computation on A&M Super Computers took more than hundred hours of computation time. For numerical simulation the commercial code CFX with SST-turbulence model was used. Extensive turbulence model studies performed on several TPFL-turbines and the numerical calculation showed the suitability of SST-model for calculating the flow quantities. For each of the calculated cases, the entire flow field including total pressure loss and the turbine efficiency were obtained. Particular attention was paid to accurately obtaining the efficiency of the turbine with the second rotor endwall contoured. Following the conventional approach applied the three-stage TPFL-HP-turbine blading shown in Figure 3.1, an example is given in Figure 3.3, where the peak is placed on the pressure side of the turbine, while varying its height and the axial position. Several fifth order polynomials were applied to define the variation of contour height and axial position in streamwise direction as shown in

Figure 3.4 shows configurations with (a) a contouring that is raised above the hub and occupies only a portion of the hub surface, called positive contouring, (b) a contouring that is raised above the hub surface but is circumferentially extended towards the suction surface, called extended partial positive, (c) a contouring with a portion that is raised above the hub followed by a portion that is lowered into the hub surface, called partial positive, negative contouring, (d) as (c) but with extended negative part and finally (e) a contouring with extended positive and negative portions that occupy the entire passage, called full passage contouring. Efficiency calculation results of the second rotor for different contouring used in this study are shown in Figure 3.5.

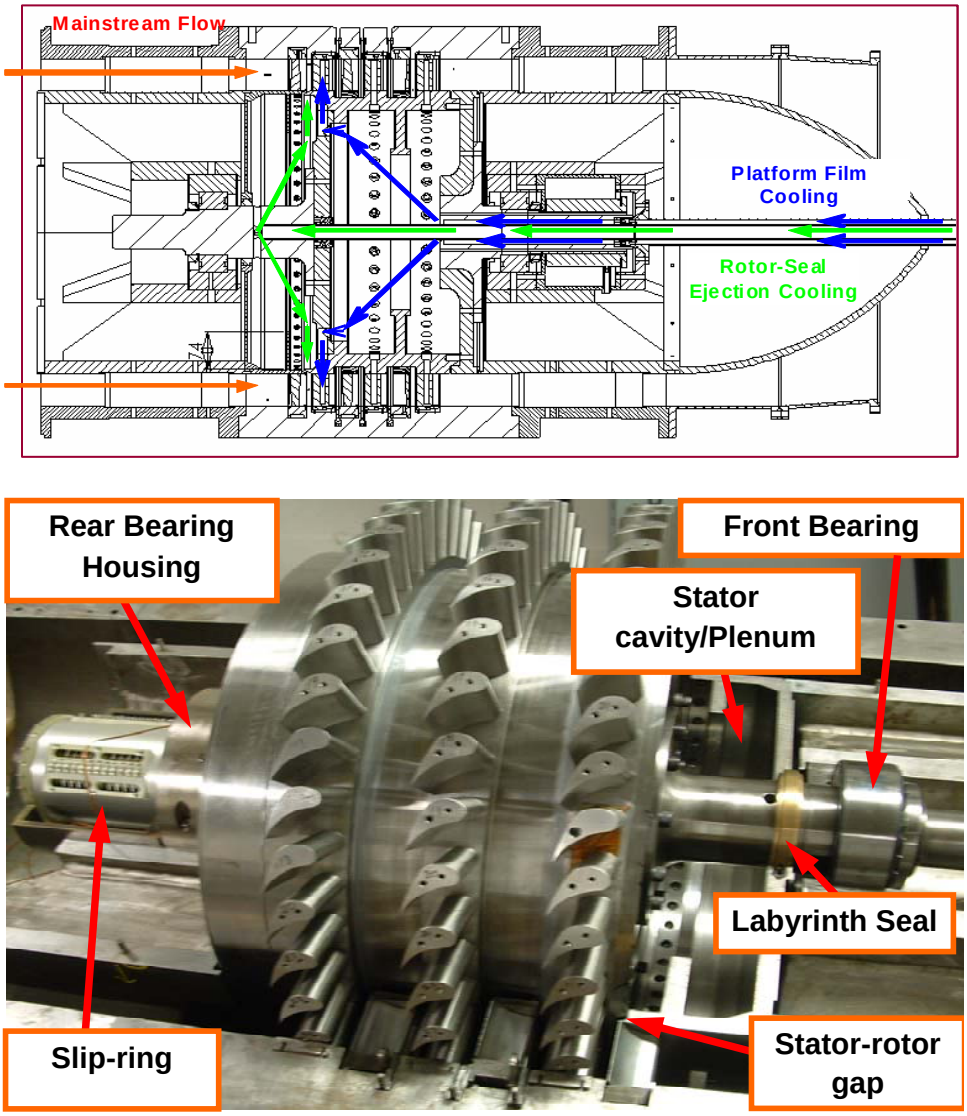

Figure 3.1: Details of the new rotor (top), the three-stage rotor (bottom).

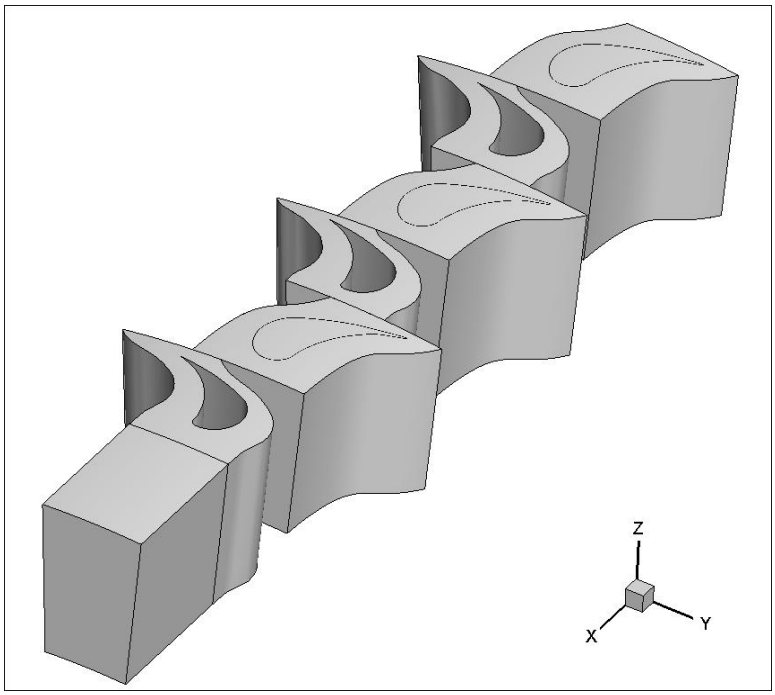

(a)

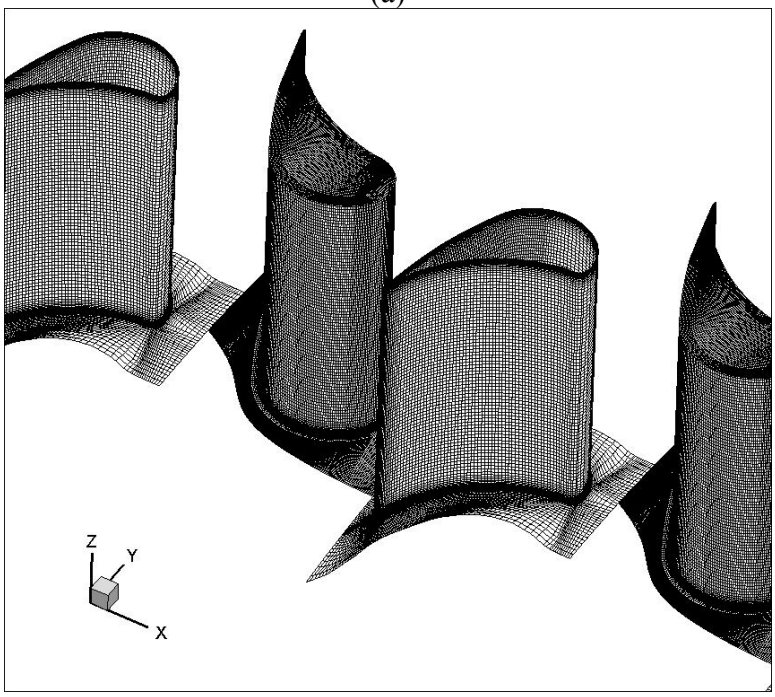

(b)

Figure 3.2: (a) Row-by-row configuration; (b) CFD mesh.

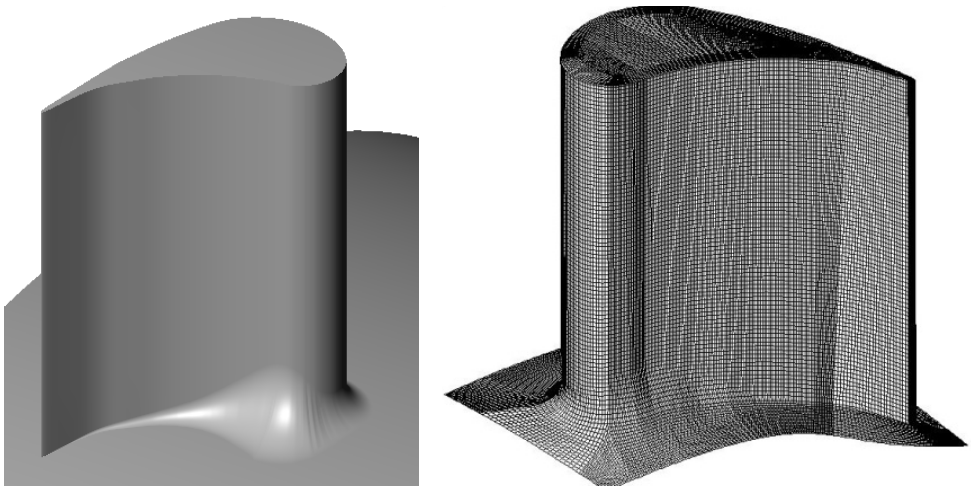

Figure 3.3: Contouring using the conventional method.

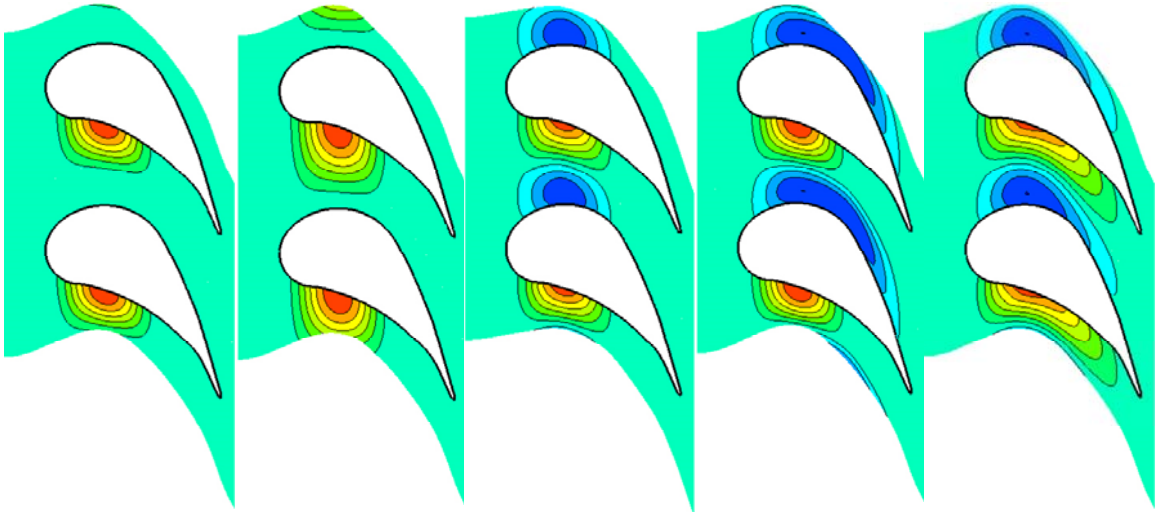

Figure 3.4: Contour variation: (a) partial positive contouring; (b) extended partial positive contouring, (c) partial positive, negative contouring; (d) extended partial positive, negative contouring; (e) full passage contouring. The maximum positive height for all cases is 6 mm, the minimum negative height is -3mm.

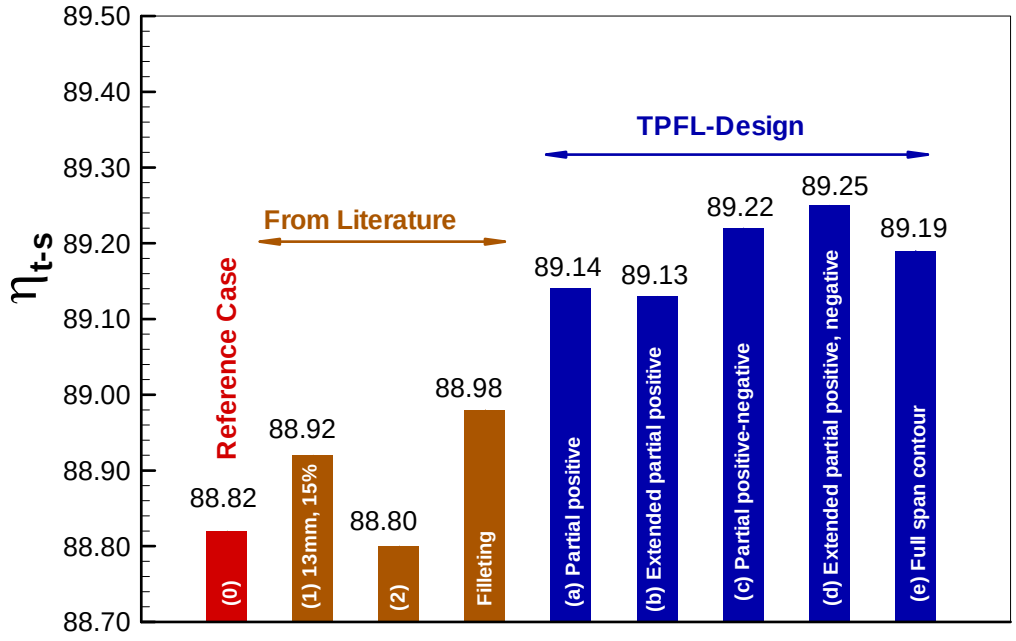

Figure 3.5: Efficiency chart of numerically investigated cases.

Using the conventional approach, several cases were numerically simulated, where the peak height and its axial location were systematically varied. After variation of the height, the peak height was kept constant at 13mm, while its axial location was varied from 15% to 30% of the axial length. As representative examples, Figure 3.5 shows the efficiency calculation results labeled with (1) and (2). In addition, the filleting was also implemented into the catalog of simulations. Assuming an optimal position of the height within the range of 10%-15%, new contour shapes were introduced to perform an optimization process with the efficiency as the objective function. For each case a new grid was generated, numerical simulations performed and the efficiency results presented in Figure 3.5 labeled with (a) through (e). As the results in Figure 3.5 show, using the trial and error approach associated with optimization process that was implemented into the numerical process has not delivered a trend toward an optimum solution. Furthermore, it was shown that the efficiencies were inconsistent throughout and the results were inconclusive to be transferred to different turbine blade types. Most importantly, the method used in the publically available literature is not suitable to provide a generalized design guideline for the research and design community. This circumstance motivated the lead author to introduce a new and physics based method to effectively design endwall contouring for any type of blading regardless its application to HP-, IP- or LP- turbine.

3.3 TPFL Innovative Method: Continuous Diffusion

Turbine blades designed for applications in power generation and aircraft gas turbines as well as in steam turbines have in general different specific stage load

coefficients, flow coefficients and degree of reaction. Furthermore, they are twisted from hub to tip to account for a prescribed radial equilibrium. The stator and rotor row for each turbine type have different solidity, aspect ratio and Zweifel number. In addition, the blades with the same inlet and exit flow angles might have different pressure distributions on pressure and suction surfaces (front- or aft- loaded). In this section we develop a step-by-step physics based method for endwall contouring that can be recommended to the turbine design community as a guideline.

Continuous diffusion method for endwall contouring

The method utilizes a continuous prescribed deceleration of the secondary flow velocity from pressure to suction surface by a diffuser type of flow path that is thought of a number of narrow diffusers with the width ΔW_i, a given inlet height and variable exit heights that produce a desired target pressure. The diffuser raises the pressure on the endwall suction side thus reducing the secondary flow velocity, the strength of the secondary vortices, the associated induced drag forces and the total pressure loss due to the latter. The method can be applied to HP-, IP-, and LP- turbines and compressors regardless the load coefficient, flow coefficient and degree of reaction. It is strongly physics based, very straight forward and easy to use. The following step-by-step instruction presents a tool for appropriately designing non-axisymmetric contours:

1) For the reference non-contoured blade place a cylindrical control surface at a radius $R_{hub}+\delta$ with δ as the boundary layer thickness developed by the secondary flow from the pressure to the suction side, Figure 3.6 (A). The boundary layer thickness can easily be estimated, [54].
2) For the reference blade obtain the pressure distribution on hub, Figure 3.6 (B).
3) For the reference (non-contoured) blade find the actual distribution of the pressure difference Δp_i between the pressure and the suction surface and define a target pressure difference $\Delta p_{target} > \Delta p_{lim}$ with Δp_{lim} as the minimum pressure difference, below which, the diffuser flow will separate. Ideally the target pressure should be close to zero. This, however, will lead to a large area ratio for the local diffuser and thus a flow separation. The attached diffuser performance, Figure 3.6 (D) allows designing an appropriate diffusion path with an optimal performance.
4) Obtain the topology of streamlines at the same radial position, sketched in Figure 3.6 (C1) based on Figure 3.7. This step determines the local velocity vector pertaining to each streamline. This combined with step 5 provides the input to construct the diffuser channels that follow the streamlines. Another alternative is decomposing the velocity vector into axial V_{ax} and circumferential V_u (pitchwise) components. This allows using V_u for constructing diffuser channels that follow the pitchwise velocity component, Figure 3.6 (C2). Both alternatives are equally applicable, however the latter has the advantage of extending the diffuser channels slightly upstream of the leading edge and downstream of the trailing edge.

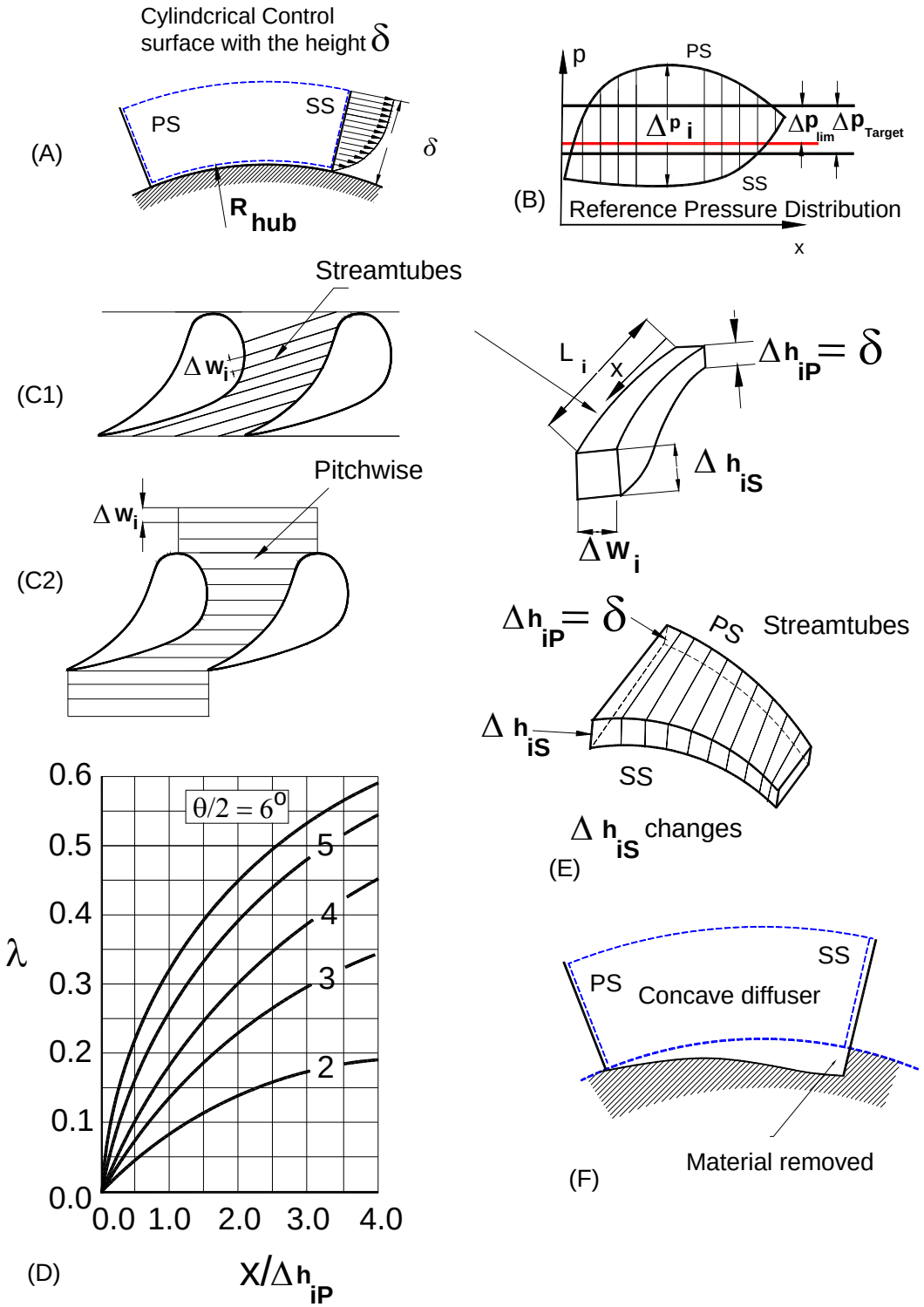

Figure 3.6: Explaining the continuous diffusion process for designing physics based endwall contouring.

5) Starting with a constant ΔWi for example ΔWi = 0.05Cax, choose a pressure recovery factor λ on the suction surface, for example λ = 0.6, by which the flow is still attached. This λ is taken from [55], where a series of diffuser performance maps for different diffuser-length/inlet-height ratios corresponding to x/Δhip are presented. Figure 3.6 (D) schematically represents one of those diagrams. With this λ, then calculate the contour height Δhis on the suction surface that establishes a pressure difference Δp defined in nomenclature that we set equal to Δptarget. Using this target pressure, the diffuser can be constructed, Figure 3.6 (E), with the constant Δhip = δ at the pressure side and variable Δhis > δ at the suction side from leading edge to trailing edge, Figure 3.6 (D).
6) Design the 3-D contour by removing the hub material, Figure 3.6 (F). A decay function at the inlet and the exit ensures a smooth transition of the contour.
7) Make sure that the throat integrity is not affected, this can be checked by using the mass flow balance.
8) Generate a high density grid for the above design and run CFD with SST turbulence model.
9) Re-evaluate the results and make changes if necessary. An "aggressive" endwall design may require a complete re-design of the entire stage.

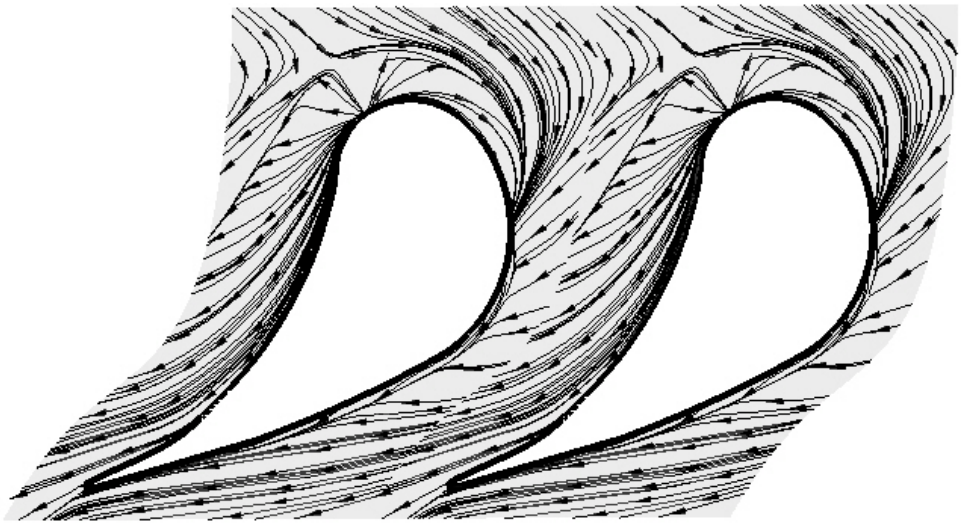

Figure 3.7: Streamlines from suction to pressure surface used for construction the diffusion channel.

4. ENDWALL CONTOURING FOR THE SECOND ROTOR

The new method is applied to the second rotor of the TPFL-HP-turbine, where steps 1 through 7 are executed. The critical range which was captured by the streamlines shown in Figure 3.7 extends from 17% to 55%. Figure 4.1 shows the construction of the new endwall contours compared to the reference case. The reduction of the total pressure loss by 27.9% and accordingly enhance of the second rotor efficiency by 0.51% was obtained based on the CFD predictions.

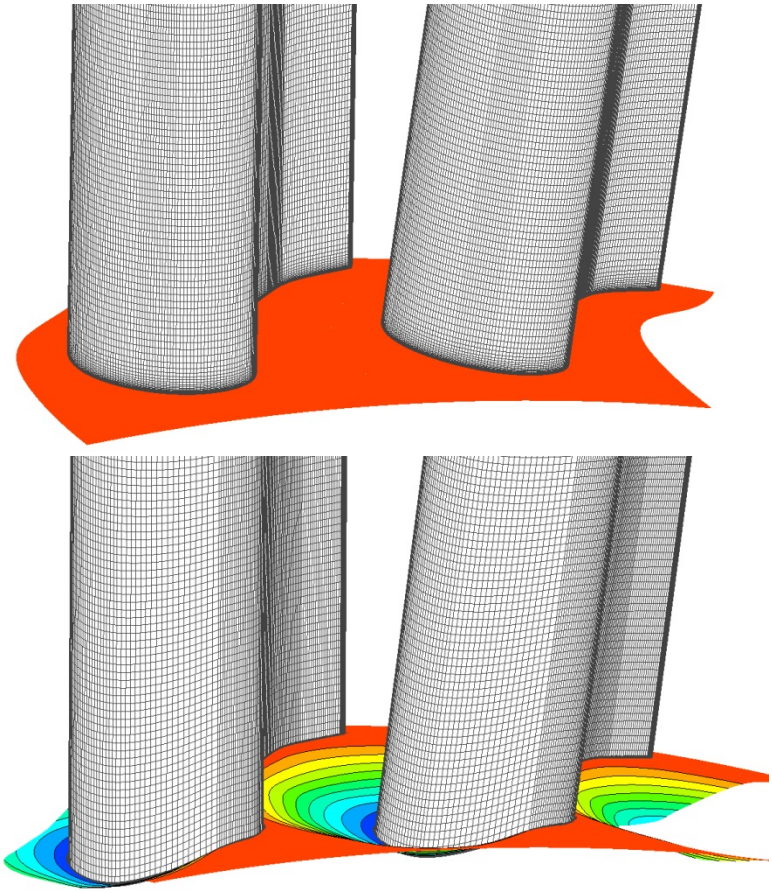

Figure 4.1: Non-contoured (top), new contouring method (bottom).

4.1 Pressure Distributions

Figure 4.2 shows the pressure distribution directly on the hub. A target pressure is constructed and the corresponding height distribution Δh_{is} was calculated using the diffuser performance map by setting λ=0.6. This allows a pressure recovery close to the separation point. With the Δh_{is}-distribution implemented into the hub of the second rotor, a high density grid was generated for the entire turbine. The subsequent numerical simulation delivered the stage flow quantities, among other things, the new pressure distribution on the hub. Figure 4.2 shows a major shift of the suction surface pressure toward the pressure surface with a maximum value of 1600 Pa and a minimum of 800

Pa. As shown, in the target pressure range, the suction surface pressure covers exactly the prescribed target pressure. From about 6% to 17% and from 55% to about 73% there are still substantial pressure gains on the suction surface reducing the suction effect. Upstream of 6% and downstream of 73%there are pressure decreases on the suction side. These can be also eliminated by extending the target pressure to upstream of 17% and downstream of 73%.

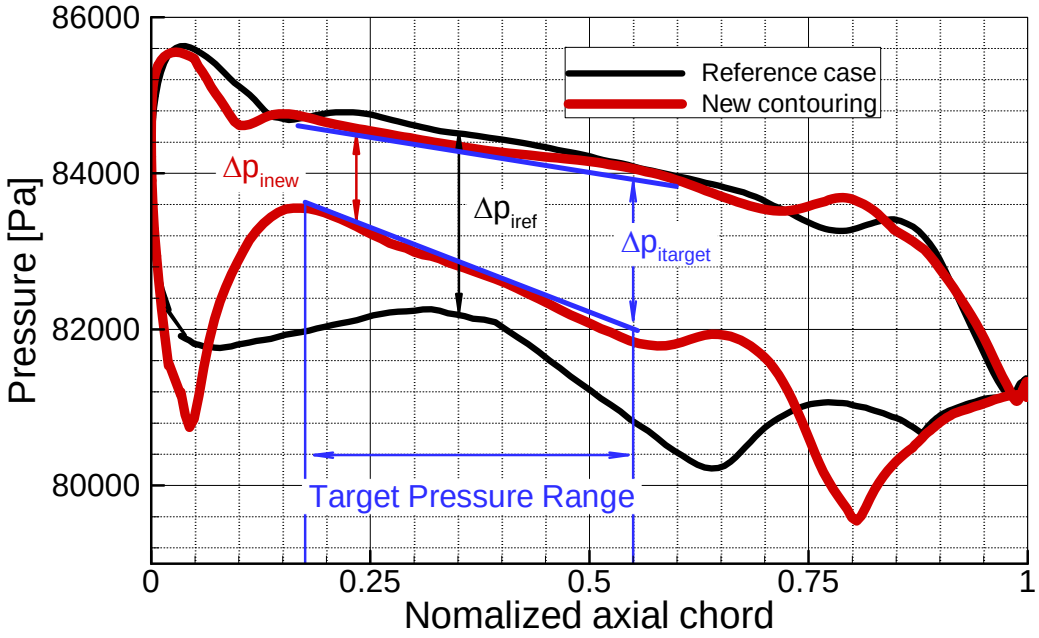

Figure 4.2: Pressure distribution directly on the hub, a target pressure is set the diffusion channel constructed that leads to endwall contouring. Black line: the reference case; Red line: the new pressure distribution.

Figure 4.3 compares three different cases: (1) the reference case, (2) the conventional case using extended partial positive (+6 mm) and extended partial negative (-3mm) shown in Figure 3.4 (d) and the new case. The conventional case is effective only in a very narrow range close to the leading edge. Its effectiveness diminishes, when moving from this region away toward the leading and the trailing edge. Its effectiveness diminishes completely when moving just a few millimeters from the hub surface as shown in Figure 4.4. It should be pointed out that the secondary vortices in this and the reference case extend above 2% span.

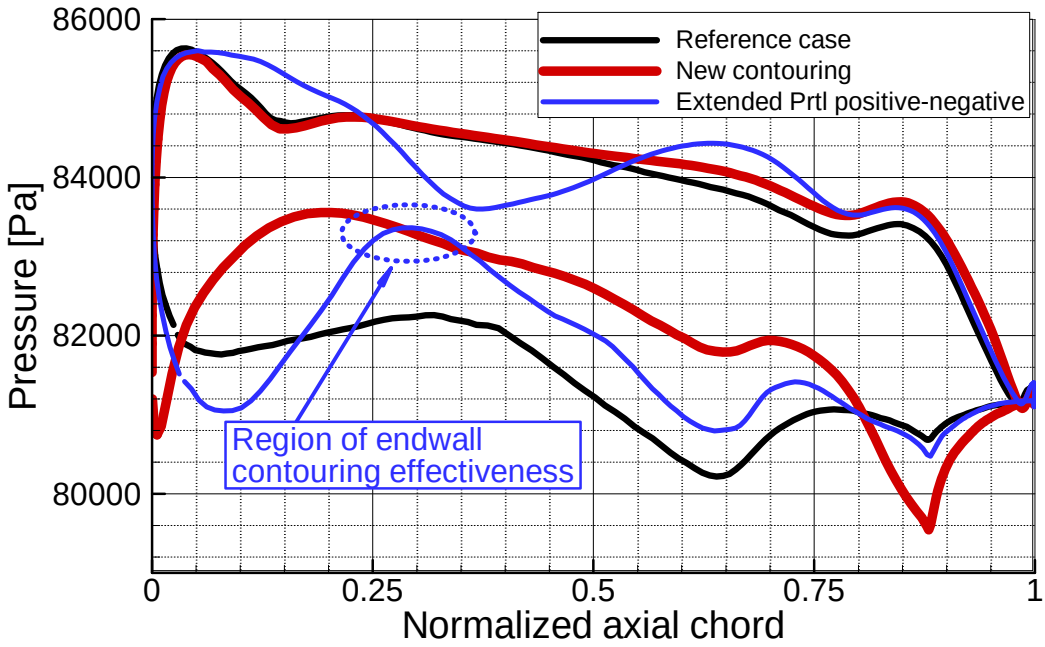

Figure 4.3: Pressure distributions on the hub.

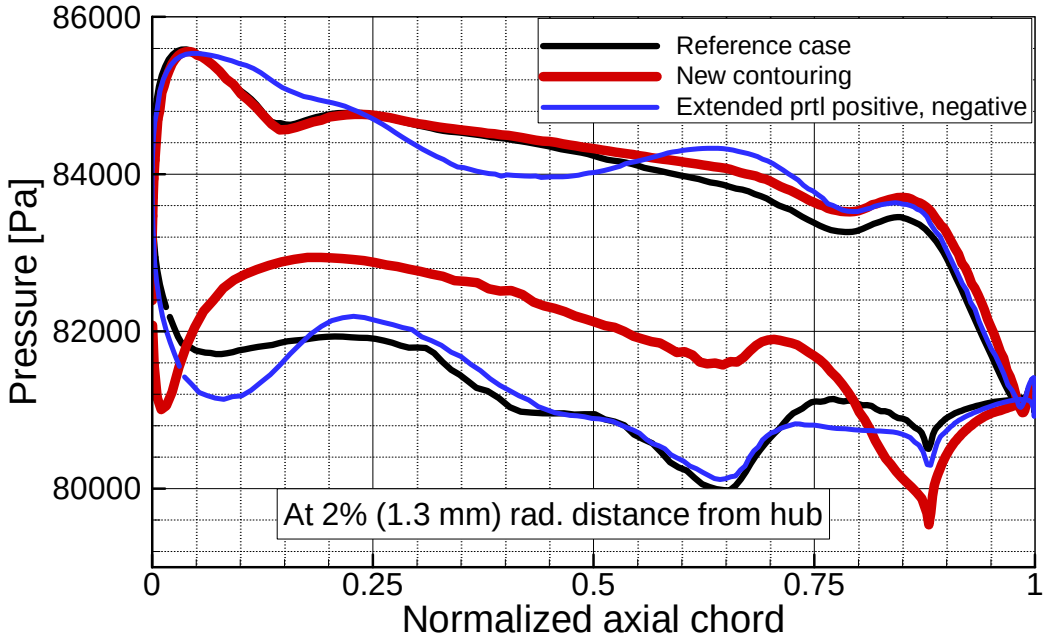

Figure 4.4: Pressure distributions above the hub.

A clear picture of the impact of the endwall contouring on the pressure distribution is seen in Figure 4.5. In the reference case (a) close to the axial location of about 28%, where the maximum positive height is located, with the exception of a wake-like pattern that is caused by the incoming horseshoe vortices, the isobars have more or less an orderly stable pattern. In pitchwise direction, however, a strong pressure gradient fieled

dominates the flow picture from the leading to the trailing edge. Keep in mind that the purpose of the endwall contouring has been to weaken this pressure gradient field. The extended partial positive-negative case (b) seems to only perturb the pressure field locally. This is quite consistent with the pressure distribution shown in Figure 4.3. A more orderly pattern of isobars associated with a much weaker pressure gradient is seen in Figure 4.5 (c) of the new contouring.

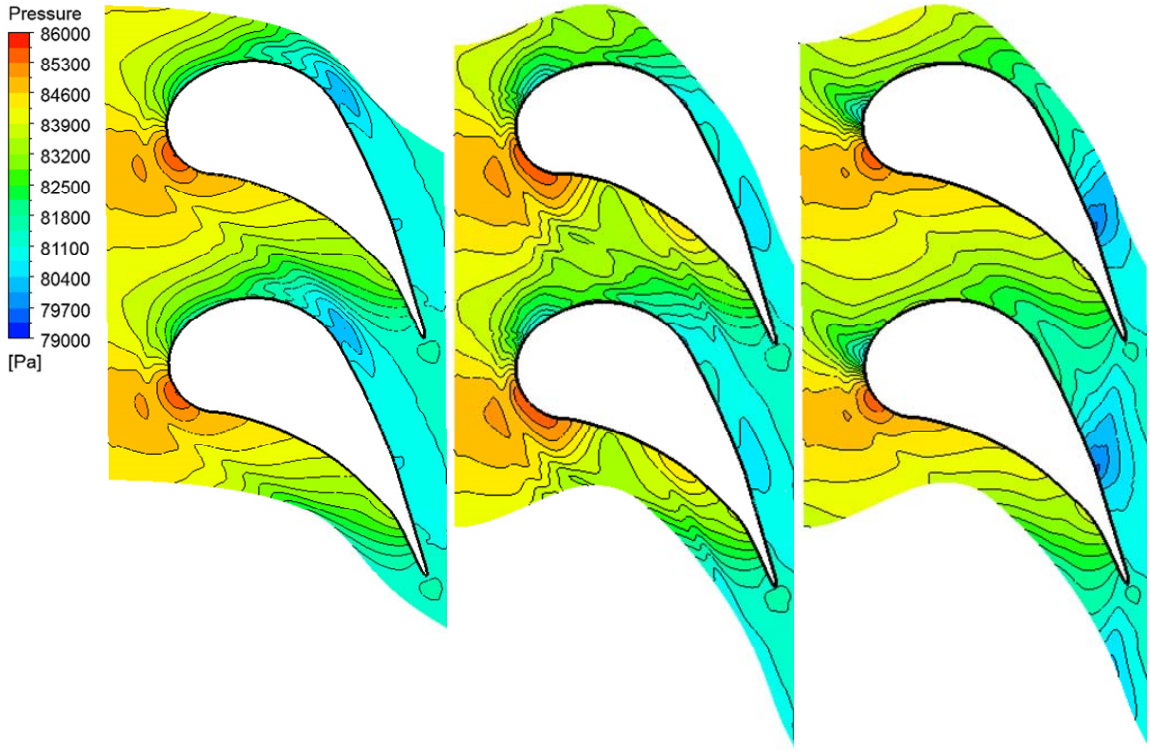

(a) Reference case (b) Extended partial positive, negative (c) New contouring

Figure 4.5: Contour plots of pressure distributions on the hub.

4.2 Efficiency and Secondary Loss

The efficiency calculation for the second rotor with the new endwall contour is presented in Figure 4.6. As seen, the new method has brought an increase of $\Delta\eta$ = 89.33-88.82 = 0.51%. This increase is quite remarkable given the fact that we defined our target pressure such that it covers the critical range of 38% of the axial length. Moreover, it has exceeded all the other values delivered by the conventional trial and error method discussed earlier. Further efficiency improvement is expected by extending the target pressure upstream of 6% and downstream of 73%.

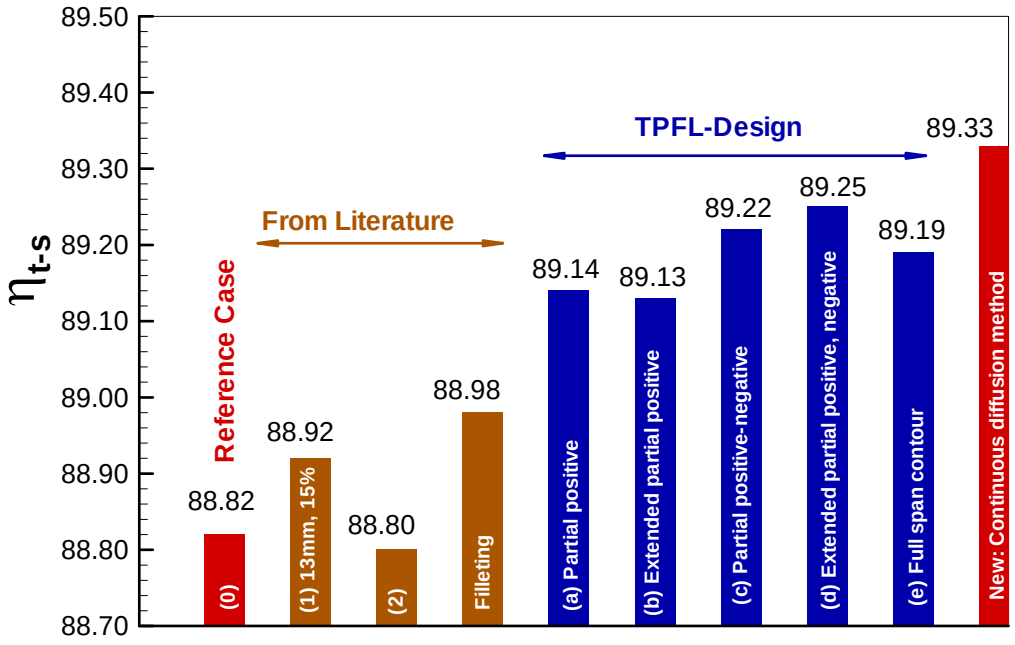

Figure 4.6: Efficiency chart of all investigated wall contours.

Figure 4.7 displays the total pressure loss coefficient for the reference case, the case with extended partial positive, negative and the new endwall contour. For the new contour, the integration of the loss coefficients resulted in a reduction of secondary flow loss relative to the reference case of $\Delta\zeta_R$ = 27.9%. In contrast, in case of the extended partial positive-negative has caused an increase in relative secondary flow loss of $\Delta\zeta_R$ = 6.3%. Considering the calculated second rotor efficiency of 89.25% which is higher than the reference efficiency of 88.82%, Figure 4.6, one may conclude that the increase of the secondary flow loss coefficient and the increase of the efficiency are contradicting each other. However, this is not the case for two reasons: (1) A relative loss coefficient increase of 6.3% has only a marginal impact on the absolute value of the rotor efficiency, (2) when calculating the rotor efficiency the entire aero-thermodynamic quantities are involved that includes total temperature, total pressure and the static pressure.

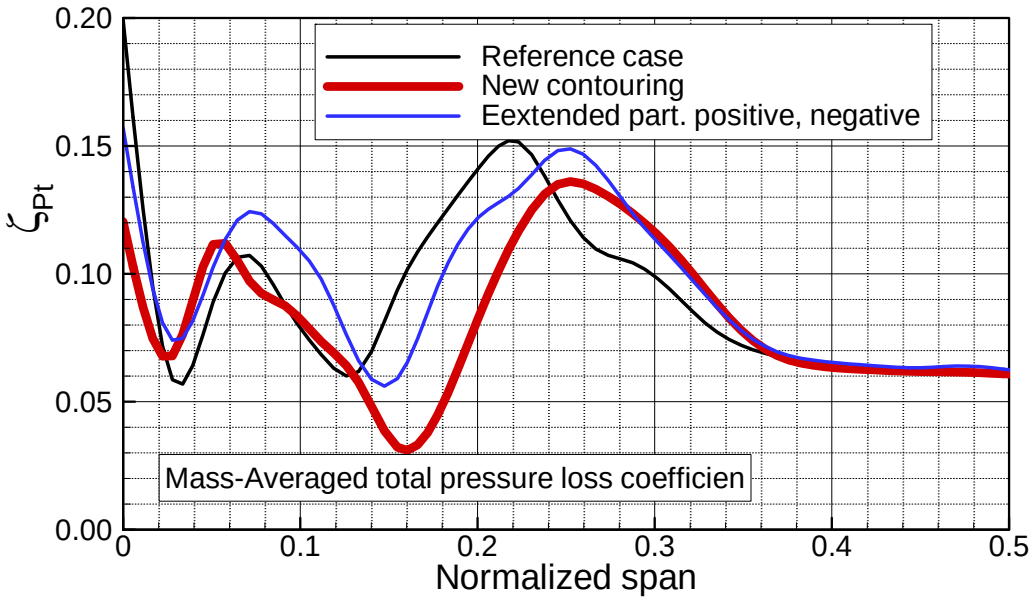

Figure 4.7: Total pressure loss coefficients for reference case, new contouring and extended partial positive, negative.

4.3 Flow Structures

Figure 4.8 depicts the streamlines near the endwall region for both the reference case and new endwall contouring case. In addition to reducing the secondary flow, Figure 4.8 also shows a substantial weakening of the upstream horseshoe vortices. Additionally, very close to the hub, the dominance of the pressure gradient from the pressure to suction surface causes the fluid particles to move pitchwise and produce a system of vortices. Figure 4.9 shows the vorticity distributions at three axial positions. The left column with three figures pertains to the reference (non-contoured) case. For the 30% C_{ax} case, the onset of the vortex seems to locate in between the suction and the pressure surface. It extends to the suction surface, where its strength becomes a maximum. Moving in axial direction its onset moves further toward the suction surface. Close to 55% axial location the onset gains more strength with a maximum that extends radially from the suction surface hub edge to the blade mid-section and beyond. The right column shows the vorticity distribution for the new endwall case. As seen, the vorticity distributions generated by the new method has lower strength than the reference case. This is true for all three axial positions shown in Figure 4.9.

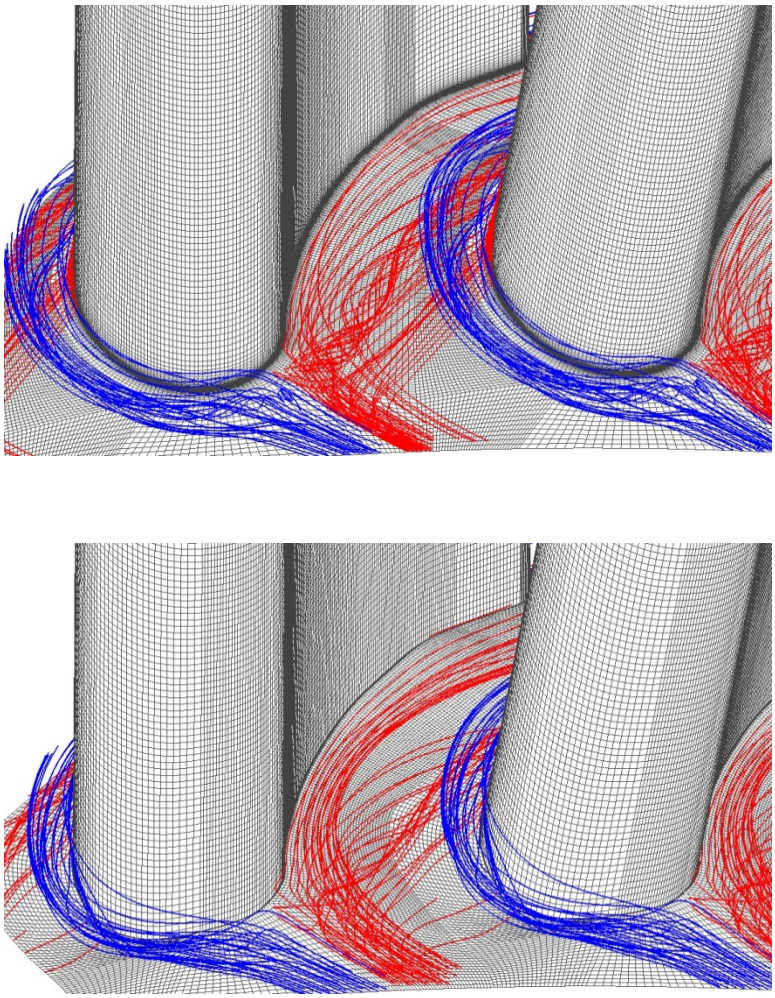

Figure 4.8: Streamlines for reference case (top) and new contouring (bottom).

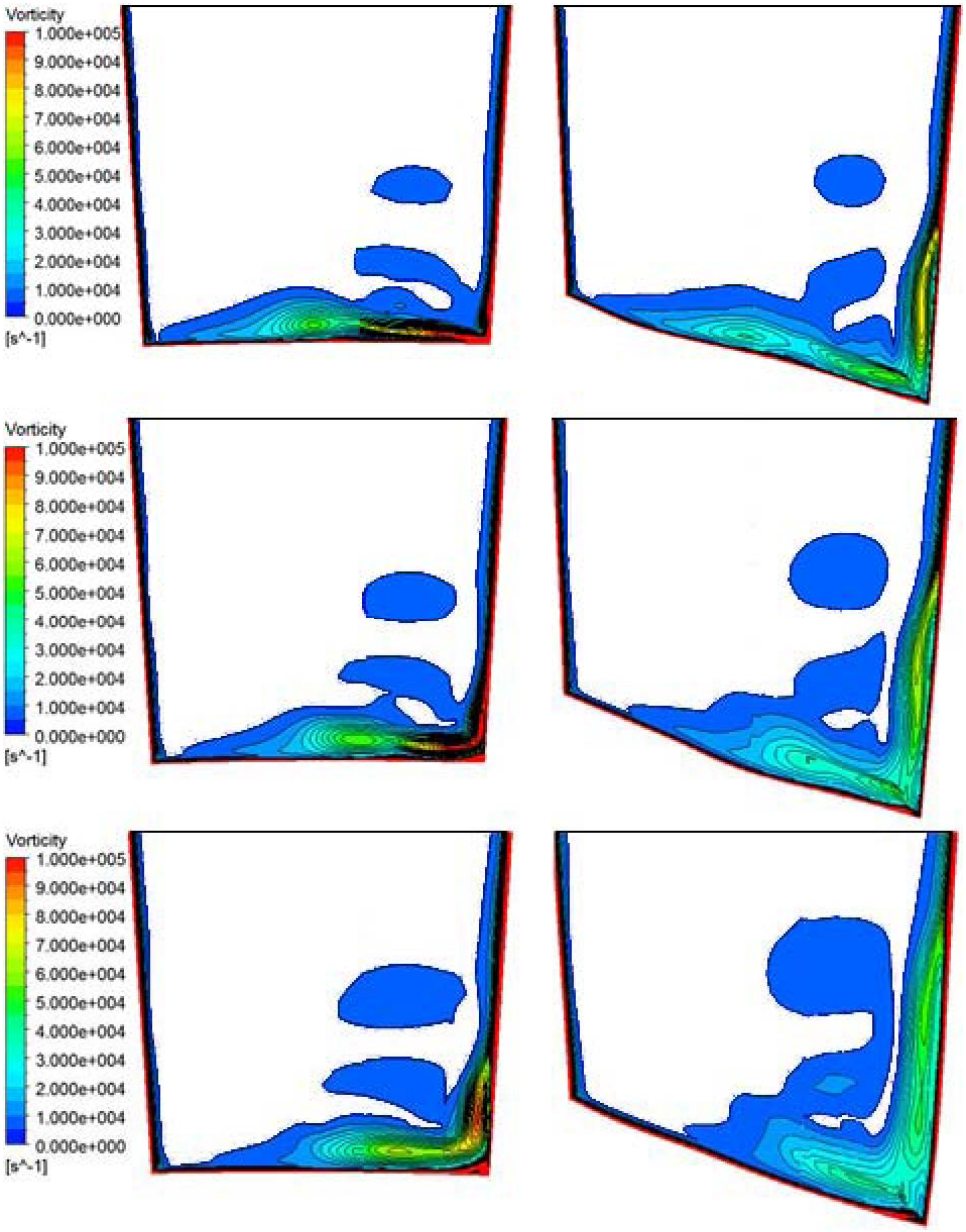

Figure 4.9: Vorticity distribution in the passage.

Reference case (left) at:	New endwall contouring (right) at:
x= 0.30 C_{ax} (top)	x= 0.30 C_{ax} (top)
x= 0.42 C_{ax} (middle)	x= 0.42 C_{ax} (middle)
x= 0.55 C_{ax} (bottom)	x= 0.55 C_{ax} (bottom)

5. COMPARISON OF EXPERIMENTS AND CFD FOR ENDWALL CONTOURING

Applying a new non-axisymmetric endwall contouring technology introduced by Turbomchinery Performance and Flow Research Laboratory (TPFL) at Texas A&M University to the second rotor row of a three-stage research turbine has shown that for a single rotor row a major turbine efficiency improvement can be achieved. Motivated by these results, comprehensive numerical and experimental investigations on the TPFL-research turbine were conducted to determine the impact of the endwall contouring on film cooling effectiveness. For this investigation, the first rotor row directly subjected to the purge flow injection was chosen to which the new contouring technology was applied. Performing an extensive RANS simulation by using the boundary conditions from the experiments, aerodynamics, performance and film cooling effectiveness studies were performed by varying the injection blowing ratio and turbine rotational speed. Performance measurements were carried out within a rotational speed range of 1800 to 3000 RPM. The corresponding CFD simulations were carried out for four rotational speeds, 2000, 2400, 2600 and 3000 rpm. Comparison of the RANS aerodynamics simulation results with experiments reveals noticeable differences. Considering the film cooling effectiveness, major differences between experiment and numerical results were observed and discussed.

5.1 Computational Details

Three-dimensional calculations using steady RANS equations were carried out for the TPFL three-stage high pressure research turbine. Figure 5.1 depicts the computational model and corresponding boundary conditions for CFD simulations. In order to represent the experimental turbine as realistically as possible, all the geometric information is taken exactly from the machine. As seen, the model consists of three stages aligned along the rotating axis. Each stage includes the upstream stator row and downstream rotor row. All the interfaces between the components (stator-to-rotor or rotor-to-stator) are using mixing Plain method. In order to numerically investigate the impact of the purge flow on the endwall film cooling, a large plenum with a narrow slot is attached to the first rotor domain which is a sector of the rotor cavity and stator-rotor gap. The axial width of the slot is 7 mm with 25º inclined angle to the rotor platform. The cavity walls (green) are assumed “Rotating” to simulate the rotating rotor disk. The coolant is supplied at three different MFRs (0.5%, 1.0% and 1.5%) through the lower part of the plenum for film cooling purpose. Otherwise, a stationary wall is put for performance studies with no purge flow. The contoured turbine has the TPFL non-axisymmetric endwall contouring installed for the first and second rotors respectively, whereas the non-contoured case refers to the reference turbine with annular platform.

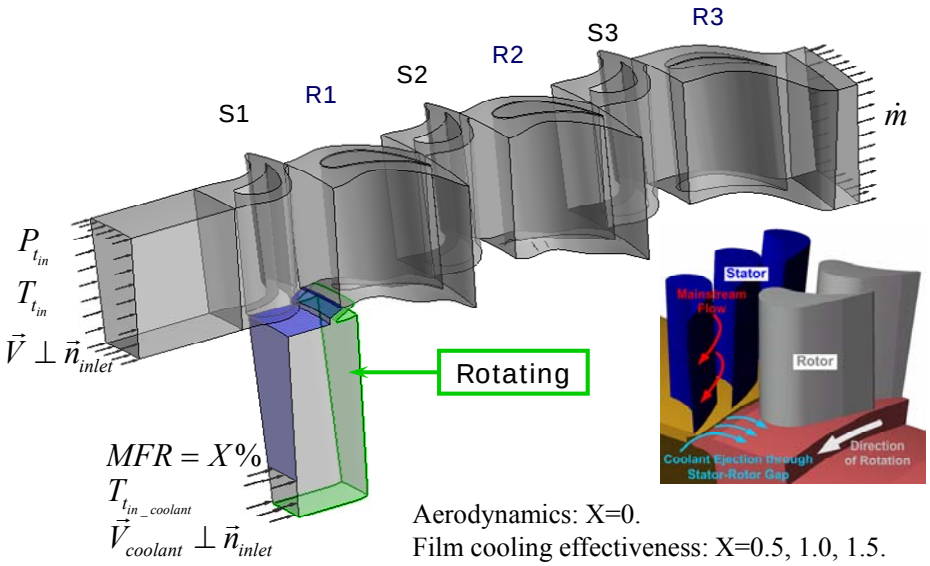

Figure 5.1: Computational domains and boundary conditions.

The boundary conditions were taken from the corresponding experimental data. At the turbine inlet, the total pressure and total temperature are given and the air enters the machine in axial direction. Meanwhile, the mass flow rate is fixed at the turbine exit. For performance calculations, the MFR is set to zero since there is no purge flow on. In total four different rotational speeds (2000, 2400, 2600 and 3000 rpm) are used for investigations of aerodynamics. However, different amount of coolant (MFR=0.5%, 1.0% and 1.5% respectively) is ejected through the first stator-rotor gap for endwall film cooling studies. The total temperature (300K) and the mass flow rate are specified as boundary conditions for the coolant. The flow velocity at the inlet is assumed normal to the boundary. Further, the study of rotation effect on the film cooling effectiveness is performed by varying the rotational speeds of 2000, 2550 and 3000 rpm. In addition, adiabatic and non-slip conditions are assumed on the walls.

The grid independence study was performed with consideration of both the performance and the film cooling purposes. The grid was refined until a constant efficiency was achieved for the entire turbine rig. This is imperative, whenever the efficiency verification is the most important outcome as is in this study. The efficiency convergence required for the rotor a mesh with over 2 million elements, 22 nodes at the wall region and around 9.3 million elements for the entire model, as seen in Figure 5.2(a). Particular attention was paid to accurately obtaining the temperature distribution on the first rotor hub, which is the critical parameter for predicting the endwall film cooling effectiveness. The cases with and without purge flow were tested to obtain the convergence of the adiabatic temperature on R1 hub, as seen in Figure 5.2(b). A part of the converged grid is shown in Figure 5.3.

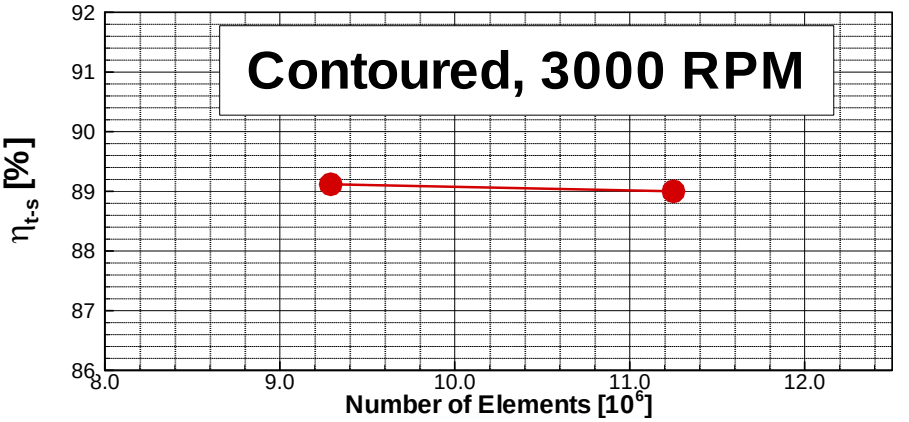

(a)

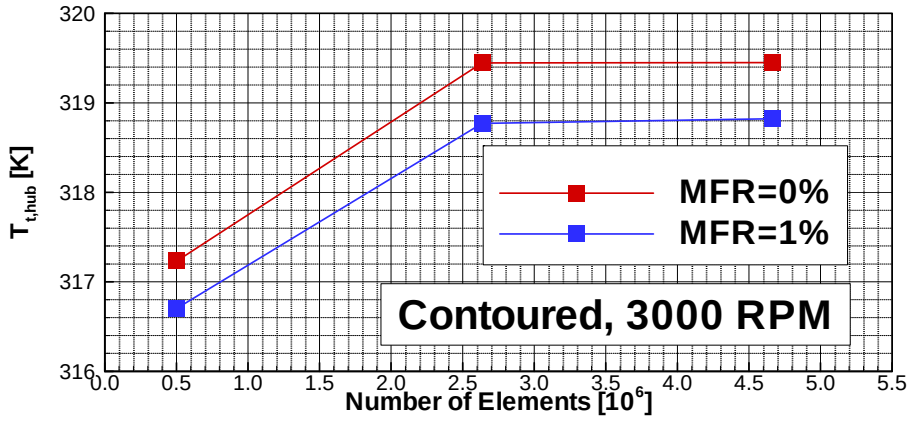

(b)

Figure 5.2: Grid sensitivity study: (a) Total-to-static efficiency of the three-stage HP turbine, (b) Area-averaged temperature on the first rotor hub with and without purge flow.

All the simulations were performed using the CFD software ANSYS CFX. The steady solutions are obtained by solving Reynolds-Averaged-Navier-Stokes (RANS) equations with a finite volume method. Menter's [56, 57] SST-turbulence model was chosen according to extensive turbulence model studies performed on several TPFL-turbines and the numerical calculations showed the suitability of the SST-model for calculating the flow quantities [58]. Each simulation was calculated until the global root mean square residuals for the RANS equations reached values below 10^{-4}. Moreover, various parameters were monitored as the solver was running. Examples include the average pressure at the exit, the mass conservation for the entire machine and the isentropic efficiency of the machine, etc. Convergence was achieved when the residuals' magnitude was lower than 10^{-4}, and the stability was observed in the monitored variables. Typically, 1,500 iterations are necessary to achieve convergence. As a result, each single case computed in the parallel mode on Texas A&M super computers consumed approximately 200 hours of computation time on average.

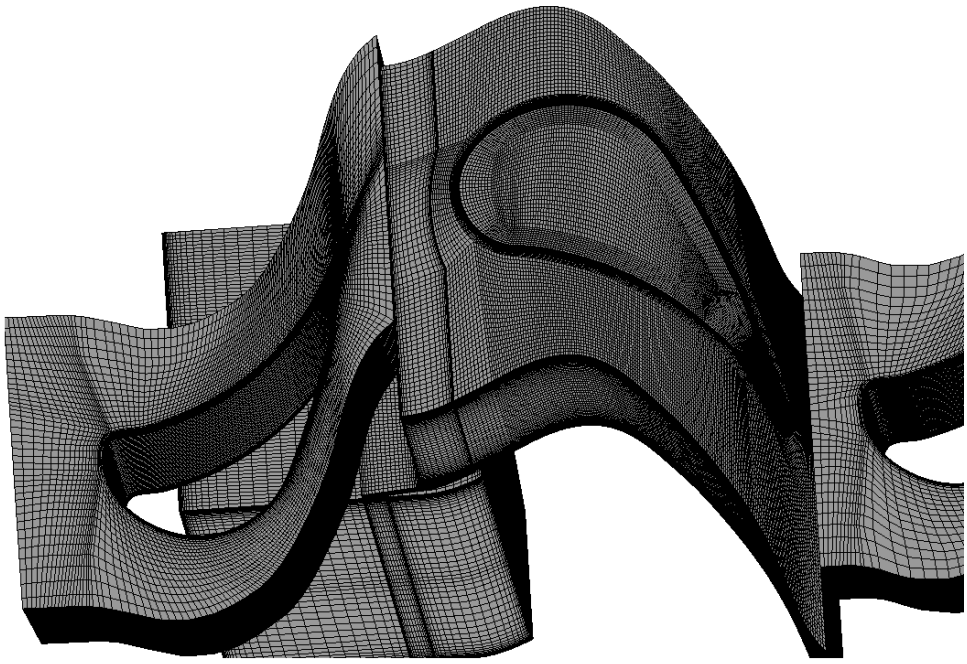

Figure 5.3: The details for the CFD mesh (part).

5.2 Impact of Endwall Contouring on Pressure Distributions

The HP-turbine, in contrast to LP-turbine, has a relatively small aspect ratio which causes major secondary flow regions close to the hub and tip. As a result, the secondary flow caused by a system of hub and tip vortices that induce drag forces resulting in an increase of secondary flow losses, as extensively discussed in [4]. Focusing on the secondary flow loss mechanisms, the fluid particles within the endwall boundary layers are exposed to a pitchwise pressure gradient in the blade channel. The particles move from the pressure side to the suction side and generate a system of vortices. These vortices induce drag forces that are the cause of the secondary flow losses. In addition, their interaction with the main flow causes angle deviation inside and outside the blade channel, resulting in additional losses due to angle deviation. The nature of different flow losses is comprehensively treated in [4]. The secondary flow loss is almost inversely proportional to the aspect ratio. Thus, in HP-turbines with small aspect ratios, the secondary flow loss of almost 40-50% is the major loss contributor.

One of the efficient methods of reducing the secondary flow zone is utilizing the compound lean blade design that reduces the secondary losses by varying the lean angle, [4]. The effectiveness of the 3-D leaned design in suppressing the secondary flow is demonstrated in efficiency and performance studies by Schobeiri and his co-workers, among others [9] and [10]. Another equally efftcive method for reducing the secondary flow losses is the endwall contouring based on a new method that uses continuous diffusion between the pressure side and suction side as detailed in [59]. The method reduces the pressure difference Δp between the suction and pressure surface. As a result, the secondary flows are significantly weakened. The new endwall contouring designed

with continuous diffusion method was applied to the first and second rotors of TPFL HP research turbine, respectively. Following the method in [59], the effectiveness of the endwall contouring is verified in terms of Δp-reduction for different rotational speeds.

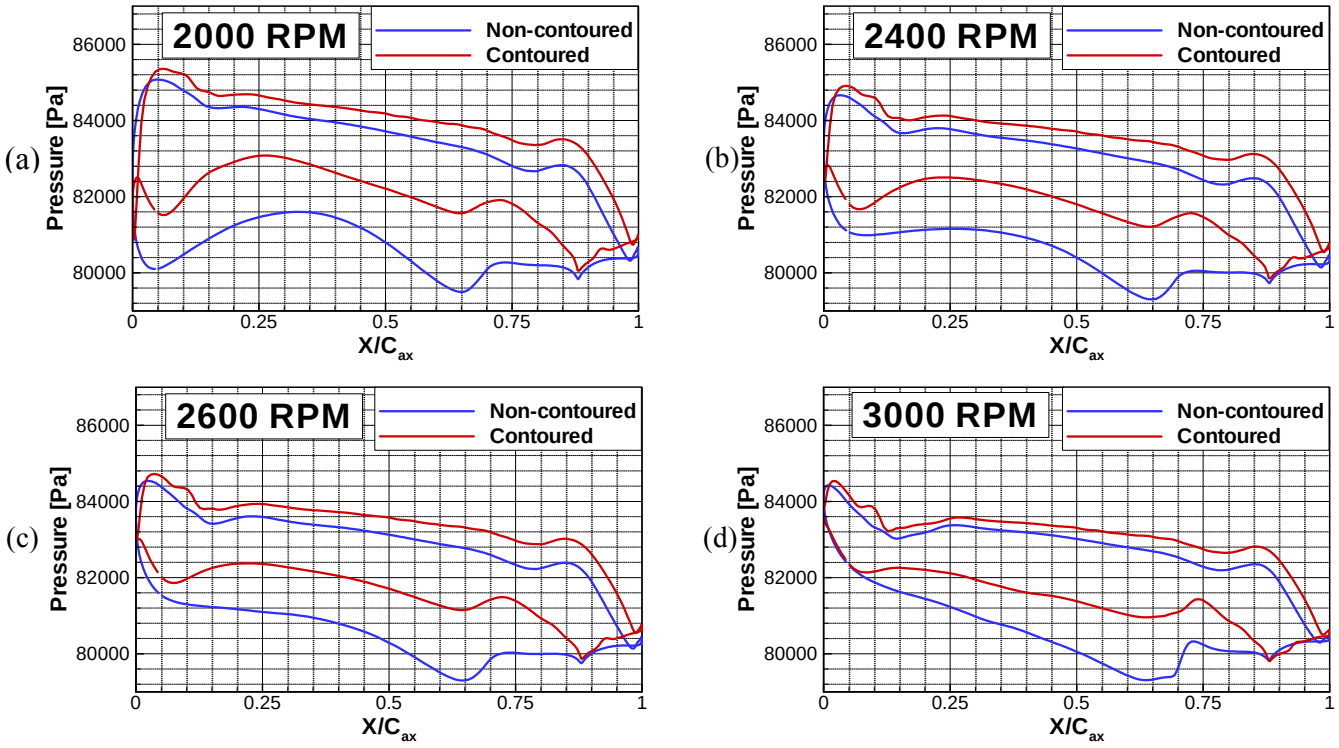

Figure 5.4: Pressure distributions (CFD) directly at the hub of second rotor under different rotational speeds: (a) 2000 rpm, (b) 2400 rpm, (c) 2600 rpm and (d) 3000 rpm.

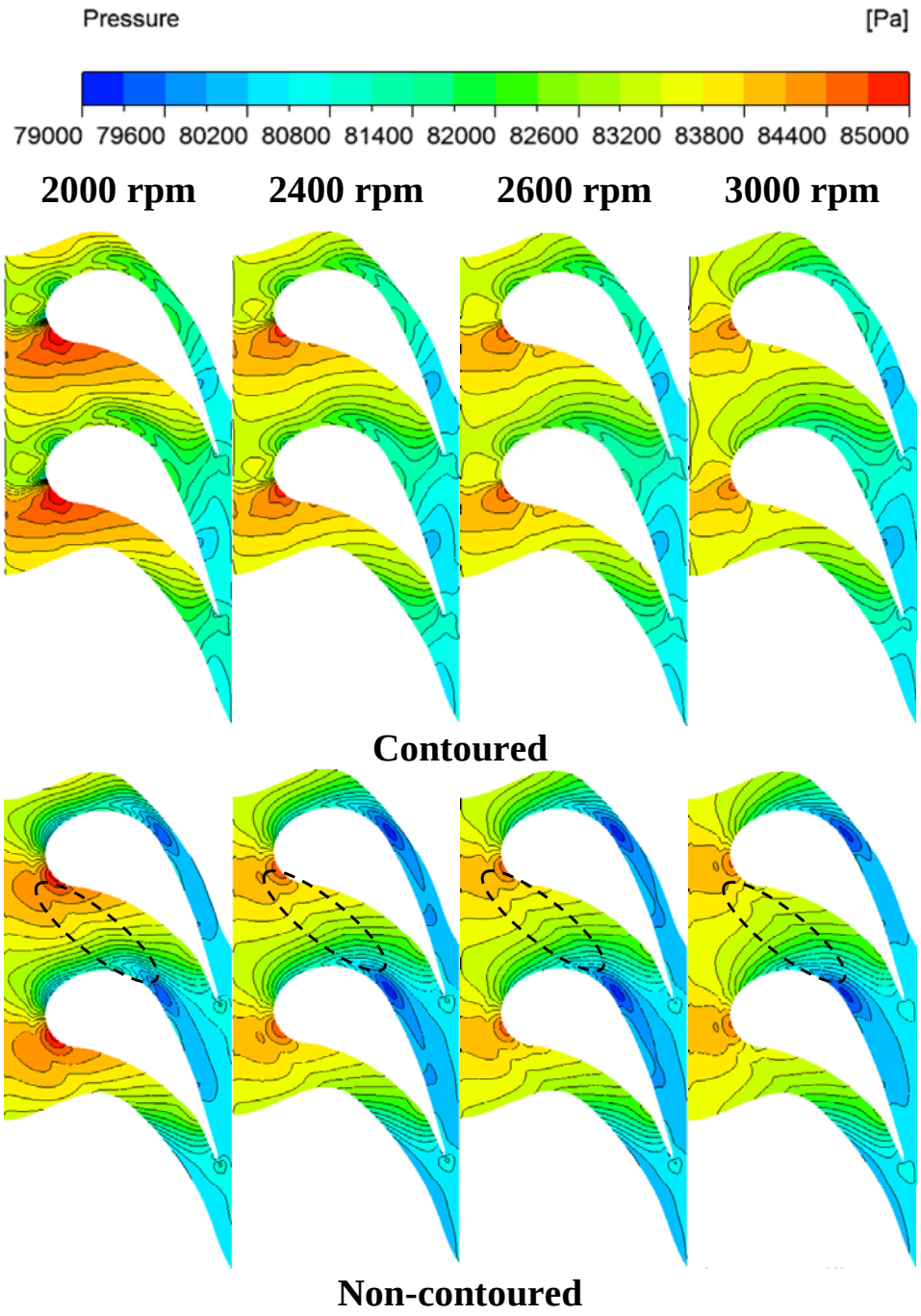

Figure 5.5: Pressure contours (CFD) on the hub of second rotor under different rotational speeds.

Figure 5.4 and Figure 5.5 depict the pressure distributions directly at the hub of the second rotor under four different rotational speeds. As seen in Figure 5.4, a comparison between the contoured and non-contoured case depicts a significant reduction of the pressure difference for the contoured case for all rotational speeds from 2000 rpm to

3000 rpm. For off-design speeds (2000 to 2600 rpm) the pressure differences for contoured and non-contoured are in general much higher than for the design speed of 3000 rpm. This is attributed to the variation of the incidence angle due to the change of the blade rotating speed. With an increase in rotational speed, the circumferential component of the velocity increases. As a result, the stagnation point tends to move towards the suction side (Figure 5.4) and thus raises the local pressure on the suction surface, which provides smaller Δp between the pressure side and suction side at leading edge. It is seen in Figure 5.4 that the presence of the endwall contouring is effective from the blade leading edge to approximately $0.88C_{ax}$ for relatively low rotational speeds of 2000, 2400 and 2600 rpm. For the case of 3000 rpm, the effectiveness is obtained from $0.10C_{ax}$ to $0.88C_{ax}$ due to the small loading at the leading edge. The evidence of the effectiveness is the significant reduction of Δp along the pitchwise direction. Particularly over 30% of reduction in loadings at the hub is obtained from $0.25C_{ax}$ to $0.75C_{ax}$. Additionally, the reduction slightly increases as the blade loading on the hub grows larger. The striking aspect of the results presented in Figure 5.4 (a,b,c and d) is that the endwall contouring not only reduced the secondary flow at design point (3000 rpm) but it also has substantially reduced the intensity of the endwall secondary flow at off-design speeds.

Figure 5.5 shows the pressure contour plots on the hub of the second rotor with varying rotational speeds. For the non-contoured case, the minimum pressure is located on the suction surface at around $0.6C_{ax}$. It acts like a sink intensifying the strength of secondary vortices. However, this point disappears due to the rise of the pressure on the blade suction side with the presence of endwall contouring. In fact, much less contour lines obtained on the contoured endwall indicate that the pressure gradient has been significantly reduced. This is consistent with the distribution of blade loadings on the hub in Figure 5.4. Additionally, each contour line has a small bump in the marked areas for non-contoured platform. The distortion of the pressure contour lines reflects the trace of the pressure leg of the horseshoe vortex. However, it is not found on the contoured endwall since the endwall contouring can, to some extent suppress the formation of horseshoe vortex, which has been shown in [59]. By looking at the pressure distributions on the hub in Figure 5.4 and Figure 5.5, the significant reduction in pressure gradient regardless of the varied rotational speeds indicates the robustness and effectiveness of the endwall contouring for both design and off-design turbine conditions.

5.3 Impact of Endwall Contouring on Secondary Losses

Figure 5.6 depicts the vorticity distributions at three different axial locations of 0.42, 0.55 and $0.69C_{ax}$ for the rotational speed of 2400 rpm. For both contoured and non-contoured cases, the vorticity has similar distributions at each cross-section of the flow passage. High vorticity is seen at the region very close to the endwall near the suction side (I). It also appears in the area closed to the lower portion of the suction surface (II). Very close to the hub, the dominance of the pressure gradient from the pressure to suction surface pushes the fluid particles to the suction surface and produce the highly vortical crossflow. Region I is a result of the movement of the crossflow. The formation of region II is mainly attributed to the mixing of the pressure and suction legs of

horseshoe vortex and rolling up of the formed complex vortex systems. As shown in Figure 5.6, from upstream to downstream, the region I is gradually shrinking whereas the region II is growing fast. Taking a look at the pressure distributions in Figure 5.5, it is seen that the pressure gradient is pointing from the leading edge to the minimum pressure point, rather than the pitchwise direction. The resulted crossflow follows the direction of the pressure gradient, traveling from the leading edge towards the downstream suction surface. Eventually the fluid particles of crossflow hit the suction surface and are swallowed by the horseshoe vortex systems. Meanwhile, by entraining the low momentum boundary layer and mainstream, the size of horseshoe vortex system keeps growing when traveling to the downstream. Therefore, a larger area of region II is obtained whereas the magnitude is decreased as approaching downstream. The conservation of the vorticity explains the decline in magnitude but increase in size. At all three axial locations, the level of vorticity is lower for contoured case compared with non-contoured one. A smaller region I is also obtained with the presence of the endwall contouring. Both phenomena reflect the reduction of the secondary flow due to the contoured hub.

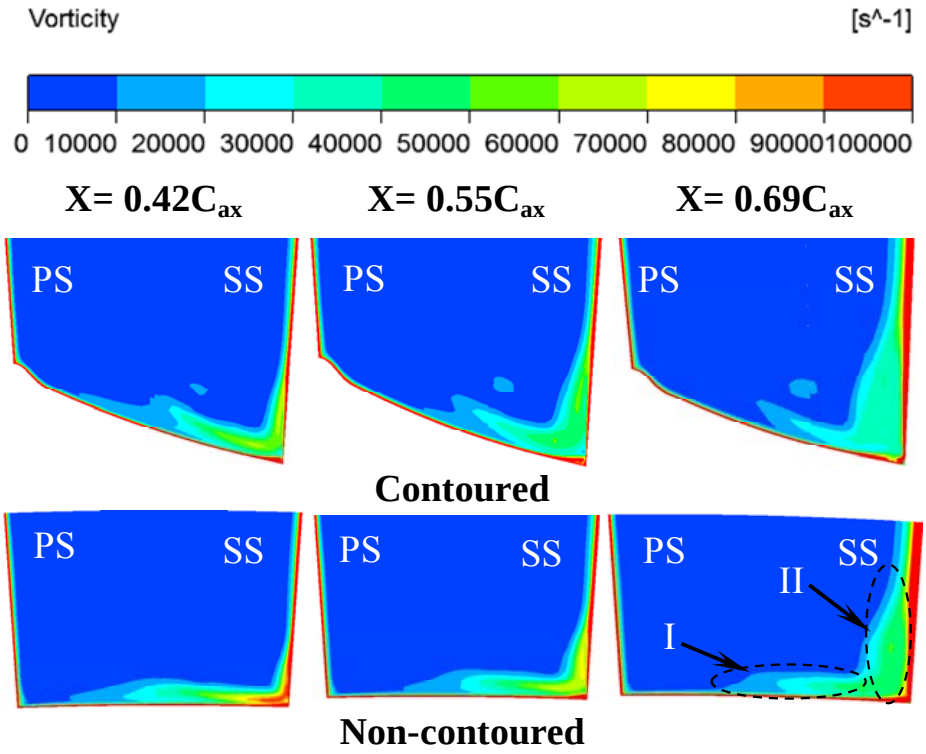

Figure 5.6: Vorticity distributions (CFD) at X=0.42, 0.55 and 0.69C_{ax} under 2400 rpm. Region I is a result of the movement of the crossflow and region II is mainly attributed to the developing passage vortex system.

The comparisons of the CSKE at 0.55 and $0.69C_{ax}$ for both contoured and non-contoured cases under 2400 rpm are shown in Figure 5.7. The distribution of the secondary kinetic energy (SKE) has high similarity with the vorticity contours in Figure 5.6. For all cases, high-level SKE is obtained in the corresponding regions I and II respectively. As extensively discussed above, the high SKE in region I is generated due to the strong crossflow. Meanwhile, the growing horseshoe vortex system contributes to the large SKE in region II. At both cross-sections, the SKE shows smaller magnitude for the contoured case compared to the non-contoured one. In other words, the intensity of the secondary flow near endwall is weakened with the presence of the endwall contouring. Consistent results were obtained for other rotational conditions. It should be noted that the value of the SKE might be over-evluated for the case with endwall contouring. Due to the concave shape of the contoured endwall in the pitchwise direction, the local radial velocity W_{rad} tends to be larger than the non-contoured case at the regions close to the endwall, which is accounted for in the SKE calculation.

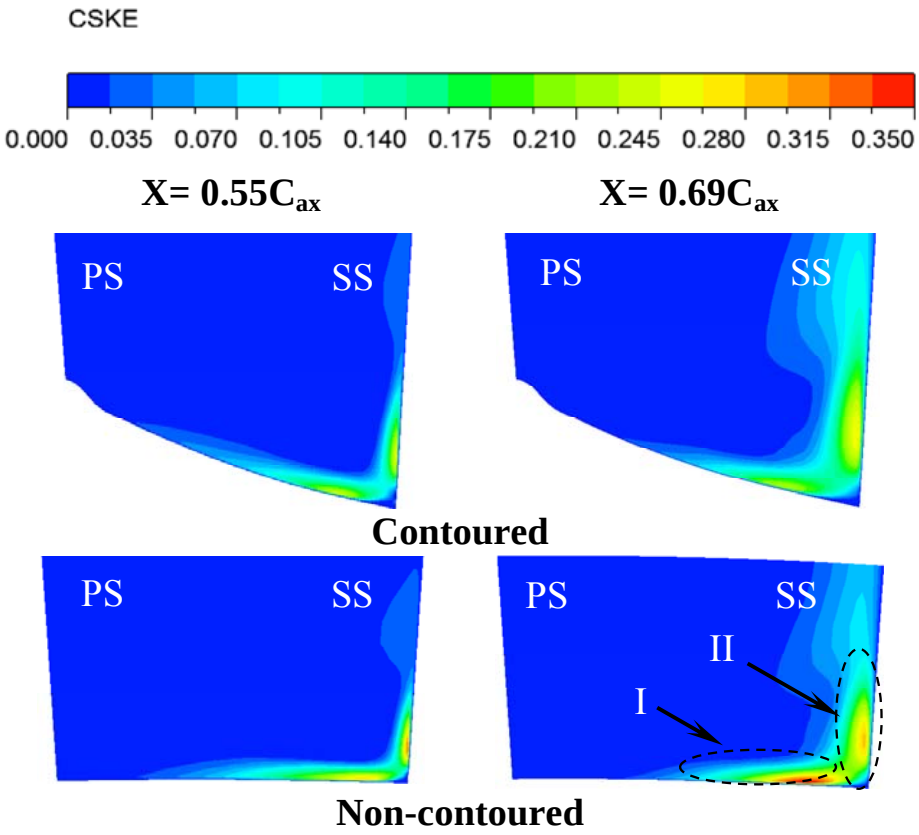

Figure 5.7: The distributions of CSKE (CFD) at X=0.55 and $0.69C_{ax}$ under 2400 rpm. Region I is a result of the movement of the crossflow and region II is mainly attributed to the developing passage vortex system.

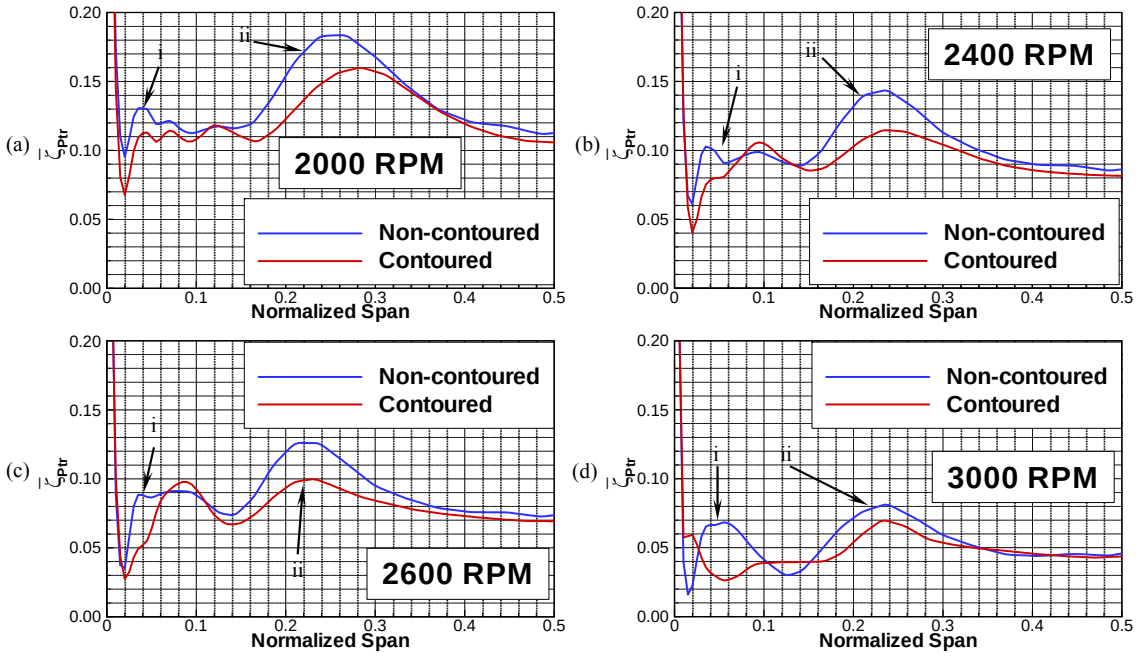

Figure 5.8: The predicted distributions of relative total pressure loss coefficient of second rotor under different rotational speeds: (a) 2000 rpm, (b) 2400 rpm, (c) 2600 rpm and (d) 3000 rpm.

Figure 5.8 shows the pitchwise-averaged loss coefficient for the second rotor at X= $1.07C_{ax}$ with varied rotational speeds. The definition of the loss coefficient is based on the relative total pressure that excludes the circumferential component created by rotation. To obtain a better resolution of the total pressure loss near the endwall, the averaged loss coefficient is plotted from the hub (0% span) up to the mid-span (50% span). As seen, for both contoured and non-contoured cases, there are two primary peaks of the total pressure loss in blade spanwise. The first one (i) covers the area from 2% to about 15% of the blade span. It is known that the loss peak i is caused due to the presence of the corner vortex and the movement of low-momentum boundary layer particles. The corner vortex is generated at the corner of the suction surface and the endwall. It travels along the corner creating secondary flow loss in the region very close to the rotor hub. Meanwhile, the endwall boundary layer contributes to the loss balance by shifting up the peak of the loss.

Another peak (ii) is able to impact the area from 15% to 40% blade span. The loss peak ii is the largest one and also the primary portion of the endwall secondary loss. Its formation mechanism needs to trace back to the generation of the horseshoe vortex at the blade leading edge. After the generation, the horseshoe vortex is divided into pressure-side and suction-side legs. Due to the pressure gradient in pitchwise, the pressure-side leg travels towards the suction surface whereas the suction-leg stays near the suction surface. Subsequently the pressure-side leg hits the suction surface and mixes with the suction-side leg. They roll up due to the wall effect and entrain the fluid particles from the crossflow and meanstream. The vortex system keeps traveling downstream and

growing meanwhile. Eventually the passage vortex is formed, which creates substantial secondary flow losses.

It is seen that the overall loss grows with the increase of the rotational speed. The lowest total pressure loss level is obtained when the turbine is running at the design point 3000 rpm. The off-design conditions create larger secondary losses mainly due to the change of the incidence angle. Under all running conditions, the endwall secondary loss is significantly reduced if the endwall contouring is applied to the rotor hub. For the off-design conditions, the reduction of the loss in region i is not as large as the design point. However, dramatic decline of secondary loss in region ii is gained for all the operating conditions. The significant drop of the endwall secondary losses reveals the excellent capability of the endwall contouring to control and suppress the strength of the secondary flows near the rotor endwall. Particularly the off-design conditions get more improvement from the application of endwall contouring. The first rotor with endwall contouring also gains certain reduction in the endwall secondary losses, but not as much as that in R2 due to the limited space for contouring design [60].

5.4 Impact of Endwall Contouring on Turbine Performance

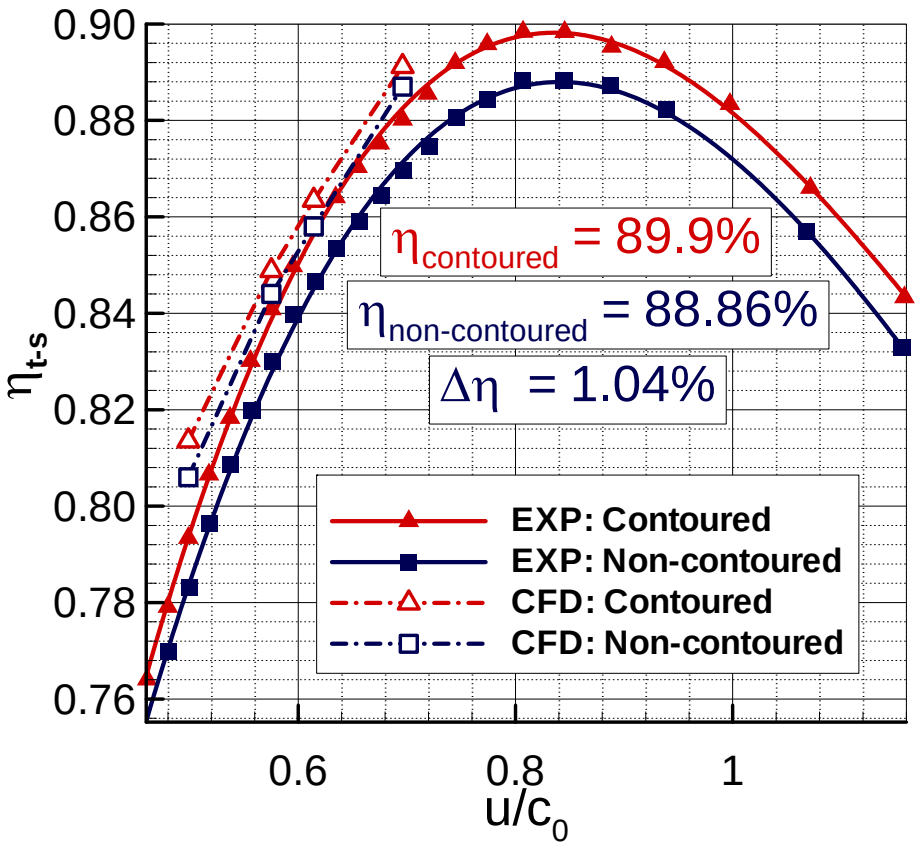

Figure 5.9: Comparison of performance between contoured and non-contoured turbines.

Figure 5.9 compares the experimental measurements and the numerical predictions for the performance of the HP turbine with and without endwall contouring. The measured performance curve (red) for contoured turbine is higher than the non-contoured one (blue) all the way. More than 1% total-to-static turbine efficiency enhancement is achieved everywhere with the presence of the endwall contouring. In particular, at the point where $u/c_o \approx 0.8$, the highest efficiency for contoured turbine reaches to 89.9%, whereas the non-contoured one obtains 88.86% in total-to-static efficiency. The corresponding turbine efficiency improvement achieves as large as 1.04%, which shows the high effectiveness of the endwall contouring and its great potential in industrial applications. The CFD numerically simulates four points for low u/co. The predictions have the same trend as the experiments that the turbine efficiency grows with the increase in u/c_o for both contoured and non-contoured turbines. Nevertheless, the CFD over predicts the magnitude of the efficiency for all cases. The correlated deviation varies approximately from 0.5% to 2%. In addition, about 0.5%~0.77% efficiency enhancement for the contoured turbine is obtained by simulations, which is considerably lower than the measured data.

Since the full inter-stage measurements are not available yet, the detailed comparison of flow parameters is not shown in this study. However, according to the prior TPFL studies [61], the over- prediction of the turbine efficiency can be attributed to shortages of the numerical model. First of all, the mixing Plains, will in effect, wash out any upstream wake via circumferential averaging and re-impose this averaged or "mixed out" profile on the subsequent blade row as inlet boundary condition. By doing such pitchwise averaging, the impact of the upstream wakes, secondary flows, turbulence intensity, etc. will be completely eliminated, which to some extent affects the turbine losses. Secondly, the study is focusing on the influence of the endwall contouring in aerodynamics and film cooling for the turbine rotors. Some features such as the stator labyrinth are not included in the computational domain and thus the losses created by the sealing leakage flow are not considered in the efficiency calculations. In addition, other factors such as the turbulence modeling, transition modeling, and round-off errors can also affect the CFD accuracy. Speaking of the under-prediction of the efficiency improvement by endwall contouring, it is found in [61] that the discrepancy could be attributed to model deficiencies in predicted secondary flows and secondary flow mixing effects. CFD codes were found to mix out any secondary effects rather rapidly when compared to experimentally observed secondary flow tendencies. This may explain why the predicted efficiency for non-contoured turbine has large difference with the experimental data due to the strong secondary flow effect. However, CFD still obtained higher efficiency for the contoured turbine when compared to the non-contoured case and provided useful information in flow behaviors and secondary loss mechanisms.

6. NUMERICAL INVESTIGATIONS FOR ENDWALL FILM COOLING

6.1 Introduction to Endwall Film Cooling

Over the past five decades, the thermal efficiency of gas turbine engines has been continuously rising as a result of an increased turbine inlet temperature. In pursuit of higher thermal efficiencies, gas turbines are operated at 1st stage inlet temperatures around 1500˚C resulting in excessive thermal stresses on the turbine components. Continuous operation under high turbine inlet temperatures enhances the possibility of thermal failure of the hot gas path components. Also, the non-uniform temperature profile of the gas exiting the combustion chambers further exposes the rotor platform to higher temperatures requiring effective thermal protection.

Film cooling is an external cooling technique commonly used in conjunction with internal cooling to protect the turbine components from the mainstream hot gas. In film cooling, a portion of the coolant used for internal cooling is ejected through slots or discrete holes over the surface of the components that need thermal protection. The coolant thus ejected displaces the mainstream boundary layer creating a protective film on the surface of the exposed component. This isolates the hot mainstream gas from the metal surface and considerably decreases the magnitude of the temperatures the hot gas path components encounter.

Rotating turbine experiments performed by Schobeiri and his co-workers [24], [25] and [62] showed that the turbine rotational speed is the most critical parameter in film cooling effectiveness distributions. At the design operating speed, the effect of rotation is displayed as quasi-elliptical shaped spots that sp radially. The measurements were done using the pressure sensitive paints (PSP). Furthermore, their systematic experimental results show that during an off-design operation, the incidence angle changes, causing the coolant film direction to change. As the detailed literature studies in [24], [25] and [62] show, the measurements in non-rotating turbine cascades do not reveal any of the pattern changes mentioned above.

Film cooling as an external cooling technique is also used to protect the hub platform from the mainstream hot gas. In this case, a portion of the secondary air stream used for rotor disc cooling is ejected through a circumferential gap over the surface of the hub platform that needs thermal protection. The ejected coolant creates a protective film on the surface of the exposed platform. This isolates the hot mainstream gas from the metal platform surface and considerably decreases the magnitude of the platform temperatures. Due to the complex nature of experimental setup and data acquisition from a rotating rig platform, studies of the effect of purge flow on the platform film cooling effectiveness has been very rare. Using a three-stage research turbine with two independent cooling loops, Suryanarayanan et al. [63] and [64] investigated the rotational effects of the purge flow on the hub platform film cooling effectiveness. Using the PSP measurement technique, the investigation reported in [63] and [64] details the effects of the purge flow under rotating condition on the platform cooling effectiveness. Increasing the rotational speed from 1500 rpm to 2550 rpm increased the magnitude of local film cooling effectiveness for upstream stator-rotor gap injection. Also it was concluded that, as the coolant to mass flow ratio (MFR) of upstream injection was increased from 0.5% to 2.00%, the effectiveness magnitude and distribution on the platform surface increased.

The coolant, from the upstream slot affected by the inlet flow incidence and passage vortex, tended to concentrate close to the blade suction side of the platform. The purge flow alone, however, did not provide sufficient film protection on the downstream region and along the pressure surface on the rotor platform for the coolant to mass flow ratios tested. To shield the downstream region and understand the effects of rotation on downstream hole coolant injection, the report presented in [64] focuses on measuring film cooling effectiveness on the first stage rotor platform of the same three-stage research turbine using nine discrete film cooling holes for three rotational speeds and several blowing ratios. In addition, film cooling tests were also conducted with simultaneous upstream stator-rotor gap. The experiments were conducted using the PSP measurement technique.

As reported in the above studies, the experiments were performed on non-contoured endwalls. In contrast to a variety of published papers dealing with steady cascade purge flow effects, there are only a few papers that deal with the purge flow effect in conjunction with endwall contouring. Abhari and his co-workers [65] and [66] presented studies that contain experimental and computational data of a 1.5-stage high work axial turbine. In [65], the authors investigate the influence of purge flow on the performance of two different non-axisymmetric endwall and the axisymmetric baseline case. They indicate that the experimental total-to-total efficiency assessment reveals that the non-axisymmetric endwalls lose some of their benefit relative to the baseline case when purge is increased. The first endwall design loses 50% of the efficiency improvement seen with low suction, while the second endwall design exhibits 34% deterioration. The subsequent paper [66] presents an experimental and computational study of non-axisymmetric rotor endwall profiling in a low pressure turbine. According to the authors, the measured efficiency revealed a strong sensitivity of the total-to-total efficiency to purge flow. The experiments showed that an efficiency deficit of 1.3% per injected percent of purge flow for the shrouded low-pressure turbine configuration with profiled endwalls investigated. The experiments revealed an 18% reduction of sensitivity to purge flow due to the endwall profiling. A Recent study by Schobeiri and Lu [59] shows that an appropriately designed endwall contouring substantially reduces the secondary flow losses and, thus, increases the efficiency of the turbine row.

As the continuation of the work presented in [63] and [64], the present study focuses on the impact of the rotating purge flow on the flow structures and film cooling effectiveness of the first stage rotor platform with non-axisymmetric endwall contouring.

6.2 Endwall Contouring for the First Rotor

To explain the issues associated with the purge flow mechanism and its impact on the contouring of the rotor row that is immediately exposed to the purge flow, the turbine facility is extensively described in [63] and [64], so only a brief description of the rotor component is given below. The three-stage turbine rotor component is shown in Figure 6.1, Figure 6.2 and Figure 6.3. As seen in Figure 6.1, two independently controlled concentric coolant loops provide the necessary mass flow for all the platform film cooling experiments. The inner loop supplies coolant mass for film cooling experiments on the hub platform through an upstream stator-rotor circumferential gap positioned

between the 1st stage stator and rotor. A concentric jet exits this circumferential gap at an angle of 25º into the mainstream (Figure 6.2 and Figure 6.3). The outer loop supplies coolant for film cooling experiments for the discrete film cooling holes on the platform in the blade passage section. Since the current numerical study is focused on the influence of purge flow, the outer loop is closed.

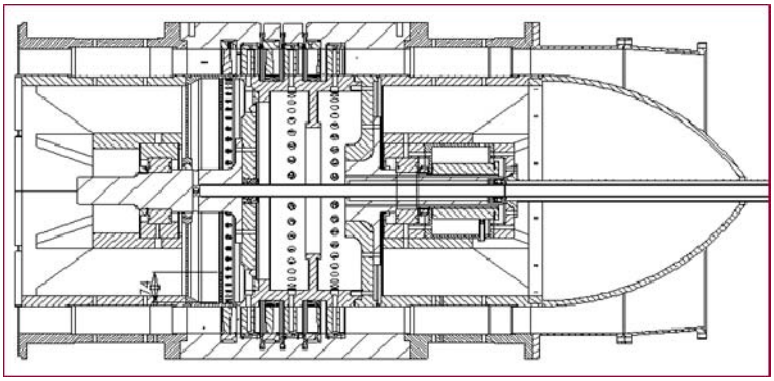

Figure 6.1: Turbine components with two independent cooling loops.

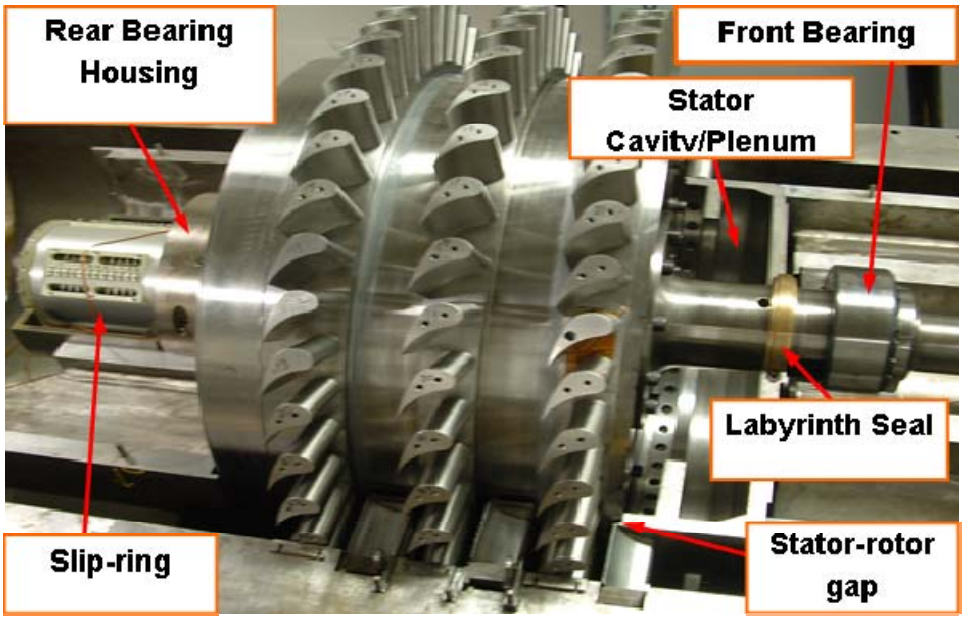

Figure 6.2: Turbine components with showing stator cavity and gap.

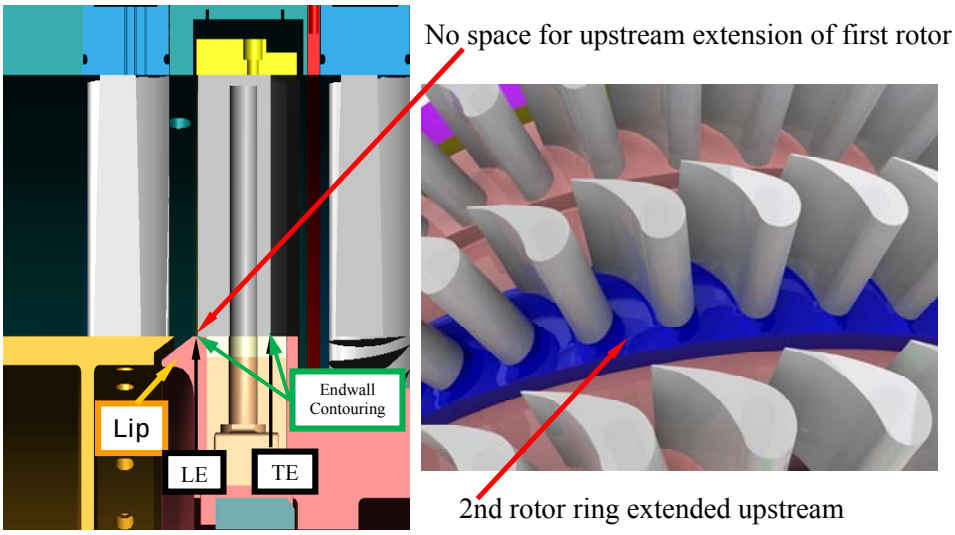

Figure 6.3: Position of the circumferential gap for ejection of purge flow (left), extension of the contouring upstream of second rotor endwall contouring.

While in the case of the second rotor, (Figure 6.3 right) the endwall contouring extended upstream has brought substantial reduction in secondary flow losses and, thus, an efficiency increase, the first rotor is directly exposed to the purge flow with no space to extend the contouring upstream of the first rotor blade leading edge. This circumstance caused a shortening of the target pressure range to design an optimum endwall contouring for the first rotor. Prior to simulating the interaction of the purge flow with the endwall contouring, extensive numerical simulation was performed using commercial solver CFX with SST as the turbulence model and high density grid similar to the one described in [59]. To investigate the effect of the gap presence on the efficiency of the reference case considering the spatial restrictions mentioned above, we started with the reference case without contouring and prescribed a target pressure that caused a sharp deceleration rate, Figure 6.4, curve R1. This resulted in an efficiency that was just slightly above the reference case without contouring. Apparently the corresponding diffuser contour experienced some flow separation. Varying the target pressure by increasing Δp_{target}, Figure 6.5, a moderate deceleration rate was achieved that resulted in a fully attached flow inside the contouring and, thus, higher efficiency as shown in Figure 6.6. As seen the new contouring labeled R1-4 has the highest efficiency of 90.81% compared to 90.47% of the reference case. This efficiency improvement is far below the one we obtained for the second rotor [59].

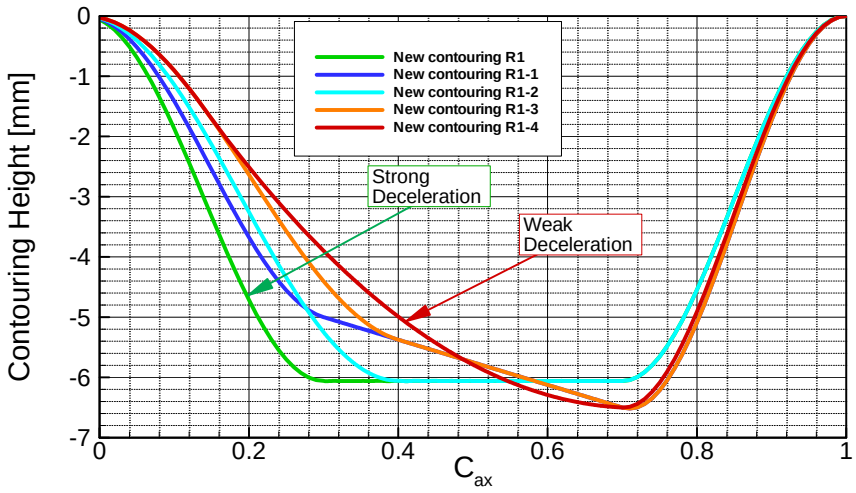

Figure 6.4: Variation of deceleration rate defined by the diffusion length to obtain the best endwall contouring efficiency.

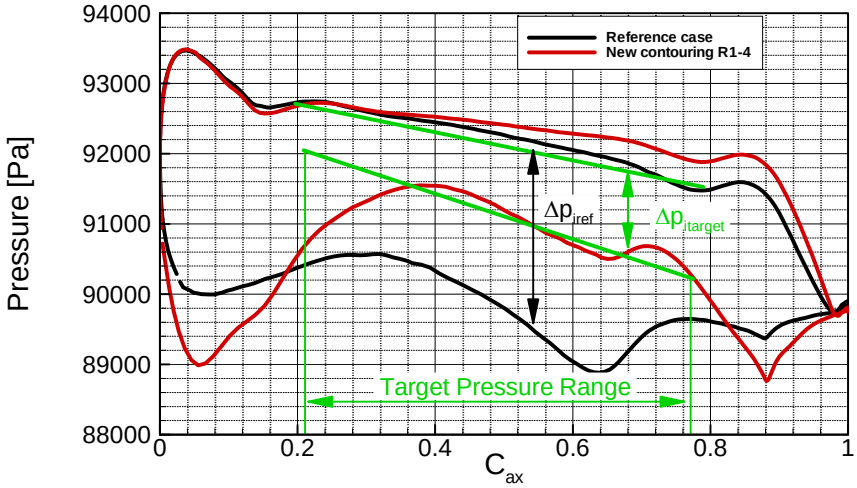

Figure 6.5: Pressure distributions directly at the hub for reference case (black: non-contoured) and contoured case (red) with target pressure to design the contouring using the technique in [59].

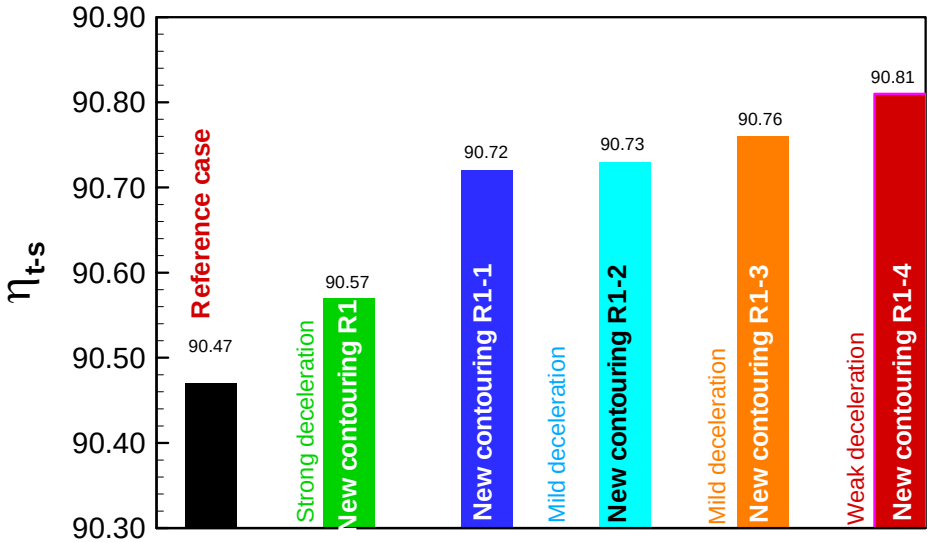

Figure 6.6: First rotor efficiency development varying deceleration rate.

6.3 Computational Details

The impact of purge flow on efficiency, aerodynamics, and heat transfer is simulated using commercial solver CFX. The turbulence model used in this study was the Shear Stress Transport model (SST), introduced by Menter [56] and [57] and implemented into CFX. This model combines k-ε and k-ω models by introducing a blending function with the objective to get the best out of these two models (for detailed discussion of turbulence models we refer to the recent textbook by Schobeiri [54]). The basic equations, assumptions and closure coefficients for the model are listed in [56] and [57]. In addition to the turbulence model, a transition model was also employed. It is worth noting that, the transition model built in the CFX-Package is an ANSYS-proprietary [67] not identical to the one published by Menter et al. [68]. A high density grid, Figure 6.7, similar to the ones described in [59], was used. Extensive preliminary tests were conducted to obtain grid independent solution. Upon the mass flow convergence, the purge mass flow ratio MFR was varied with MFR = 0.0, 0.5, 1.0 and 1.5. The numerical simulations were conducted at a rotational speed of 2400 rpm using the steady Reynolds averaged Navier-Stokes (RANS). For each MFR, the entire flow and thermodynamic quantities were obtained and the total to-static efficiency of the first rotor efficiency was calculated.

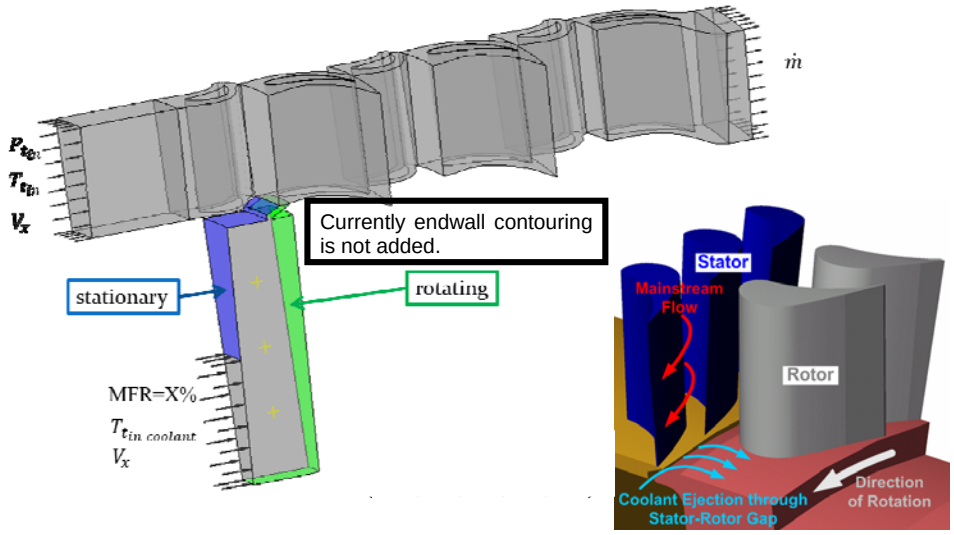

Figure 6.7: Numerical grid containing a segment of the three-stage turbine with the purge flow cavity.

6.4 Results and Discussions

Pressure distributions

Pressure distributions at 0% span (directly on the hub) for the reference case and contoured endwall are displayed in Figure 6.8. For MFR = 0, a noticeable change in pressure distribution on the suction surface is observed for the contoured case (e) compared to the no-contoured one (a). Although this change is not substantial, it does reflect an interesting phenomenon, which does not exist in a cascade flow: At the MFR = 0, due to rotation and centrifugation of the boundary layer, fluid discharges from the cavity leaving behind a temporary "vacuum" within the cavity. Because of the pitchwise pressure distribution, with lower pressure being predominant on the suction surface, the fluid particles tend to eject toward the suction side of the blades. After the vacuum level has reached a certain threshold the vacuum breaks down. Fluid from the main stream flows back, filling the cavity and the periodic process of emptying and re-filling starts all over again. This periodic unsteady process cannot be captured by steady Reynolds averaged Navier-Stokes (RANS) code, which averages the results. Consequently, to capture the periodic changes of all quantities, the unsteady version, URANS, must be used. As MFR increases, the changes in pressure distribution pattern become more pronounced. At the ratio MFR = 1.0, Figure 6.8 (c, reference) the first signature of a periodic unsteady ejection appears in form of a quasi-periodic distribution of low pressure spots in pitchwise direction. Finally at the ratio MFR = 1.5%, a clear manifestation of pitchwise high and low pressure spots is seen in Figure 6.8(d). In contrast, the pressure patterns of the contoured cases with MFR = 0.5, 1.0 and 1.5%, Figure 6.8(g, h) suggest that the presence of contouring exerts certain control mechanism that forces the flow the cavity ejects asymmetrically from the gap without noticeable pitchwise periodic signature.

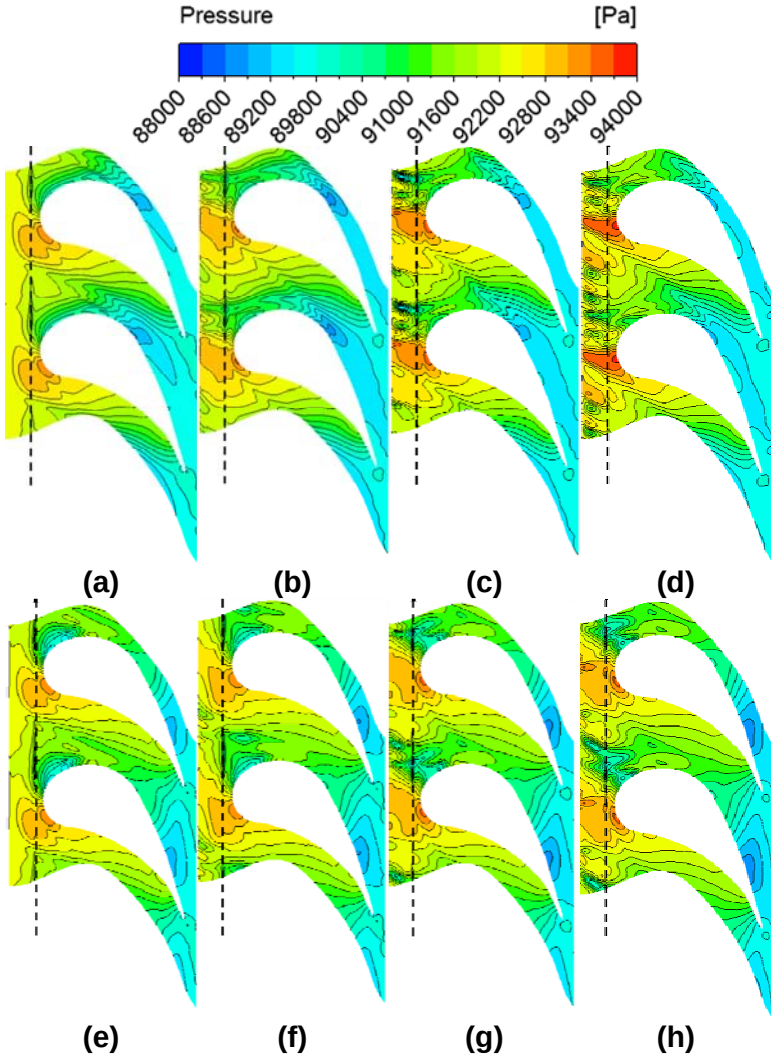

Figure 6.8: Pressure distribution at 0% span: (a) Reference case with MFR=0%; (b) Reference case with MFR=0.5%; (c) Reference case with MFR=1.0%; (d) Reference case with MFR=1.5%; (e) New contouring with MFR=0%; (f) New contouring with MFR=0.5%; (g) New contouring with MFR=1.0%; (h) New contouring with MFR=1.5%.

Total-to-Static Efficiencies

The effect of ejection associated with contouring on the total -to static efficiency is shown in Figure 6.9 and Figure 6.10. Generally, the efficiency reduces with increasing the mass flow ratio regardless of the presence of contouring. This is directly explained through the energy balance. As seen, for MFR = 0%, efficiency has not experienced any changes. For a small mass flow ratio of MFR = 0.5%, the efficiency of contoured case reduces below the reference case with a difference of $\Delta\eta_{t\text{-}s}$ = -0.09% , indicating that for relatively small MFRs, contouring not only does not contribute to efficiency improvement, but it also has a detrimental effect on efficiency. The situation reverses at

higher MFRs. As seen, for MFR = 1.0% the contouring brings a very small improvement of $\Delta\eta_{t\text{-}s}$ = 0.05%. Increasing MFR to 1.5%, results in slightly higher $\Delta\eta_{t\text{-}s}$ = 0.22%. These marginal negative and positive changes of efficiency do suggest that contouring for the first rotor that is directly exposed to purge flow is not recommendable.

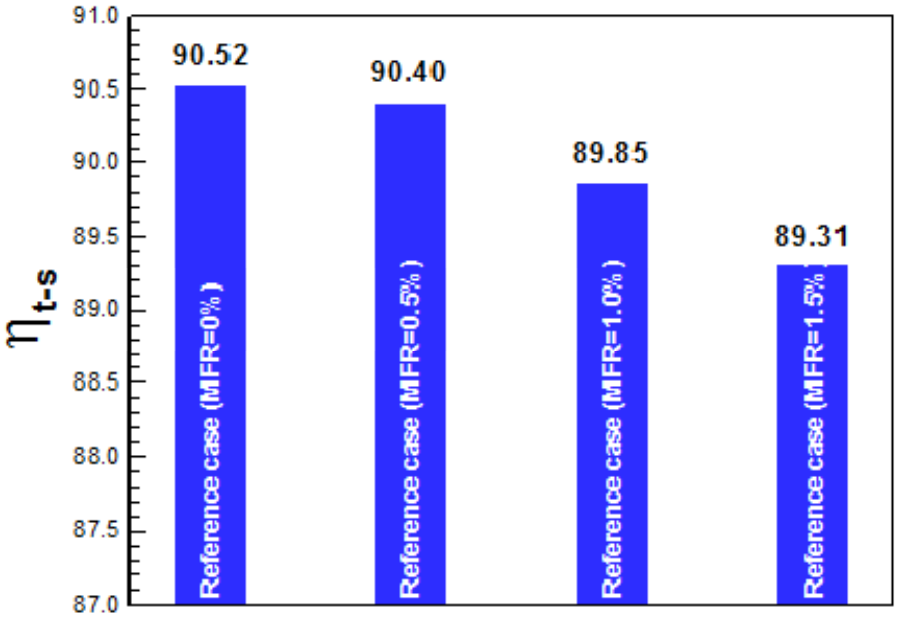

Figure 6.9: Total-to-static efficiency for reference case at different MFRs.

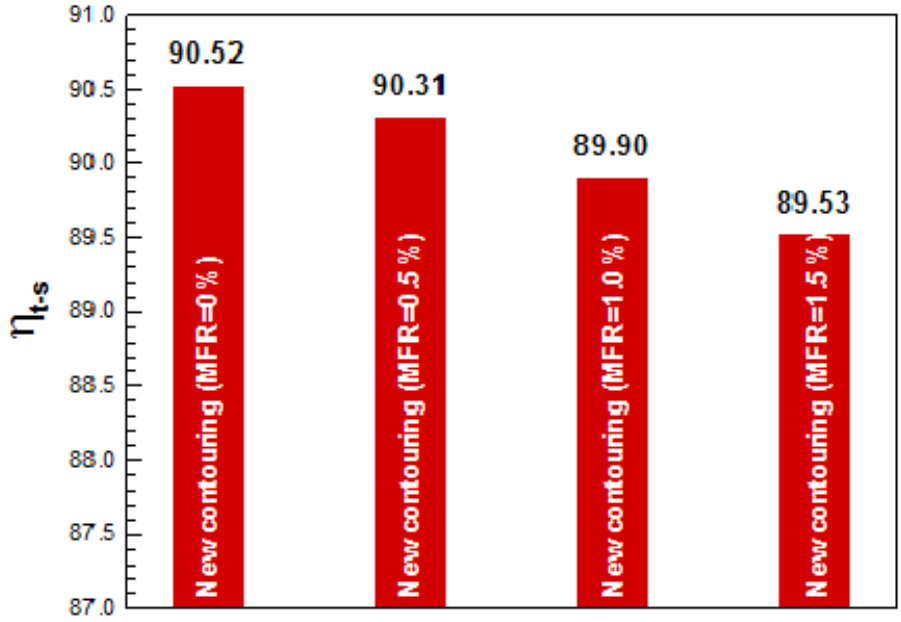

Figure 6.10: Total-to-static efficiency for contoured case at different MFRs.

Adiabatic film cooling effectiveness

Figure 6.11 shows the impact of the MFR or blowing ratio on the adiabatic film cooling effectiveness on both the contoured and non-contoured rotating first rotor hub with fixed rotational speed of 3000 rpm. The comparisons for three different MFRs of 0.5%, 1.0% and 1.5%, which are corresponding to blowing ratios M= 0.12, 0.24 and 0.36, are shown. For both contoured and non-contoured cases, larger MFRs give more cooling mass as well as higher coolant momentum. As a result, more coolant particles are capable to penetrate into the highly vortical secondary flow region near the endwall and thus travel further downstream, which usually provides higher film cooling effectiveness. However, if the blowing ratio is too high, the coolant tends to shoot into the mainstream rather than stay close to the endwall, which does not necessarily provide good protection for the hub surface. In this study, the blowing ratio is less than unity and therefore both the measurements and predictions show enhance in film cooling effectiveness on the platform with increasing MFR or M.

Looking at the contour plots of the film cooling effectiveness obtained by the experiments, the endwall contouring delivers better film cooling protection than the non-contoured platform for all MFRs. As seen in Figure 6.11, for non-contoured cases, relatively high cooling effectiveness is obtained near the leading edge since more coolant is ejected out in this region due to the pressure distribution within the stator-rotor gap. The coolant particles can travel along the suction side from approximately 25% up to 50% C_{ax} with varying MFRs. However, the coverage of the cooling film decreases fast from the suction side to the pressure side. The surface near the pressure side can hardly be cooled for MFR=0.5% and 1.0%. It becomes better when the MFR increases to 1.5% since more coolant is ejected. Still the film cooling effectiveness fades rapidly long the pressure side which resulting a triangular area covered by the cooling film. This triangular-shape area (with less cooled at pressure side) is formed due to the strong secondary flow system. The large pressure gradient between the pressure- and suction-side pushes the pressure-side leg horseshoe vortex and the crossflow from the pressure side to the suction surface. These secondary flows entrain the coolant film and take the coolant particles to travel laterally. Therefore the pressure side is much less cooled.

In contrast, more coolant particles travel along the pressure side and much larger travelling distance is obtained when the endwall contouring is used. As a result the cooling film covers more platform surface area than the non-contoured platform. Particularly the region covered by the coolant for MFR=1.0% and 1.5% transforms from the triangular shape to trapezoidal shape. Additionally the effectiveness distribution is more uniform in the pitchwise direction as well. Apparently the improvement of the film cooling is benefited from the presence of the endwall contouring. Since the contouring is able to greatly decrease the pressure difference between the blade pressure- and suction-side and to some extent suppress the horseshoe vortex, the strength of the secondary flow is significantly weakened. As a result, the coolant can travel along the streamwise with much less interference by the secondary flow and thus spread more uniformly on the hub surface.

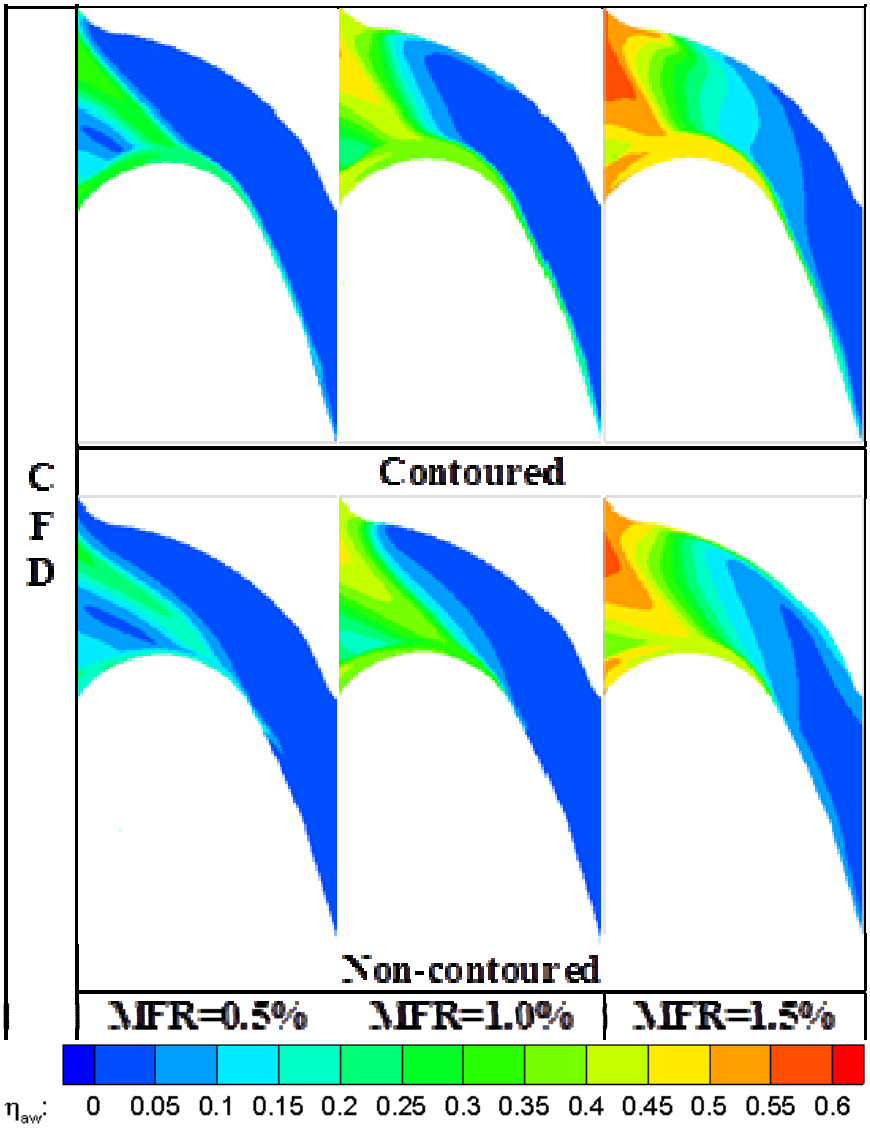

Figure 6.11: Predicted film cooling effectiveness distribution on the contoured and non-contoured rotating platform with different MFRs for fixed rotation speed of 3000 rpm.

The investigation of the rotation effect on the platform film cooling is performed and shown in Figure 6.12. This chapter exhibits in total three different rotational speeds of 2400 rpm, 2550 rpm and 3000 rpm with the fixed typical MFR=1.0%. Generally, when the turbine is running under off-design conditions with lower rotational speeds compared to design speed, the flow deflection becomes larger or in other words the incidence angle is increased. As a result, the stagnation point moves towards the blade pressure side forming a higher pressure zone along the pressure side. The direct consequence is certain increase in blade loads or pressure gradient between the pressure- and suction-side. Accordingly the strength of the secondary flow system to some extent grows due to the

stronger driving force. Meanwhile the high pressure gradient further pushes the incoming cooling film away from the pressure side to the suction side once it exits from the stator-rotor gap. Hence, at the lower rotational speeds, the film coverage will be partially eroded and the cooling effectiveness is going to be reduced. This is evidently seen from the experimental results in Figure 6.12 that the coolant covered area gradually shrinks and the effectiveness magnitude slightly declines as the rotational speed drops from 3000 rpm to 2400 rpm.

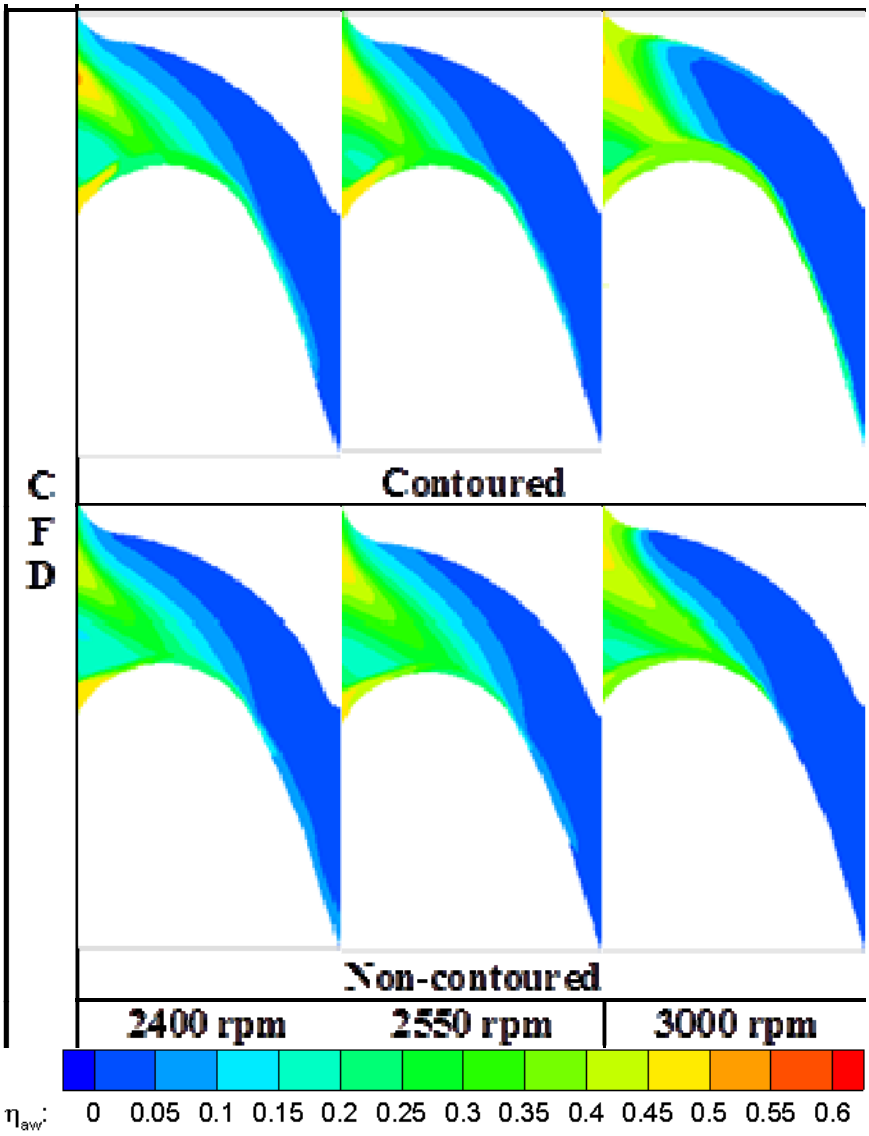

Figure 6.12: Predicted film cooling effectiveness distribution on the contoured and non-contoured rotating platform with different rotation speeds for MFR=1.0%.

The CFD simulations show the tendency that the distribution of the cooling effectiveness shifts from the pressure side to the suction side for both contoured and

non-contoured rotor platforms as lowering the rotational speed. However, it seems that the predicted effectiveness is less sensitive to the rotational speed of 2400 rpm and 2550 rpm. Only slight shrink in the covered area is observed when the rotating speed switches from 2550 rpm to 2400 rpm. In addition, the predicted film coverage on the contoured platform merely shows marginable improvement compared to the non-contoured case under lower rotation speeds. However, a streak with relative high cooling effectiveness is observed along the suction side for contoured hub. The streak is thicker and with higher effectiveness for contoured cases compared to non-contoured ones under all running conditions. It may be the result of the weakened suction-side leg horseshoe vortex by the endwall contouring and thus the coolant particles are able to travel to further downstream.

Nevertheless, even though the effectiveness of the film cooling tends to reduce by lowering down the turbine rotational speed, the contoured platform obtains slightly better film cooling than non-contoured hub for off-design conditions. In other words, the presence of the endwall contouring is able to partially compensate the reduced cooling effectiveness due to the off-design deviations and therefore reduce the potential risk of platform burnout. It also possibly implies that the cooling mass can be to some extent lessened, which enhances the turbine aerodynamic performance affected by over-amount coolant mass but meanwhile maintains good film cooling protection. Overall, the above discussion explicitly demonstrates the excellent performance and robustness of the endwall contouring for general turbine design and off-design running conditions.

The pitchwise-averaged film cooling effectiveness of both contoured and non-contoured platform with different MFRs is plotted in Figure 6.13. All the results were obtained under reference rotational speed of 3000 rpm. Apparently increasing the MFR leads to the growth of cooling effectiveness magnitude for all cases. However, the averaged plots show a rapid decrease in effectiveness magnitude for the region beyond $0.6C_{ax}$ remaining mostly uncovered with average effectiveness magnitudes below 0.1. Noticeably, the endwall contouring exhibits superiority in improving film cooling on platform for all studied MFRs. Up to 40% higher effectiveness can be seen from the leading edge to $0.25C_{ax}$.

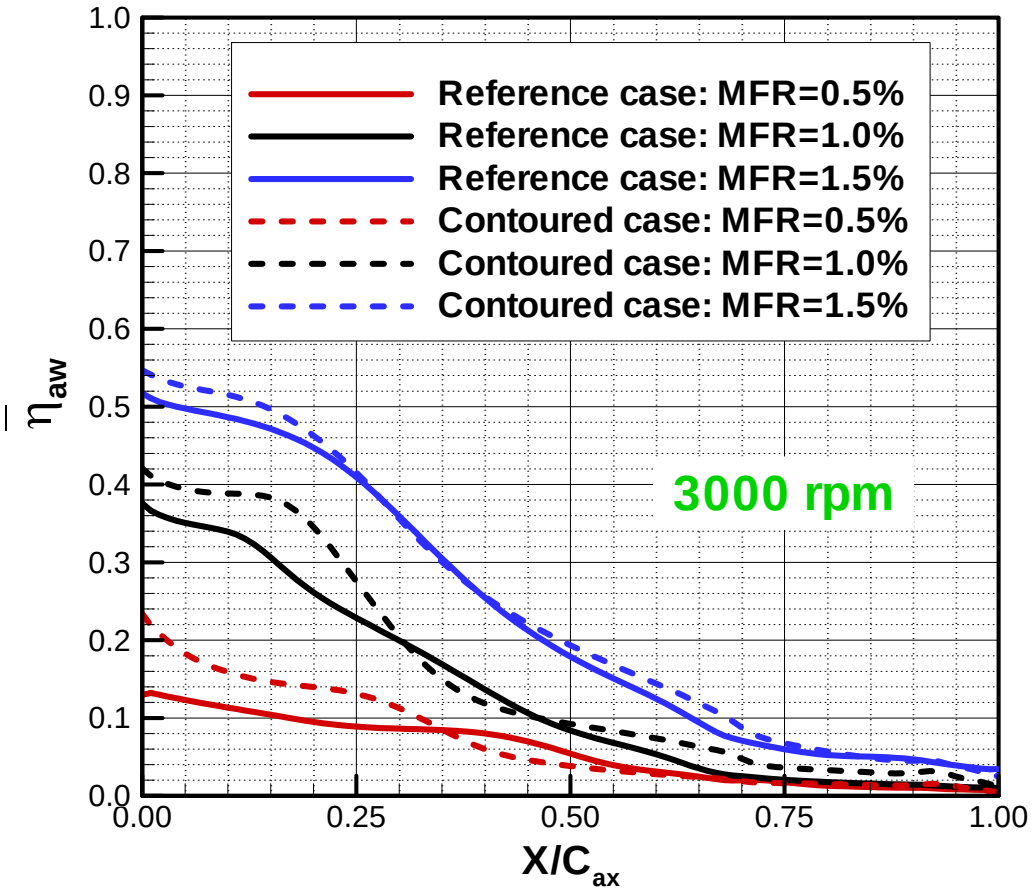

Figure 6.13: Pitchwise-averaged film cooling effectiveness distribution of both contoured and non-contoured rotating platform with different MFRs for rotation speed of 3000 rpm.

Figure 6.14 depicts the impact of the rotational speeds on the pitchwise-averaged film cooling effectiveness on the rotor platform. The plots compare the contoured to non-contoured hub with 1.0% of the coolant ejected. The averaged effectiveness grows with the increasing turbine rotational speed. However, in the predicted speed range, the cooling effectiveness is not as sensitive to the rotating speed as to the MFR or blowing ratio. Thus, increasing the coolant mass should be a preferred means to achieve better platform film cooling. As expected, the presence of endwall contouring can increase the film cooling effectiveness up to a percentage of 30% for the first half axial chord. Yet the predicted cooling effectiveness on contoured hub decays rapidly so that the benefit vanishes at about $0.35C_{ax}$.

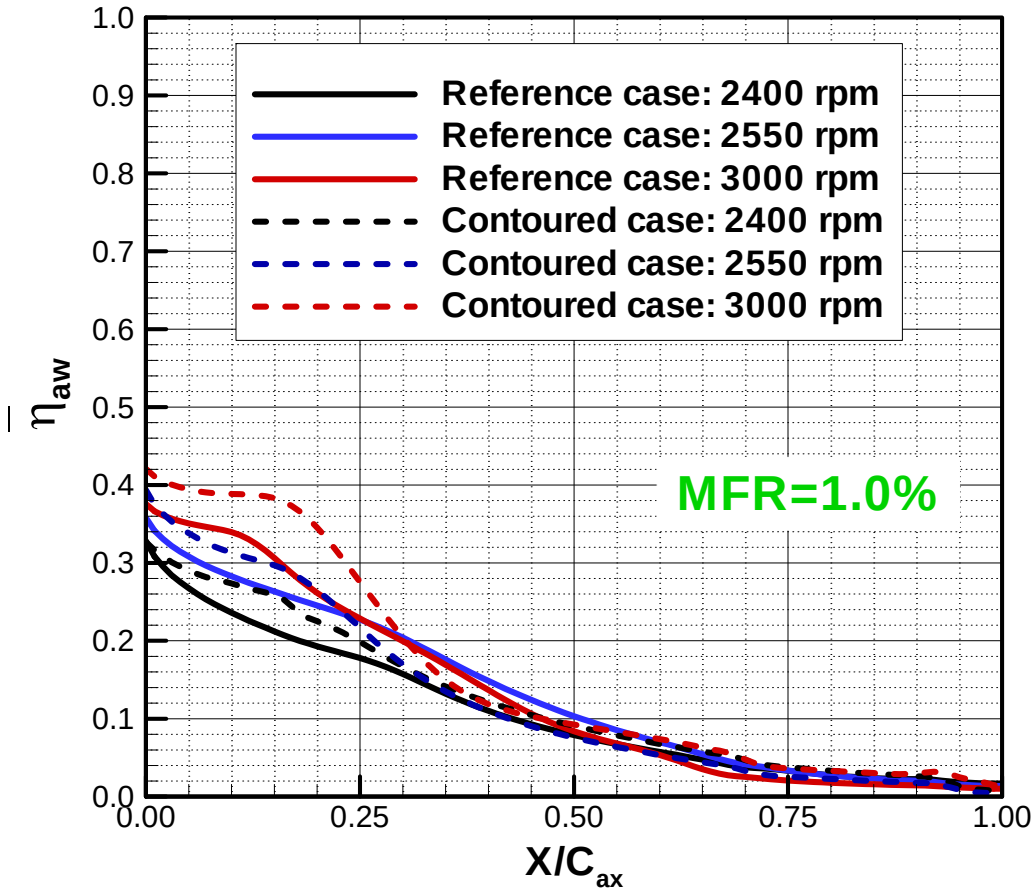

Figure 6.14: Pitchwise-averaged film cooling effectiveness of both contoured and non-contoured rotating platform with different rotation speeds for MFR=1.0%.

The area-averaged cooling effectiveness can be found in Figure 6.15 and Figure 6.16 where the former illustrates the impact of MFR and the latter depicts the rotation effect. As seen, the overall effectiveness monotonously reduces with decreasing MFR as well as rotational speed, which is consistent with the contour plots and pitchwise averaged values. Speaking of the absolute augmentation in the effectiveness, the endwall contouring achieves its highest performance with 1.0% coolant ejected while rotates in a speed of 3000 rpm. It is also seen that the blowing ratio has larger impact on the area-averaged effectiveness.

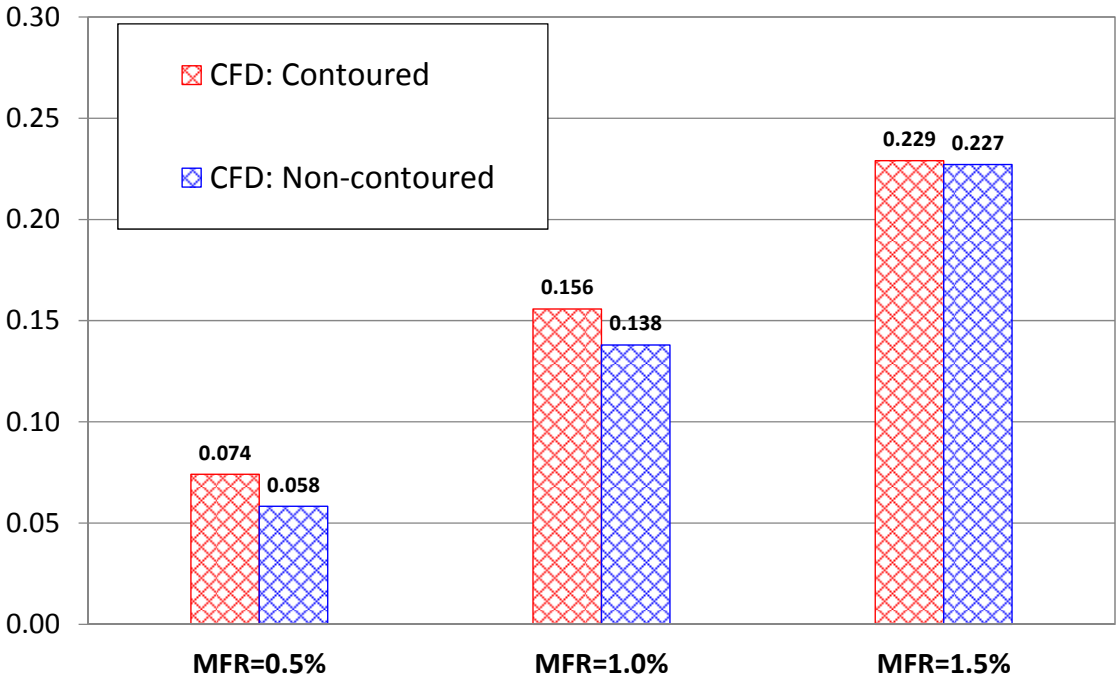

Figure 6.15: Area-averaged film cooling effectiveness of both contoured and non-contoured rotating platform with different MFRs for rotation speed of 3000 rpm.

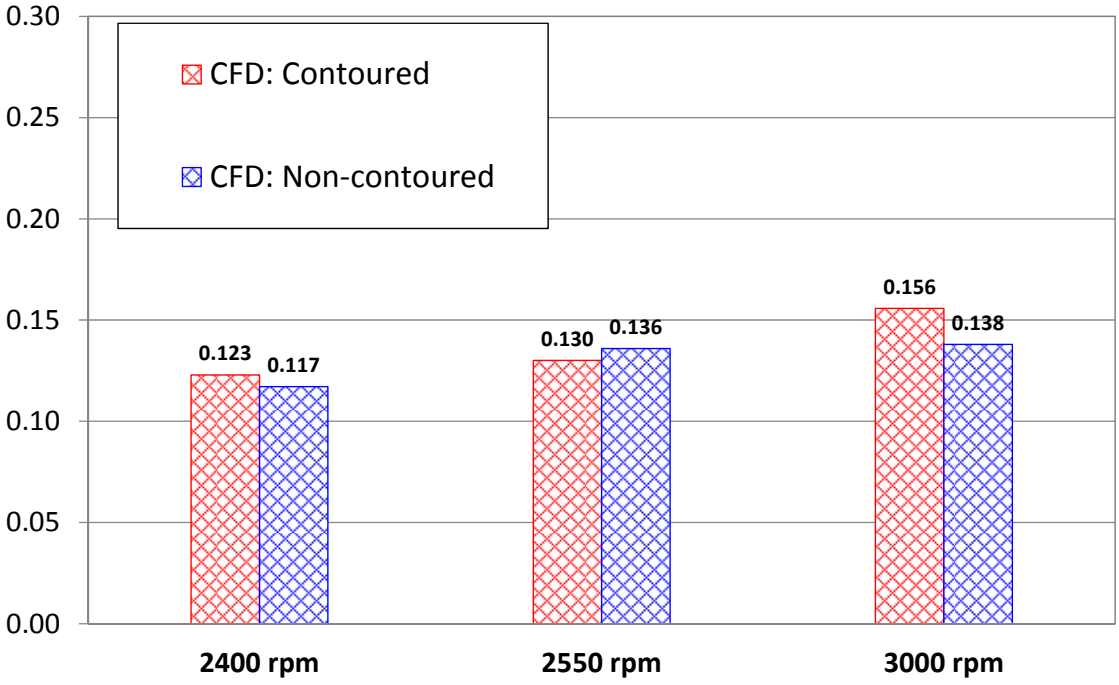

Figure 6.16: Area-averaged film cooling effectiveness of both contoured and non-contoured rotating platform with different rotation speeds for MFR=1.0%.

7. EXPERIMENTAL INVESTIGATIONS FOR ENDWALL FILM COOLING

7.1 Experimental Facility

The research turbine facility used for the current experiments was designed by Schobeiri [69] to address aerodynamic performance and heat transfer issues of high pressure (HP), intermediate pressure (IP), and low pressure (LP) turbine components. Detailed aerodynamic, efficiency, loss and performance measurements were carried out to verify and document the efficiency and performance of several high efficiency turbine blades designed for major original turbine manufacturers. To compare the results of the investigations reported in [69] with those for 2-D cylindrical blades, aerodynamic measurements were conducted and summarized in the subsequent reports [70] and [71].

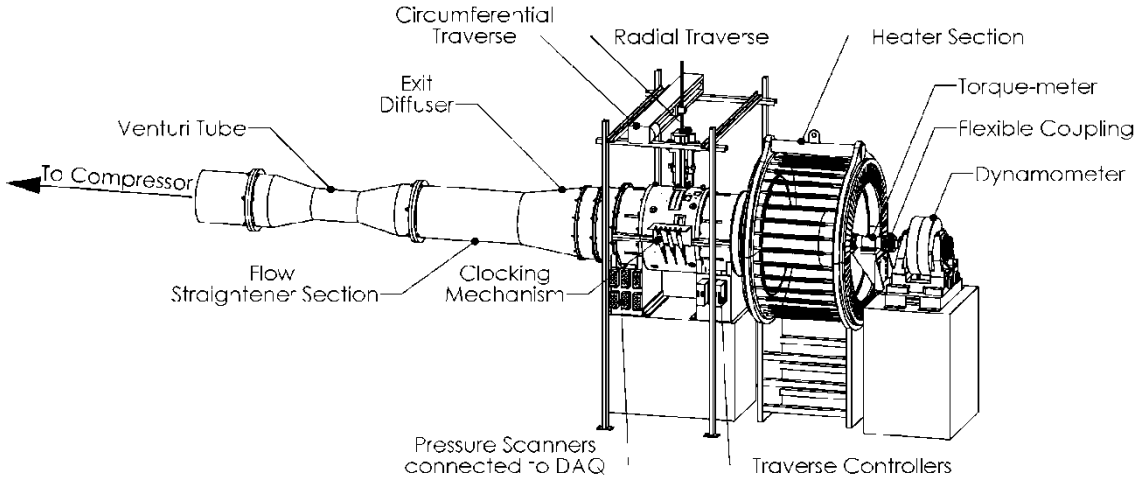

Figure 7.1: The overall layout of TPFL-research turbine facility.

The overall layout of the test facility is shown in Figure 7.1. It consists of a 300HP (223.71 kW) electric motor connected to a frequency controller which drives a three-stage centrifugal compressor capable of supplying air with a maximum pressure difference of 55 kPa and a volumetric flow rate of $4m^3/s$. The compressor operates in suction mode and its pressure and volume flow rate can be varied by the frequency controller operating between 0 to 66 Hz. A pipe with a smooth transition piece connects the compressor to a Venturi mass flow meter used to measure the mass flow through the turbine component. The three-stage turbine has an automated data acquisition system for detailed flow measurement at each blade row location in the radial and circumferential direction. The turbine inlet has an integrated heater that prevents condensation of water from humid air during experiments. Turbine dimension and operating condition is shown in Table 7-1.

Table 7-1: Turbine dimensions and operating conditions

Stage no., N	3	Mass flow	3.58 kg/s
Tip Diameter	685.8mm	*Hub Diameter*	558.8mm
Reference speed	3000 rpm	Current speed range	1800 to 3000 rpm
α_2	19^o	β_3	161^o
C_x	41.6 mm	*Re* at Rotor 1 inlet	231400

To determine the film cooling effectiveness under rotating conditions for different kinds of film cooling (Ahn et al.[25], [62] and Suryanarayanan et al. [63], [64]), the existing turbine rotor described in [69] was modified to integrate the coolant loop through the downstream section of the hollow turbine shaft and into the cylindrical hub cavity. Two independently controlled, concentric coolant loops provide the necessary mass flow for film cooling experiments. The outer loop supplies coolant for film cooling experiments in the tip of the blade but is not used in this paper. The inner loop coolant jet ejecting from a circumferential gap between the 1st stator and rotor provides for hub platform cooling (Figure 3.1 top).

A concentric jet exits this circumferential gap at an angle of 25º into the mainstream (Figure 7.2). The maximum normal gap width is designed to be 3 mm. However, it can be decreased to 0.5mm by translating the entire rotor towards the front bearing. For the current study the normal gap was set to 2.3 mm and it is fixed during all of the experiments. Similar to the optimization of the trailing edge slot ejection described in detail by Schobeiri [72] and Schobeiri and Pappu [29], the reduction of slot width is instrumental in establishing an optimum ejection ratio while keeping the cooling mass flow constant.

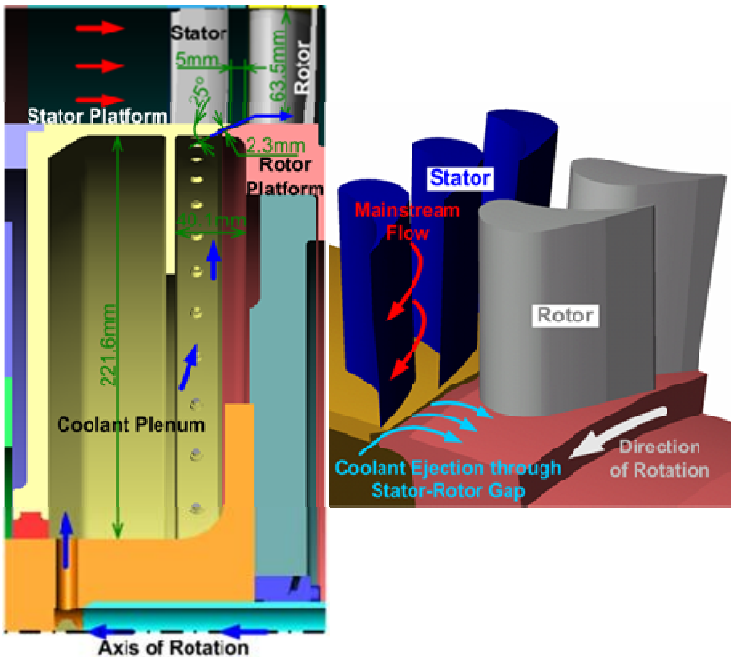

Figure 7.2: Detailed view of the stator-rotor gap design for the rotating platform.

7.2 Endwall Contouring Exposed to Purge Flow

For the current investigation, the contouring method described in chapters 3 and 4 was also applied to the first rotor row. Extensive numerical simulations were performed to obtain an optimum geometry for contouring the first rotor endwall. Since the first rotor row was immediately exposed to the circumferential gap, there was no axial space to extend the contouring upstream of the blades to achieve the same efficiency that we

achieved in the second rotor row. This configuration resulted in lower turbine efficiency as discussed earlier. Considering this circumstance, efforts have been made to improve the efficiency by varying the endwall contouring of the first rotor row as shown in Figure 7.3. This figure shows the variation of the contour depth along the suction surface. A strong deceleration rate characterized by a steep gradient of the contouring height, pertaining to R1, R1-1, R1-2 and R1-3-curves, caused flow separation within the contouring. This resulted in an efficiency that was just slightly above the reference case without contouring. It turned out that the contouring R1-4 that was originally generated by the continuous diffusion method yielded the best efficiency improvement [60].

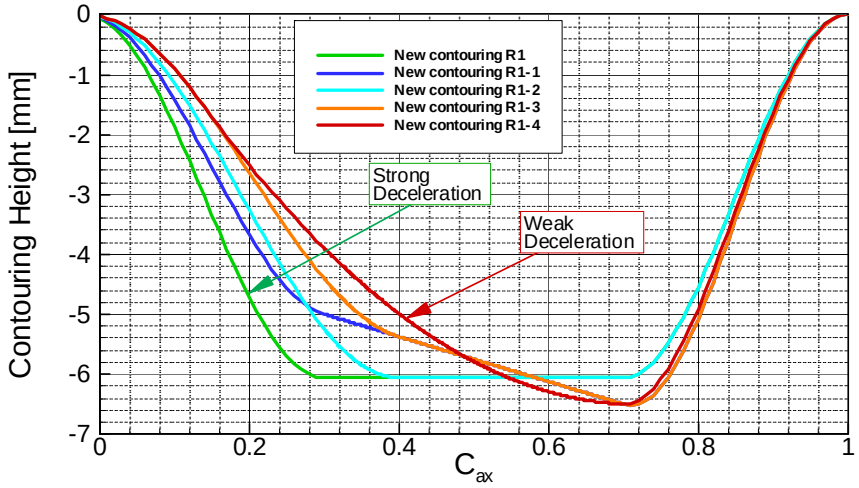

Figure 7.3: Variation of contour depth along the suction surface to obtain the best endwall contouring efficiency.

For each of the calculated cases, the entire flow field including total pressure loss and the turbine efficiency were obtained. Considering the spatial restrictions mentioned above, particular attention was paid to accurately obtain the efficiency of the turbine with the first rotor endwall contoured. Based on this variation, results showed that Contouring R1-4 had the highest efficiency and was used for every endwall between the blades of the first rotor. Figure 7.4 shows the first rotor endwall contouring geometry.

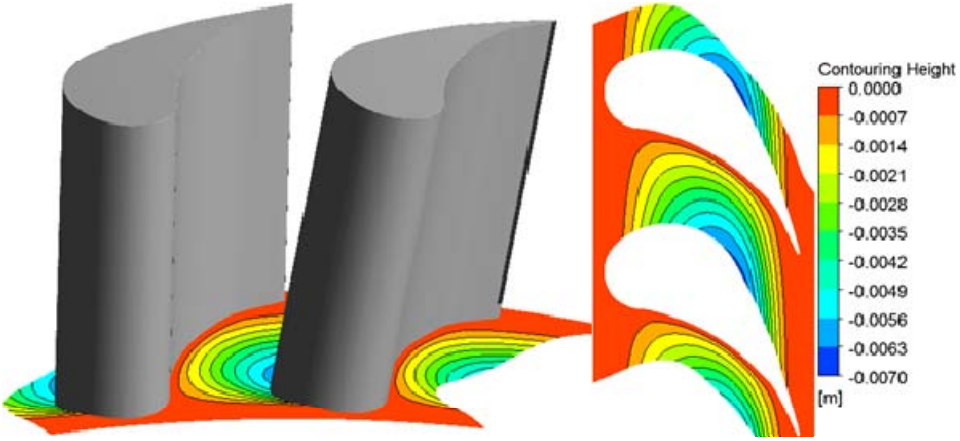

Figure 7.4: Contour geometry for first rotor.

7.3 Film Cooling Effectiveness Measurement and Data Analysis

Data for film cooling effectiveness is obtained using the PSP technique. This technique was described in several papers, among others (Ahn et al. [25], [62] and Suryanarayanan et al. [63], [64]), thus only a brief description is given below. PSP consists of photo-luminescent molecules held together by a binding compound. The luminous particles in the PSP emit light when excited, with the emitted light intensity being inversely proportional to the partial pressure of oxygen in the surroundings. The emitted light intensity can be recorded using a CCD camera and corresponding oxygen partial pressures can be obtained by calibrating emitted intensity against the partial pressure of oxygen. The image intensity obtained from PSP by the camera during data acquisition is normalized with a reference image intensity taken under no-flow conditions. Background noise in the optical setup is removed by subtracting the image intensities with the image intensity obtained under no-flow conditions without excitation. The resulting intensity ratio can be converted to pressure ratio using the previously determined calibration curve and can be expressed as:

$$\frac{I_{ref} - I_{blk}}{I - I_{blk}} = f\left(\frac{\left(P_{O_2}\right)_{air}}{\left(P_{O_2}\right)_{ref}}\right) = f\left(P_{ratio}\right) \tag{1}$$

where I denotes the intensity obtained for each pixel and f(Pratio) is the relation between intensity ratio and pressure ratio obtained after calibrating the PSP. Further details in using PSP for pressure measurements are given in McLachlan and Bell [73].

Calibration for PSP was performed using a vacuum chamber at several known pressures varying from 0 to 2atm with corresponding emitted intensity recorded for each pressure setting. A sample calibration curve is shown in Figure 7.5. PSP is sensitive to temperature with higher temperatures resulting in lower emitted light intensities. Hence, the paint was also calibrated for temperature. It was observed that if the emitted light intensity at a certain temperature was normalized with the reference image intensity taken at the same temperature, the temperature sensitivity can be eliminated. Hence, during data acquisition, the reference image was acquired immediately after the experiment was completed to avoid errors related to temperature variation. Reference images were acquired after the rotor came to a halt and the temperature change from rotating to stationary condition was small enough to disregard its effect on PSP measurement. Coolant flow and platform surface temperatures were monitored using thermocouples placed along the individual coolant loops and on the platform surface close to the suction side respectively. The thermocouples were wired through the slip-ring and connected to a microprocessor thermometer with a digital readout.

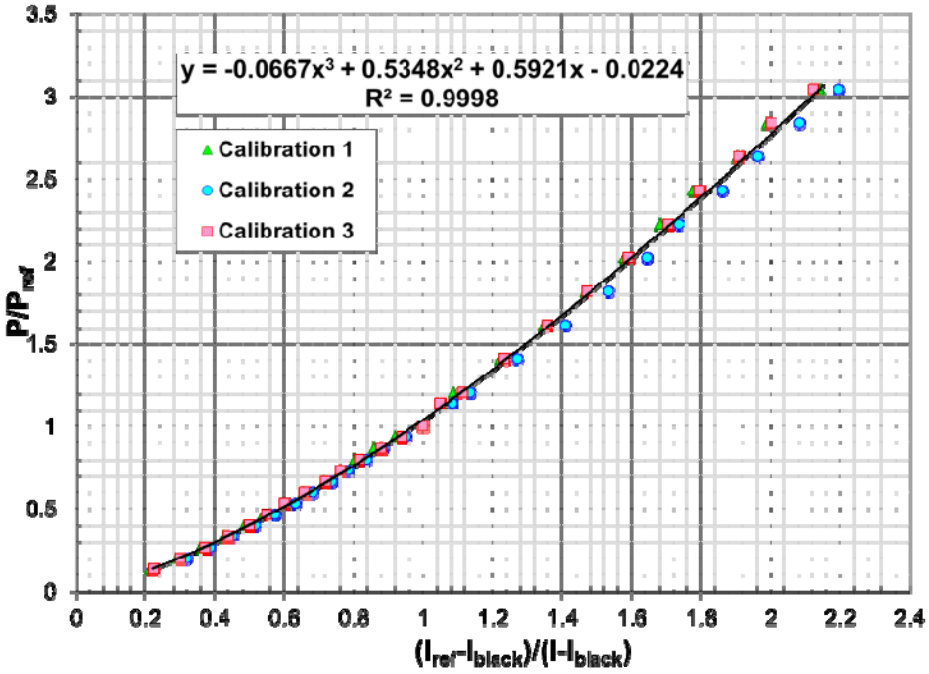

Figure 7.5: PSP calibration curve.

To obtain film cooling effectiveness, air and nitrogen were used alternately as coolant. Nitrogen which has approximately the same molecular weight as the air displaces the oxygen molecules on the surface causing a change in the emitted light intensity from PSP. By noting the difference in emitted light intensity and subsequently the partial pressures between the air and nitrogen injection cases, the film cooling effectiveness can be determined using the following equation:

$$\eta = \frac{C_{mix} - C_{air}}{C_{N_2} - C_{air}} = \frac{C_{air} - C_{mix}}{C_{air}} = \frac{\left(P_{O_2}\right)_{air} - \left(P_{O_2}\right)_{mix}}{\left(P_{O_2}\right)_{air}} \quad (2)$$

where C_{air}, C_{mix} and C_{N2} are the oxygen concentrations of mainstream air, air/nitrogen mixture and nitrogen on the test surface respectively and are directly proportional to the partial pressure of oxygen. The definition of adiabatic film cooling effectiveness is:

$$\eta = \frac{T_f - T_m}{T_c - T_m} \quad (3)$$

The accuracy of the PSP technique for measuring film-cooling effectiveness has been compared by Wright et al. [74] on a flat plate with compound angled ejection holes against several measurement techniques such as steady and transient liquid crystal, IR camera and using a foil heater with thermocouples. Results were obtained for a range of blowing ratios and show consistency with each other. Study by Wright et al. [74] for flat-plate film cooling shows the superiority of using PSP compare to conventional IR measurement. From their study, the accuracy analysis shows the difference of

effectiveness result of 15%. In addition, Rallabandi et al. [75] reports a good comparison between PSP and other methods such as naphthalene mass-transfer method and traditional thermocouples measurement technique, for basic flat-plate film cooling with one row of compound angle holes.

7.4 Experimental Procedure

The platform passage under investigation was layered with 7 to 9 coats of PSP using an air brush. This coated surface was excited using a strobe light fitted with a narrow bandpass interference filter with an optical wavelength of 520nm. Upon excitation from this green light, the PSP coated surface emitted red light with a wavelength higher than 600nm. A 12-bit scientific grade CCD camera (high speed SensiCam with CCD temperature maintained at -15^{o}C and using 2-stage Peltier cooler) fit with a 35mm lens and a 600nm longpass filter was used to record intensity images. The filters were chosen such that the camera blocked the light reflected from the target surface and only captured the actual data. A schematic of the optical setup used in the data acquisition is shown in Figure 7.6. The camera, the strobe light and the data acquisition system were triggered simultaneously using an optical sensor triggered off the rotor shaft. By detecting the same angular position, the camera was able to view the same region of interest at every rotation, making it possible to average the image intensities without blurring the information. A minimum exposure time of 17μs was used for image capture from the camera. Estimated rotor movement during image capture at 2550 rpm, for a 17μs exposure time was approximately 1.1mm. A total of 200 images were captured for each experiment with air and nitrogen injection and the pixel intensity for all images was averaged. A computer program was used to convert these pixel intensities into pressure using the calibration curve and then into film cooling effectiveness. The coolant flow rate was set using a rotameter based on prior calculation for the desired blowing and mass flow ratio. The coolant was heated to the same temperature as mainstream air (45°C) before injection through the gap to eliminate the temperature effects of PSP.

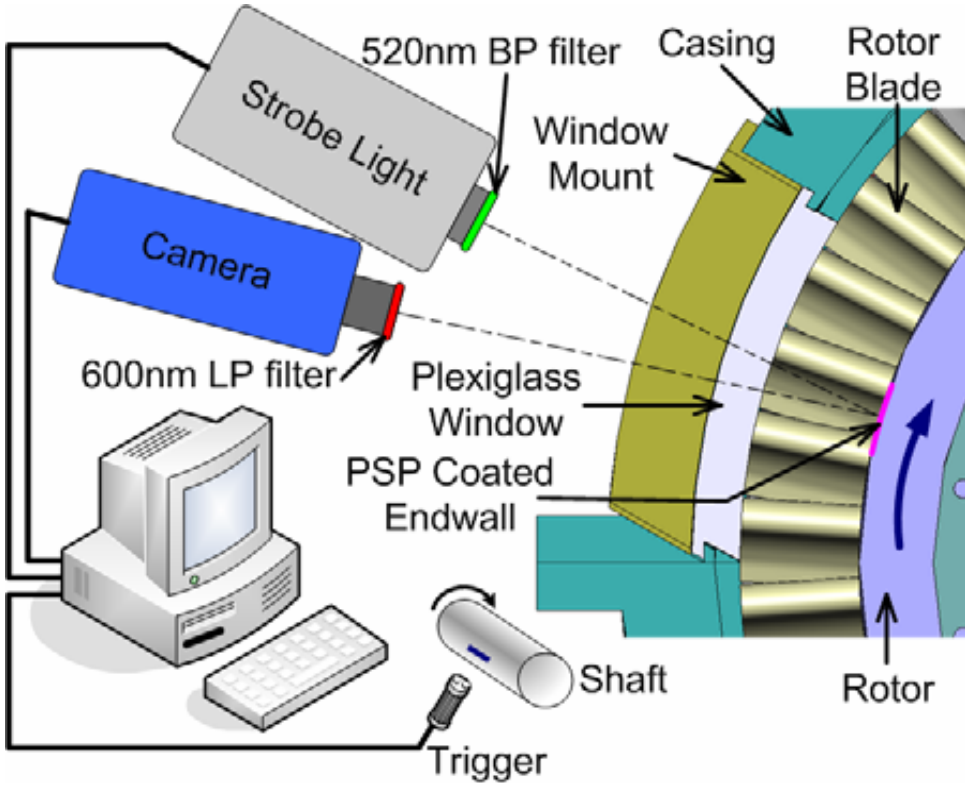

Figure 7.6: Optical set-up for PSP data acquisition.

Uncertainty calculations were performed based on a confidence level of 95% and are based on the uncertainty analysis method of Coleman and Steele [76]. Lower effectiveness magnitudes have higher uncertainties. For an effectiveness magnitude of 0.8, uncertainty was around ±1% while for effectiveness magnitude of 0.07, uncertainty was as high as ±10.3%. This uncertainty is the cumulative result of uncertainties in calibration (4%) and image capture (1%). The absolute uncertainty for effectiveness varied from 0.01 to 0.02 units. Thus, relative uncertainties for very low effectiveness magnitudes can be very high (>100% at effectiveness magnitude of 0.01). However, it must be noted that very few data points exist with such high relative uncertainty magnitudes. Uncertainties for the average blowing ratio calculations are estimated to be approximately 3.5% using Kline-McClintock analysis and are discussed in detail by Holman [77].

7.5 Results and Discussions

Film cooling effectiveness measurements were performed for three coolant-to-mainstream mass flow ratios (MFR) of 0.5%, 1.0% and 1.5%. Film cooling data was also obtained for three rotational speeds; 3000 rpm (reference condition), 2550 rpm and 2400 rpm, and they were compared with non-contoured endwall data. For 3000 rpm two more MFRs of 0.75% and 1.25% were performed to give a better view of how film cooling effectiveness is changing.

Total mass flow in the engine was 3.58 kg/s and was ensured to be the same for all three rpms by adjusting the blower frequency through the frequency controller. The three MFRs corresponded to blowing ratios (M_{gap}) of approximately 0.14, 0.28 and 0.42 respectively after assuming that the coolant exits the gap axially. Blowing ratios for each rotating speed differed slightly as the relative mainstream velocity at the rotor inlet changes with the rotating speed.

The film cooling effectiveness resulting from using PSP for the reference rotating condition of 3000 rpm are plotted in Figure 7.7. The figure shows the contour plots for all five mass flow ratios tested. The contour plots also show the location of the stator-rotor gap upstream of the passage and the path of the mainstream and coolant flow. The effectiveness in the gap as the coolant escapes through it could not be recorded, as the plexiglass window through which the rotor platform was viewed was not wide enough.

For both contoured and non-contoured endwalls, higher mass flow ratios resulted in coolant injection with higher momentum. As this momentum increases, it can be observed that the spread of the coolant as well as the effectiveness magnitudes are increased. The injected coolant is at the same density as the mainstream i.e. the coolant to mainstream density ratio is 1. Hence, the injected coolant velocity is higher for higher mass flow ratios. This affects the secondary flow structure in the passage.

At lower blowing ratios, the low momentum coolant is not capable of penetrating into the highly vortical secondary flow region on the hub platform. It mixes with the main flow where its kinetic energy dissipates, making only a marginal contribution to effectiveness improvement. For the lowest mass flow ratio (MFR = 0.5%), the maximum effectiveness magnitude is less than 0.2. As the mass flow ratio increases, the coolant injection velocity increases because the coolant can penetrate the complex secondary flows in the passage, resulting in higher effectiveness on the platform.

In non-contoured platform a strong pressure gradient exists within the passage from the pressure to the suction side, with the static pressure near the pressure side being much higher due to lower mainstream velocities and blade curvature. The coolant traces show slightly higher effectiveness magnitudes towards the suction side near the leading edge. More coolant gets diverted away from the higher pressure stagnation region on the leading edge of the blade and finds its way towards the suction side. Effectiveness magnitudes on the pressure side begin to fade away rapidly as the coolant travels along the axial chord. As the passage vortex moves towards the suction side while gaining strength, it entrains the mainstream on the platform surface damaging the coolant film and resulting in a sharp drop in effectiveness magnitudes. This sudden drop gives a good indication of the path traced by the passage vortex.

On the other hand, in the contoured platform, effectiveness magnitude spreads uniformly from leading edge to trailing edge as shown in Figure 7.7 to Figure 7.10. This is the consequence of the endwall contouring that has reduced the pressure difference between the pressure and suction surface leading to lower secondary flow velocities.

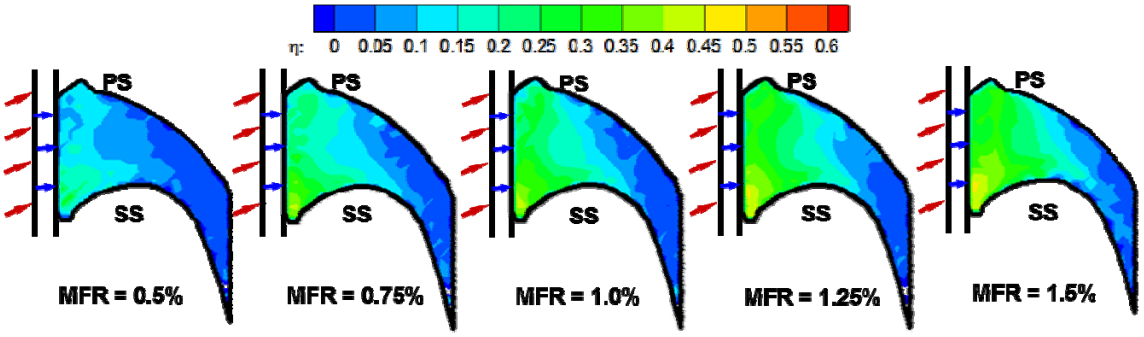

Figure 7.7: Film cooling effectiveness distribution on the contoured rotating platform for 3000 rpm.

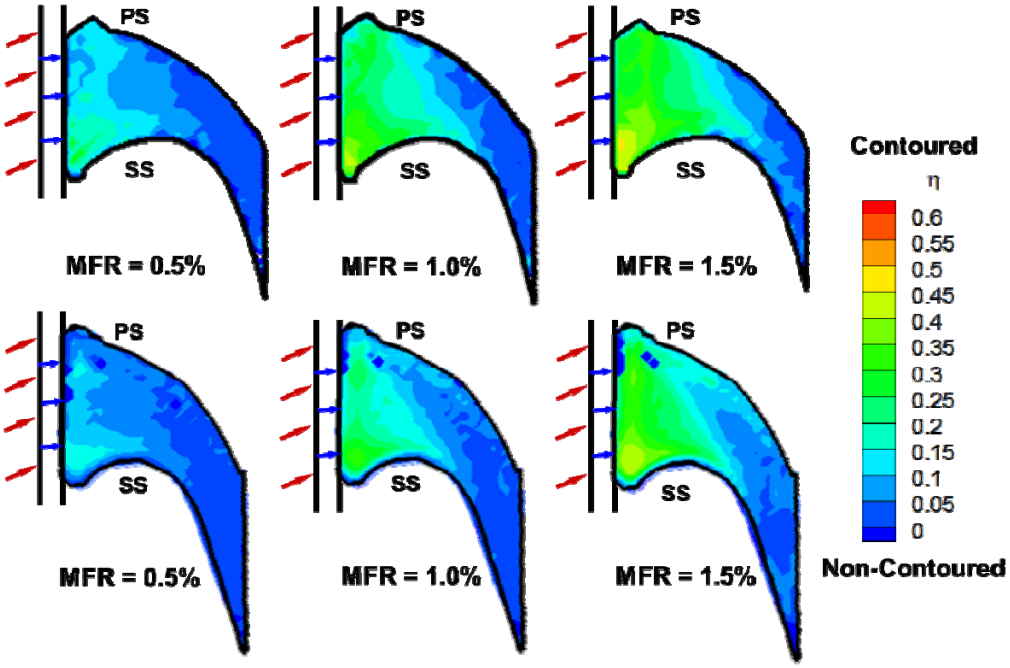

Figure 7.8: Comparison of film cooling effectiveness distribution on the contoured and non-contoured rotating platform for 3000 rpm.

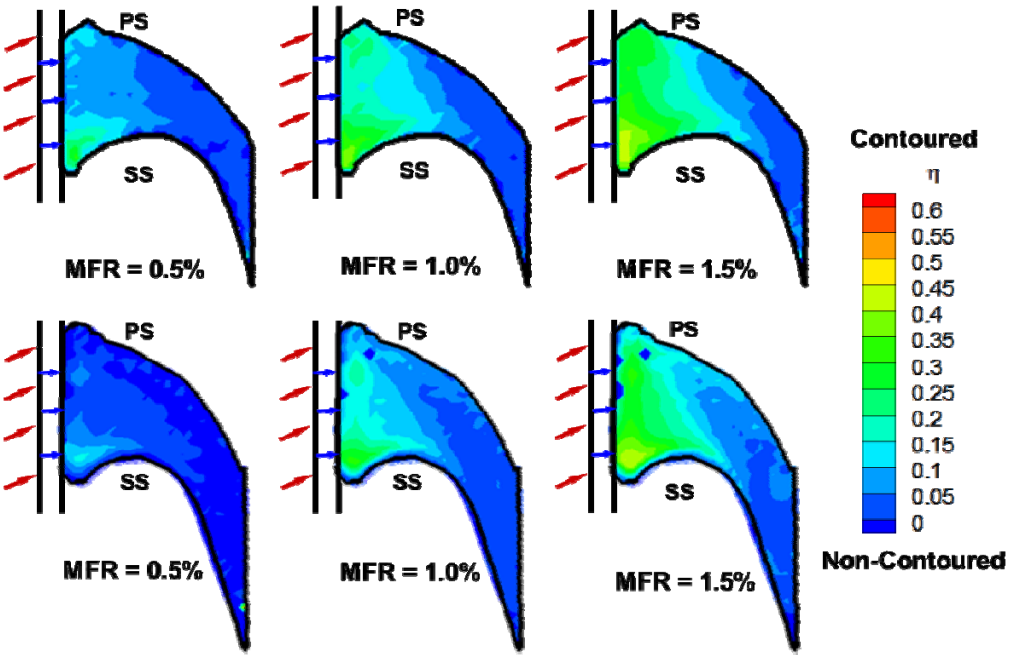

Figure 7.9: Film cooling effectiveness distribution on the contoured and non-contoured rotating platform for 2550 rpm.

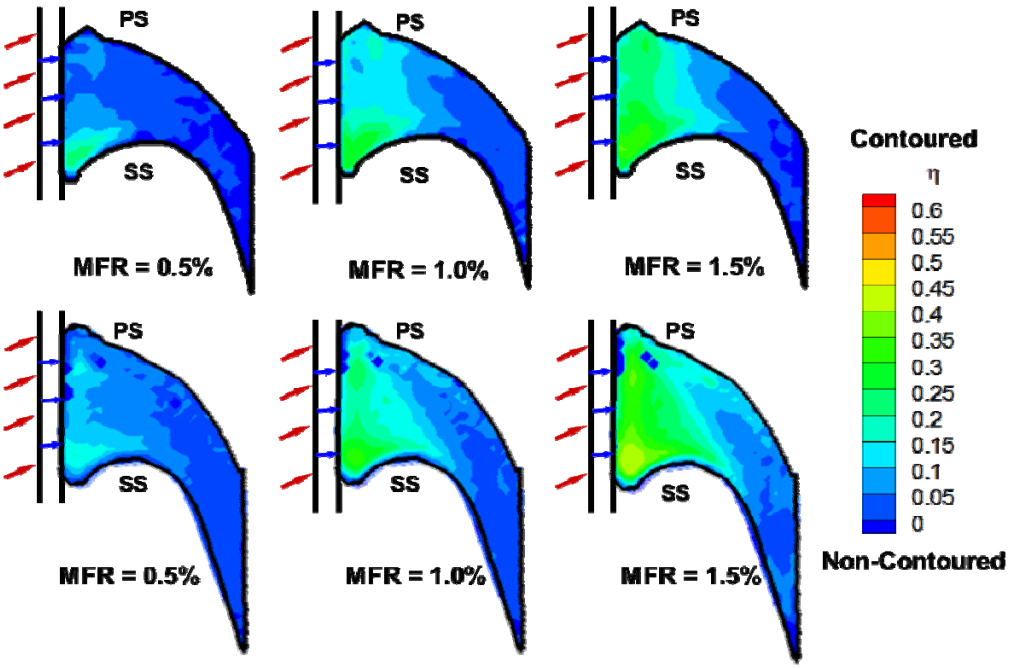

Figure 7.10: Film cooling effectiveness distribution on the contoured and non-contoured rotating platform for 2400 rpm.

7.6 Variation of Rotating Conditions

At rotational speeds lower than the design speed, the blade flow deflection becomes larger leading to higher specific stage load coefficient, and the stagnation region moves towards the pressure side as the flow incidence angle increases, as sketched in Figure 7.11. At lower rotating speeds, the stagnation point will further move towards the blade pressure side resulting in a higher pressure zone close to the pressure surface. The concentration of higher pressure on the pressure side causes a significant movement of the coolant film on the platform surface when it exits from the stator-rotor gap. The local coolant mass flow is pushed toward the suction surface causing the film to cover only smaller portions of the suction surface leading edge. This phenomenon can be clearly observed from data taken for 2550rpm and 2400rpm as shown in Figure 7.9 and Figure 7.10. Both figures include contour plots for 3 different mass flow ratios. More coolant appears to come out from near the suction side of the platform where the pressure difference across the gap is larger with the lower rotational speed.

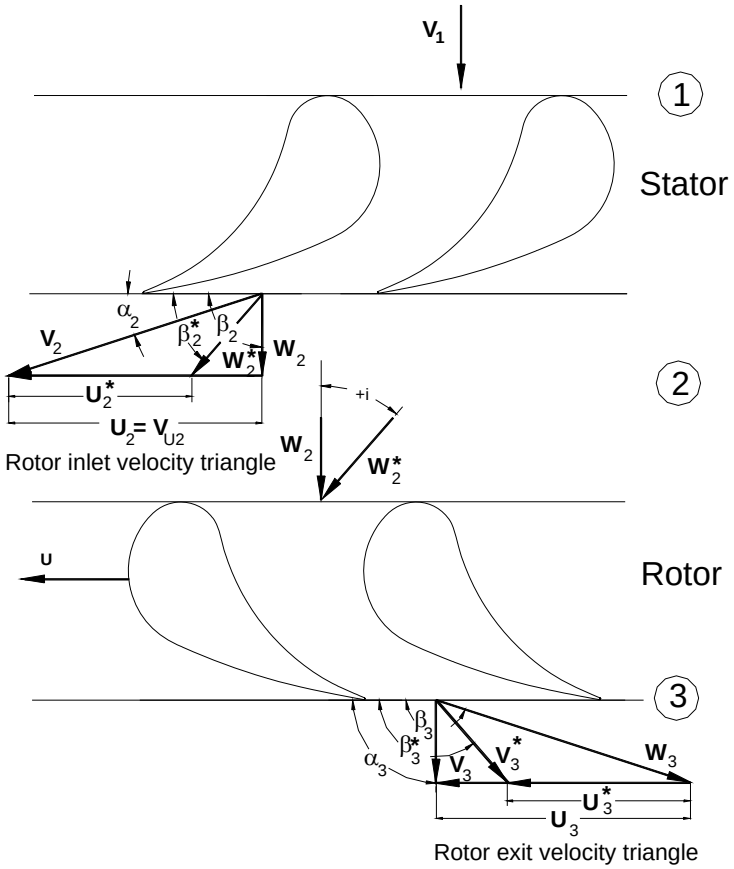

Figure 7.11: Velocity triangles and relative inlet and exit flow angles for design speed and off-design rotating speeds.

After comparing Figure 7.9 and Figure 7.10 for lower rotating speeds with Figure 7.7 at 3000 rpm (reference speed), it can be observed that the effectiveness magnitudes decrease with lower rpm for the same mass flow ratio. This may be a result of stronger

horseshoe vortices close to the suction side due to the shift in the flow incidence angle at lower rpm. For both reference and lower rotating speeds, the region downstream of the throat remains uncooled. The secondary flow vortices in the passage erode the coolant film before it reaches the throat.

In addition to the effect on static pressure distribution and film cooling due to the change in incidence angle of the inlet flow along with rotational speed, rotation also affects the coolant flow as it exits the stator-rotor gap. The gap and the disk cavity are bounded by two walls, the stator endwall and the rotor platform. The enclosed coolant mass in the disk cavity will rotate with a certain frequency due to the cavity wall shear stress. High shear stresses, caused by relative motion in the circumferential gap, introduce some swirl in the coolant flow as it exits. Hence, a tangential component exists in the coolant flow as it exits the stator-rotor gap. This causes some additional spreading of the coolant which cannot be achieved for film cooling studies in stationary cascades. This might also explain the larger coolant spread with increasing rotational speeds due to a larger tangential velocity component in the coolant as it exits the gap. The determination of the swirl angle as well as the measurement of this tangential velocity component was not the subject of the current paper. However, these are items of high importance along with the inter-stage measurements.

7.7 Pitchwise-Averaged Film Cooling Effectiveness

The film cooling effectiveness results were averaged along the pitch-wise direction and the averaged data for all coolant-to- mainstream mass flow ratios and rotational speeds are presented in Figure 7.12 along the axial chord. The increase in effectiveness magnitudes with increasing mass flow ratio can be clearly observed from these figures. The averaged plots show a sharp decrease in effectiveness magnitude along the axial chord as indicated earlier with the region beyond X/C_{ax} = 0.6 remaining mostly uncovered with average effectiveness magnitudes below 0.1. The decrease in effectiveness with lower rotational speeds can also be discerned.

Figure 7.12 depicts the averaged effectiveness distribution in axial direction with mass flow ratio as a parameter for contoured and non-contoured reference cases for given rotational speeds of 3000 rpm, 2550 rpm and 2400 rpm. As seen, for the given MFRs close to the leading edge, the patterns of the contoured cases differ substantially from the non-contoured ones. While the effectiveness distributions of non-contoured cases at the leading edge start at much lower effectiveness, the contoured cases systematically reveal higher effectiveness distributions from the leading edge to the trailing edge. These systematic distributions of the film effectiveness with higher starting values are the consequence of the endwall contouring that made possible a continuous reduction of the secondary flow velocity from the pressure to suction surface. This systematic pattern is observed for all three rotational speeds even for the 2400 rpm, which is an extreme off-design condition. By comparing the contoured and non-contoured plots and Figure 7.12, it is concluded that the pressure difference between pressure side and suction side is lower than non-contoured which causes uniform distribution of film cooling effectiveness in the contoured platform. Moreover, the lower pressure difference between the pressure side and suction side reduces the strength of

horseshoe vortices and therefore less mixing occurs between the coolant and the mainstream flow and as a result there is higher film cooling effectiveness in contoured platform.

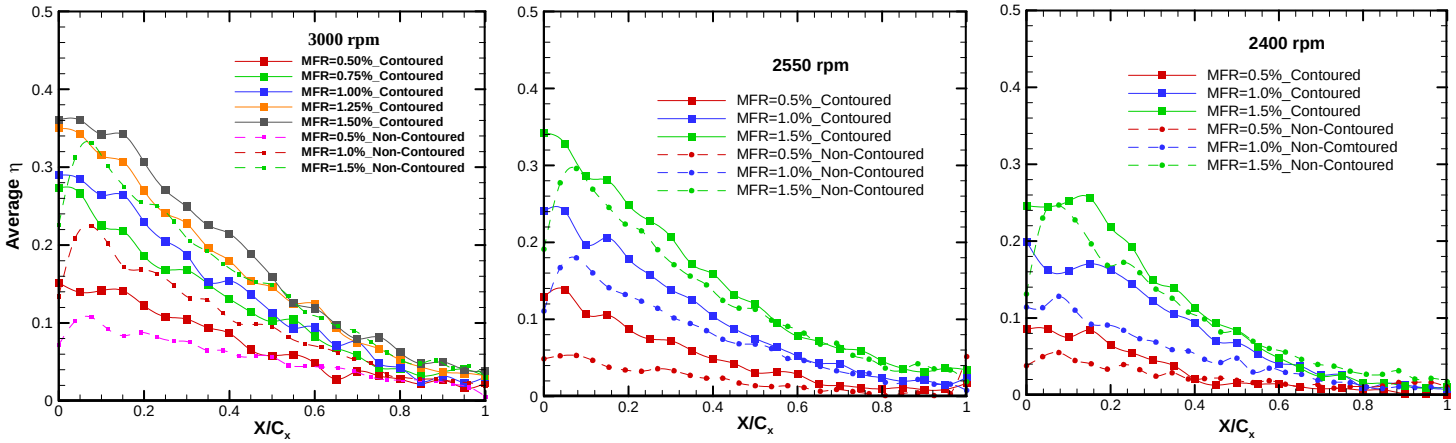

Figure 7.12: Pitchwise-averaged film cooling effectiveness distribution along axial chord for different rpms.

The impact of the rotational speed on the film cooling effectiveness is illustrated in three diagrams of Figure 7.13. It shows the pitch-wise averaged film cooling effectiveness results plotted for the three different MFRs. The impact of turbine rotational speeds on film cooling effectiveness can be clearly perceived from these plots. As rpm increases, the effectiveness magnitudes increase for the same mass flow ratio.

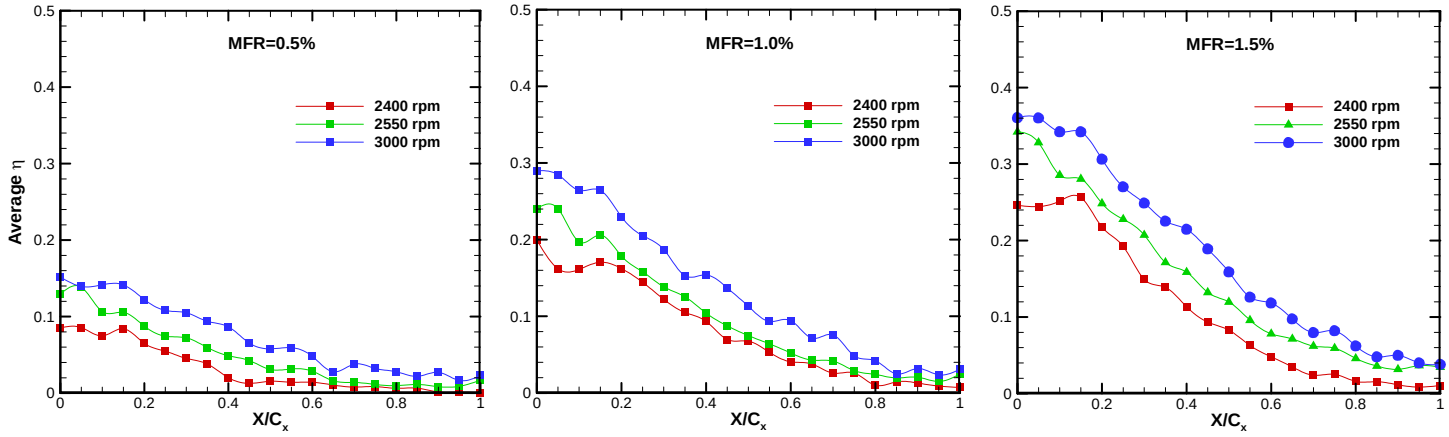

Figure 7.13: Pitchwise-averaged film cooling effectiveness distribution along axial chord for contoured platform for different MFRs.

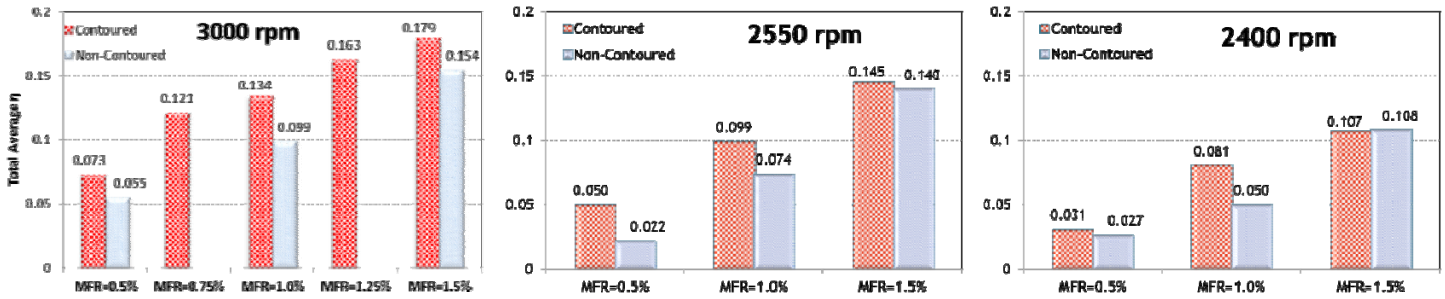

Figure 7.14: Area-averaged film cooling effectiveness for different rpms.

As seen from Figure 7.12 and Figure 7.13, for the contouring endwall, the first 30% of the endwall is sufficiently covered. In non-contoured cases, the coverage of the first 10% is not satisfactory. This reduces the non-contoured coverage to 20% only. Regarding the remaining 70%, different cooling schemes such as installing film cooling holes must be applied as detailed in [5] and [6].

Further information relative to the impact of contouring on total averaged effectiveness is provided by Figure 7.14 to evaluate the overall impact of contouring on effectiveness. For all rotational speeds, the contoured endwall shows higher values. As it is shown by increasing the MFR to 1.5% the difference between total average film cooling effectiveness in contoured and non-contoured becomes lower.

7.8 Influence of Coolant Density on Contoured Endwall Film Cooling

The Majority of the work on film-cooling has been implemented with coolant-to-mainstream density ratios close to 1.0. This is far from the actual density ratio in real turbines due to the temperature difference between the coolant and the hot mainstream. According to different gas turbine designs for platform film cooling, the density ratio changes from 1.5 to 2.0. In this investigation two PSP tests at density ratios of DR=1.0 (using N2 as coolant) and 1.5 (using CO2 as coolant) were performed on the same platform geometry at 3000 rpm and MFR=1%.

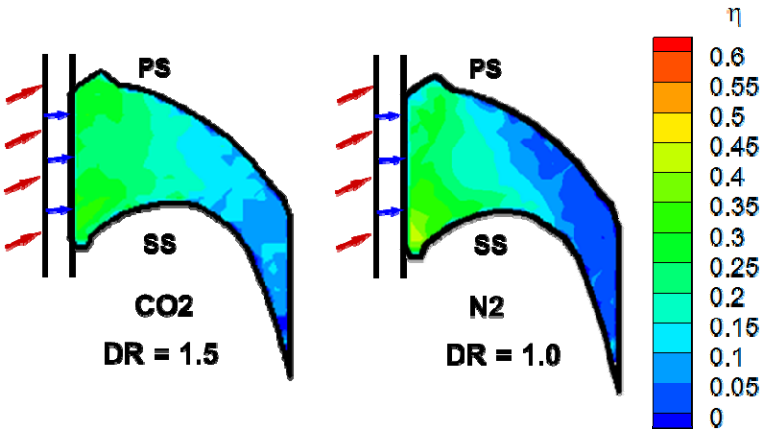

Figure 7.15: Film cooling effectiveness distribution at two different density ratios at 3000 rpm and MFR=1%.

According to Narzary et al. [78], for coolant-to-mainstream density ratio greater than 1.0, the equation 2 could be modified to:

$$\eta = 1 - \frac{1}{\left\{\left(\frac{p_{O_2,m}}{p_{O_2,c}} - 1\right)\frac{MW_c}{MW_m} + 1\right\}} \tag{4}$$

As shown in Figure 7.15 and Figure 7.16, film-cooling effectiveness improved with increasing density ratio. In DR=1.5 the passage platform is almost covered with film cooling. Due to conservation of mass, since the density is increasing, the velocity must decrease which causes the momentum to decrease, and provides higher effectiveness downstream along the endwall passage (compare to lower density coolant like N_2).

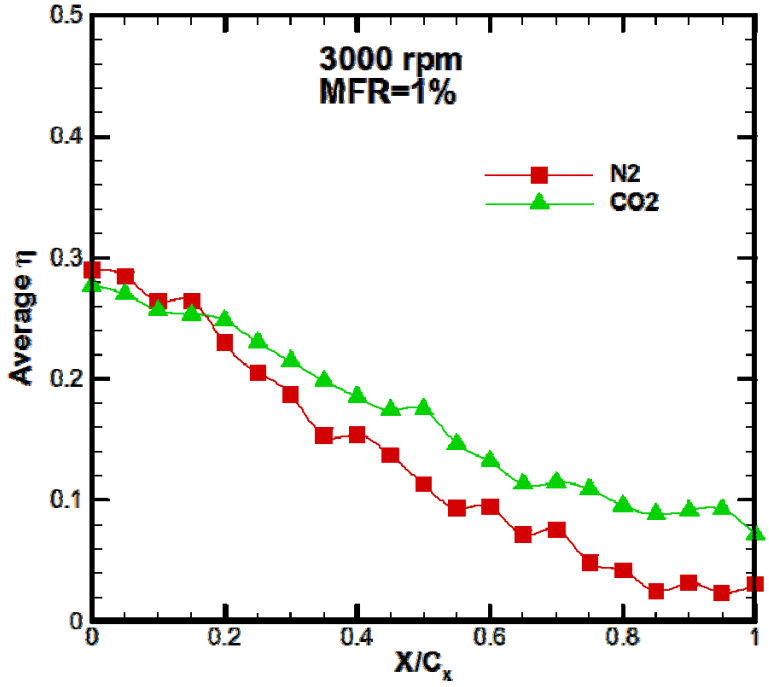

Figure 7.16: Pitchwise-averaged film cooling effectiveness distribution for two different coolant at 3000 rpm, MFR=1%.

8. COMPARISON OF EXPERIMENTS AND CFD FOR ENDWALL FILM COOLING

Besides the detailed analysis of the impact of the R2 endwall contouring on the turbine performance, the TPFL also compared its influence on the film cooling effectiveness for first rotor via both measurements and simulations. The film cooling effectiveness on the R1 hub is experimentally obtained by PSP technique which is based on mass analogue, whereas the CFD evaluation is followed the conventional definition that takes the aerodynamic heating into account [79].

8.1 Stator-Rotor Cavity Flow

Figure 8.1 shows the detailed turbine stator-rotor cavity flow by CFD visualization. At the stator-rotor gap, the distributions of pressure, temperature and relative velocity exhibit strong aperiodic features, as seen in Figure 8.1(a). At the cross section A-A the maximum pressure point is located upstream at the stagnation line. Similarly, the local pressure near the pressure side is higher than the suction side, which generates certain pressure gradient in the gap along the pitchwise direction. Because of the presence of pressure gradient, the purge flow tends to eject out of the stator-rotor gap asymmetrically rather than uniformly.

As a matter of fact, the majority of the coolant particles exits the cavity at higher relative velocity, where it encounters the lower pressure field close to the suction surface. This high velocity field is associated with lower temperature as shown in Figure 8.1(a).

For better understanding the local flow behavior within the gap, two pitchwise cross-sections are created according to the distributions of radial velocity and temperature, as seen in Figure 8.1(c) and (d). Figure 8.1(c) depicts the corresponding location where the majority of coolant is ejected out. The surface streamlines reveals the flow activities at this location. As seen, the coolant flow travels along the inclined purge slot and eventually ejects through the stator-rotor gap. The ejected coolant particles penetrate into the mainstream with certain positive radial velocity and the mixing between the mainstream and purge flow happens primarily out of the gap. However, the purge flow behaves differently at the cross-section B-B in Figure 8.1(d). Due to the resistance created by the local high pressure, the coolant flow can hardly eject trough the slot. A small portion of the mainstream flow from the upstream boundary layer is entrained into the stator-rotor gap, which afterwards mixes with the coolant in the narrow slot. It is seen from the local streamlines, temperature distribution as well as the negative radial velocity (Figure 8.1(a)). It is noted that at some particular locations the hot mainstream particles will be swallowed in the slot and directly impinge on the slot surface which is going to form local hot spots and thus lead to risky burnout. In addition, some amount of the mainstream flow particles travel further into the stator-rotor cavity as shown in Figure 8.1(b).

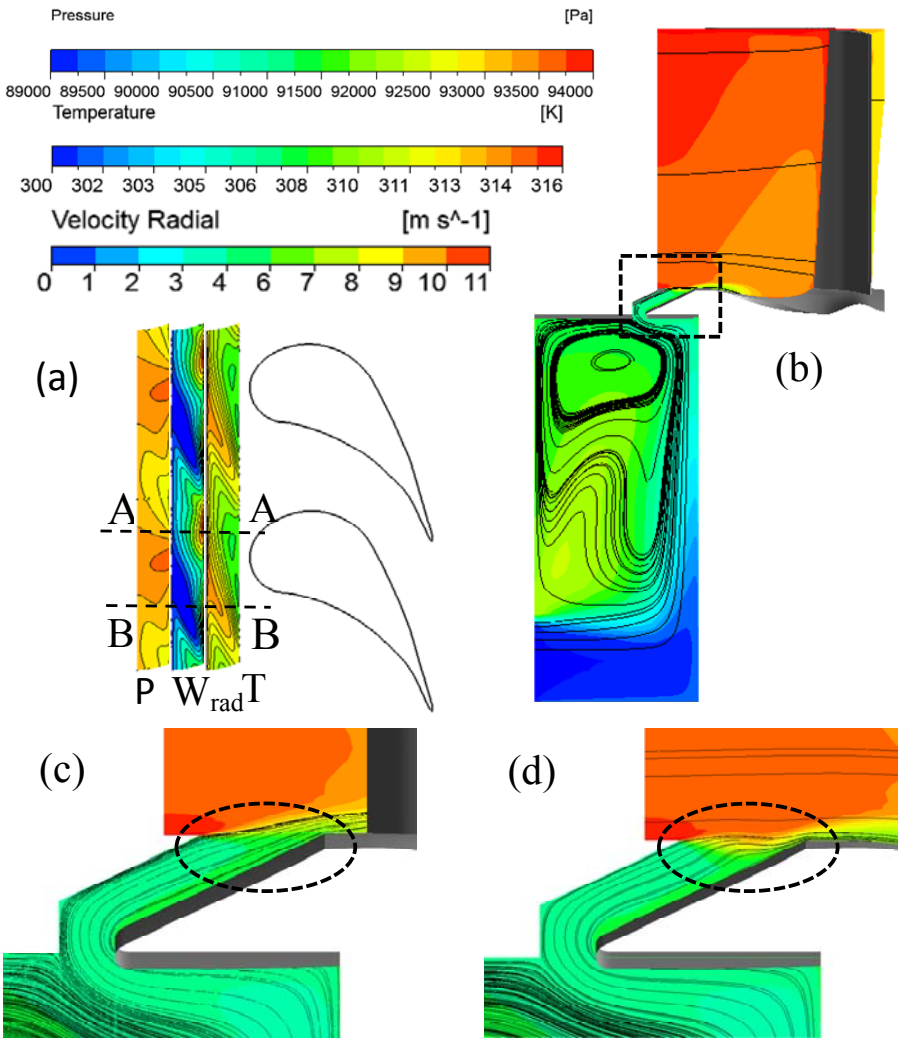

Figure 8.1: CFD visualized stator-rotor cavity flow: (a) Distributions of pressure, radial velocity and temperature at stator-rotor gap; (b) Streamlines and temperature contours for the cavity flow; (c) Streamlines and temperature contours at A-A cross-section; (d) Streamlines and temperature contours at B-B cross-section.

They participate in the large flow circulation within the cavity due to the relative motion between the high-speed rotating rotor disk and stationary wall. Those hot mainstream particles slightly rise up the cavity flow temperature via the mixing process from the circulation, which to some extent declines the cooling capability of the purged coolant. It should be pointed out that the above discussion is based on the steady RANS calculations. In the real engine condition, the phenomena mentioned above can repeat periodically in both the time and space due to the strong stator-rotor interactions which is highly three-dimensional and unsteady. In such a circumstance, URANS must be run in order to fully capture the unsteadiness.

8.2 Impact of Blowing Ratio on Adiabatic Film Cooling Effectiveness

Figure 8.2 shows the impact of the MFR or blowing ratio on the adiabatic film cooling effectiveness on both the contoured and non-contoured rotating first rotor hub with fixed rotational speed of 3000 rpm. Also the CFD predictions are compared with the experimental results. The comparisons for three different MFRs of 0.5%, 1.0% and 1.5%, which are corresponding to blowing ratios M= 0.12, 0.24 and 0.36, are shown. For both contoured and non-contoured cases, larger MFRs give more cooling mass as well as higher coolant momentum. As a result, more coolant particles are capable to penetrate into the highly vortical secondary flow region near the endwall and thus travel further downstream, which usually provides higher film cooling effectiveness. However, if the blowing ratio is too high, the coolant tends to shoot into the mainstream rather than stay close to the endwall, which does not necessarily provide good protection for the hub surface. In this study, the blowing ratio is less than unity and therefore both the measurements and predictions show enhance in film cooling effectiveness on the platform with increasing MFR or M.

Looking at the contour plots of the film cooling effectiveness obtained by the experiments, the endwall contouring delivers better film cooling protection than the non-contoured platform for all MFRs. As seen in Figure 8.2, for non-contoured cases, relatively high cooling effectiveness is obtained near the leading edge on suction side since more coolant is ejected out in this region due to the pressure distribution within the stator-rotor gap (as discussed for Figure 8.1). The coolant particles can travel along the suction side from approximately 25% up to 50% Cax with varying MFRs. However, the coverage of the cooling film decreases fast from the suction side to the pressure side. The surface near the suction side can hardly be cooled for MFR=0.5% and 1.0%. It becomes better when the MFR increases to 1.5% since more coolant is ejected. Still the film cooling effectiveness fades rapidly long the pressure side which resulting a triangular area covered by the cooling film. This triangular-shape area (with less cooled at pressure side) is formed due to the strong secondary flow system. The large pressure gradient between the pressure- and suction-side pushes the pressure-side leg horseshoe vortex and the crossflow from the pressure side to the suction surface. These secondary flows entrain the coolant film and take the coolant particles to travel laterally. Therefore the pressure side is much less cooled.

In contrast, more coolant particles travel along the pressure side and much larger travelling distance is obtained when the endwall contouring is used. As a result the cooling film covers more platform surface area than the non-contoured platform. Particularly the region covered by the coolant for MFR=1.0% and 1.5% transforms from the triangular shape to trapezoidal shape. Additionally the effectiveness distribution is more uniform in the pitchwise direction as well. Apparently the improvement of the film cooling is benefited from the presence of the endwall contouring. Since the contouring is able to greatly decrease the pressure difference between the blade pressure- and suction-side and to some extent suppress the horseshoe vortex [59], therefore the strength of the secondary flow is significantly weakened. As a result, the coolant can travel along the streamwise with much less interference by the secondary flow and thus spread more uniformly on the hub surface.

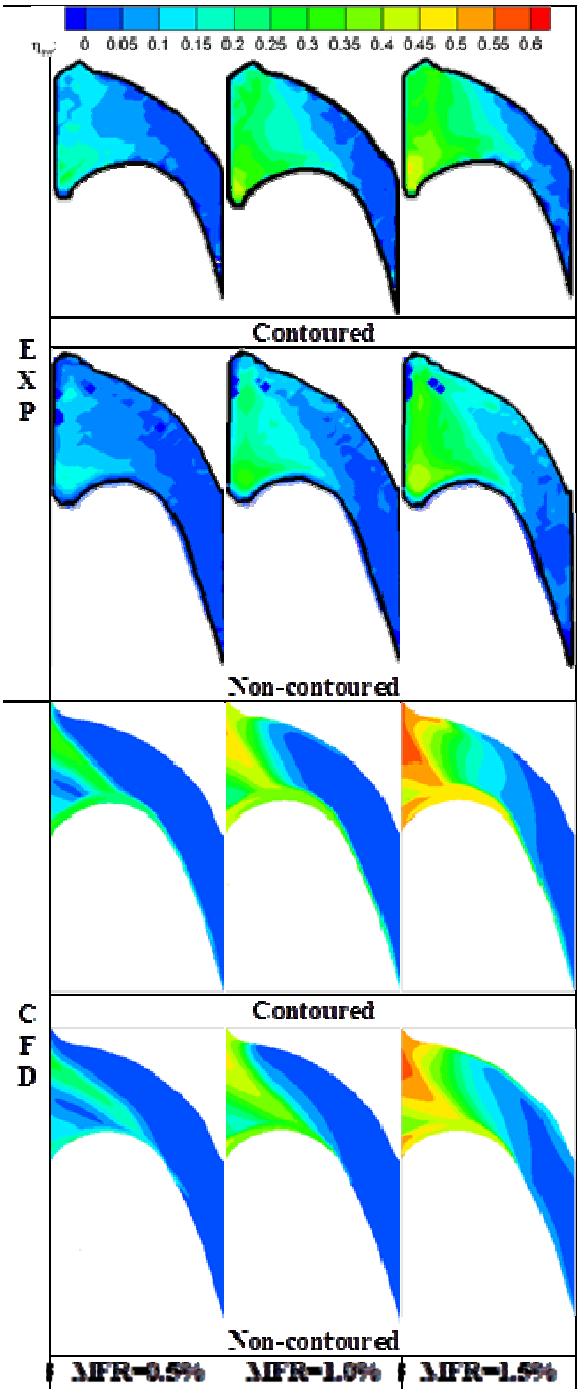

Figure 8.2: Comparison of measured (EXP) and predicted (CFD) film cooling effectiveness distribution on the contoured and non-contoured rotating platform with different MFRs for fixed rotation speed of 3000 rpm.

The CFD predictions also show that the coolant particles can travel to further downstream along the pressure side if the endwall contouring is utilized, especially for

MFR=1.0% and 1.5%. Meanwhile the coolant coverage along the streamwise tends to be more uniform with the presence of the endwall contouring. Both indicate that the film cooling has improved as concluded from the experimental results. However when compared to the experiments, both the effectiveness distribution and the magnitude show considerable differences. Unlike the contour plots for experiment, it seems that the majority of the coolant exits from the gap portion near the pressure side rather than the suction side. Moreover, the magnitude shows higher number from the CFD calculations. The discrepancy between the CFD and experiment will be discussed in a separate paragraph later.

8.3 Impact of Rotation Speed on Adiabatic Film Cooling Effectiveness

The effect of rotation on the platform film cooling is shown in Figure 8.3. This study deals with three different rotational speeds of 2400 rpm, 2550 rpm and 3000 rpm with the fixed typical MFR=1.0%. Generally, when the turbine is running under off-design conditions with lower rotational speeds compared to design speed, the flow deflection becomes larger or in other words the incidence angle is increased. As a result, the stagnation point moves towards the blade pressure side forming a higher pressure zone along the pressure side. The direct consequence is a certain increase in blade loads or pressure gradient between the pressure- and suction-side directly on the endwall. Accordingly the strength of the secondary flow system grows due to the stronger driving force. Meanwhile, the high pressure gradient further pushes the incoming cooling film away from the pressure side to the suction side once it exits from the stator-rotor gap. Hence, at the lower rotational speeds, the film coverage and thus, the film cooling effectiveness will be partially reduced. This is evidently seen from the experimental results in Figure 8.3 that the coolant covered area gradually shrinks and the effectiveness magnitude slightly declines as the rotational speed drops from 3000 rpm to 2400 rpm.

Nevertheless, even though the effectiveness of the film cooling tends to reduce by lowering down the turbine rotational speed, the contoured platform obtains better film cooling than non-contoured hub for all tested off-design conditions. In other words, the presence of the endwall contouring is able to partly compensate the reduced cooling effectiveness due to the off-design deviations and therefore reduce the potential risk of platform burnout. It also implies that the cooling mass can be to some extent reduced, which enhances the turbine aerodynamic performance associated with lower cooling mass flow.

Overall, the above discussion explicitly demonstrates the excellent heat transfer performance and the robustness of the endwall contouring for general turbine design and off-design running conditions. The CFD simulations also show the tendency that the distribution of the cooling effectiveness shifts from the pressure side to the suction side for both contoured and non-contoured rotor platforms as lowering the rotational speed. However, it seems that the predicted effectiveness is less sensitive to the rotational speed of 2400 rpm and 2550 rpm. Only slight shrink in the covered area is observed when the rotating speed switches from 2550 rpm to 2400 rpm. In addition, the predicted film coverage on the contoured platform merely shows marginable improvement compared to the non-contoured case under lower rotation speeds.

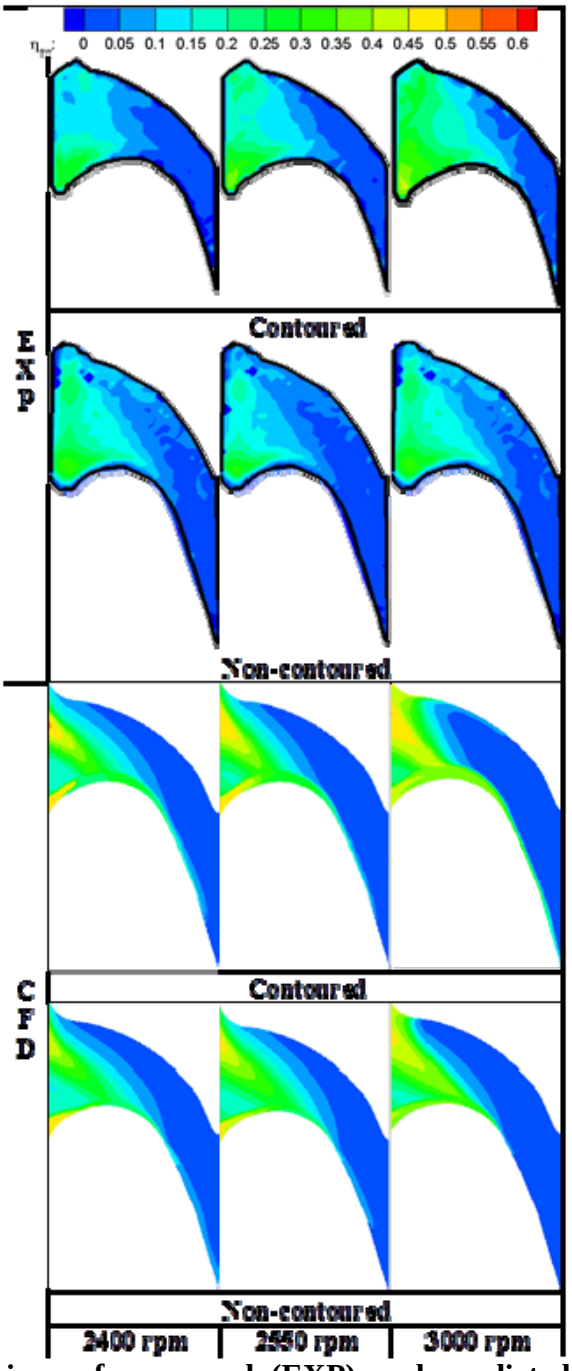

Figure 8.3: Comparison of measured (EXP) and predicted (CFD) film cooling effectiveness distribution on the contoured and non-contoured rotating platform with different rotation speeds for MFR=1.0%.

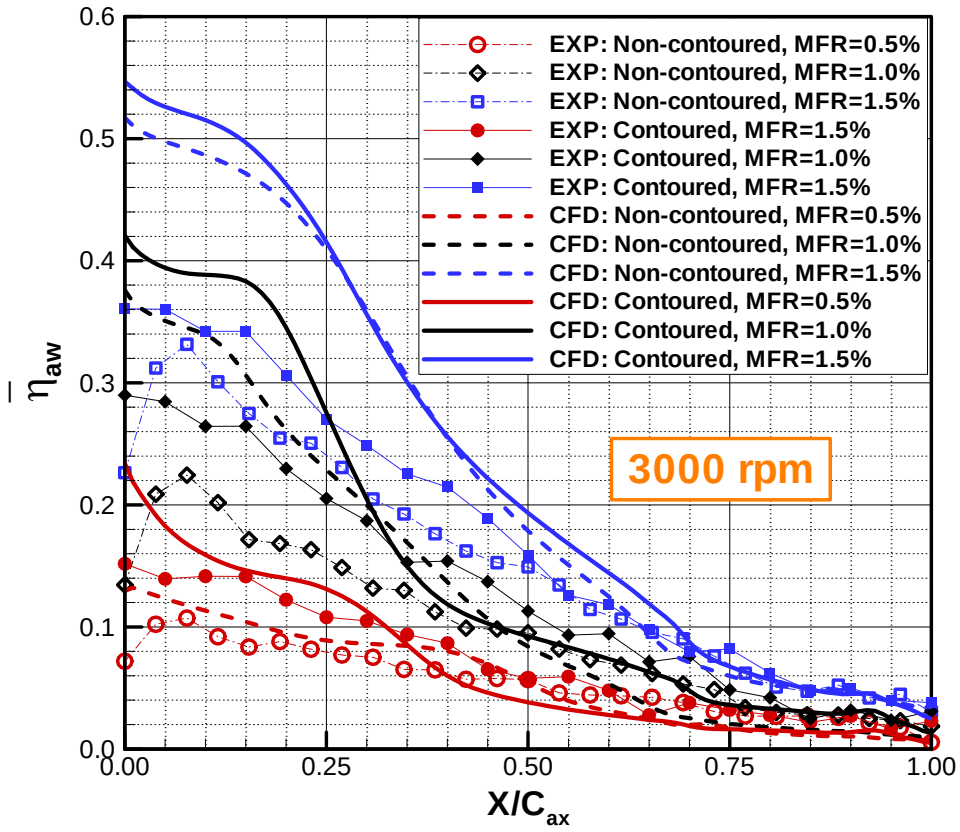

Figure 8.4: Pitchwise-averaged film cooling effectiveness distribution (experiment and CFD) of both contoured and non-contoured rotating platform with different MFRs for rotation speed of 3000 rpm.

The pitchwise-averaged film cooling effectiveness of both contoured and non-contoured platform with different MFRs is plotted in Figure 8.4. Both experimental and CFD results were obtained under reference rotational speed of 3000 rpm. Apparently increasing the MFR leads to the growth of cooling effectiveness magnitude for all cases. However, the averaged plots show a rapid decrease in effectiveness magnitude for the region beyond $0.6C_{ax}$ remaining mostly uncovered with average effectiveness magnitudes below 0.1. Noticeably, the endwall contouring exhibits superiority in improving film cooling on platform for all studied MFRs. The observed improvement extend up to $0.6C_{ax}$ for measured data whereas approximately $0.4C_{ax}$ for predicted values. Hence, CFD has under-predicted coolant film coverage as discussed earlier. However, effectiveness is overpredicted compared to the measurements. Up to 50% higher effectiveness can be seen from the leading edge to $0.25C_{ax}$.

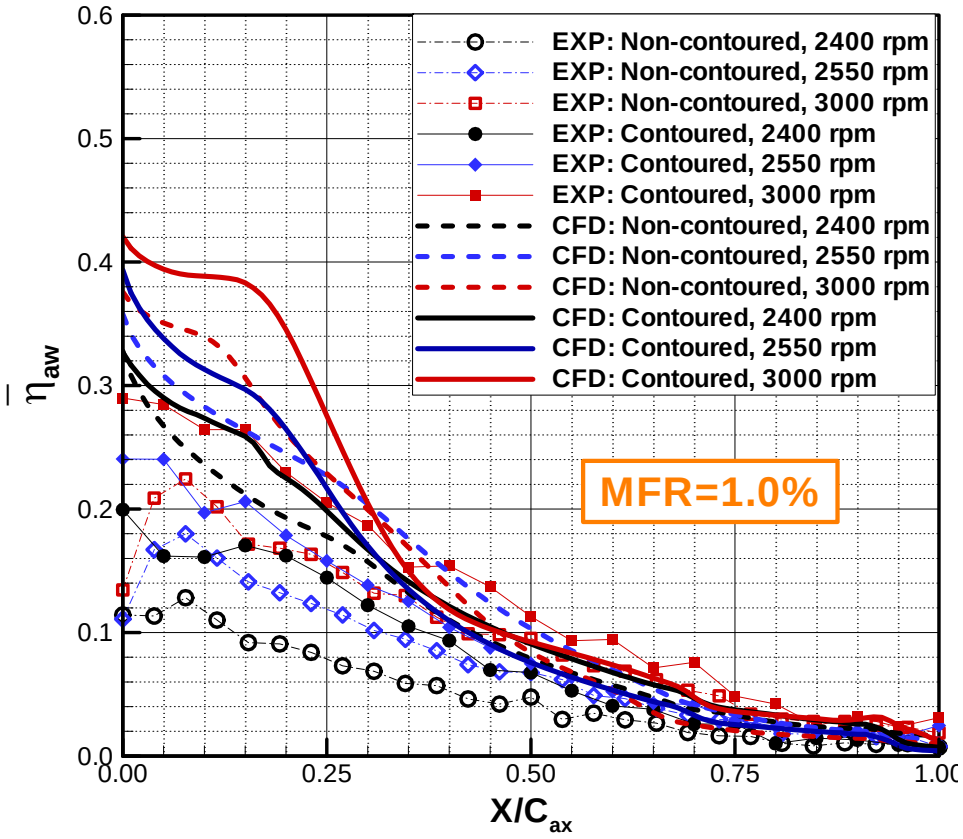

Figure 8.5: Pitchwise-averaged film cooling effectiveness distribution (experiment and CFD) of both contoured and non-contoured rotating platform with different rotation speeds for MFR=1.0%.

Figure 8.5 depicts the impact of the rotational speeds on the pitchwise-averaged film cooling effectiveness on the rotor platform. The plots compare both the experiments and CFD for contoured and non-contoured hub with 1.0% of the coolant ejected at different rotational speed. The averaged effectiveness grows with the increasing turbine rotational speed for both experiments and CFD. However, in the tested speed range, the cooling effectiveness is not as sensitive to the rotating speed as to the MFR or blowing ratio. As expected, the presence of endwall contouring significantly boosts the measured film cooling effectiveness up to a percentage of 100% for the first half axial chord. Yet similarly, the predicted cooling effectiveness on contoured hub decays more rapidly so that the benefit vanishes at about $0.35C_{ax}$. Moreover, overprediction in the effectiveness magnitude appears for all studied rotational speeds.

The area-averaged cooling effectiveness can be found in Figure 8.6 and Figure 8.7 where the former illustrates the impact of MFR and the latter depicts the rotation effect. As seen, the measured overall effectiveness monotonously reduces with decreasing MFR as well as rotational speed. The endwall contouring achieves its highest performance with 1.0% coolant ejected while at a rotational speed of 3000 rpm. Considering the averaged values, it is noted that CFD is capable of providing consistent tendency with

acceptable accuracy for different MFRs. It also delivers similar trend with the experiments when studying the rotation effect on contoured endwall, nevertheless fails for non-contoured case.

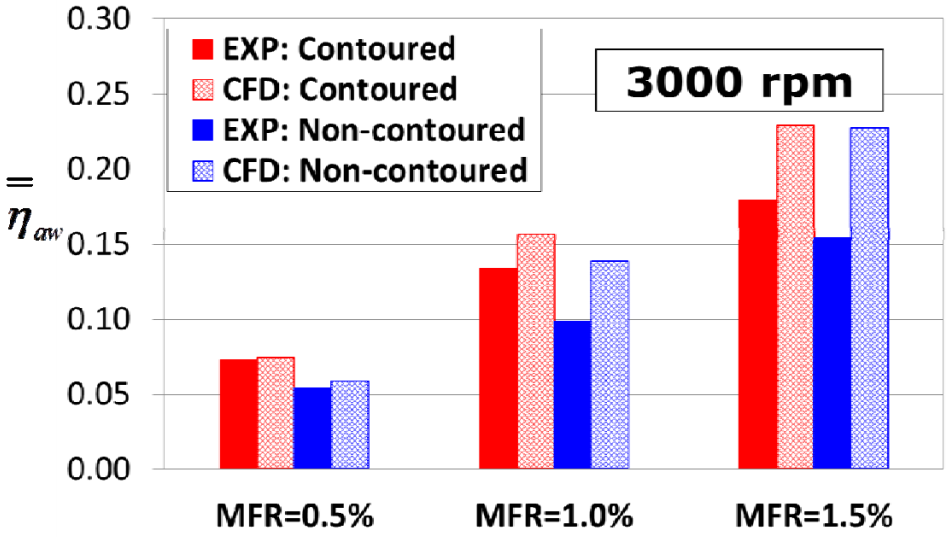

Figure 8.6: Area-averaged film cooling effectiveness distribution (experiment and CFD) of both contoured and non-contoured rotating platform with different MFRs for rotation speed of 3000 rpm.

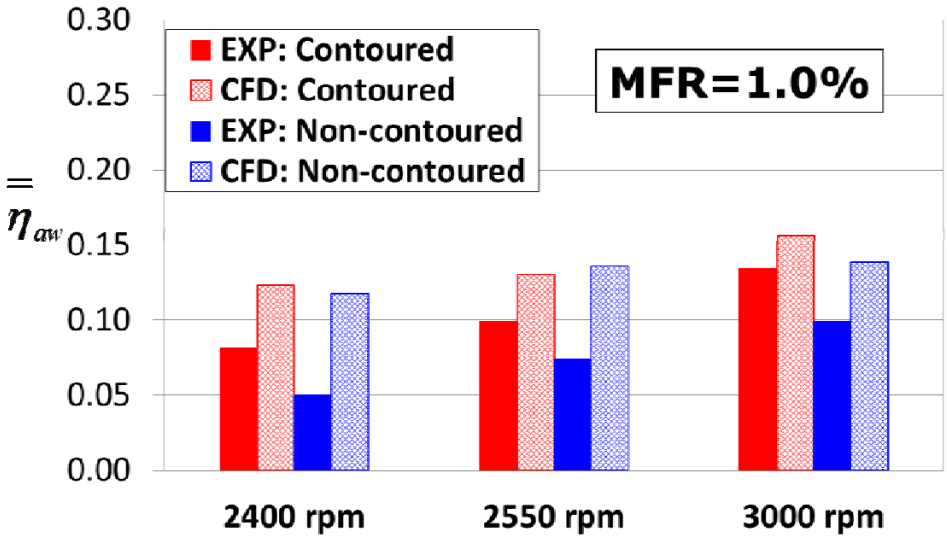

Figure 8.7: Area-averaged film cooling effectiveness distribution (experiment and CFD) of both contoured and non-contoured rotating platform with different rotation speeds for MFR=1.0%.

Through the comparison of film cooling effectiveness obtained by PSP measurements and CFD simulations in this paper, it is seen that the commercial CFD codes are generally able to qualitatively capture the physical phenomena and well

predict the tendency. However, a quantitative prediction of aerodynamics and heat transfer performance is associated with deviations compared with experiments and the prediction accuracy as well.

8.4 Discussions on Discrepancy between CFD and Experiment

Through the comparison of film cooling effectiveness obtained by PSP measurements and CFD simulations in this paper, it is seen that the commercial CFD codes are generally able to qualitatively capture the physical phenomena and well predict the likely tendency however usually deliver more or less deviation from the experiments in quantitative analysis. Looking back at the cooling effectiveness contour plots, the considerable discrepancy should be attributed to the dissimilar methodologies utilized in experiments and simulations. First of all, the PSP technique needs to capture the reflected spectrum which eventually converts to the cooling effectiveness. For the rotating rig, it is very difficult to attach the camera to the rotational portion (rotor) that rotates at a speed of 3000 rpm. Instead the camera is fixed outside of the turbine to capture the reflection at the instant when the painted piece of the hub passing its field of view. Each time at that particular moment, the rotor blades always keep a relative position with the upstream stators. Hence the information acquired by the camera is always corresponding to a fixed instant of the periodic stator-rotor interaction rather than the time-averaged value.

In contrast, the CFD has to give up the unsteady simulation due to its unaffordable computing resource. As an alternative, the steady calculations with mixing Plain interface treatment were carried out. The mixing Plain performs the circumferential average at the interface where the upstream distributed characteristics are fully wiped. Therefore, the cavity flow shown in Figure 8.1 is based on the steady calculations, which illustrate neither the unsteadiness nor a single instant of the flow field. For such purge flow with intense stator-rotor interactions, using steady simulations is a compromising solution. Consequently, it is hasty to conclude that CFD fails in the prediction of cooling effectiveness distribution, since some consistent details such as better cooling at the pressure side for contoured hub are obtained. However in such case, unsteady analysis or even frozen rotor might be more appropriate.

Speaking of the deviation in the magnitude prediction, it is primarily attributed to gap between the CFD models and physical facts. For instance, the stator wakes, upstream turbulence intensity, secondary flow systems and so on can probably reduce the film cooling effectiveness, whereas these substantial characteristics have been eliminated by mixing Plain interfaces. Some other factors such as approximations on the turbine geometries may affect the prediction accuracy as well. For example, this study uses smaller volume to represent the huge stator-rotor cavity due to the computing limitation. This may lead to under-estimation diluting effect caused by entrained hot mainstream flow. Importantly, inherent deficiency of the turbulence models in predicting very close-to-wall heat transfer and lacking of proper boundary layer transition models essentially create the difficulty for CFD software in quantitative prediction. Therefore researchers often use CFD tool as a helpful assistant to attain some details which are difficult to measure in order to draw more complete pictures of the research objects.

9. NUMERICAL INVESTIGATIONS FOR BLADE TIP FILM COOLING

This chapter presents the numerical investigations of the aerodynamics and film cooling effectiveness of high pressure turbine blade tips. Four different rotor blade tip configurations have been studied: the Plain tip with tip hole cooling, the squealer tip with tip hole cooling, the Plain tip with pressure-side-hole cooling and the squealer tip with pressure-side-hole cooling. The geometry of the blades is determined based on the blade profiles within the three-stage multi-purpose turbine research facility at the Turbomachinery Performance and Flow Research Laboratory (TPFL), Texas A&M University. Seven perpendicular holes along the camber line are used for the tip hole cooling, whereas seven 45˚ compound angle holes for pressure-side-edge cooling. The clearance between the blade tip and casing is 1.0% of the blade span. For each blade tip configuration, the coolant is ejected through the cooling holes under three different blowing ratios. In this chapter, a comparison between the Plain tip and the squealer tip has been presented. The detailed flow structures and film cooling effectiveness are discussed.

9.1 Introduction into Blade Tip Film Cooling

As mentioned in Chapter 6, one of the major parameters for improving the thermal efficiency of gas turbines is to increase the temperature of the turbine inlet. However, this has inevitably resulted in a larger thermal load on turbine components. The blade tip is one of the parts susceptible to excessive thermal stresses associated with cooling difficulties. For the unshrouded blade, failure of the blade tip is caused mainly by hot tip leakage flow entrained in the tip clearance. Due to the pressure difference between the pressure and the suction sides, the hot free stream gas is driven to penetrate through the tip gap, resulting in a thin boundary layer and the transfer of high heat. Continuous operation under high turbine inlet temperatures enhances the possibility of thermal failure of the hot gas path components [80]. Hence, state-of-the-art cooling techniques must be developed and utilized on the blade tip to avoid blade failure due to the heavy thermal loads.

Understanding the complex mechanism of heat transfer on the turbine blade tips is a prerequisite for effectively designing the blade tip cooling systems. Metzger et al. [81] used a narrow slot-type channel with one of the bounding walls containing a transverse rectangular cavity to model the grooved turbine blade tips. A general reduction of overall heat transfer on the cavity floor was observed as the cavity depth was increased. Bunker [82] provided a comprehensive review and summary of the blade tip heat transfer based on the early public fundamental studies. Azad and Han [83, 84] experimentally investigated the heat transfer coefficient and static pressure distributions on gas turbine blades with Plain and squealer tips installed in a five-bladed linear cascade. All measurements were conducted with tip gap clearances of 1%, 1.5% and 2.5% of the blade span. The results showed that a larger tip gap leads to a stronger heat transfer process. Bunker and Ameri et al. [85, 86] performed comprehensive experimental and numerical studies to investigate the heat transfer on the first-stage blade tip for a large power generation turbine. The detailed distribution of heat transfer

coefficients was reported for different tip geometries at various inlet turbulence intensity levels.

Recently, more researchers have shown interest in the film cooling on turbine blade tips. Kim and Metzger [87] developed an experimental approach to model and measure the heat transfer on turbine blade tips with film cooling. Kim [88] continued the experimental work presented in [87] to study the effects of film cooling on the turbine blade tip heat transfer. The results indicated that the blade tip geometry and injection locations significantly affect the film cooling performance. Kwak and Han [89] measured the heat transfer coefficients and film effectiveness on a gas turbine blade Plain tip with film cooling holes along the camber line and near the tip region of the pressure-side. They found that both the heat transfer coefficient and film effectiveness increased as the tip clearance increased. Meanwhile, increasing the blowing ratio would increase the film cooling effectiveness but decrease the heat transfer coefficient. Kwak and Han [90] also performed similar measurements on the squealer tip with a 4.22% recess of a gas turbine blade. The experimental results showed that the overall heat transfer coefficients increased as the tip clearance increased but decreased as the blowing ratio increased. Nevertheless, the overall film cooling effectiveness increased as the blowing ratio increased. Compared to the Plain tip, the squealer tip would obtain higher overall film cooling effectiveness and lower heat transfer coefficients. Acharya et al. [91] presented numerical simulations of flow and heat transfer for a GE-E3 turbine blade with a film-cooled tip under three different tip clearances. For the flat tip, high film cooling effectiveness and low heat transfer coefficients are obtained along the cooling film, while the squealer tip alters the trajectory of the cooling jets therefore reducing the effectiveness. Adiabatic effectiveness for turbine blades with cooling holes placed along the pressure side tip as well as dirt purge holes placed on the tip was measured by Christophel and Thole et al. [92]. Yang and Chen et al. [93] presented the numerical prediction of film cooling and heat transfer on the Plain and squealer turbine blade tip with different cooling-hole arrangements. The predicted heat transfer coefficients were consistent with those in Kwak and Han's [89], [90] experiments. It was noted that the predicted film cooling effectiveness of the camber arrangement for both the Plain and squealer tips would not increase more with increasing blowing ratio after the blowing ratio reached unity. Nasir et al. [94] investigated the effect of tip gap film cooling for a plain and squealer tip in a four-blade linear cascade. Some effect was observed on plain tips but the effect for squealer tips could be negligible. Gao et al. [95] experimentally studied the effect of inlet flow angle on film cooling effectiveness for a cutback squealer blade tip under average blowing ratios of 0.5, 1.0, 1.5 and 2.0. The coolant jet direction and hence the cooling effectiveness was altered when the incidence angle was changed. However, the flow angles had no significant effect on the area-averaged film cooling effectiveness. Park et al. [96] measured the heat transfer coefficients and film cooling effectiveness on the tip and inner rim walls of a rotor blade with a squealer rim equipped in a three-blade linear cascade. The high heat transfer and film cooling effectiveness regions were obtained near the film-cooling holes. Acharya et al. [97] conducted a numerical study of heat transfer and film cooling effectiveness on a squealer tip with pressure-side and tip coolant holes. In this paper, larger region of film

cooling effectiveness with higher values between the camber line and suction side was reported with higher blowing ratio. Naik et al. [98] experimentally and numerically investigated the flow, heat transfer, and film cooling effectiveness of the high pressure turbine blades with a full rim squealer tip and a partial squealer tip. They found that the suction-side rim within the mid-chord region exhibits the highest heat transfer coefficients.

However, only few papers that consider rotating blades can be found in public studies, due to the difficulty of measurements. Metzger et al. [99] developed a simple model of the leakage flow to estimate both tip and shroud heat transfer. Dunn et al. [100] reported their heat-flux measurements studying the influence of blade tip recess on the tip-region heat transfer for a full-stage rotating transonic turbine. Srinivasan and Goldstein [101] used a moving endwall belt mounted on the top of a five-blade linear cascade to simulate the effect of relative motion between the rotor tip and shroud. The results indicated a reduction of around 9% in mass/heat transfer levels for 0.6% chord clearance. The pressure gradients on the blade tip were decreased as well. Zhou et al. [102] numerically investigated the effects of the endwall motion on the aero-thermal performance of a winglet tip without and with film cooling. With the endwall motion, the overall tip leakage loss was reduced by 15%. The cooling effectiveness was increased by 9% and the associated heat flux on the winglet tip was decreased by 31%. Acharya et al. [103] performed a numerical study to investigate the blade tip heat transfer and flows with both pressure side and tip coolant in the presence of relative motion between the blade and casing. It was confirmed that the relative motion between the tip and shroud had significant effects and thus the statement of pressure-driven leakage flows was not appropriate. Yang et al. [104] numerically simulated the effect of the blade rotation on the flow and heat transfer for turbine blades with Plain and squealer tips. The prediction indicated that the rotation effect on the flow behaviors and heat transfer primarily came from the relative motion of the shroud, especially for the squealer tip. Three different turbine blade tip configurations with film cooling under different rotation speeds were numerically investigated by Zhang et al. [105]. The numerical prediction indicated that the overall heat transfer coefficient increased and overall film cooling effectiveness decreased as the blade rotation speed was increased. This trend was reversed when the blowing ratio was increased. Due to the difficulty of acquiring data on a rotating blade, literature studying the effect of rotation is very scarce. Dring et al. [106] reported film cooling effectiveness in a rotating configuration in a low speed tunnel. Takeishi et al. [107] also studied film cooling effectiveness on a stator-rotor stage, simulating a heavy duty gas turbine. Measured effectiveness values on the suction side for the rotating turbine blade seemed to match the data from the stationary cascade whereas the rotating effectiveness on the pressure side seemed to be significantly lower than the nonrotating case. Effects of rotation are attributed to the deflection of the film cooling jet due to centrifugal forces. Abhari and Epstein [108] reported film cooling heat transfer coefficients by the superposition method on the short-duration MIT blowdown turbine facility using heat flux gauges. Time resolved heat transfer coefficient data was obtained and the benefit of using film cooling on the blade surface is evident. Rotating turbine experiments performed by Ahn et al. [109] and [110]

showed that the turbine rotational speed is the most critical parameter in film cooling effectiveness distributions. The measurements were done using the pressure sensitive paints (PSP). Furthermore, their systematic experimental results show that during an off-design operation, the incidence angle changes, causing the coolant film direction to change.

The objective of the study is to numerically investigate the flow structures and film cooling effectiveness for turbine blades with a Plain tip and squealer tip within a rotating HP turbine. In contrast to the stationary cascades, the rotating blade tip exhibits distinct differences in film cooling effectiveness. Hence, the relative motion between the blade tip and shroud must be taken into account.

9.2 Film Cooling System and Blade Geometry

All the present work is based on the three-stage multi-purpose high-pressure (HP) turbine research facility in TPFL, which is extensively described in [111] and [112]. Since the turbine blades with film cooling holes were recently equipped within the machine, it is necessary to exhibit a brief description of the turbine cooling systems corresponding to the blade tips with film cooling. As seen in Figure 9.1, two independently controlled concentric coolant loops provide the necessary coolant flow for all the cooling measurements either on the turbine platform or on the blade tips. The inner loop (marked by red arrows) supplies coolant mass for film cooling experiments on the hub platform through an upstream stator-rotor circumferential gap positioned between the 1st stage stator and rotor. The outer loop (marked by blue arrows) provides coolant mass for cooling experiments for the discrete film cooling holes on both Plain tips and squealer tips of the first rotor blades. The coolant flow is discharged through a long annular pipe entering the rotor internal cavity. After passing through a cylindrical hole drilled at the center of the bolt that fastens the rotor blade, the coolant mass is ejected into a plenum through eighteen radially distributed tiny holes near the bolt tip, as shown in Figure 9.2. Eventually the coolant flow is injected into the mainstream from seven discrete film cooling holes located either on the blade tip or at the pressure-side edge near tip region. Since the current study is focused on the rotor blade tip film cooling, only the outer loop is turned on.

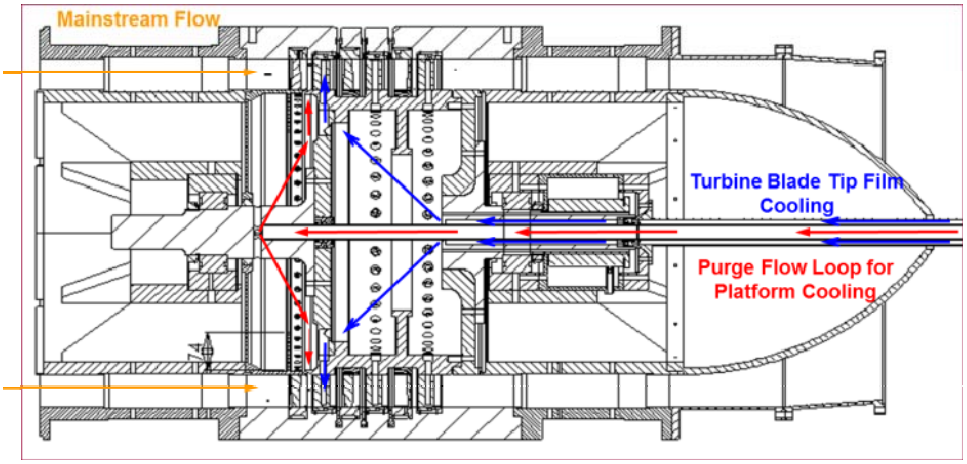

Figure 9.1: Turbine components with two independent cooling loops.

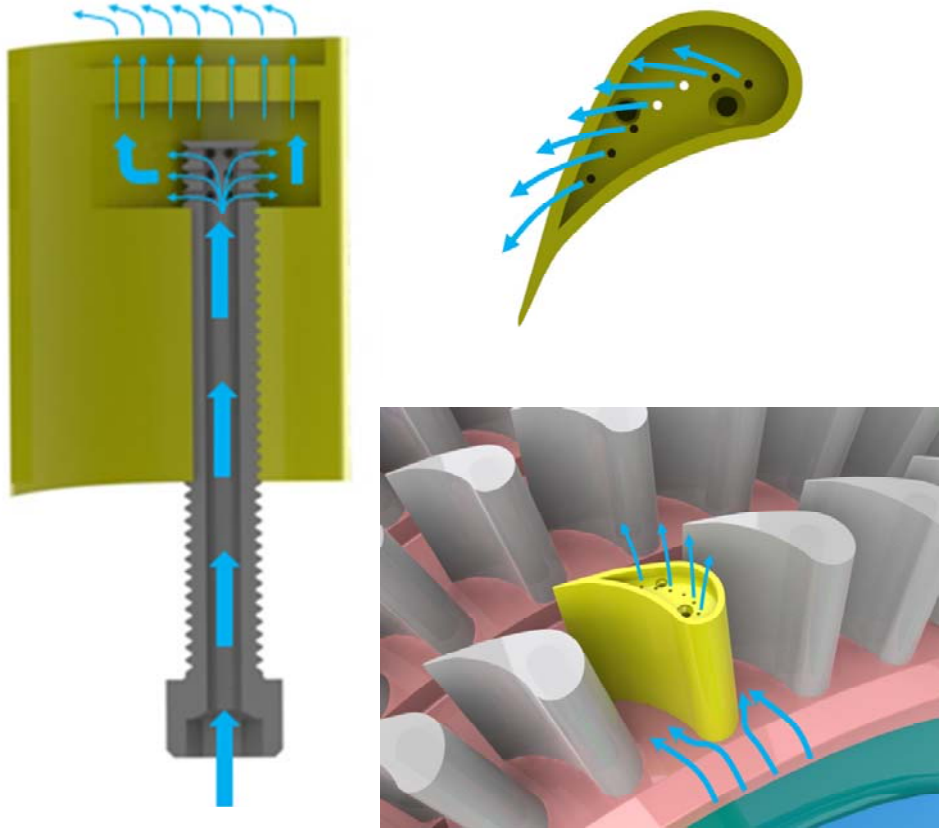

Figure 9.2: Schematic of the blade tip film cooling system.

In fact, TPFL designed and manufactured four pairs of rotor blades with four different film cooling arrangements: the Plain tip with tip hole cooling (red), the Plain tip with pressure-side-edge compound angle hole cooling (green), the squealer tip with tip hole cooling (yellow), and the squealer tip with pressure-side-edge compound angle hole

cooling (blue), as shown in Figure 9.3. Seven perpendicular holes evenly distributed along the camber line are used for the tip hole cooling, whereas eight compound angle holes are used for pressure-side-edge cooling. The four pairs of rotor blades with film cooling holes were axis-symmetrically installed at the first rotor row (Figure 9.3 top). Currently, film cooling effectiveness measurements under rotating conditions are being performed on blade tips with four cooling arrangements, Figure 9.3.

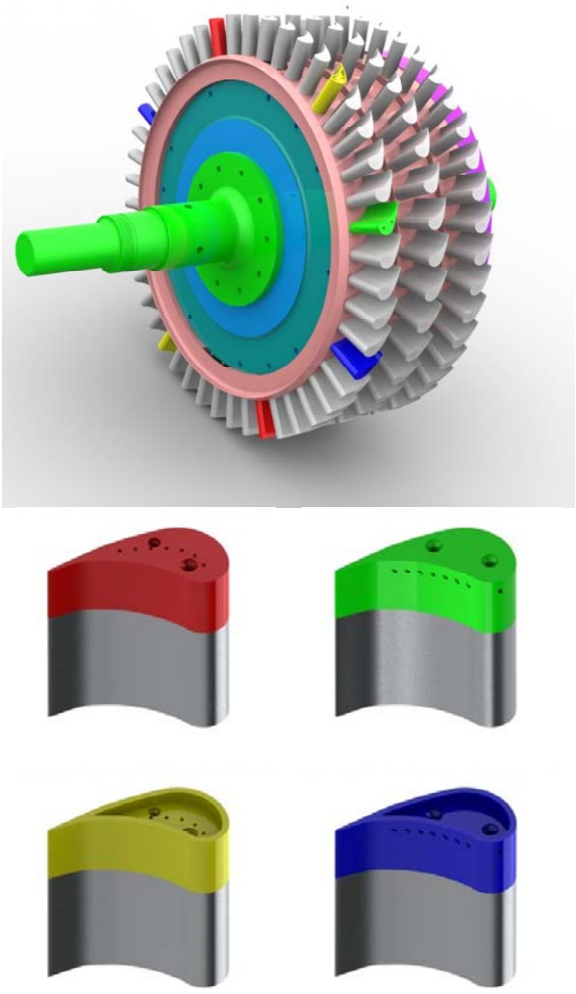

Figure 9.3: Four different rotor blade tip configurations: Plain tip with tip hole cooling (red), Plain tip with pressure-side-edge compound angle hole cooling (green), squealer tip with tip hole cooling (yellow) and squealer tip with pressure-side-edge compound angle hole cooling (blue).

The current numerical study focuses on the flow characteristics and film cooling effectiveness for the Plain tip with tip hole cooling as well as the squealer tip with tip hole cooling. Figure 9.4 depicts these two different blade tip configurations. Each blade

was manufactured according to the rotor blade profile of the first rotor row within the TPFL HP turbine. Seven cylindrical cooling holes that are evenly distributed along the camber line are aligned perpendicularly to the blade tip surface. The diameter (d) of each cooling hole is 1.27 mm and the length has a typical value of 4d that is 5.08mm. Moreover, the squealer tip has a rim width of 2mm and a recess of 4 mm. A plenum is created inside the blade to provide adequate space for establishing a highly uniform pressure distribution. The tip clearance is 1% of the blade span.

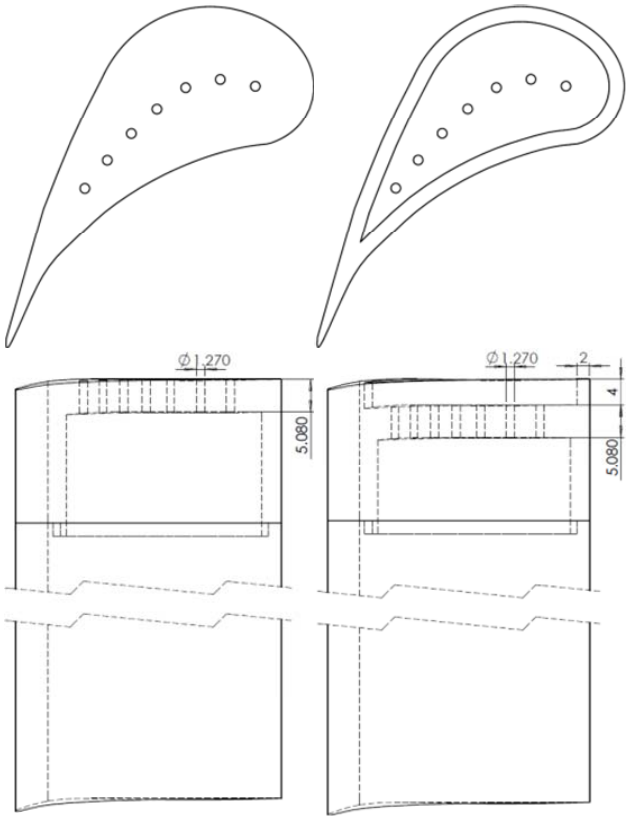

Figure 9.4: Detailed geometry of blade tips: Plain tip (left); Squealer tip (right).

9.3 Computational Details

Three-dimensional calculations were carried out for the first 1.5 turbine stages, which include the first-stage stator (S1), the first-stage rotor (R1) and the second-stage stator (S2), as shown in Figure 9.5 (left). In order to represent the experimental turbine as realistically as possible, all the geometric information is taken exactly from the machine. Especially for R1, the endwall contouring and related purge system [60] are involved according to the turbine structure. To reduce the complexity of the less important parts and decrease the difficulty of mesh generation for correlated geometry, the bolt with eighteen circumferentially distributed discrete holes (Figure 9.2 left) is simplified as a

cylinder (Figure 9.5 bottom). The cylinder incorporates a bolt with inner hole, within which the coolant is injected.

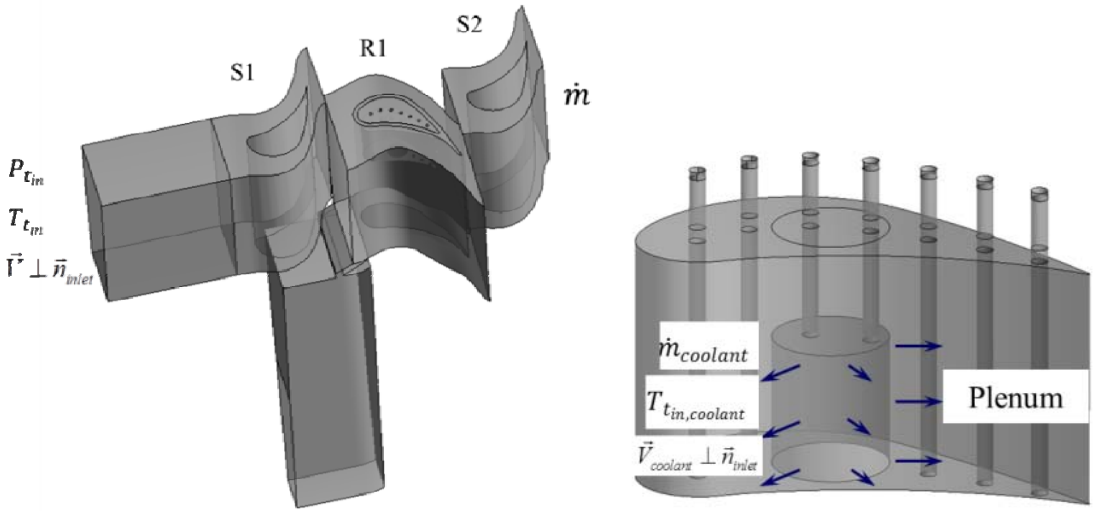

Figure 9.5: Computational domain and boundary conditions for mainstream (left); Details of plenum and boundary conditions for coolant (right).

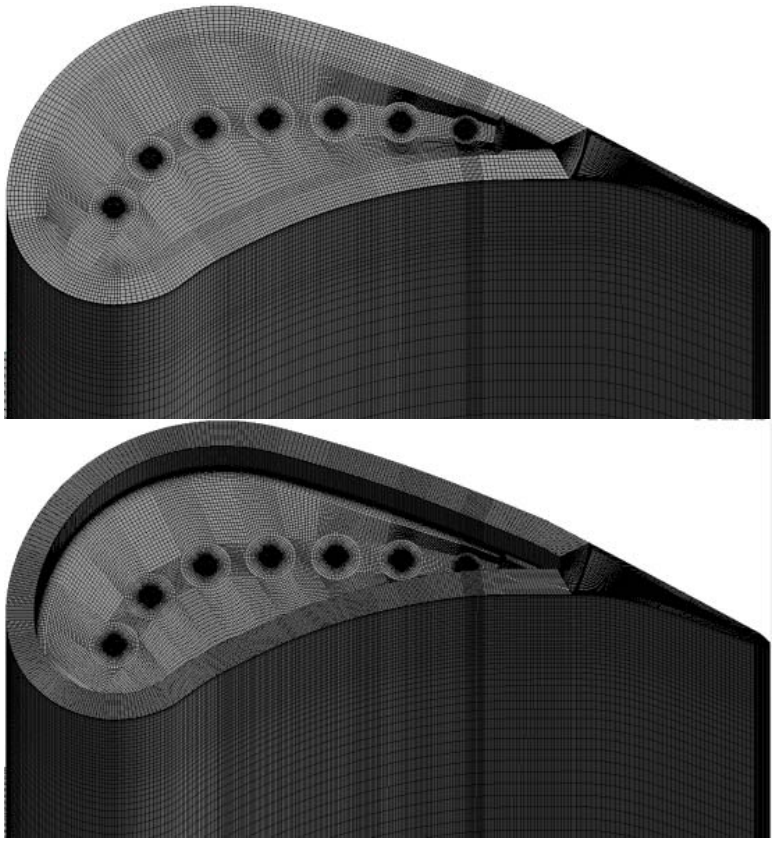

Figure 9.6: Detailed grid distribution of the Plain tip (top) and squealer tip (bottom).

Since R1 is the portion with tip film cooling, the finest mesh is used within this domain, especially at the blade tip region (Figure 9.6). The ANSYS product ICEM CFD is used to generate the hexahedral grids for R1. In total 5,202,620 hexahedral elements are generated for the Plain tip and this number is increased to 6,333,988 for the squealer tip due to the squealer cavity configuration. In both cases, the grids are clustered in the tip gap region. At least 22 nodes are distributed within the boundary layer and the first node is as small as possible to keep y^+ in the order of unity.

All the simulations were performed using the CFD software ANSYS CFX. The steady solutions are obtained by solving Reynolds-Averaged-Navier-Stokes (RANS) equations with a finite volume method. The SST-turbulence model was chosen according to extensive turbulence model studies performed on several TPFL-turbines and the numerical calculations showed the suitability of the SST-model for calculating the flow quantities [58].

With regard to boundary conditions (Figure 9.5), the total pressure and total temperature are given at the turbine inlet. Meanwhile, the mass flow rate is fixed at the turbine exit. The total temperature and the mass flow rate are specified as boundary conditions for the coolant. The flow velocity at all inlets is assumed normal to the boundaries and a typical turbulence intensity (5%) is specified. Additionally, adiabatic and non-slip conditions are used for the walls. For each blade tip configuration, the numerical simulations were conducted under global blowing ratios of M=0.5, 1.0 and 1.5, respectively.

The global blowing ratio is based on the average of the velocity between the rotor inlet and exit. The rotor rotates at its designed rotational speed of 3000 rpm with the best performance point corresponding to the highest turbine efficiency for the test rig simulated in this paper.

Each simulation was calculated until the global root mean square residuals for the RANS equations reached values below 10^{-4} (10^{-5} for energy). Moreover, various parameters were monitored as the solver was running. Examples include the average pressure at the exit, the mass conservation for the entire machine and each cooling hole, and the isentropic efficiency of the machine, etc. Convergence was achieved when the residuals' target value was reached, and the stability was observed in the monitored variables. Typically, 2,500 iterations are necessary to achieve convergence. As a result, each single case computed in the parallel mode on Texas A&M super computers consumed several hundred hours of computation time.

The grid independence study was performed for the Plain tip at M=1.0. Three different grids with 2,447,434, 5,202,620 and 9,653,609 elements were numerically tested respectively. By examining the differences among the three solutions in Figure 9.7, the second mesh was chosen considering the accuracy, time, and resources. For the squealer tip, mesh with the similar density was generated within the squealer cavity, while the rest of the parts obtain the same node clustering as the Plain tip.

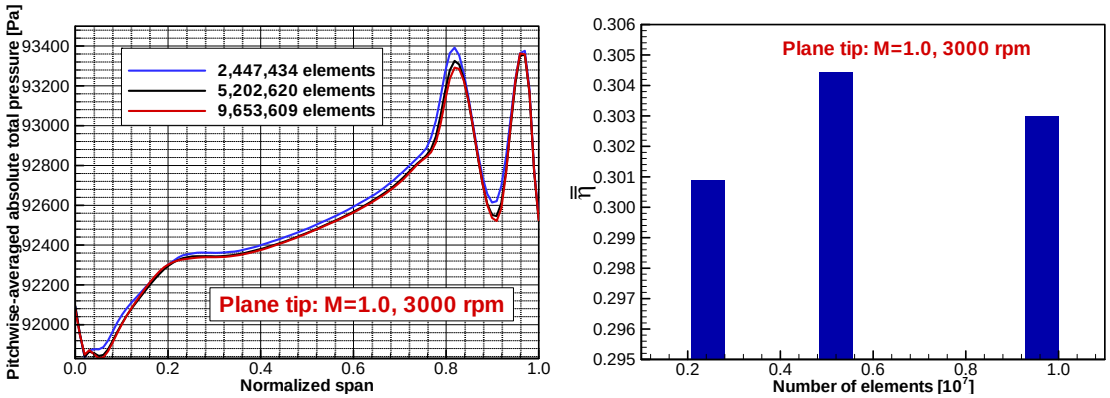

Figure 9.7: Grid sensitivity study: Pitchwise-averaged absolute total pressure from the hub to tip at the rotor exit (left); Overall global film cooling effectiveness on the blade tip (right).

9.4 Tip Hole Cooling

9.4.1 Impact of Blowing Ratio, Plain Tip

Figure 9.8 depicts the static pressure distribution at the blade tip region for both the Plain tip and the squealer tip for blowing ratios of M=0.5, 1.0 and 1.5. For the Plain tip without film cooling holes, the typical pressure distribution is obtained. The pressure side (PS) has the highest pressure and the pressure is gradually decreased towards the suction side (SS). The resulted pressure gradient pointing from PS to SS is the primary driving force of the tip-gap leakage flow. Note that the contours of pressure are smooth everywhere implying a gradual transition of the potential field. Relatively low pressure is observed at the trailing edge mainly due to the expansion process through the blade channel. Figure 9.9(d) depicts the corresponding streamline patterns at the blade tip region. Since the object of the current study is a rotor blade rotating at 3000 rpm with the tip speed of 215.34 m/s, the streamlines are plotted based on the relative velocity in the rotating coordinates. Due to the blunt and round leading edge of the blade, the pressure gradient at the leading edge is not as big as that between the pressure side and suction side. Consequently, the mainstream particles entering the tip gap are not deflected immediately. Nevertheless, they keep traveling a distance along the initial direction until the pressure gradient becomes high enough to push them to the suction side at about 30% of C_{ax}. As a result, a small amount of flow leaks from the pressure side of the leading edge, whereas the majority moves towards the suction side forming a system of tip vortices. After 30% C_{ax}, the pressure gradient is dominant.

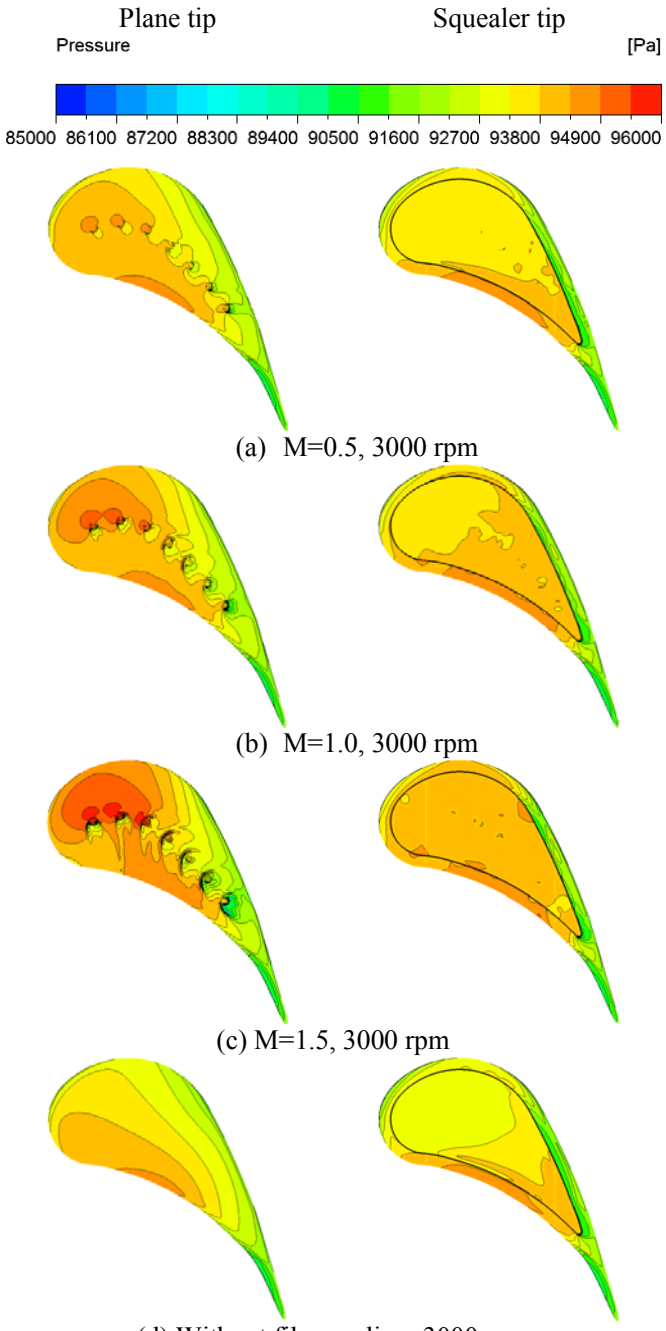

(a) M=0.5, 3000 rpm

(b) M=1.0, 3000 rpm

(c) M=1.5, 3000 rpm

(d) Without film cooling, 3000 rpm

Figure 9.8: Distribution of the static pressure at 3000 rpm: Blade tip for the Plain tip (left); Cavity floor and rim for the squealer tip (right).

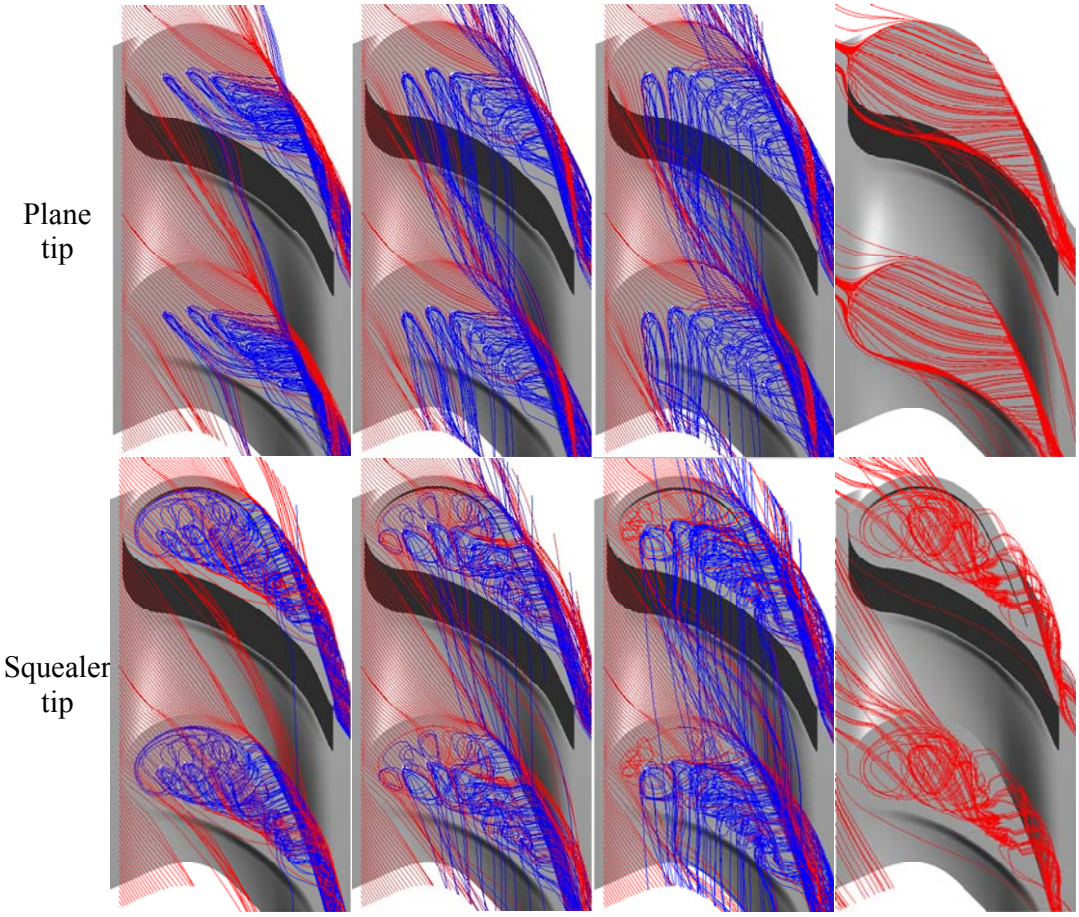

Figure 9.9: Streamlines based on the relative velocity at the blade tip region at 3000 rpm (blue indicates cooling air, red is freestream air).

Comparing Figure 9.8 (a, b, c), that pertains to the film cooling injection to the figure without injection (d), shows that the presence of film cooling significantly changes the pressure field, especially in the vicinity of the cooling jets. This change of the pressure field is directly related to the blowing ratio, which reflects the ratio of the cooling jet momentum and the momentum of the mainstream. For M = 0.5, the cooling jet does not have the momentum to overcome the main mass flow momentum. As a result, it dissipates and contributes to higher tip clearance total pressure losses. The situation changes when M is increased. At M= 1.0, the injected jet has enough momentum to significantly impact the pressure field. The radially ejecting jets at this ratio impinge on the turbine casing and generate locally a quasi-stagnation zone with higher pressure. This is illustrated for the first three holes. At M =1.5, the front portion of the blade tip is occupied by a pressure field that is about 3.6% (3,300 Pa) above the zero injection case (d). With the increasing blowing ratio, the pressure near the leading edge tends to increase. In addition, the high-pressure area at the pressure side preserves the same shape

for the non-cooling cases and cases under blowing ratios of M=0.5 and 1.0. When it comes to the blowing ratio of M=1.5, the area is significantly extended towards the suction side.

The presence of the cooling injections significantly alters the flow field as well (Figure 9.9(a, b, c)). It can be clearly seen that the freestream (red) and the cooling jets (blue) have strong interactions. Such interactions are dramatically affected by the global blowing ratio. For M=0.5, almost all of the cooling jets are deflected towards the suction side, except that a small amount of coolant ejecting from the first cooling hole moves to the pressure side and then leaves the tip gap together with the leakage flow on the pressure side. However, most of the coolant mixes with the mainstream particles and directly exits the tip gap from the suction side generating a system of tip secondary vortices.

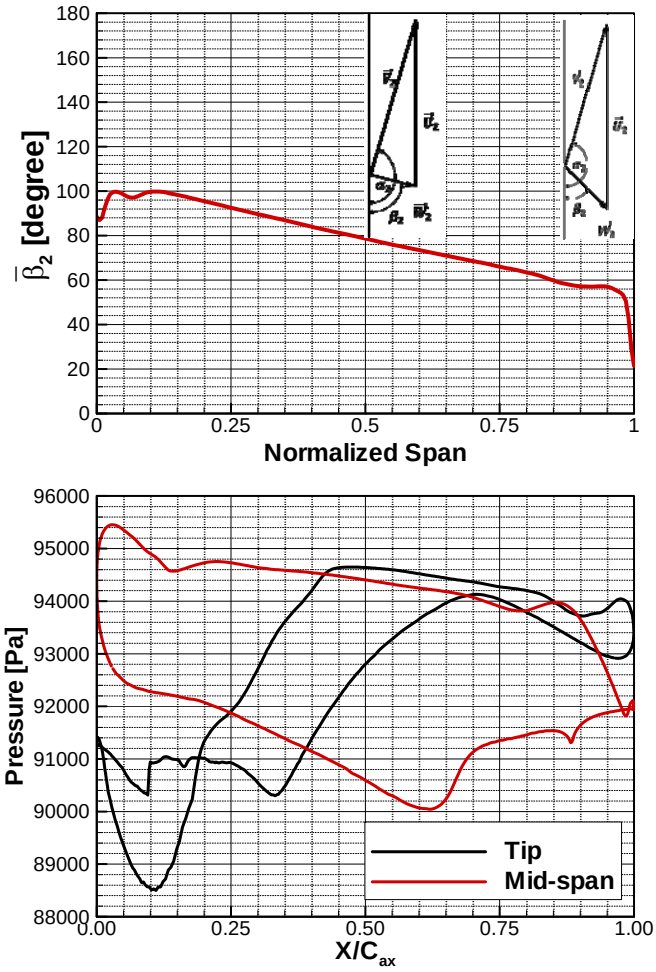

Figure 9.10: Pitchwise-averaged flow angle at the rotor inlet (top); Blade loading at tip and mid-span (bottom).

Under blowing ratio M=1.0, all the coolant particles exiting from the first and second cooling holes travels across the pressure side and form a passage flow by mixing with the mainstream. Small amount of coolant from other holes is observed to behave similarly. Meanwhile, the rest of the majority appears to accumulate in the vicinity of cooling-hole exits. The coolant spreads more widely and covers more of the tip, which is virtually the result of the impact of both the pressure gradient and the relative motion between the tip and shroud. Such flow behavior tends to be more salient when the blowing ratio is increased to M=1.5. In addition, the directions of the coolant jets vary slightly with increasing blowing ratio.

It is seen that the coolant particles tend to travel in the opposite direction of rotation, especially for the cooling jets exiting from the first three cooling holes. This phenomenon is due to the rotation and does not exist in a stationary cascade. While in this particular hole configuration, the jets tend to exit radially, and the circumferential motion of the rotor causes the blade tip to move away from the jets. As a result the particle moving along a relative streamline with a relative velocity tangent to the streamline is presented in Figure 9.9. Therefore, the pattern of the film cooling effectiveness (Figure 9.12) does not have any similarity with the ones measured in stationary cascades.

Note that all the blades are 2D cylindrical blades with no compound lean design, which does not take into account the variations of the flow angle along the blade span due to the increase of the rotational speed from hub to tip. As a result, the flow angle at rotor inlet tends to decrease when approaching the tip, as shown in Figure 9.10 (top). Additionally, due to the non-slip assumption on the wall, the boundary layer close to the casing has very high velocity gradient and thus the magnitude of the absolute velocity decreases fast. After superposition with the large circumferential component near the shroud, the relative flow angle tends to be small. The correlated loadings at the blade tip and mid-span has distinct differences too, as shown in Figure 9.10 (bottom).

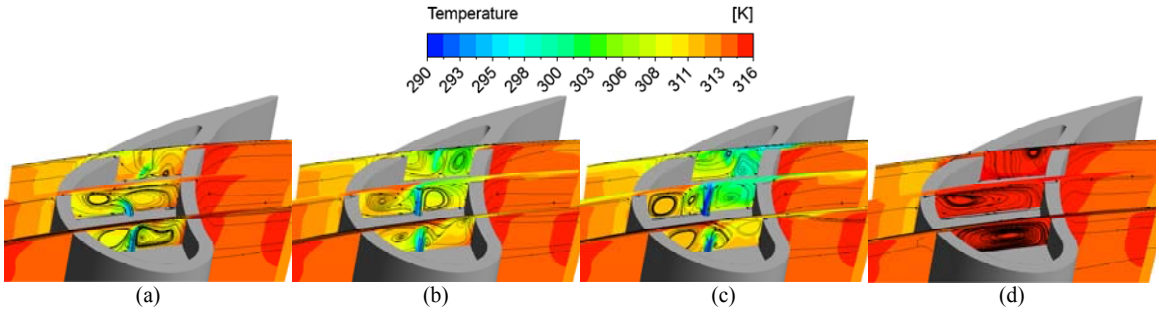

Figure 9.11: Temperature contours and streamlines at three axial locations of the squealer tip: (a) M=0.5, (b) M=1.0, (c) M=1.5, (d) without film cooling.

9.4.2 Impact of Blowing Ratio, Squealer Tip

The pressure on the squealer tip shows dramatically different distributions compared with that on the Plain tip. As shown in Figure 9.8, the most noticeable characteristic is that the pressure distribution on the cavity floor tends to be uniform and thus the

pressure gradient on the cavity floor is significantly decreased. This is resulted from the presence of the large cavity on the tip. As seen in Figure 9.9, after crossing over the narrow gap between the casing and the squealer rim, the freestream flow is squeezed in the squealer cavity. Sudden expansion induces flow circulations within the cavity which entraps the freestream particles. Meanwhile, strong interactions between the leakage flow and the cooling jets intensify the mixing which forms three-dimensional complex vortex systems. The majority of the mixture of the leakage flow and the coolant continues to roll and travels downstream along the cavity. Eventually, the flow particles accumulate at the trailing end of the cavity and afterward escape from the cavity by crossing over the suction side rim, which generates the suction-side tip vortex. Unlike the case for Plain tips, some coolant particles (marked with blue streamlines) are transported to the leading edge portion by complicated vortices circulating at the surrounding area. Such transportation is able to partially relieve the heat loads and thus provide certain cooling protection to the cavity walls near the leading edge. However, the leading edge of the Plain tip is directly exposed to the hot freestream and at risk of overheating. This is an advantage of the squealer tip. Thus, quasi homogeneous pressure distribution on the cavity floor is obtained due to the strong mixing effect. Note that the locations of the cooling holes are not detectable by seeing the pressure field, unlike the locally quasi stagnation spots on the Plain tip. This is because the cavity protects the freestream from rushing against the coolant jets at the exit. The pressure field on the rim differs a lot from that on the cavity floor. As expected, high pressure is obtained on the pressure-side rim. On the contrary, low pressure is observed on the suction-side rim.

Although all the flow structures show significant similarities, the magnitude of blowing ratios definitely affects the flow field. At M=0.5, almost all the coolant leaks from the suction side starting from nearly 50% C_{ax}. However, parts of the coolant particles travel across the pressure-side rim and mixes with the cross flow in the passage when the blowing ratio is increased to M=1.0. Even more coolant leaks to the pressure side for the case of M=1.5. In fact, the flow patterns at three axial locations shown in Figure 9.11 reveal the correlated mechanism. Note that the blowing ratio is associated with the flow momentum. At the low blowing ratio of M=0.5, the coolant jets do not penetrate all the way to the shroud since the relative low momentum can hardly overcome the cavity flow. Instead, they are deflected and diffused with the vortices before they mix with the leakage flow. Those circulations constrain the coolant flow particles in the cavity and afterwards carry them to leak from the suction side. Nevertheless, the situation changes when it comes to M=1.0. The coolant jets penetrate all the way to the shroud and split the cavity vortex. As a result, some coolant particles mix with the leakage flow and are carried to the pressure side. Increasing the blowing ratio to M=1.5 enhances this mass transportation. In addition, in the case without film cooling (Figure 9.11(d)), sudden expansion of the leakage flow forms one large circulation at the center of the cavity, which acts as typical cavity flow with one moving boundary. With the presence of cooling ejections, two vortices rolling in the same direction are formed and divided by the cooling jet for the case of M=0.5 and 1.0 (Figure 9.11(a, b)). However, three circulations are observed when the blowing ratio reaches 1.5

(Figure 9.11(c)). The two outer circulations rotate in one direction while the middle one rotates in the opposite direction.

Figure 9.12 depicts the contours of adiabatic film cooling effectiveness at the blade tip region. The definition of the adiabatic film cooling effectiveness is given by

$$\eta_{aw} = \frac{T_{aw,f_0} - T_{aw,f}}{T_{aw,f_0} - T_c} \tag{5}$$

where T_{aw,f_0} is the adiabatic wall temperature obtained with the coolant that is as hot as the mainstream, $T_{aw,f}$ is the adiabatic wall temperature obtained with the coolant that is cooler than the mainstream, and T_c is the coolant temperature that is lower than the mainstream. Such definition completely eliminates the impact brought by different flow structures. In order to obtain the film cooling effectiveness, two cases that supply coolants with different temperatures must be calculated respectively for each blowing ratio. Eventually 318K is used to obtain T_{aw,f_0} according to the experimental running conditions and 300K is arbitrarily chosen for calculating $T_{aw,f}$.

Essentially the film cooling effectiveness is dimensionless temperature. Looking at the shape of the high effectiveness area, the shape has high coincidence with the trajectories of cooling jets. Hence the adiabatic film cooling effectiveness largely reflects the consequence of the flow behaviors. Many factors can affect the film cooling effectiveness. One of the critical parameters is the blowing ratio. Another one is the blade tip geometry. The Plain tip is discussed first. At M=0.5 (Figure 9.12(a)), the trajectory of each hole appears as a narrow streak and can be clearly differentiated from each other due to the relatively small blowing ratio. The cooling effectiveness is around 0.3 within the coolant trajectories. The highest value of nearly 0.6 is obtained right at the downstream of the cooling-hole exits. The downstream cooling effectiveness is gradually decreased due to the diffusion of cooling jets and the mixing between the coolants and the leakage flow. As the blowing ratio increases to M=1.0 (Figure 9.12(b)), each coolant trajectory tends to diffuse more and thus covers more area. The trajectories of the cooling jets exiting from the first, the second and the seventh holes are easily identified, whereas a large area with high effectiveness appears in the vicinity of the rest of the cooling holes due to the coolant accumulation. It is noticeable that the highest film cooling effectiveness (above 0.7) is observed in the vicinity of the last four cooling holes. Around 50% area of the blade tip is covered by film cooling. In the case of M=1.5 (Figure 9.12(c)), the trajectory tends to be thicker and thus the film cooling performance is even better as expected. Higher film cooling effectiveness is achieved especially when it comes to the last four cooling holes due to the coolant accumulation. More than 50% of the blade tip surface is well covered by the film coolant.

The difference of the cooling capability among seven cooling holes can be explained by the local blowing ratio shown in Figure 9.14(a). Because the coolant is discharged from the plenum, the pressure difference between the inlet and the exit of each cooling hole is hardly identical. This leads to different mass flow for each single hole and thus different local blowing ratio. Because of the relatively lower pressure at exit, the last

four cooling holes eject more coolant and therefore create higher local blowing ratios. Accordingly, larger local blowing ratios provide locally higher film cooling effectiveness.

Different effectiveness contours were obtained when it comes to the squealer tip. At M=0.5 (Figure 9.12(a)), nearly the entire cavity floor is to some extent protected by the cooling film. Apparently the area of the cavity close to the pressure side is not cooled, whereas cooling effectiveness on the rest of the cavity floor is above 0.1. Effectiveness as high as 0.2 is observed within the flame-shaped streaks pointing from the cooling-hole exit to the suction side. The mechanism is illustrated in Figure 9.11(a). The coolant particles participating in the suction-side circulation roll down and meet the cavity floor causing little mixing with the hot leakage flow. Therefore higher cooling effectiveness is obtained on the side of hole exit near suction side. The pressure-side circulation rolls up the rest of the coolant particles. Then the coolant is strongly mixed with the leakage flow. The mixture becomes hot before it reaches the cavity floor. Hence the cavity floor near the pressure side is less cooled than the area near the suction side. Relatively high effectiveness is obtained at the suction-side rim between 50% C_{ax} and 90% C_{ax} due to the leakage originating from the cavity. However, the rest of the rim has not been protected by the film coolant. For M=1.0 (Figure 9.12(b)), those flame-shaped streaks disappear. Instead, a large area with relatively high effectiveness on the cavity floor is observed near the suction side and the trailing end of cavity. The reason is that the cooling jets penetrate higher towards the shroud due to higher momentum, which leads to better mixing and therefore more uniform cooling effectiveness. The resulted cooling effectiveness on the cavity floor close to the pressure side is slightly increased up to 0.1. Maximum effectiveness is found in the vicinity of the cavity trailing end due to the accumulation of coolant coming from the upstream. More coolant leaking from the suction side causes higher cooling effectiveness. It is noticed that part of the pressure-side rim has effectiveness as high as 0.2 since some coolant leaks across this area. Better film cooling is provided when the blowing ratio is raised to M=1.5 (Figure 9.12(c)), especially from 50% C_{ax} to 90% C_{ax}. Even higher cooling effectiveness at the suction-side rim and especially the pressure-side rim is obtained due to larger amount of coolant ejected. Furthermore, Figure 9.13 depicts the film cooling effectiveness on the cavity inner wall of the squealer tip. Spots with relatively high cooling effectiveness are observed near the cavity trailing end since the majority of the coolant travels downstream and the accumulation takes place. However, the effectiveness is not as high as that on the Plain tip where the accumulation occurs. Apparently, the intense interactions between the coolant and the leakage flow considerably diminish the cooling effectiveness. In this study, more area of the squealer tip is protected by the film cooling when compared with the Plain tip. However, the local cooling effectiveness on the squealer tip tends to be lower.

The impact of the local blowing ratio on the cooling effectiveness might be less important for the squealer tip. For high blowing ratios of M=1.0 and 1.5, the local blowing ratio is almost identical for each cooling hole, as shown in Figure 9.14(b). But the local blowing ratio monotonously goes down from the first hole to the seventh hole

for M=0.5. The possible reason is that the small amount of cooling flow is prone to be sensitive to the slight pressure difference.

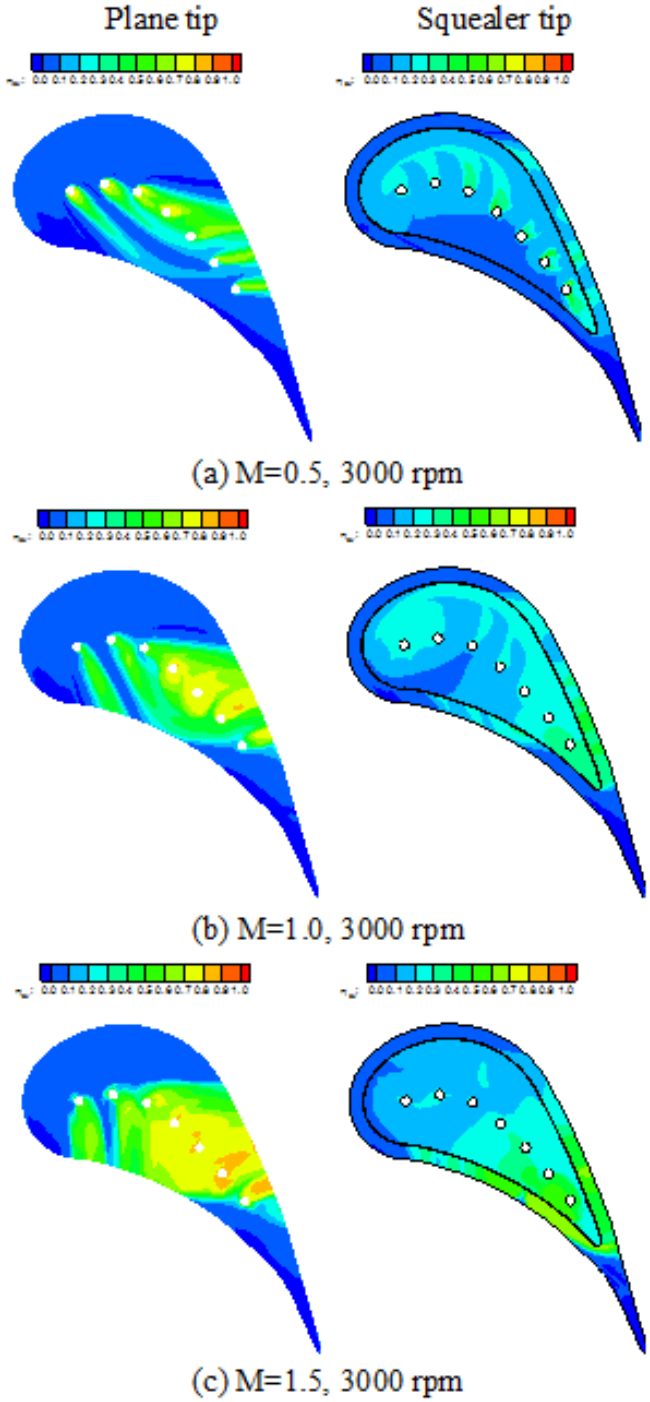

Figure 9.12: Distribution of the adiabatic film cooling effectiveness at 3000 rpm: Blade tip for the Plain tip (left); Cavity floor and rim for the squealer tip (right).

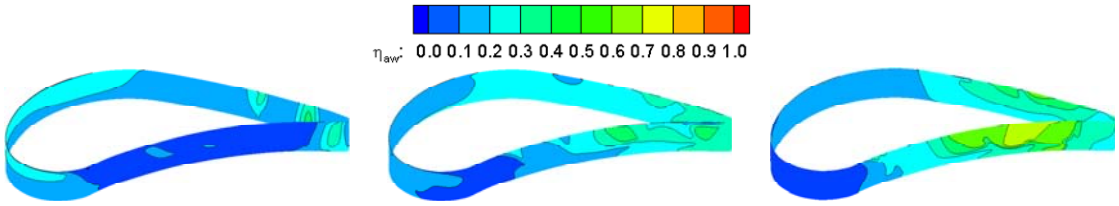

(a) (b) (c)

Figure 9.13: Distribution of the adiabatic film cooling effectiveness on the cavity inner wall of the squealer tip: (a) M=0.5, (b) M=1.0, (c) M=1.5.

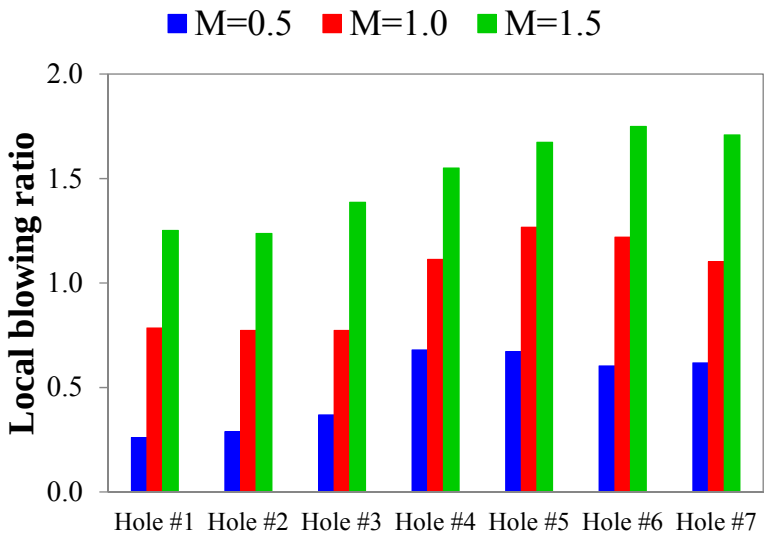

(a)

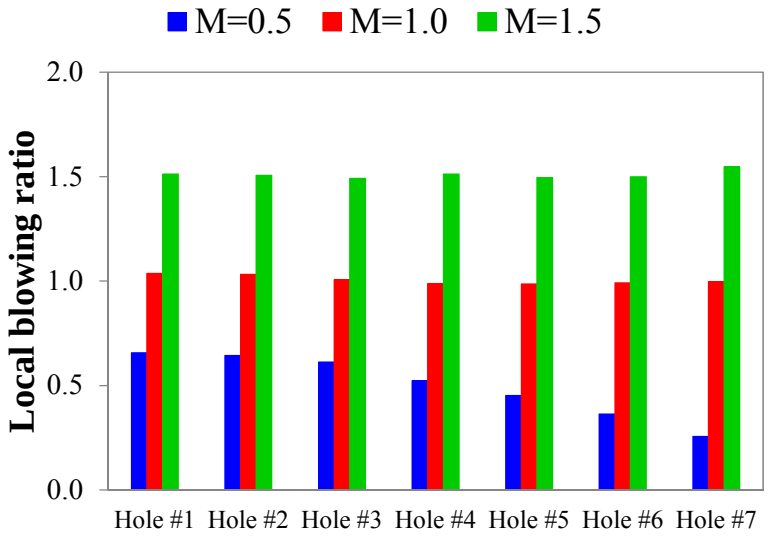

(b)

Figure 9.14: Local blowing ratio for each cooling hole: (a) Plain tip, (b) Squealer tip.

The film cooling effectiveness at the blade tip region is pitchwise averaged and shown in Figure 9.15. The discussion is made for the Plain tip first. It is seen that the coverage of the film cooling starts from nearly 15% C_{ax} and ends at 90% C_{ax}. For M=0.5, the averaged value seems to gradually increase along the C_{ax} within the covered area. Seven peaks are observed and each of them represents the location of every film cooling hole. At M=1.0, the averaged film cooling effectiveness is slightly lower than 0.2 from 20% C_{ax} to 40% C_{ax}. This area corresponds to the first three cooling holes which is consistent with the contour plots. However, the averaged value dramatically increases when it reaches 50% C_{ax}. Between 50% C_{ax} and 80% C_{ax}, the averaged film cooling effectiveness is as high as 0.4. This is due to the relatively large local blowing ratios of the rear four cooling jets. Even higher film cooling effectiveness is obtained when the blowing ratio reaches M=1.5.

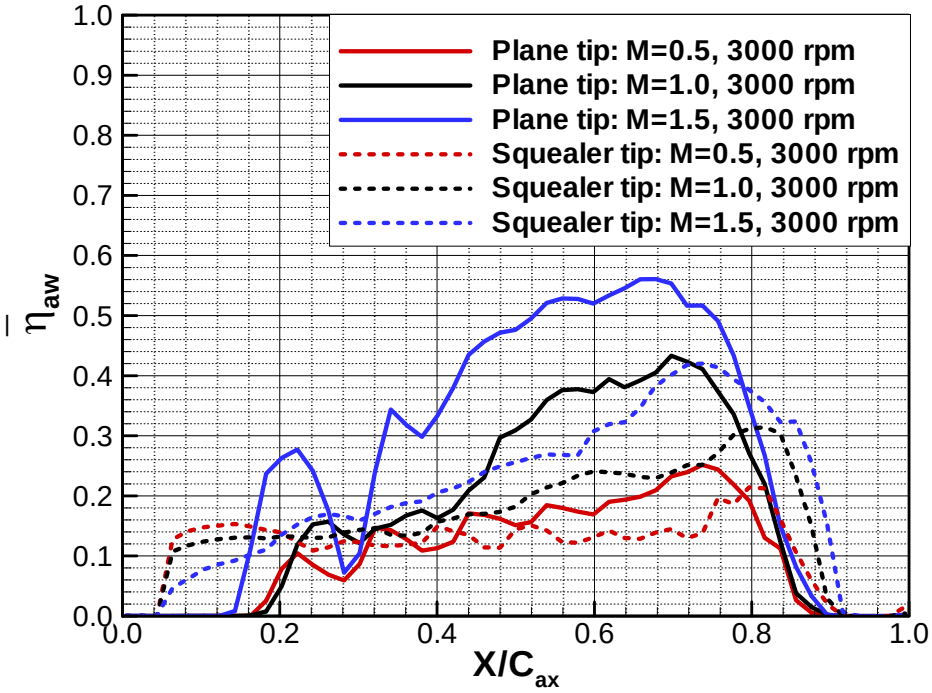

Figure 9.15: Pitchwise-averaged film cooling effectiveness along axial chord on the blade tip at 3000 rpm.

The squealer tip shows quite different trends in Figure 9.15. Note that the squealer tip is comprised of the squealer cavity floor, the squealer cavity inner wall, and the rim. The film cooling is effective from about 5% C_{ax} to 90% C_{ax} for all the blowing ratios. For M=0.5, the pitchwise-averaged film cooling effectiveness is stabilized around 0.14 until it bumps up a bit at 80% C_{ax}. However, the averaged cooling effectiveness gradually grows from 0.1 to 0.3 when the blowing ratio becomes 1.0. A similar trend is obtained for the blowing ratio M=1.5, but the average slope is slightly larger compared with M=1.0. The highest value of 0.42 appears at about 70% C_{ax} where it is believed to be close to the cavity trailing end. In fact, the peak value is found in the same area for all

three blowing ratios. Moreover, it is seen that the leading edge rim is not cooled at all, as well as the trailing edge portion. Further, within 40% C_{ax} and 80% C_{ax}, the Plain tip offers higher averaged cooling effectiveness than the squealer tip does.

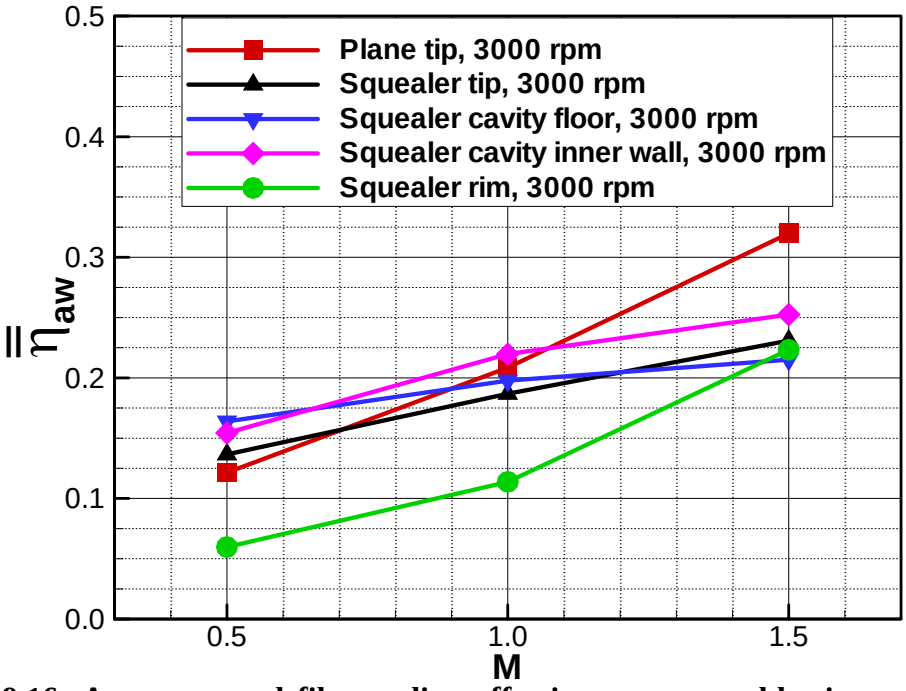

Figure 9.16: Area-averaged film cooling effectiveness versus blowing ratio at the blade tip region.

The area-averaged film cooling effectiveness versus the blowing ratio at the blade tip region is shown in Figure 9.16. It is seen that the overall film cooling effectiveness for every part increases monotonously as the blowing ratio is increased. This is consistent with the contour plots in Figure 9.12 and Figure 9.13. Note that the overall effectiveness on the Plain tip is slightly lower than that on the squealer tip for M=0.5. With increasing blowing ratios, the situation is altered. Higher overall effectiveness is obtained on the Plain tip for both M=1.0 and 1.5. The value reaches 0.32 for the Plain tip at M=1.5 whereas this number for the squealer tip is as high as 0.23. For the Plain tip, the coolant accumulating in the vicinity of the rear four cooling holes partially blocks the leakage flow passing through and weakens the mixing process. Such accumulation significantly increases the local cooling effectiveness. This is essentially the result of the high blowing ratio and the tip-shroud relative motion. However, in case of the squealer tip, the mechanism is altered. On the one hand, higher blowing ratio delivers more coolant and thus higher effectiveness. On the other hand, it also causes stronger mixing of the coolant and the leakage flow, which to some extent weakens the cooling capability of the coolant. This is confirmed by looking at the averaged cooling effectiveness on both the cavity floor and the side wall at M=1.5. As a result, the squealer tip with tip hole cooling does not provide as much protection as the Plain tip under high blowing ratios.

Additionally, among the three parts of the squealer tip, the cavity inner wall has the largest contribution on overall effectiveness. It is observed that the rim of the squealer tip is the part least cooled for blowing ratios of M=0.5 and 1.0 but gets improved at M=1.5. Generally, higher blowing ratios corresponds to better film cooling performance on the blade tips. From the point of view of the overall film cooling effectiveness, the Plain tip with M=1.5 provides the best protection to the blade tip in this study.

The flow field and film cooling effectiveness on the Plain and squealer tips within a HP turbine have been numerically presented in this chapter. Several major conclusions made from this study are as follows:

1) The presence of the film cooling significantly alters the pressure field at the blade tip, which is true for both the Plain tip and squealer tip. However, the Plain tip with film cooling tends to increase the non-homogeneousness of the pressure distribution whereas the squealer tip with film cooling decreases it.
2) The film cooling ejections on both the Plain tip and squealer tip dramatically affect the flow behaviors at the tip region. Strong interactions between the cooling jets and the leakage flow have been observed on both blade tips. However the flow characteristics on the Plain tip differ from those on the squealer tip.
3) The film cooling is effective in the vicinity of the cooling hole exit and directly downstream for the Plain tip. However, more area of the blade tip is covered by the film cooling when it comes to the squealer tip. Neither blade tip configuration with film cooling provides adequate protection to the leading and trailing edge for currently studied objects.
4) The local blowing ratio varies for each cooling hole on the Plain tip, but tends to be identical when it comes to the squealer tip.
5) Pitchwise-averaged film cooling effectiveness indicates that high film cooling performance appears within 40% C_{ax} and 80% C_{ax}.
6) The overall film cooling effectiveness monotonously increases by increasing blowing ratios for both configurations. Although the squealer tip has slightly higher overall effectiveness than the Plain tip does at M=0.5, the Plain tip provides better overall film cooling for both M=1.0 and 1.5. In present study, the highest value of 0.32 is achieved on the Plain tip at M=1.5.
7) The coolant accumulation on the Plain tip is the result of a combined impact of the pressure gradient and the rotational motion which is not found in the stationary cascades.

9.4.3 Impact of rotation speed, Plain & Squealer Tip

After discussing the impact of blowing ratio on the cooling effectiveness in last section, this section is focusing on the effect of the rotation speed on the cooling effectiveness for both the Plain tip and squealer tip. Accordingly, the blowing ratio is fixed at M=1.0 while three different rotational speeds (2000 rpm, 2550 rpm and 3000 rpm) are studied.

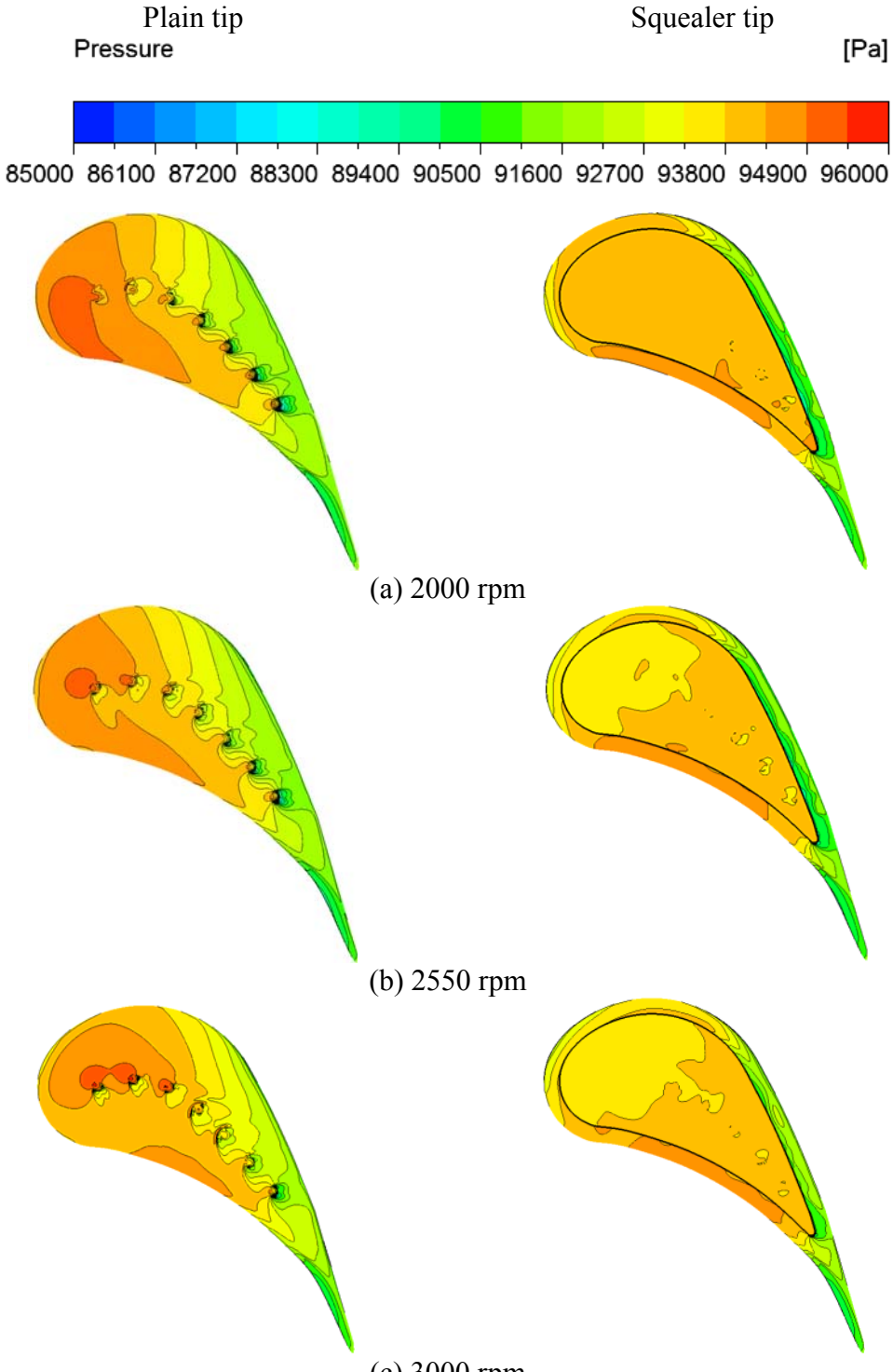

(a) 2000 rpm

(b) 2550 rpm

(c) 3000 rpm

Figure 9.17: Distribution of the static pressure at M=1.0: Blade tip for the Plain tip (left); Cavity floor and rim for the squealer tip (right).

Figure 9.17 depicts the pressure distribution at the blade tip region for both the Plain tip and squealer tip. For the Plain tip, the pressure distribution on the tip surface is not smooth due to the presence of the cooling jets. The pressure contour lines are broken in the vicinity of cooling hole exits. It is shown that the variation of rotation speed significantly affect the pressure distribution on the tip surface. At 2000 rpm, the leading edge portion is occupied by high pressure. This high-pressure region extends from leading edge to approximately 25%C_{ax}, which is due to the resistance of the cooling jets. As the rotation speed increases, this area shrinks and deforms due to the movement of the stagnation point. When the rotation speed reaches 3000 rpm, this area is much smaller than 2000 rpm and another high-pressure area is obtained at pressure side. However, the circumstance becomes different when it comes to squealer tip. Although high pressure is obtained at the pressure-side rim and low pressure for the suction-side rim, the pressure field on the squealer cavity floor shows quite uniform distribution. Unlike the Plain tip, the locations of cooling holes cannot be identified only from the pressure distribution for squealer tip. At 2000 rpm, the pressure on the cavity floor is almost constant. However, an area with slightly low pressure can be seen for 2550 rpm and 3000 rpm, which might be attributed to the circulation of leakage flow in the cavity. In sum, the change of rotation speed can dramatically impact the pressure distribution for Plain tip, since the cooling jets directly encounters the mainstream with different incidence. However, only negligible effect of the rotation speed can be observed for squealer tip due to the presence of the squealer cavity.

Basically the variation of rotation speed will change the inlet flow angle and therefore alter the flow behaviors. Figure 9.18 illustrates the streamlines near the blade tip for both the Plain tip and squealer tip. It is seen that the mainstream inlet flow incidence has significant impact on the behaviors of cooling jets for Plain tip. At 2000 rpm, almost all the coolant jets are pointing to the suction side and most of the coolant leaks from the suction side. When the rotation speed increases to 2550 rpm, a small amount of the coolant from the first three holes leaks from the pressure side due to the incidence change. The majority exits the tip clearance from the suction side. For 3000 rpm, the directions of first two cooling jets are completely altered. As a result, all the coolant from first two holes leaks from the pressure side. Also it is noticed that part of the coolant from the third hole travels to the pressure side. Some coolant accumulates in the vicinity of the last four cooling hole exits, which might be attributed to pressure gradient and rotation effect. Overall, the first three cooling jets are influenced primarily by the incidence angle, since they directly face to the incoming mainstream. However the last four jets are dominated by pressure gradient from pressure side to suction side. Although inlet flow incidence change can be seen clearly for the squealer tip, the flow structure in the squealer cavity does not show obvious relevance to the variation of rotation speed. It is seen that the mainstream is entrained into the squealer cavity, mixing with the ejected coolant while traveling along the pressure-side inner wall and eventually leaking from the suction side. Similar process takes place for all rotation speeds. Therefore, the rotation speed has negligible impact on the flow behaviors near the blade tip region for squealer tip.

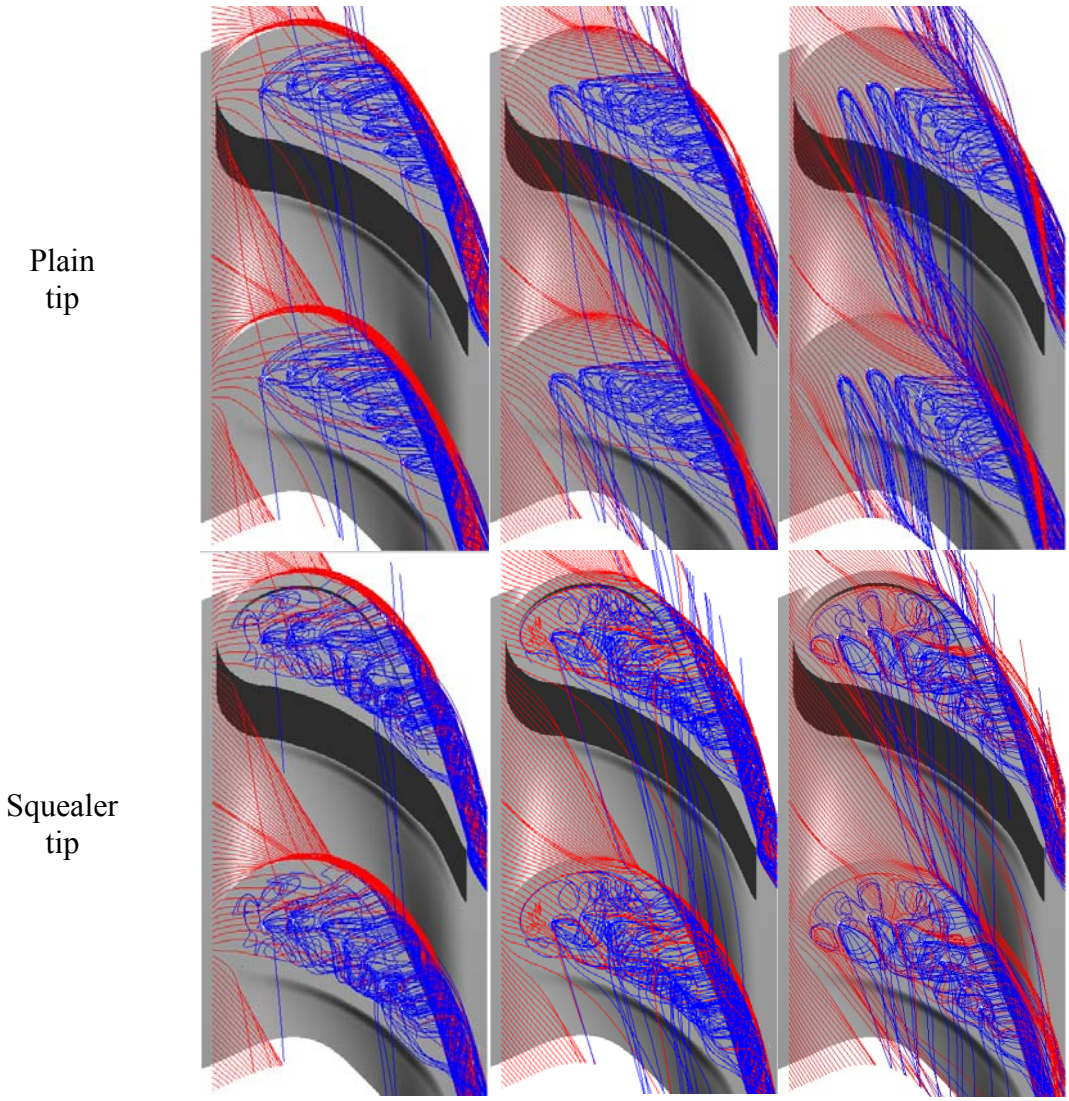

Figure 9.18: Streamlines based on the relative velocity at the blade tip region at M=1.0 (blue indicates cooling air, red is freestream air).

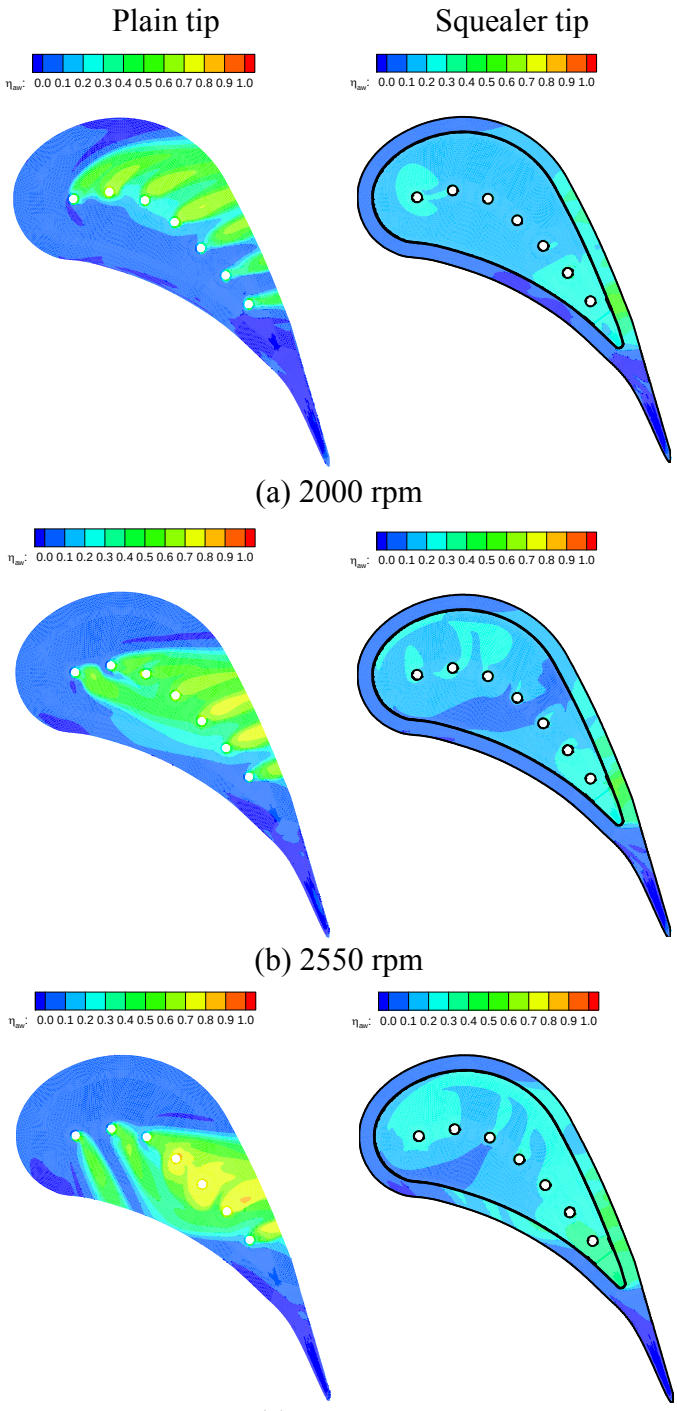

Figure 9.19: Distribution of the adiabatic film cooling effectiveness at M=1.0: Blade tip for the Plain tip (left); Cavity floor and rim for the squealer tip (right).

The flow structure directly determines the film cooling effectiveness. Figure 9.19 depicts the distribution of adiabatic film cooling effectiveness at the blade tip region for

both the Plain and squealer tip. Evidently, the distribution of cooling effectiveness shows substantial difference for Plain tip with varied rotational speed. For the rotation speed of 2000 rpm, since all the coolant jets are altered to the suction side (Figure 9.18 (a)), the cooling film covers the blade tip surface close to the suction side. Streaks with relatively high effectiveness are found right downstream of the cooling hole exits. Almost all the trace of cooling jets can be identified from these streaks. Within the covered area, the cooling effectiveness is approximately as high as 0.4. At 2550 rpm, because the first cooling jet is turned by the mainstream, it cools part of the tip surface near the pressure side. However, the rest of the coolant leaks from the suction side and therefore cools the tip surface at its downstream near suction side. Similar streaks are observed for the last four holes. The effectiveness distribution shows completely different pattern when it comes to 3000 rpm. The first two cooling jets and part of the third jet are pushed to the pressure side. Consequently, more area near the pressure side is protected than that at 2550 rpm. Additionally, the accumulation of coolant contributes to high effectiveness in the vicinity of the last four cooling hole exits. However, the leading edge is not protected by the cooling film for all rotation speeds. Hence, the rotation speed has considerable impact on the film coverage and cooling effectiveness for Plain tip. In contrast, few effect of the rotation speed can be observed when it comes to squealer tip. The distribution of cooling effectiveness exhibits similar profiles for all rotation speed. Almost uniform distribution of low effectiveness is seen on the cavity floor. Relatively high effectiveness appears at the region of cavity trailing edge since most of the coolant exits from this location. In addition, nearly half of the suction-side rim is cooled for all rotation speeds but the pressure-side rim is partially protected at 3000 rpm. However, it does not change the fact that the rotation speed barely impacts the cooling effectiveness for squealer tip.

Figure 9.20 and Figure 9.21 show the pitchwise- and area-averaged for both Plain and squealer tip respectively. As seen in Figure 9.20, the cooling film covers from $20\%C_{ax}$ to $85\%C_{ax}$ for the Plain tip with all rotating speeds. Within the range of $20\%\sim50\%C_{ax}$, the averaged cooling effectiveness increases from 0.1 to approximately 0.25 for all rotation speeds. However, the averaged effectiveness increases monotonously with the rotation speed. This is attributed to the change in directions of the cooling jets, which leads to more coolant leaking from this location when the rotation speed is higher. The peak value is about 0.44 at 70% C_{ax}. However, the distribution lines are different for the squealer tip. The presence of squealer cavity extends the coverage to $5\%\sim90\%$ C_{ax}, However, within the range of $5\%\sim50\%C_{ax}$, the averaged effectiveness is around 0.15 for all rotation speeds. From $50\%C_{ax}$, the effectiveness gradually increases and the peak value is reached at $85\%C_{ax}$. Basically the rotation speed does not have substantial effect on the averaged effectiveness for squealer tip. Slightly higher effectiveness at 3000 rpm is due to the coolant leakage from the pressure side. The peak value is about 0.3 for the squealer tip which is lower than Plain tip. For overall effectiveness in Figure 9.21, different trends are obtained for the Plain tip and squealer tip respectively. The overall effectiveness increases monotonously with the rotation speed for the Plain tip. However, the overall effectiveness of squealer tip is almost identical for 2000 rpm and 2550 rpm, but slightly increases at 3000 rpm. Separate parts

of the squealer tip show similar trends. Additionally as expected, the squealer rim is the least cooled portion.

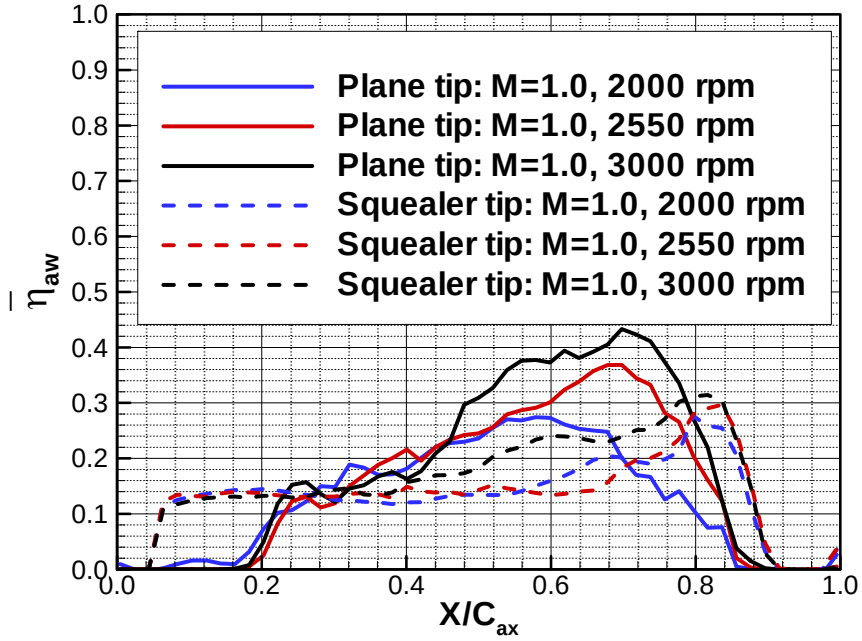

Figure 9.20: Pitchwise-averaged film cooling effectiveness along axial chord on the blade tip at M=1.0.

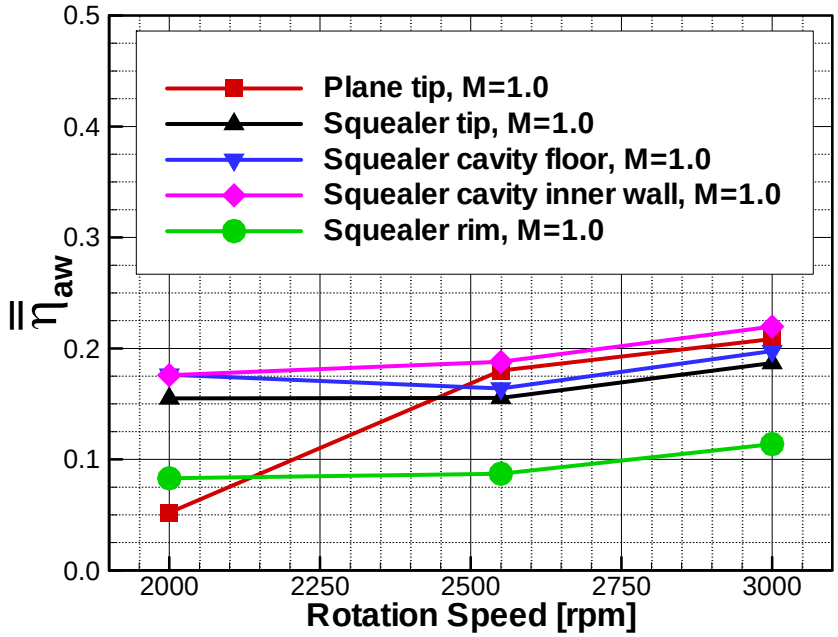

Figure 9.21: Area-averaged film cooling effectiveness versus rotation speed at the blade tip region.

9.5 Pressure-Side Hole Cooling

9.5.1 Impact of Blowing Ratio, Plain Tip

Figure 9.22 depicts the static pressure distribution near the blade tip region of the Plain tip for blowing ratios of M=0.75, 1.25 and 1.75. For the Plain tip with pressure-side hole cooling, the typical pressure distribution is obtained on the tip surface for all blowing ratios. The pressure side (PS) has the highest pressure and the pressure is gradually decreased towards the suction side (SS), which is as same as the case without film cooling (Figure 9.8 (d) left). The similarity indicates that the film coolant from the pressure-side holes does not have apparent impact on the pressure distribution at the blade Plain tip. However, the pressure field in the vicinity of the cooling holes is broken by the ejected cooling jets, which is similar to the case for Plain tip with tip hole cooling. Thus, the ejected coolant jets will significantly affect the pressure distribution in the surrounding area. Nevertheless, the presence of the cooling jets considerably alters the flow structures of the blade tip leakage flow, as shown in Figure 9.23.

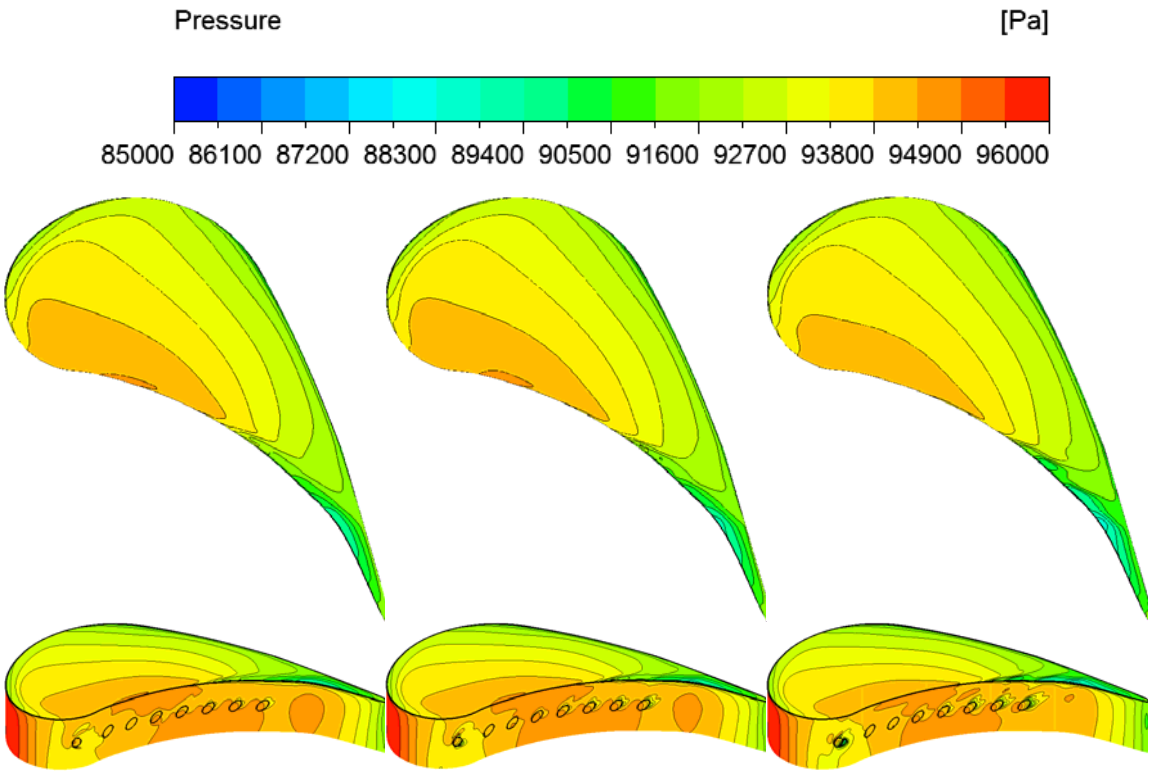

(a) M=0.75 (b) M=1.25 (c) M=1.75

Figure 9.22: Distribution of the static pressure near the blade tip region for Plain tip with pressure-side hole cooling at 3000 rpm.

Since the rotor blade is rotating at 3000 rpm with the tip speed of 215.34 m/s, the flow angle near the tip is much smaller than that at mid-span (Figure 9.10). Meanwhile, due to the geometric factor of the inclined and compound angle of the cooling holes, the majority of the ejected coolant travels along the pressure side towards to the trailing

edge and eventually exits the rotor row. During the process of approaching downstream, the coolant jets interfere with each other and mainstream forming a complex vortex system. Its size increases with the blowing ratio since more coolant is ejected to the mainstream for higher blowing ratio. Also the cooling jets are able to penetrate further into the mainstream due to the higher momentum for larger blowing ratio. It is seen that a portion of the coolant particles climbs up to the tip and cross the pressure-side edge then travels towards the suction side like the leakage flow. Eventually those particles leaks from the suction side and afterwards are entrained by the tip vortex system. The primary driving force is the pressure gradient between the PS and SS. However, the leaking of the coolant takes place after approximately 50% C_{ax} due to the particular flow direction near the blade tip. The impact of the incidence angle will be discussed in next section. In addition, the traces of the cooling jets can be identified for M=0.75, because the jets are altered immediately after they are ejected from the cooling holes due to the relatively low momentum. The mixing between the coolant and leakage flow becomes stronger when the blowing ratio is larger than one.

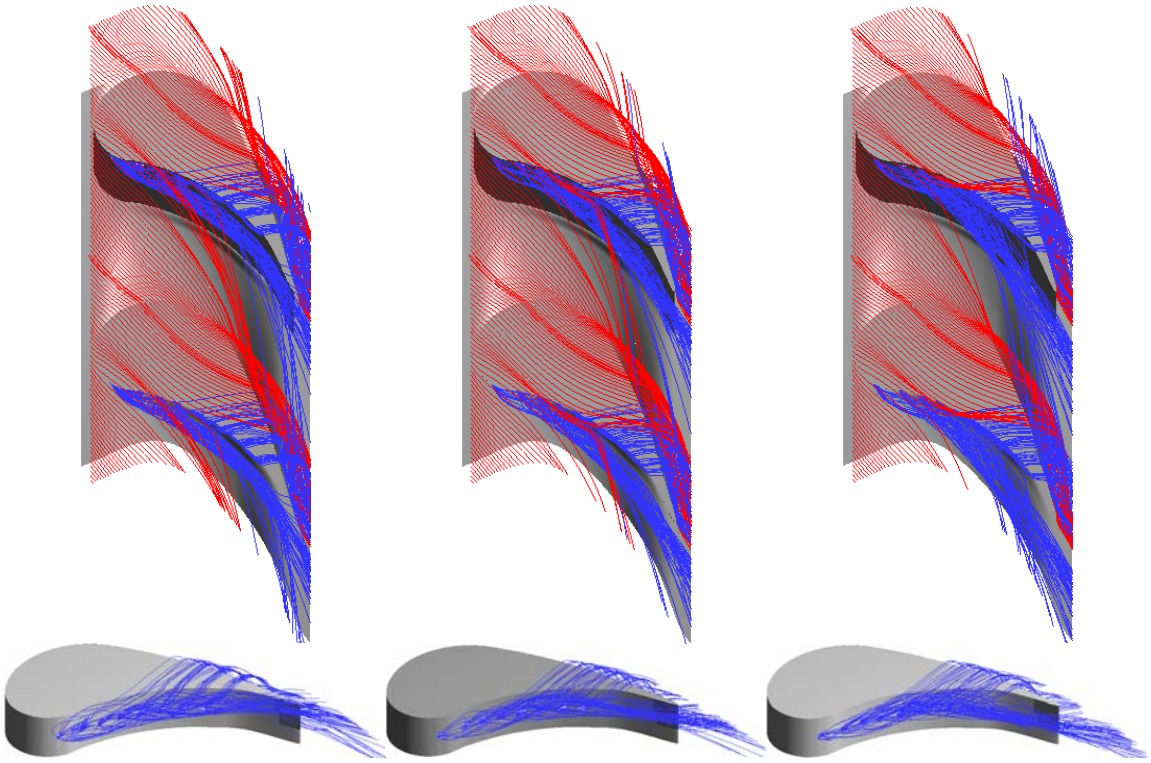

(a) M=0.75 (b) M=1.25 (c) M=1.75

Figure 9.23: Streamlines based on the relative velocity near the blade tip region for Plain tip with pressure-side hole cooling at 3000 rpm (blue indicates cooling air, red is freestream air).

The distribution of the temperature near the blade tip region also reflects the similar phenomenon, as shown in Figure 9.24. It is clearly shown that there are several streaks

with low temperature on the blade tip surface indicating the traveling path of the altered coolant jets. However, the streaks expand and diffuse with the increasing blowing ratio. Those streaks disappear for M=1.75, instead large areas with low temperature are obtained on the tip surface. The difference can be attributed to the enhancement of mixing between the coolant and leakage due to the increase in blowing ratio. The blowing ratio also impacts the cooling effectiveness on the pressure surface. It is seen that the coverage of the cooling film on pressure surface decreases with the increase in blowing ratio. For M=0.75, the cooling film almost covers the surface above the cooling holes, especially in the vicinity of the five holes at upstream. Three coolant streaks with low temperature are observed for the three holes at downstream. When the blowing ratio increases to 1.25, smaller area is covered by the coolant film from the five holes at upstream. The streaks become more diffusive than those for M=0.75 (Figure 9.24 (b)). For M=1.75, the coolant from the five holes upstream can hardly cool the pressure surface, as shown in Figure 9.24 (c). In addition, the coolant from the three holes at downstream turns to be even more diffusive. At low blowing ratio, the coolant jets possess lower momentum than the mainstream, which does not allow the jets to overcome the mainstream and pressure gradient. Instead, after the coolant jets are ejected from holes, they are immediately altered by the pressure gradient and attach the pressure surface, resulting larger coverage on the surface. However, at higher blowing ratio, the coolant jets are able to overwhelm the momentum of the mainstream and pressure gradient, and therefore tend to lift off from the surface which leads to smaller coverage on the pressure surface.

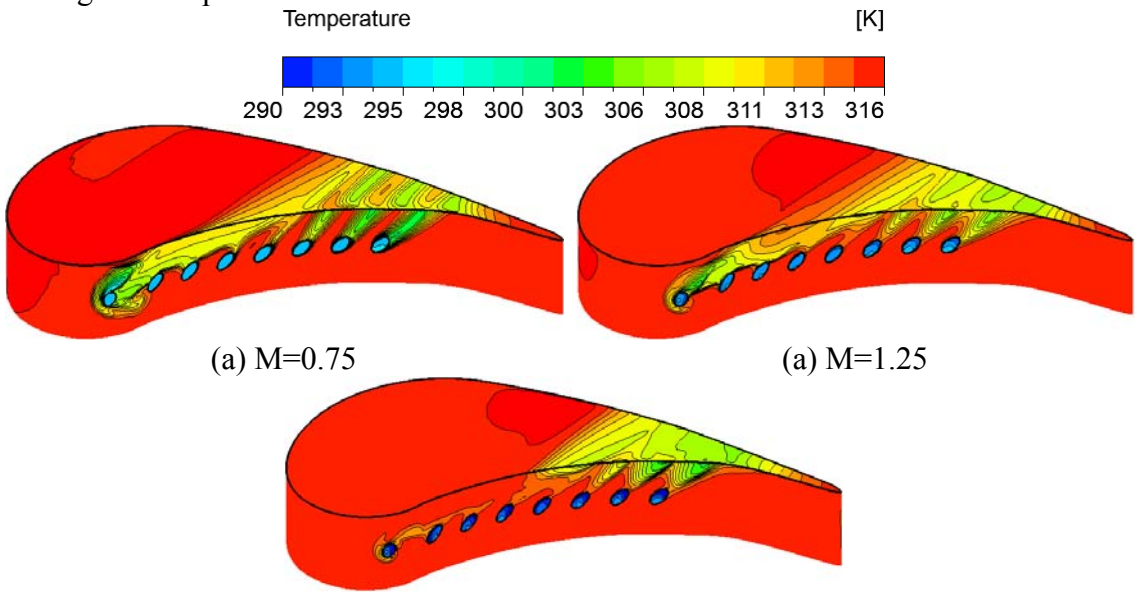

(a) M=0.75 (a) M=1.25

(c) M=1.75

Figure 9.24: Distribution of the temperature near the blade tip region for Plain tip with pressure-side hole cooling at 3000 rpm.

Figure 9.25 depicts the distribution of the adiabatic film cooling effectiveness at blade tip with varying blowing ratios. As discussed earlier, due to the impact of the flow

incidence, the blade tip surface is cooled after approximately 50%C_{ax} and the corresponding coolant-covered area is much less than 50% of the blade tip. At M=0.75, several streaks with high effectiveness can be seen from around 65%~90%C_{ax}. These streaks are associated with the low-temperature areas in Figure 9.24. Similarly, these streaks become larger and more diffusive when the blowing ratio increases to 1.25. A patchy area with high effectiveness is obtained for M=1.75. In these area with high effectiveness, the effectiveness magnitude is between 0.3~0.4, whereas approximately η_{aw}≈0.1~0.2 is obtained in other covered areas. The leading edge portion is not cooled at all no matter what blowing ratio is applied. In addition, the area covered by cooling film decreases with the increasing blowing ratio, since the cooling jets are easier to be altered at lower blowing ratio that is associated with smaller momentum. The distribution of the cooling effectiveness is consistent with the temperature distribution in Figure 9.24.

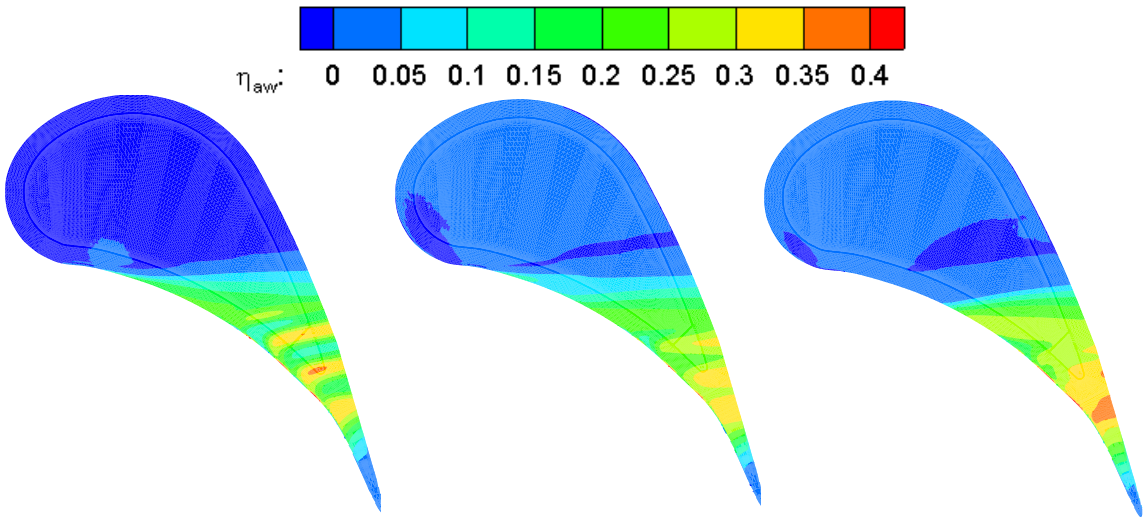

(a) M=0.75 (b) M=1.25 (c) M=1.75

Figure 9.25: Distribution of the adiabatic film cooling effectiveness at blade tip for the Plain tip with pressure-side hole cooling at 3000 rpm.

9.5.2 Impact of Blowing Ratio, Squealer tip

Unlike the Plain tip in Figure 9.22, the pressure distribution near the tip region for squealer tip shows different contours. Due to the presence of the squealer cavity, the pressure distribution tends to be more uniform on the cavity floor. Especially there is a large area occupied by relatively lower pressure near leading edge, which is attributed to the circulation generated by entrained mainstream flow. However, similar to the Plain tip, the high pressure is obtained at the pressure-side rim whereas the low pressure for suction side. In fact as seen for Plain tip, the variation of blowing ratio does not create noticeable impact on the pressure distribution near the blade tip region, although the area with relatively low pressure right downstream of the cooling hole exits tends to expand with increasing blowing ratio.

Figure 9.27 depicts the streamlines near the blade tip region for squealer tip with pressure-side hole cooling at 3000 rpm, which reveals the local flow behaviors. It is

shown that the presence of the squealer cavity significantly affects the local flow field near the tip region. Some mainstream particles are entrained in the cavity flow, forming several circulations in the cavity. As a result most of the cavity space is occupied by the mainstream particles. These particles continue to travel towards the cavity trailing end and eventually leak from the suction side, generating the tip vortices. It is noticed that a small amount of the coolant is able to cross the pressure-side edge and enter the tip clearance due to the part of the coolant jets is altered by the pressure gradient and mainstream momentum. Consequently, part of the pressure-side rim is cooled by the cooling film. However, since the coolant leaks from the rear portion of the blade tip, the cooling particles is difficult to enter the squealer cavity. Instead, they travel across the rim near the trailing edge. As a consequence, the cavity floor and inner wall can be hardly cooled by the cooling film. In addition, the coolant jets tend to lift off the pressure surface when the blowing ratio is increasing and therefore less coolant can go through the tip clearance and cool the blade tip.

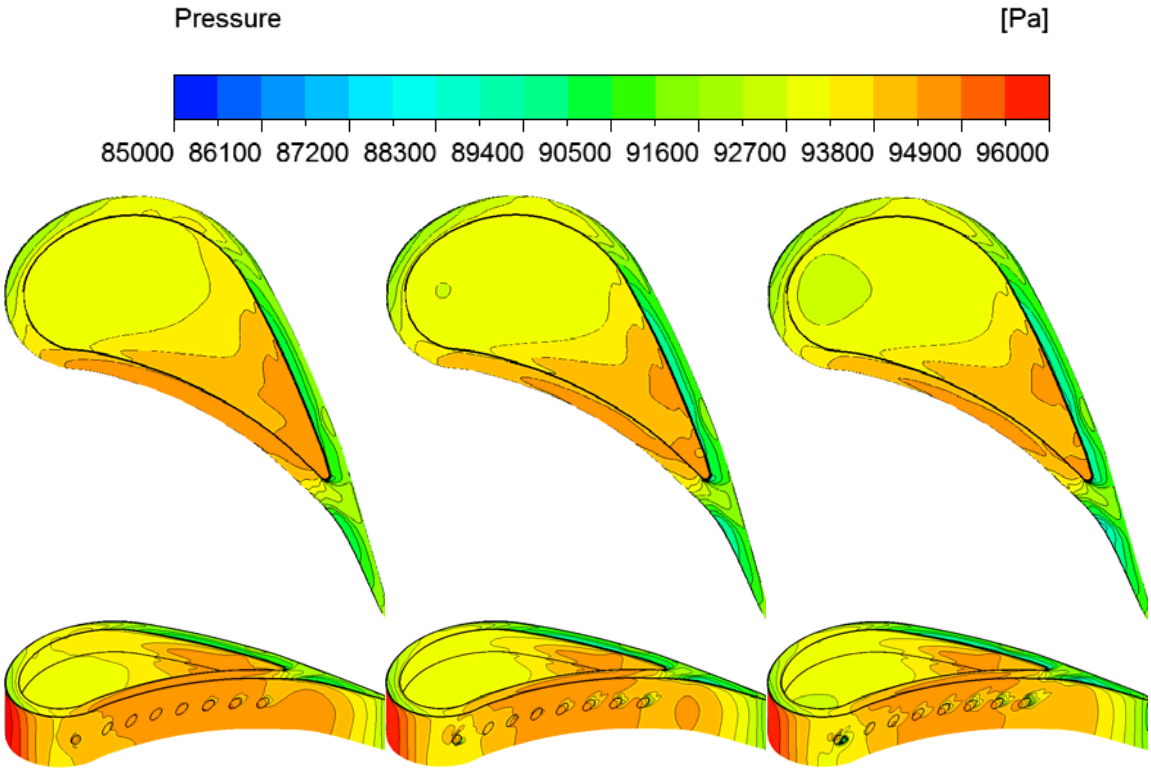

(a) M=0.75 (b) M=1.25 (c) M=1.75

Figure 9.26: Distribution of the static pressure near the blade tip region for squesler tip with pressure-side hole cooling at 3000 rpm.

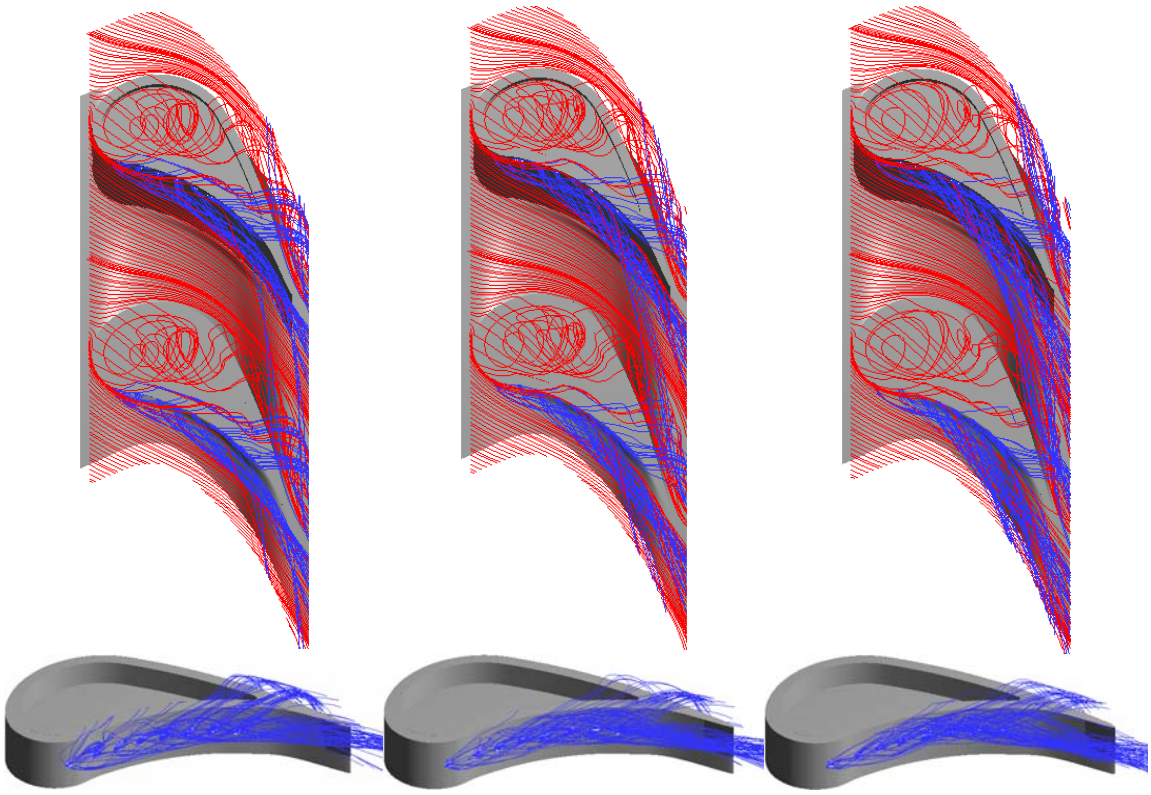

(a) M=0.75 (b) M=1.25 (c) M=1.75

Figure 9.27: Streamlines based on the relative velocity near the blade tip region for squealer tip with pressure-side hole cooling at 3000 rpm (blue indicates cooling air, red is freestream air).

The impact of the blowing ratio on the temperature distribution is shown in Figure 9.28. For M=0.75, more part of the pressure-side rim is cooled by the cooling film since more coolant particles are pushed towards the suction side when the blowing ratio is lower. The cooled area of the pressure-side rim becomes smaller as the blowing ratio increases. However, the area covered by cooling film becomes larger if the blowing ratio grows. Similar to the situation for Plain tip, smaller blowing ratio can provide better cooling coverage on the pressure surface due to the easier re-attachment of the coolant jets with lower momentum. The distribution of film cooling effectiveness at the blade tip shows consistency in Figure 9.29. It is seen that the more portion of the pressure side rim is cooled at M=0.75. The covered area shrinks as the blowing ratio increases. However, higher local effectiveness is obtained when it comes to M=1.75. The effectiveness magnitude is as high as 0.4 for M=1.75 whereas it declines to about 0.25 for M=0.75. Additionally, as shown above, the cavity floor and suction-side rim is not cooled at all no matter what blowing ratio is used. Therefore, the pressure-side hole cooling has worse performance for the squealer tip compared to Plain tip.

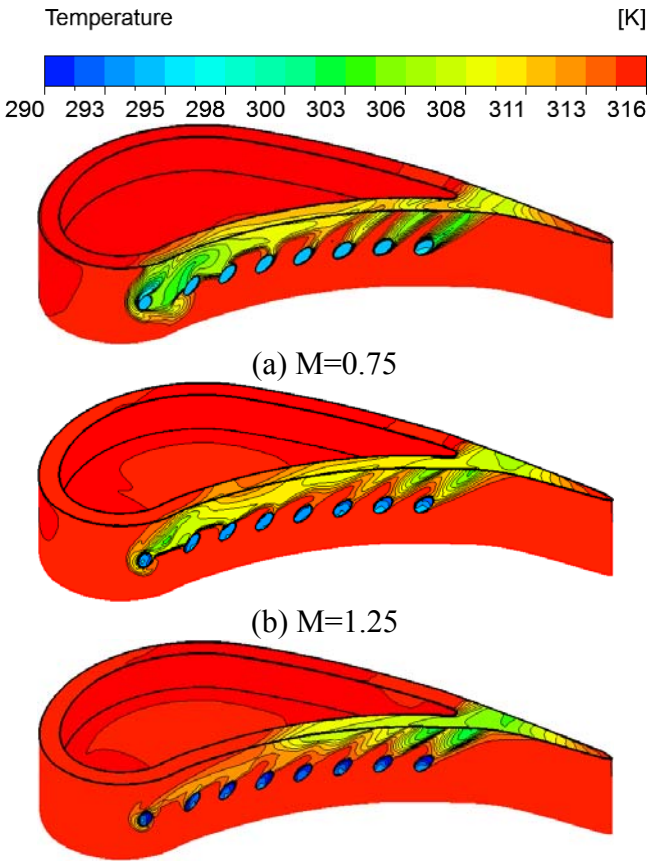

(a) M=0.75

(b) M=1.25

(c) M=1.75

Figure 9.28: Distribution of the temperature near the blade tip region for squealer tip with pressure-side hole cooling at 3000 rpm.

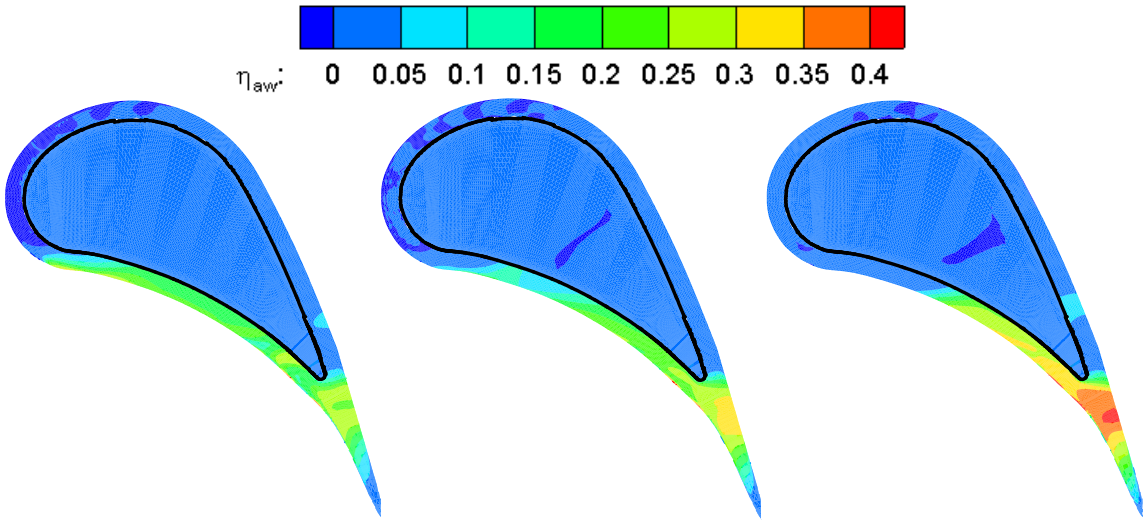

(a) M=0.75 (b) M=1.25 (c) M=1.75

Figure 9.29: Distribution of the adiabatic film cooling effectiveness at blade tip for the squealer tip with pressure-side hole cooling at 3000 rpm.

9.5.3 Impact of Rotation Speed, Plain Tip

This section is focusing on the impact of the rotation speed on the film cooling effectiveness for pressure-side hole cooling. Figure 9.30 shows the influence of the rotation speed on the pressure distribution near the blade tip region for Plain tip. In order to eliminate the impact of blowing ratio (even though little influence can be observed in Figure 9.22), the blowing ratio is fixed as 1.25 whereas three rotation speeds (2000 rpm, 2550 rpm and 3000 rpm) are compared. It is seen that the change of rotation speed can significantly affect the pressure distribution. Due to the variation of rotating speed, the circumferential velocity will change and accordingly the flow incidence will be altered. As shown in Figure 9.30, the stagnation point moves towards the pressure side as the rotation speed decreases. As a result, the high-pressure area on the blade tip surface moves from the pressure side to the leading edge. The shape of the correlated area is transforming as well. In addition, it is noticed that the pressure in the vicinity of the cooling holes enhances too due to the movement of the stagnation point.

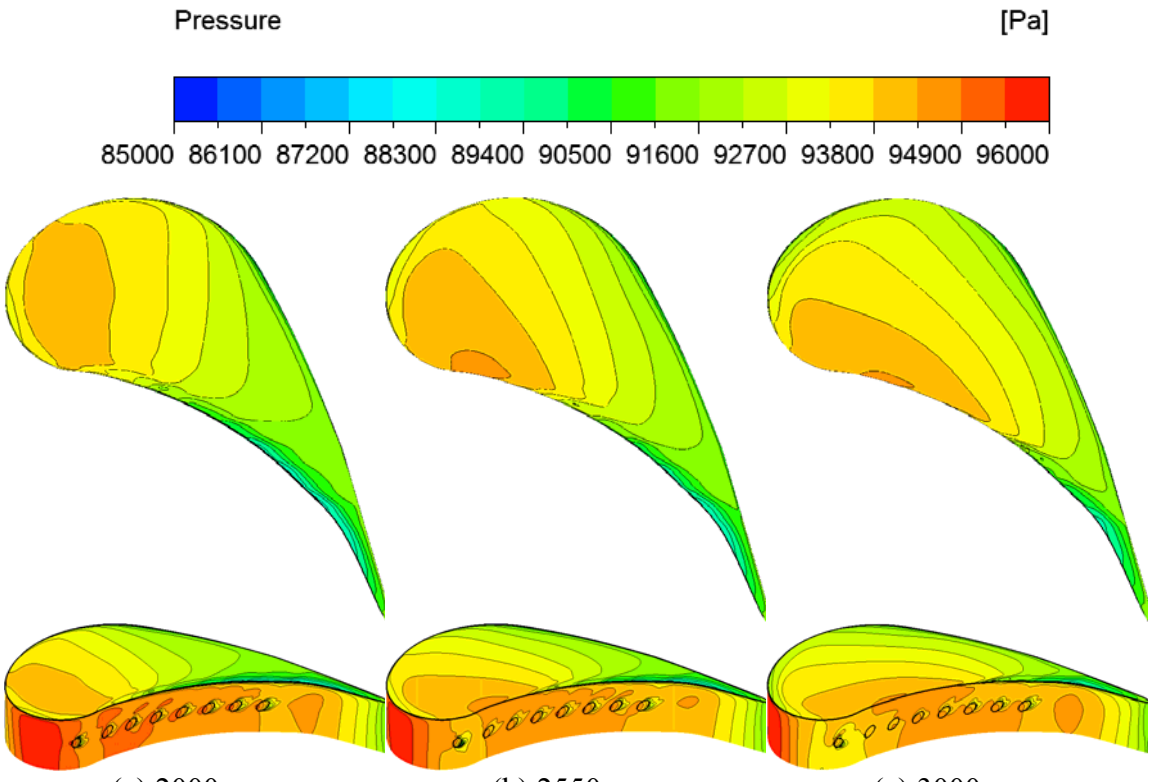

(a) 2000 rpm (b) 2550 rpm (c) 3000 rpm

Figure 9.30: Distribution of the static pressure near the blade tip region for Plain tip with pressure-side hole cooling at M=1.25.

The change of the pressure field near the tip region is associated with the variation of the local flow behaviors. Figure 9.31 shows the streamlines based on the relative velocity near the blade tip region with different rotation speeds. The alteration of direction of red streamlines (mainstream) shows the change in flow incidence angle. As

a result, the coolant jets are significantly affected. As shown in Figure 9.31 (a), the coolant jets from all cooling holes are pushed towards the suction surface immediately after the coolant particles are ejected out of the holes. Almost all of the coolant crosses the pressure-side edge and then travels towards the suction side. Eventually these coolant particles leaks from the suction side edge contributing to formation of tip vortex system. This is due to the smaller incidence angle and relatively high local pressure. As the rotation speed increases to 2550 rpm (Figure 9.31 (b)), the directions of most coolant jets are also altered and accordingly majority of the coolant particles leak from the suction side. However, for the rotation speed of 3000 rpm (Figure 9.31 (c)), only a small amount of the coolant particles are pushed to the suction side, whereas the rest of the coolant lifts off the pressure surface and mixes with the mainstream while traveling downstream. It is easily noticed that more blade tip surface is covered by the cooling film when the rotation speed is lower.

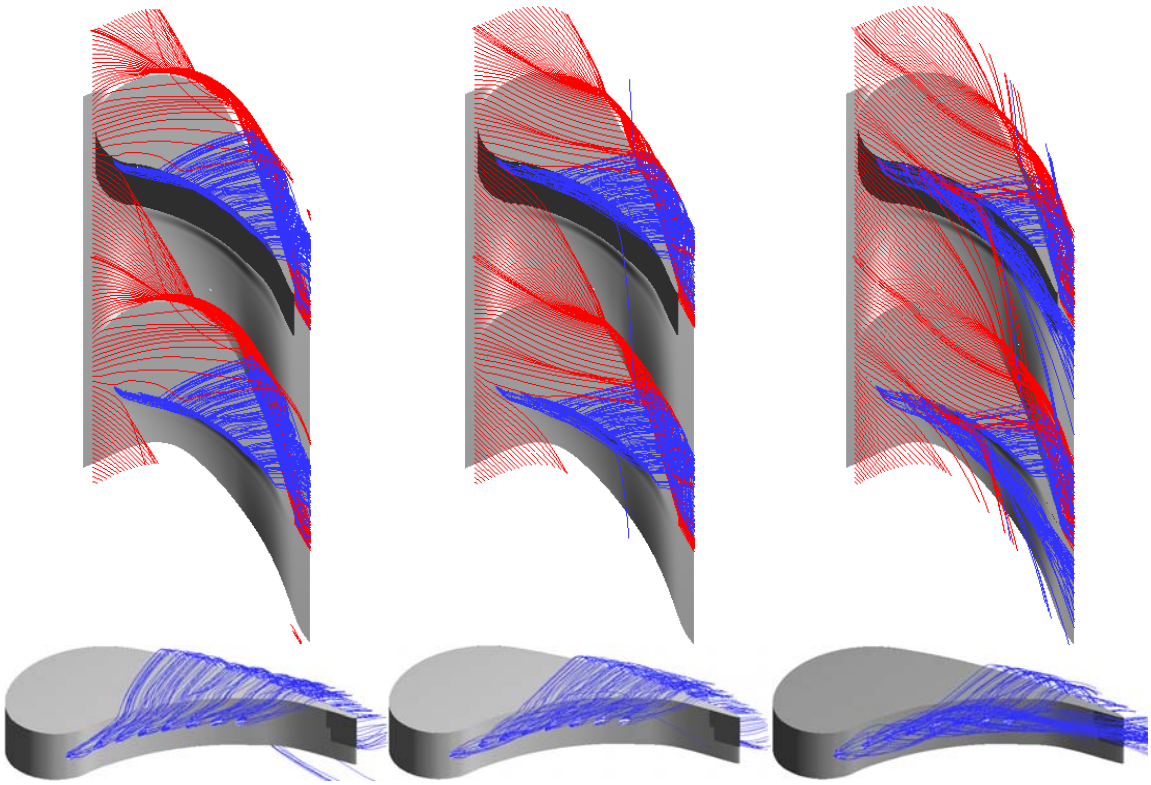

(a) 2000 rpm (b) 2550 rpm (c) 3000 rpm

Figure 9.31: Streamlines based on the relative velocity near the blade tip region for Plain tip with pressure-side hole cooling at M=1.25 (blue indicates cooling air, red is freestream air).

Figure 9.32 depicts the distribution of the temperature near the blade tip region for Plain tip at M=1.25. As mentioned above, almost all the coolant jets re-attach to the pressure surface at 2000 rpm, forming distinct streaks with low temperature right at downstream of the cooling hole exits. No obvious interaction is observed among the

cooling jets. However, when the rotation speed increases to 2550 rpm, the coolant jets from the first two holes start to interfere with each other. For the rotation speed of 3000 rpm, only the cooling jets from the last three holes show reattachment to the pressure surface, whereas most of the rest coolant lifts off the surface and travels downstream along with mainstream particles. Noticeably, since more coolant travels through the tip clearance at lower rotation speed, more tip surface is covered by the cooling film. Meanwhile the temperature is lower as well in the covered area. Based on current geometries and running conditions, the pressure-side hole cooling has better performance at off-design conditions.

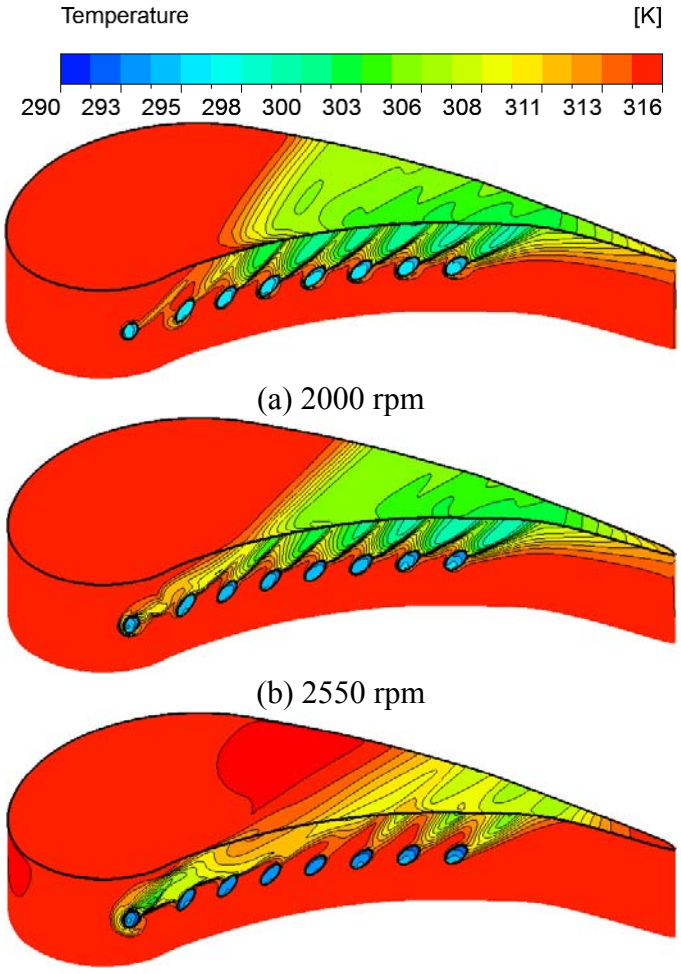

(a) 2000 rpm

(b) 2550 rpm

(c) 3000 rpm

Figure 9.32: Distribution of the temperature near the blade tip region for Plain tip with pressure-side hole cooling at M=1.25.

Figure 9.33 shows the impact of the rotation speed on the film cooling effectiveness at the blade tip surface for Plain tip. The blowing ratio is fixed at a moderate level of M=1.25. It is seen that at lower rotation speed, the cooling film is able to cover more blade tip surface than the case at higher rotation speed. Meanwhile the magnitude of

effectiveness is higher as well. Therefore the cooling effectiveness highly depends on the amount of cooling particles that travel across the blade tip surface. However, the leading edge is not cooled at all, which might be improved by putting cooling holes at the leading edge. The corresponding mechanism has been explained above. Compared to the influence of the blowing ratio in Figure 9.25, the impact of the rotation speed is more significant for the pressure-side hole cooling with Plain tip.

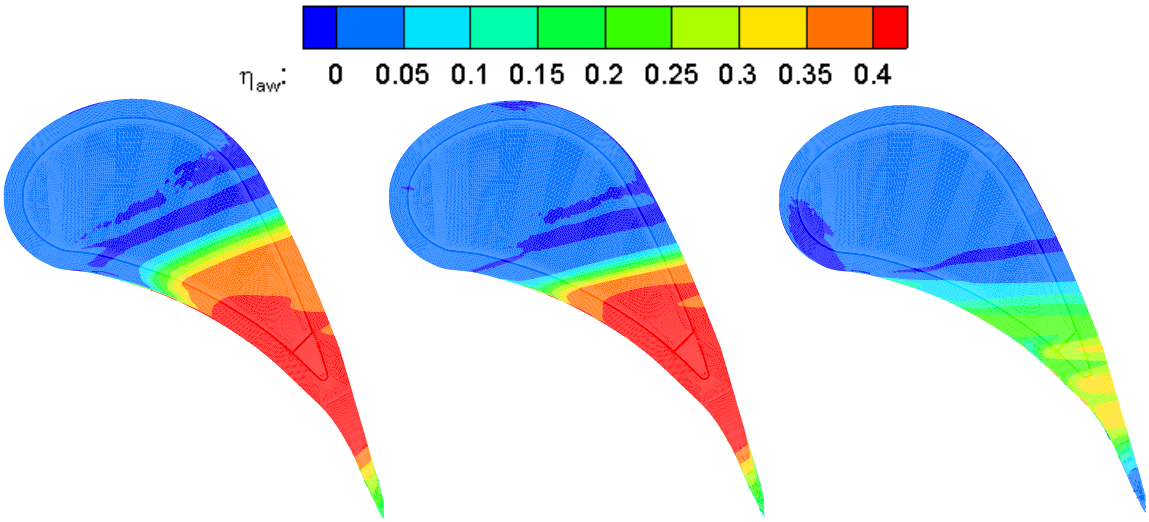

(a) 2000 rpm (b) 2550 rpm (c) 3000 rpm

Figure 9.33: Distribution of the adiabatic film cooling effectiveness at blade tip for the Plain tip with pressure-side hole cooling at M=1.25.

9.5.4 Impact of Rotation Speed, Squealer Tip

Figure 9.34 depicts the impact of the rotation speed on the pressure distribution near the blade tip region for squealer tip at M=1.25. It is seen that the variation of rotation speed can significantly influence the pressure distribution on the blade tip. Similarly, due to the decrease in rotating speed, the stagnation point moves towards the pressure side and the incidence angle declines as well. As a result, the high-pressure area on the squealer cavity floor moves along the suction-side inner wall from the cavity trailing end to upstream. The correlated area is deforming as well. However, the pressure on the cavity floor appears more uniform than it on Plain tip surface (Figure 9.30). In addition, the pressure in the vicinity of the cooling holes enhances too due to the movement of the stagnation point.

Figure 9.35 shows the streamlines near the blade tip region for squealer tip with three different rotation speeds. The turning of red streamlines (mainstream) shows the impact of the rotation speed on flow incidence angle. Unlike the Plain tip, the presence of the squealer cavity significantly alters the behaviors of the leakage flow and thus affects the cooling film. It is seen that most of the coolant passes through the tip clearance however very few coolant particles are entrained in the squealer cavity. Consequently, the cavity floor and inner wall can be hardly cooled. Similar to the Plain tip, the coolant jets are

significantly affected by the rotation speed. In Figure 9.35 (a), the coolant jets from all cooling holes are pushed towards the suction surface immediately after the coolant particles exit the holes. Almost all of the coolant crosses the pressure-side edge and then travels towards the suction side. Eventually these coolant particles leak from the suction side edge contributing to formation of tip vortex system. This is due to the smaller incidence angle and relatively high local pressure. As the rotation speed increases to 2550 rpm (Figure 9.35 (b)), most of the coolant jets are also turned and accordingly majority of the coolant particles leak from the suction side. However, for the rotation speed of 3000 rpm (Figure 9.35 (c)), only a small amount of the coolant particles travels to the suction side, whereas the rest of the coolant lifts off the pressure surface and mixes with the mainstream while traveling downstream. It is easily concluded that more rim surface is covered by the cooling film when the rotation speed is lower.

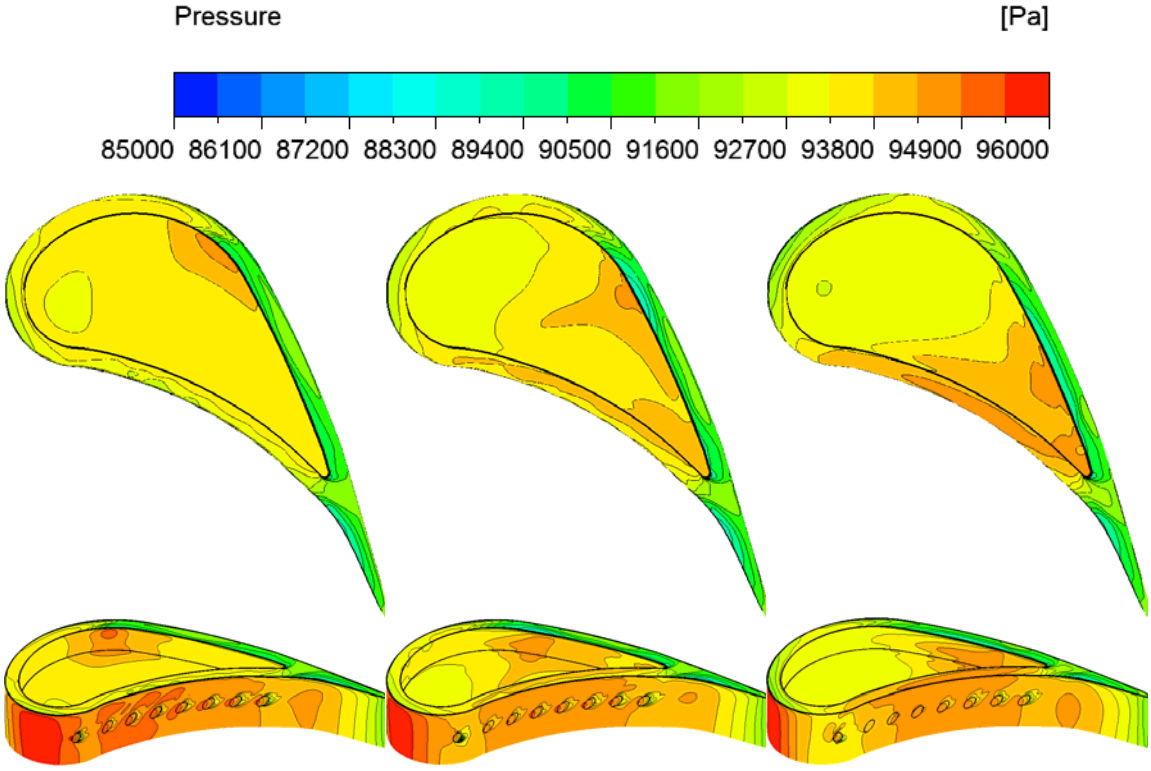

(a) 2000 rpm (b) 2550 rpm (c) 3000 rpm

Figure 9.34: Distribution of the static pressure near the blade tip region for squealer tip with pressure-side hole cooling at M=1.25.

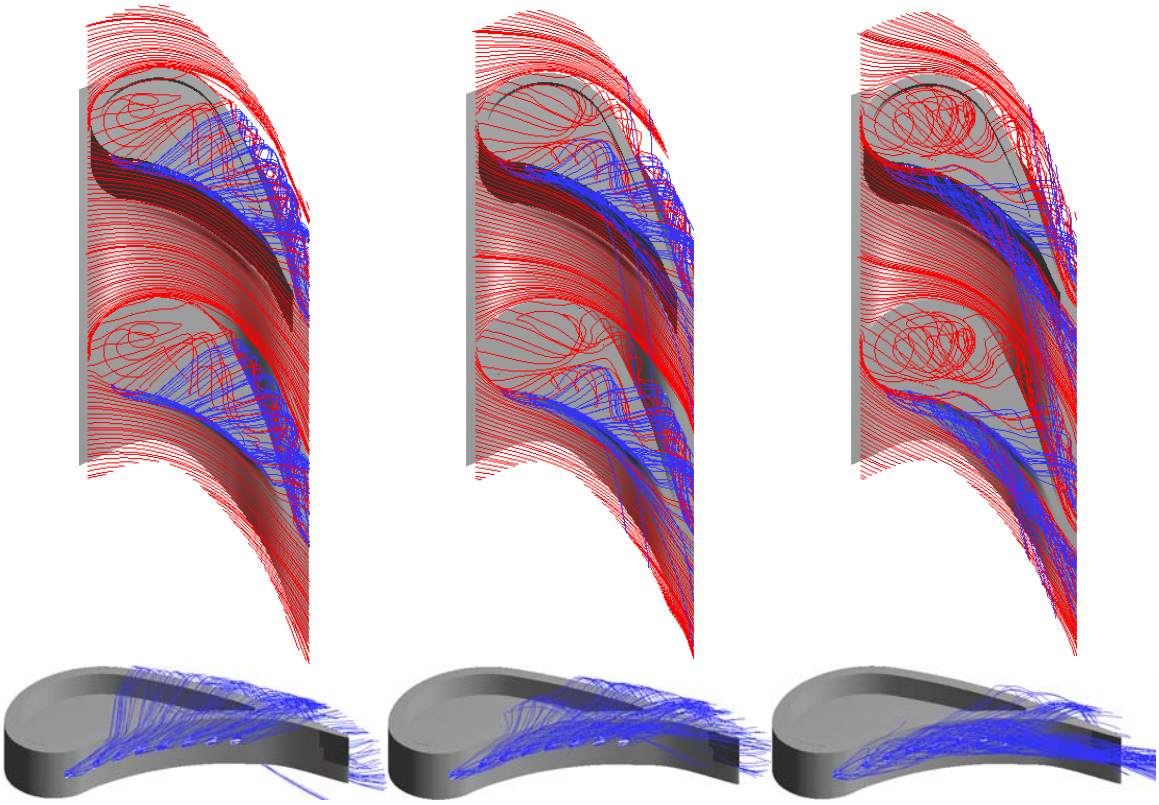

(a) 2000 rpm (b) 2550 rpm (c) 3000 rpm

Figure 9.35: Streamlines based on the relative velocity near the blade tip region for squealer tip with pressure-side hole cooling at M=1.25 (blue indicates cooling air, red is freestream air).

Figure 9.36 depicts the distribution of the temperature near the blade tip region for squealer tip at M=1.25. Similar to the Plain tip, almost all the coolant jets re-attach to the pressure surface at 2000 rpm. As a result, different streaks with low temperature right at the cooling-hole exits are generated. No noticeable interaction takes place among the cooling jets. When the rotation speed increases to 2550 rpm, the coolant jets from the first two holes interfere with each other. For the rotation speed of 3000 rpm, only the last three cooling jets reattach to the pressure surface, whereas most of the rest coolant lifts off the surface and penetrate into the mainstream. It has been seen in Figure 9.35 that larger area of the rim is cooled if the rotation speed is lower. For 2000 rpm and 2550 rpm, the pressure-side rim is well cooled and the surface temperature is lower than the case of 3000 rpm. In addition, part of the suction-side rim and cavity inner wall is cooled for 2000 rpm and 2550 rpm, which is due to the entrainment of coolant particles into the cavity. Because the rotation speed varies, the location of the cooled area changes too. However, the suction-side rim is not cooled at all when the blade rotates at 3000 rpm, since the leaking location of the coolant is at downstream of the cavity trailing end. Although the pressure-side hole cooling can also cover more blade tip area at off-design

conditions for squealer tip, it shows even worse cooling performance when compared to the Plain tip.

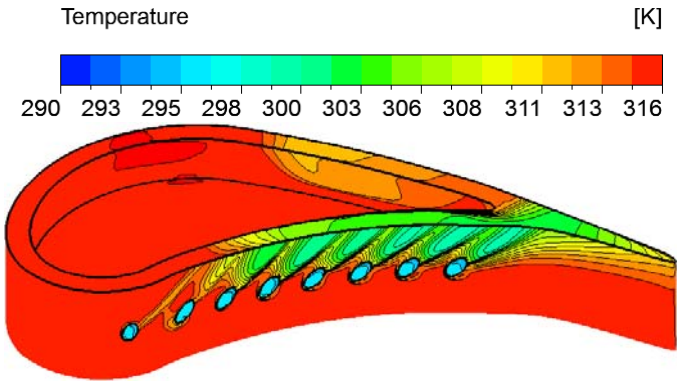

(a) 2000 rpm

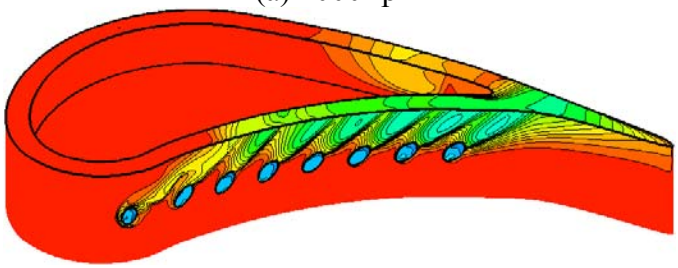

(b) 2550 rpm

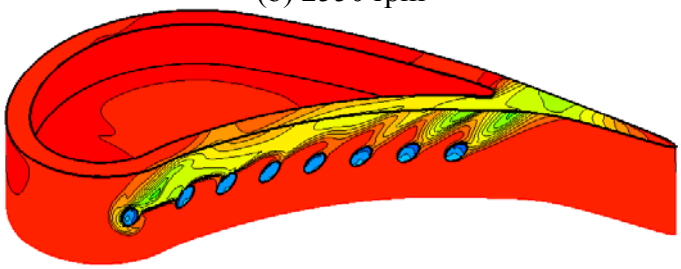

(c) 3000 rpm

Figure 9.36: Distribution of the temperature near the blade tip region for squealer tip with pressure-side hole cooling at M=1.25.

Figure 9.37 depicts the impact of the rotation speed on the film cooling effectiveness at the blade tip region for squealer tip. The blowing ratio is fixed at M=1.25. It is seen that at lower rotation speeds of 2000 rpm and 2550 rpm, the cooling effectiveness on the pressure-side rim is as high as 0.4. The corresponding coverage extends from 30%~80%C_{ax}. However, the effectiveness on the pressure-side rim does not exceed 0.25 for 3000 rpm, since less coolant travels through the tip clearance than lower rotating conditions. As mentioned above, part of the suction-side rim is cooled at lower rotation speeds. More cooled area of the suction-side rim is obtained at 2000 rpm than 2550 rpm. However, no effective cooling is observed on the suction-side rim for 3000 rpm. Additionally, the cooling film does not provide any protection for the leading-edge rim and cavity for all rotation speeds due to the path of coolant through the tip clearance.

Although the impact of the rotation speed is more significant than blowing ratio on the pressure-side hole cooling, the benefit is marginal for squealer tip.

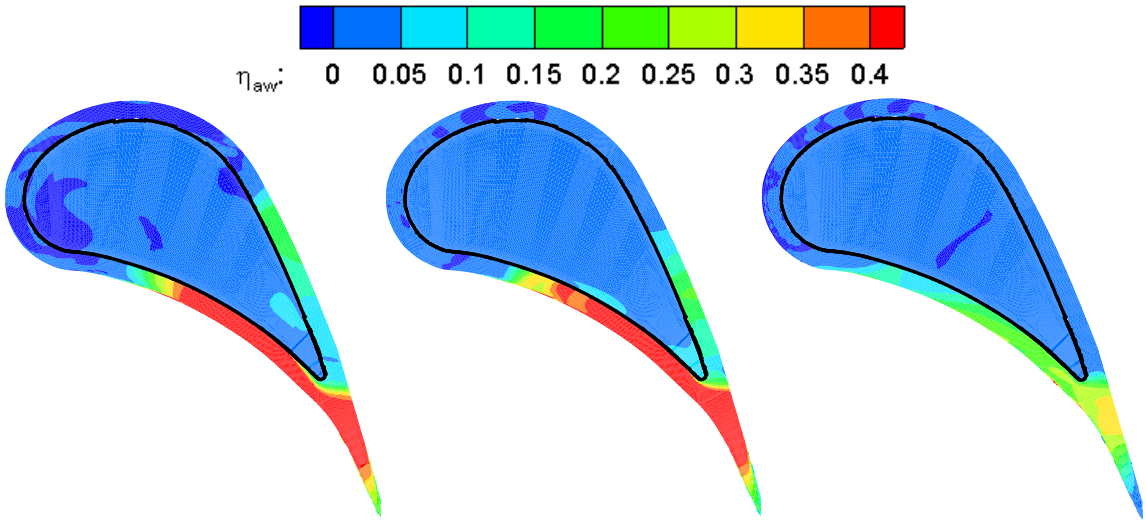

(a) 2000 rpm (b) 2550 rpm (c) 3000 rpm

Figure 9.37: Distribution of the adiabatic film cooling effectiveness at blade tip for the squealer tip with pressure-side hole cooling at M=1.25.

10. EXPERIMENTAL INVESTIGATIONS FOR BLADE TIP FILM COOLING

10.1 Experimental Procedure

The platform passage under investigation was layered with 7 to 9 coats of PSP using an air brush. This coated surface was excited using a strobe light fitted with a narrow bandpass interference filter with an optical wavelength of 520nm. Upon excitation from this green light, the PSP coated surface emitted red light with a wavelength higher than 600nm. A 12-bit scientific grade CCD camera (high speed SensiCam with CCD temperature maintained at -15^{o}C and using 2-stage Peltier cooler) fit with a 35mm lens and a 600nm longpass filter was used to record intensity images. The filters were chosen such that the camera blocked the light reflected from the target surface and only captured the actual data. A schematic of the optical setup used in the data acquisition is shown in Figure 10.1.

The camera, the strobe light and the data acquisition system were triggered simultaneously using an optical sensor triggered off the rotor shaft. By detecting the same angular position, the camera was able to view the same region of interest at every rotation, making it possible to average the image intensities without blurring the information. A minimum exposure time of 17μs was used for image capture from the camera. Estimated rotor movement during image capture at 2550 rpm, for a 17μs exposure time was approximately 1.1mm. A total of 200 images were captured for each experiment with air and nitrogen injection and the pixel intensity for all images was averaged. A computer program was used to convert these pixel intensities into pressure using the calibration curve and then into film cooling effectiveness. The coolant flow rate was set using a rotameter based on prior calculation for the desired blowing and mass flow ratio. The coolant was heated to the same temperature as mainstream air (45°C) before injection through the gap to eliminate the temperature effects of PSP.

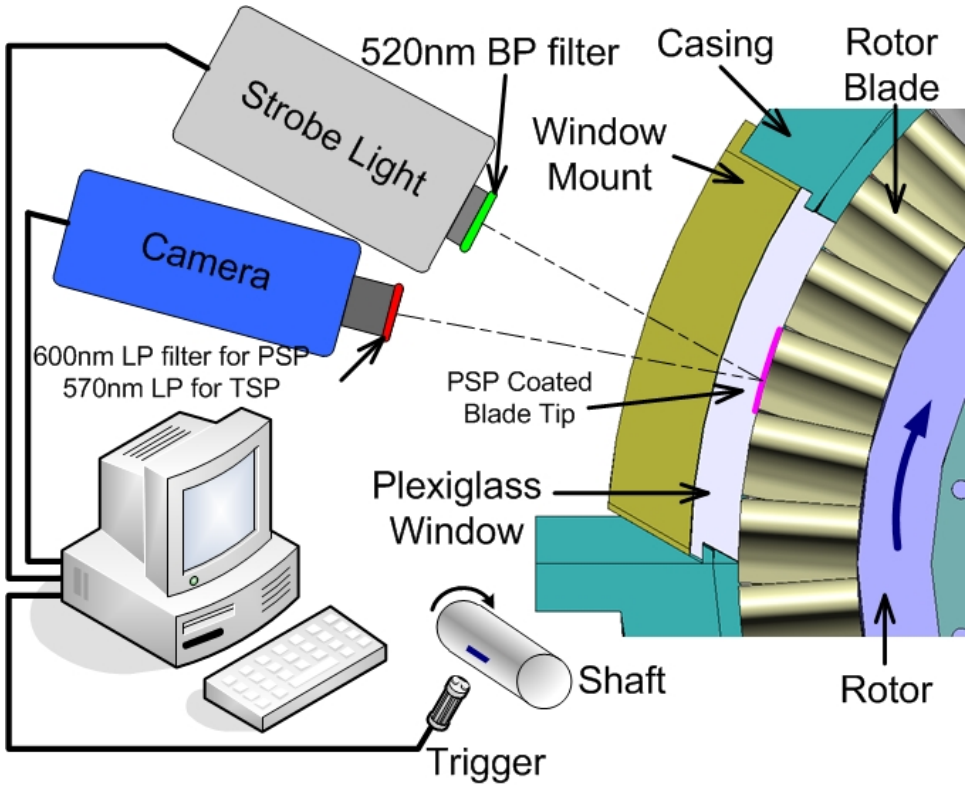

Figure 10.1: Optical set-up for PSP data.

Uncertainty calculations were performed based on a confidence level of 95% and are based on the uncertainty analysis method of Coleman and Steele. Lower effectiveness magnitudes have higher uncertainties. For an effectiveness magnitude of 0.8, uncertainty was around ±1% while for effectiveness magnitude of 0.07, uncertainty was as high as ±10.3%. This uncertainty is the cumulative result of uncertainties in calibration (4%) and image capture (1%). The absolute uncertainty for effectiveness varied from 0.01 to 0.02 units. Thus, relative uncertainties for very low effectiveness magnitudes can be very high (>100% at effectiveness magnitude of 0.01). However, it must be noted that very few data points exist with such high relative uncertainty magnitudes. Uncertainties for the average blowing ratio calculations are estimated to be approximately 3.5% using Kline-McClintock analysis and are discussed in detail by Holman [77].

10.2 Results and Discussions

In this section blowing ratio effect and rotation effect will be discussed for each configuration. Film cooling effectiveness measurements were performed for three blowing ratios (M) of 0.75, 1.25 and 1.75. Film cooling data was also obtained for three rotational speeds; 3000 rpm (reference condition), 2550 rpm and 2000 rpm. Experimental measurement and numerical simulation have been done for four different tip configurations: Plain tip with tip hole cooling, squealer tip with tip hole cooling, Plain tip with pressure-side-edge compound angle hole cooling and squealer tip with pressure-side-edge compound angle hole cooling.

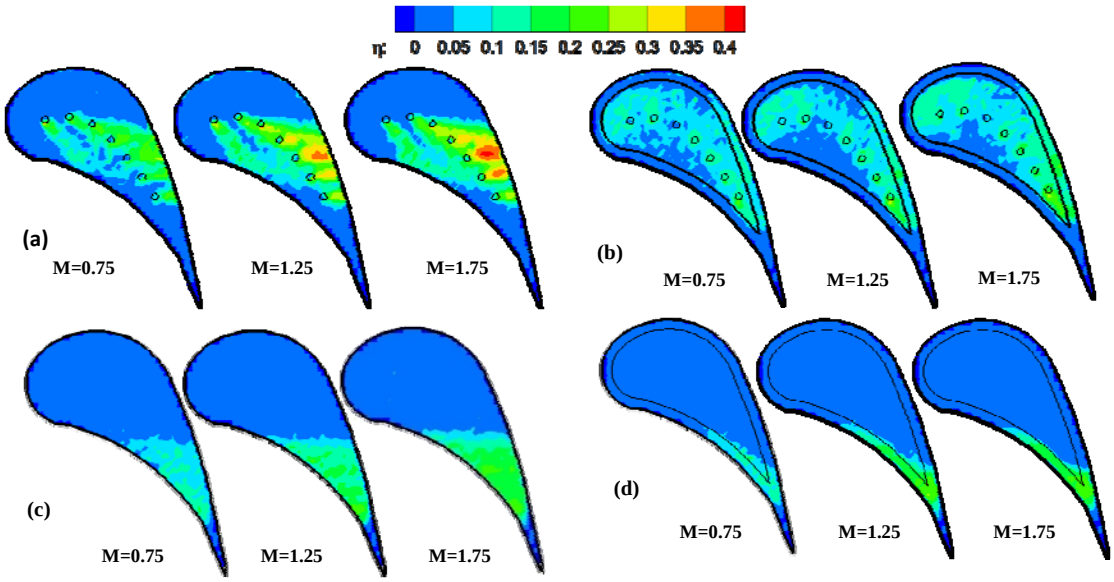

Figure 10.2: Film cooling effectiveness distribution on the Plain tip at 3000 rpm for different blowing ratio. (a) Plain tip with tip hole cooling, (b) squealer tip with tip hole cooling, (c) Plain tip with PS hole cooling and (d) squealer tip with PS hole cooling.

10.2.1 Blowing ratio effect, Plain tip with tip hole cooling

For all cases higher blowing ratios resulted in coolant injection with higher momentum. The injected coolant is at the same density as the mainstream i.e. the coolant to mainstream density ratio is unity. Hence, the injected coolant velocity is higher for higher blowing ratios. This affects the secondary flow structure in the passage for each configuration.

The film cooling effectiveness resulting from using PSP for the reference rotating condition of 3000 rpm are plotted in Figure 10.2(a). The figure shows the contour plots for all three blowing ratios tested on the Plain tip. The contour plots also show the location of the seven tip cooling holes.

At M=0.75 the trajectory of each hole appears as a narrow streak and can be approximately differentiated from each other due to the relatively small blowing ratio. The cooling effectiveness is around 0.2 within the coolant trajectories. The highest value of nearly 0.3 is obtained right at the downstream of the cooling-hole exits. The downstream cooling effectiveness is gradually decreased due to the diffusion of cooling jets and the mixing between the coolants and the leakage flow. As the blowing ratio increases to M=1.25 each coolant trajectory tends to diffuse more and thus covers more area. The trajectories of the cooling jets exiting from the first, the sixth and the seventh holes are easily identified, whereas a large area with high effectiveness appears in the vicinity of the rest of the cooling holes due to the coolant accumulation. It is noticeable that the highest film cooling effectiveness (above 0.35) is observed in the vicinity of the last four cooling holes. In the case of M=1.75, the trajectory tends to be thicker and thus

the film cooling performance is even better as expected. Higher film cooling effectiveness is achieved especially when it comes to the last four cooling holes due to the coolant accumulation. Around 50% of the blade tip surface is covered by the film coolant.

Looking at the shape of the high effectiveness area, the shape has high coincidence with the trajectories of cooling jets. Hence the adiabatic film cooling effectiveness largely reflects the consequence of the flow behaviors. Figure 10.3(a) depicts the corresponding streamline patterns at the blade tip region. Since the object of the current study is a rotor blade rotating at 3000 rpm with the tip speed of 215.34 m/s, the streamlines are plotted based on the relative velocity in the rotating coordinates.

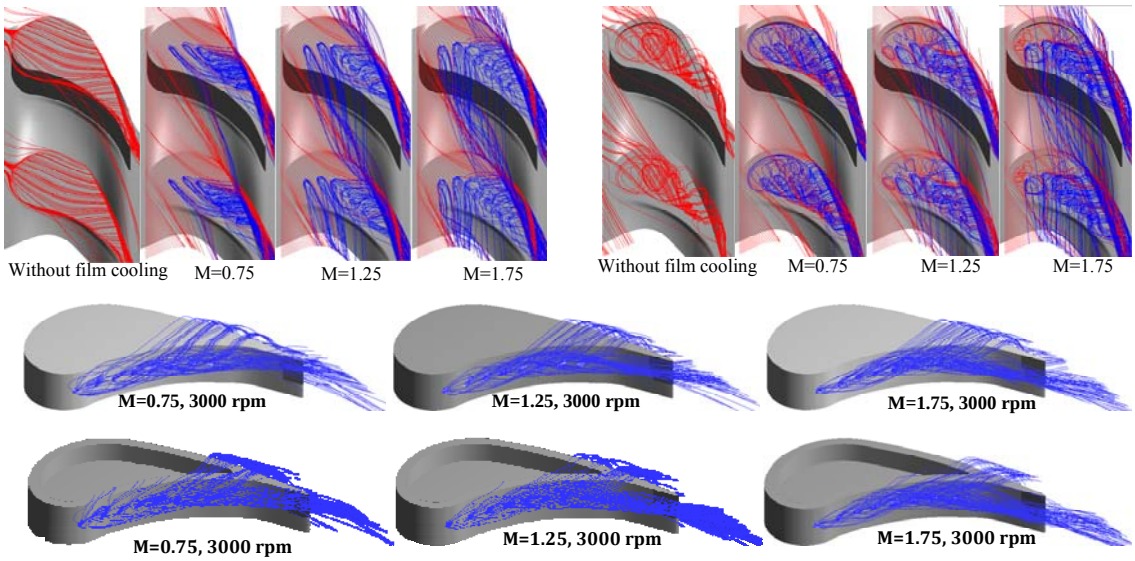

Figure 10.3: Streamlines based on the relative velocity at 3000 rpm (blue indicates cooling air, red is freestream air). (a) Plain tip with tip hole cooling, (b) squealer tip with tip hole cooling, (c) Plain tip with PS hole cooling and (d) squealer tip with PS hole cooling.

Many factors can affect the film cooling effectiveness. One of the critical parameters is the blowing ratio. Another one is the blade tip geometry. Due to the blunt and round leading edge of the blade, the pressure difference at the leading edge is not as high as that between the pressure side and suction side. Consequently, the mainstream particles entering the tip gap are not deflected immediately. Nevertheless, they keep traveling a distance along the initial direction until the pressure difference becomes high enough to push them to the suction side at about 30% of C_{ax}. As a result, a small amount of flow leaks from the pressure side of the leading edge, whereas the majority moves towards the suction side forming a system of tip vortices.

Figure 10.4(a) depicts the static pressure distribution at the blade tip region for blowing ratios of M=1.25 at 3000 rpm. For the Plain tip without film cooling holes, the typical pressure distribution is obtained. The pressure side (PS) has the highest pressure

and the pressure is gradually decreased towards the suction side (SS). The resulted pressure difference pointing from PS to SS is the primary driving force of the tip-gap leakage flow.

Based on the Figure 10.2(a) and Figure 10.3(a) all the coolant particles exiting from the first and second cooling holes travels across the pressure side and form a passage flow by mixing with the mainstream. Meanwhile, the rest of the majority appears to accumulate in the vicinity of cooling-hole exits. The coolant spreads more widely and covers more of the tip, which is virtually the result of the impact of both the pressure difference and the relative motion between the tip and shroud.

It is shown that the coolant particles tend to travel in the opposite direction of rotation, especially for the cooling jets exiting from the first two cooling holes. This phenomenon is due to the rotation and does not exist in a stationary cascade. While in this specific hole configuration, the jets tend to exit radially, and the circumferential motion of the rotor causes the blade tip to move away from the jets. As a result the particle moving along a relative streamline with a relative velocity tangent to the streamline.

10.2.2 Blowing Ratio Effect, Squealer Tip with Tip Hole Cooling

Different effectiveness contours were obtained when it comes to the squealer tip. As shown in Figure 10.2(b), more area of the squealer tip is protected by the film cooling when compared with the Plain tip. However, the local cooling effectiveness on the squealer tip tends to be lower. The impact of the blowing ratio on the cooling effectiveness might be less important for the squealer tip.

At all blowing ratios, nearly the entire cavity floor is to some extent protected by the cooling film. Apparently the area of the cavity close to the pressure side is not cooled, whereas cooling effectiveness on the rest of the cavity floor is almost above 0.1. Maximum effectiveness is found in the vicinity of the cavity trailing end due to the accumulation of coolant coming from the upstream. More coolant leaking from the suction side causes higher cooling effectiveness.

As seen in Figure 10.3(b), after crossing over the narrow gap between the casing and the squealer rim, the freestream flow is squeezed in the squealer cavity. Sudden expansion induces flow circulations within the cavity which entraps the freestream particles. Meanwhile, strong interactions between the leakage flow and the cooling jets intensify the mixing which forms three-dimensional complex vortex systems. Major portion of the mixture of the leakage flow and the coolant continues to roll and travels downstream along the cavity. Eventually, the flow particles accumulate at the trailing end of the cavity and afterward escape from the cavity by crossing over the suction side rim, which generates the suction-side tip vortex. Unlike the case for Plain tips, some coolant particles are transported to the leading edge portion by complicated vortices circulating at the surrounding area. Such transportation is able to partially relieve the heat loads and thus provide certain cooling protection to the cavity walls near the leading edge. However, the leading edge of the Plain tip is directly exposed to the hot freestream and at risk of overheating. This is an advantage of the squealer tip.

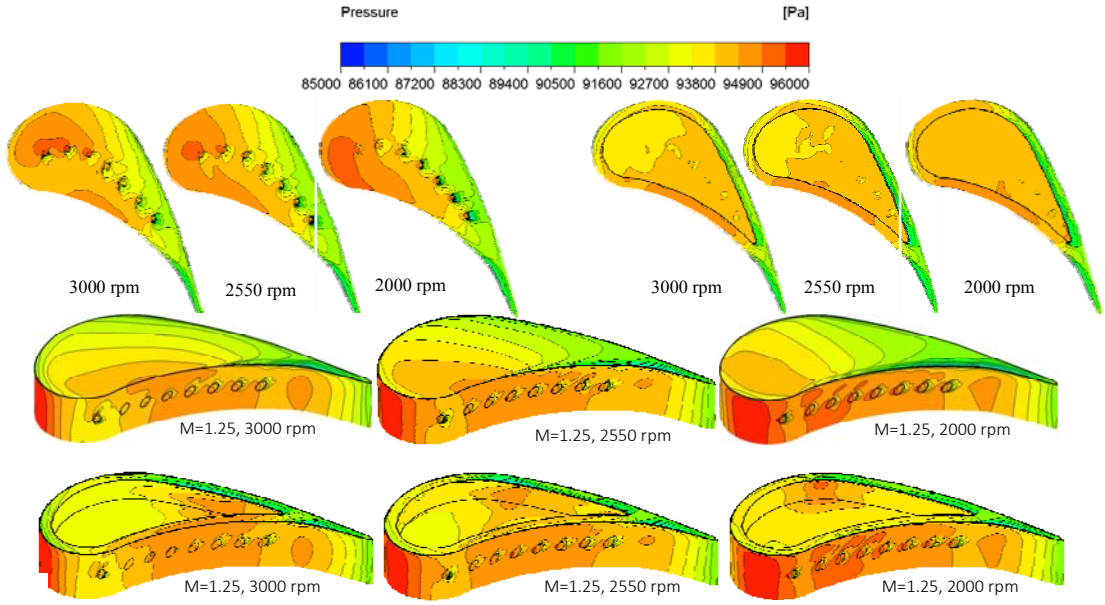

Figure 10.4: Distribution of the static pressure at: (a) Plain tip with tip hole cooling, (b) squealer tip with tip hole cooling, (c) Plain tip with PS hole cooling and (d) squealer tip with PS hole cooling.

The pressure on the squealer tip shows dramatically different distributions compared with that on the Plain tip. As shown in Figure 10.4(b), the most noticeable characteristic is that the pressure distribution on the cavity floor tends to be uniform and thus the pressure gradient on the cavity floor is significantly decreased. This is resulted from the presence of the large cavity on the tip.

10.2.3 Blowing Ratio Effect, Plain Tip with Pressure-Side Hole Cooling

The film cooling effectiveness contour plots for three blowing ratios at the reference rotating condition of 3000 rpm are plotted in Figure 10.2(c). The maximum film cooling effectiveness among three cases is about 0.25 with maximum value occurring at pressure side near trailing edge. As blowing ratio increases from M=0.75 to M=1.75, overall film cooling effectiveness increases. This is due to higher mass flow rate of the coolant injected through the holes resulting in a larger film covered area. The film-covered area extends further downstream with a higher maximum value for film-cooling effectiveness as blowing ratio increases.

Figure 10.3(c) shows streamlines based on the relative velocities near the blade tip. As it is shown, due to high mainstream velocities on pressure side, coolant injected through these pressure side holes can get diverted towards the trailing edge. Thus, effectiveness for the first three holes is almost negligible. Due to the blade geometry and round leading edge, the pressure gradient at the leading edge is not as big as pressure gradient between the pressure side and suction side near trailing edge. Therefore, almost the first 50% of chord length is not covered. As it is shown in Figure 10.3(a) (Tip

streamlines without cooling) leakage flow almost starts at 50% of chord length. So cooling flow follows the leakage flow in that region and covers that area.

The relative flow velocity through the gap is dictated by the blade tip rotational speed. Since the dynamic pressure of the relative velocity is much larger than the static pressure difference along the first 50% on the blade tip, the fluid particle within the gap are pushed in the opposite direction of the rotation, thus the major portion of the surface close to the suction side is not covered.

10.2.4 Blowing Ratio Effect, Squealer Tip with Pressure-Side Hole Cooling

Figure 10.2(d) shows film cooling effectiveness distribution for squealer blade tip with pressure side-edge compound angle hole cooling. The film-covered area for squealer tip is smaller as compared to Plain tip. The highest film cooling value among three cases is around 0.25 that occurs at pressure side near trailing edge. Film-cooling effectiveness increases with increasing blowing ratio. Similar to the Plain tip with PS cooling, by increasing the coolant mass flow rate, more cooling flow covered the area. For the region from the mid-chord of the blade to the trailing edge on the pressure side rim, the effectiveness is higher. A noticeable trace can be detected on the trailing edge, which is probably due to some carrying over of the coolant over the rim from the pressure side.

As it is shown in Figure 10.3(d), the presence of a squealer tip reduces the leakage flow from pressure to suction side of the blade. The squealer cavity acts like labyrinth seal and does not allow the leakage flow goes from pressure side to suction side.

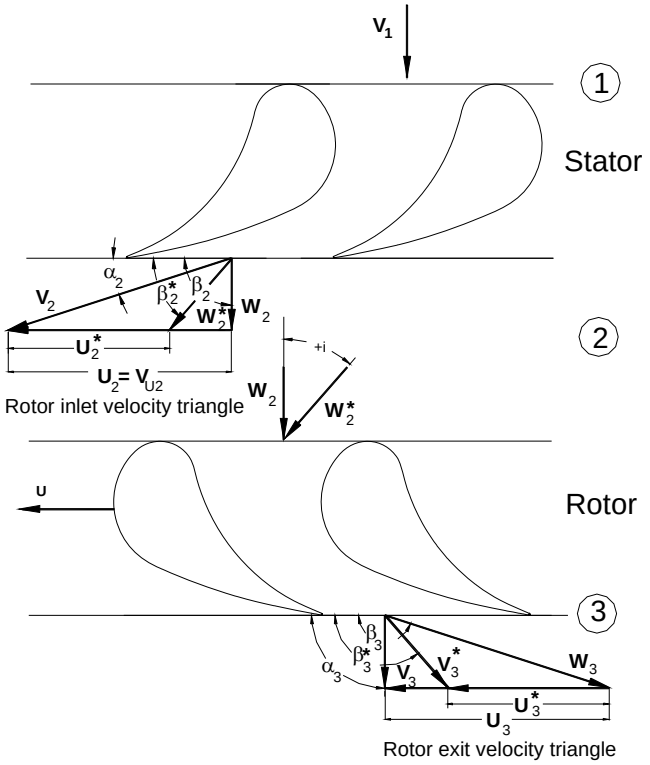

Figure 10.5: Velocity triangles and relative inlet and exit flow angles for design and off-design speed.

10.2.5 Effect of Rotation Speed Change, Plain Tip with Tip Hole Cooling

In this section effect of rotation for all four configurations is investigated. Film cooling effectiveness data is taken for blowing ration M=1.25 for three different rpm: 3000 rpm, 2550 rpm and 2000 rpm.

At rotational speeds lower than the design speed, the blade flow deflection becomes larger leading to higher specific stage load coefficient, and the stagnation region moves towards the pressure side as the flow incidence angle increases, as sketched in Figure 10.5. At lower rotating speeds, the stagnation point will further move towards the blade pressure side resulting in a higher pressure zone close to the pressure surface.

Figure 10.6(a) shows film cooling effectiveness contour for plain tip with tip hole cooling. As it is shown, more coolant appears to go to the suction side of the blade where the pressure difference across the blade is larger with the lower rotational speed.

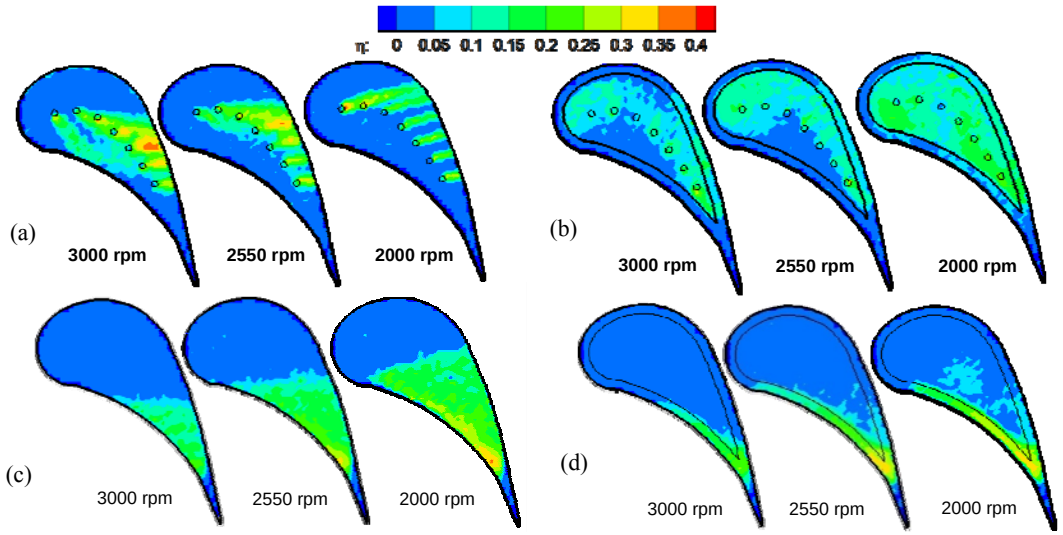

Figure 10.6: Effect of rotation on film cooling effectiveness distribution on the Plain tip for M=1.25. (a) Plain tip with tip hole cooling, (b) squealer tip with tip hole cooling, (c) Plain tip with PS hole cooling and (d) squealer tip with PS hole cooling.

This phenomenon can be clearly observed from static pressure distribution shown in Figure 10.4(a). By decreasing the rpm from 3000 rpm to 2000 rpm, pressure increases at pressure side and decreases at suction side. According to Figure 10.7(a), almost all of the cooling jet's streamlines at 2000 rpm follow the leakage flow and go to the suction side.

For 2550 rpm, almost all of the cooling jets are deflected towards the suction side, except that a small amount of coolant ejecting from the first cooling hole moves to the pressure side and then leaves the tip gap together with the leakage flow on the pressure side. For 2000 rpm, all of the cooling jets are deflected towards the suction side.

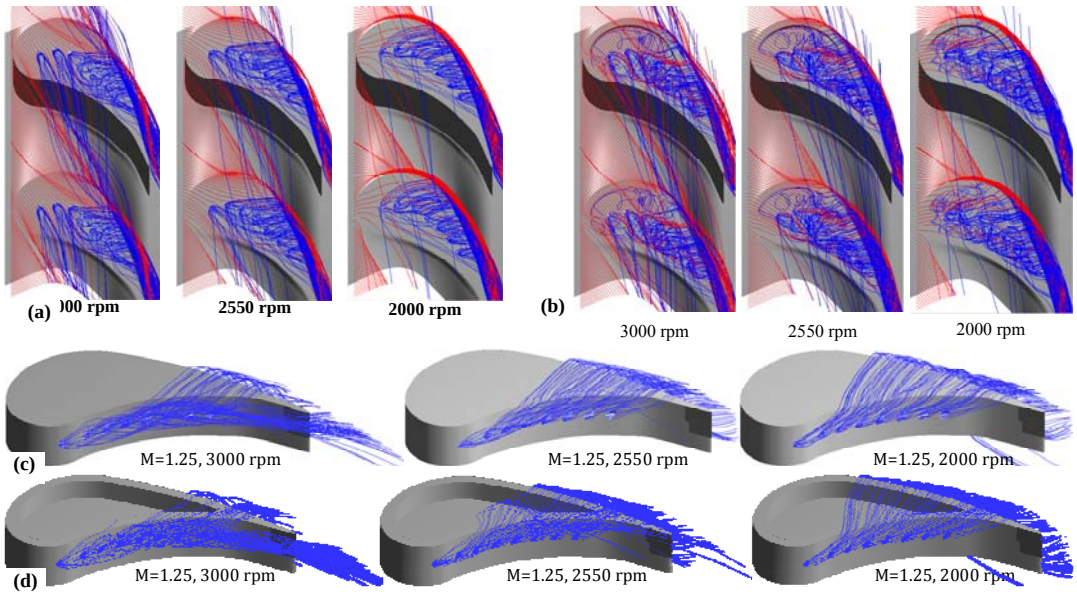

Figure 10.7: Pitch Streamlines based on the relative velocity at 3000 rpm (blue indicates cooling air, red is freestream air). (a) Plain tip with tip hole cooling, (b) squealer tip with tip hole cooling, (c) Plain tip with PS hole cooling and (d) squealer tip with PS hole cooling.

10.2.6 Effect of Rotation Speed Change, Squealer Tip with Tip Hole Cooling

In squealer tip, by decreasing the speed, the effectiveness and film cooling coverage increase. As shown in Figure 10.6(b), in 2000 rpm the film cooling effectiveness is almost above 0.15. As shown in Figure 10.4(b), by decreasing the rpm flow incidence angle increases and the stagnation region moves towards the pressure side resulting in a higher pressure zone close to the pressure surface. This affects the flow behavior inside the cavity. In 3000 rpm, it is observed that the region between the pressure side and the holes is not covered by the coolant. The coolant flow goes to the suction side after flow reattachment, so the coolant jets are directed toward the suction side. When the incidence angles changes the flow reattachment location also changes. In the positive incidence angle, the leakage flow is stronger and the flow circulation inside the cavity is enhanced. The coolant is more dispersed in the tip cavity and as a result film cooling effectiveness increases over the cavity floor. In 2000 rpm, coolant gets accumulated inside the squealer cavity in the region between the mid-chord and the trailing edge due to flow recirculation in the contracting squealer passage.

10.2.7 Effect of Rotation Speed Change, Plain Tip with Pressure-Side Hole Cooling

Similar trend like squealer tip is obtained when it comes to plain tip with pressure side-edge cooling. As shown in Figure 10.6(c), more area of the tip surface is protected by coolant flow by decreasing rotational speed. Figure 10.4(c) shows the pressure distribution on pressure side and tip surface. As it is shown, stagnation point moves toward pressure side and it is close to first hole. Higher pressure on pressure side

increases the leakage flow to suction side. Figure 10.7 depicts the streamline at Plain tip with pressure side cooling. In 2000 rpm, compare to 3000 rpm, less flow is diverted towards leakage flow and followed main-stream velocity inside the passage between blades. The highest value of nearly 0.4 is obtained at 2000 rpm near trailing edge due to accumulation of coolant.

10.2.8 Effect of Rotation Speed Change, Squealer tip with pressure-side hole cooling

In squealer tip with pressure side cooling less leakage flow goes from pressure side to suction side due to existence of cavity. By decreasing the rpm, incidence angle increases, and also pressure increases on pressure side (Figure 10.4(d)). This increase enhances the film cooling effectiveness on pressure side rim. The highest film cooling value among three rpms is around 0.35 that occurs at pressure side near trailing edge at 2000 rpm (Figure 10.6(d)). At 2000 rpm and 2550 rpm some coolant streamlines cover some area on suction side rim. As it is shown in Figure 10.7(d) some coolant streamlines reattach the cavity floor at 2000 rpm and covered small area there.

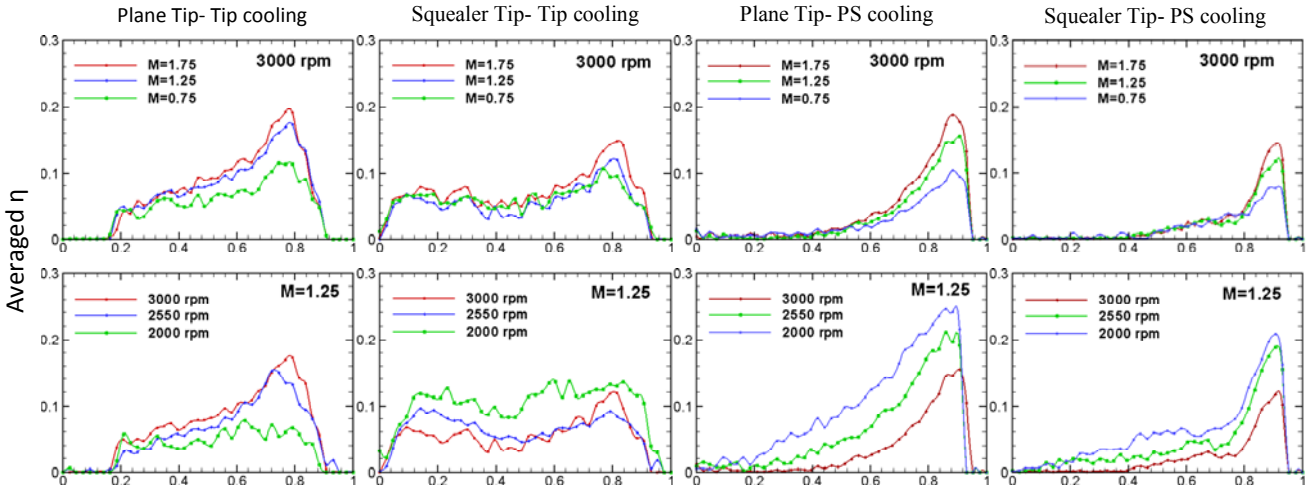

Figure 10.8: Pitch-wise average film cooling effectiveness for four different configurations: different blowing ratio at 3000 rpm (top), different rpm at M=1.25 (bottom).

10.3 Pitch-wise average film cooling effectiveness

The film cooling effectiveness results were averaged along the pitch-wise direction and the averaged data for all blowing ratios and rotational speeds are presented in Figure 10.8 along the axial chord.

In Plain tip, it is shown that the coverage of the film cooling starts from nearly 15% C_{ax} and ends at 90% C_{ax}. For M=0.75, the averaged value seems to gradually increase along the C_{ax} within the covered area. Several peaks are observed and each of them represents the location of every film cooling hole. At M=1.25, the averaged film cooling effectiveness is slightly lower than 0.1 from 20% C_{ax} to 60% C_{ax}. However, the averaged

value dramatically increases when it reaches 65% C_{ax}. Between 65% C_{ax} and 80% C_{ax}, the averaged film cooling effectiveness is as high as 0.18. Even higher film cooling effectiveness is obtained when the blowing ratio reaches M=1.75.

The squealer tip shows quite different trends in Figure 10.8. The film cooling is effective up to 90% C_{ax} for all the blowing ratios. For M=0.75, the pitchwise-averaged film cooling effectiveness is stabilized around 0.06 until it bumps up a bit at 80% C_{ax}. However, the averaged cooling effectiveness gradually grows 0.12 when the blowing ratio becomes 1.25. A similar trend is obtained for the blowing ratio M=1.75, but the average slope is slightly larger compared with M=1.25. The highest value of 0.15 appears at about 80% C_{ax} where it is believed to be close to the cavity trailing end. In fact, the peak value is found in the same area for all three blowing ratios. As discussed earlier the impact of the blowing ratio on the cooling effectiveness might be less important for the squealer tip.

Within 40% C_{ax} and 80% C_{ax}, the Plain tip offers higher averaged cooling effectiveness than the squealer tip does. The impact of the rotational speed on the film cooling effectiveness is also illustrated in Figure 10.8. It shows the pitch-wise averaged film cooling effectiveness results plotted for M=1.25. The impact of turbine rotational speeds on film cooling effectiveness can be clearly perceived from these plots.

The squealer tip shows quite different trends in Figure 10.8. The film cooling is effective up to 90% C_{ax} for all the blowing ratios. For M=0.75, the pitchwise-averaged film cooling effectiveness is stabilized around 0.06 until it bumps up a bit at 80% C_{ax}. However, the averaged cooling effectiveness gradually grows 0.12 when the blowing ratio becomes 1.25. A similar trend is obtained for the blowing ratio M=1.75, but the average slope is slightly larger compared with M=1.25. The highest value of 0.15 appears at about 80% C_{ax} where it is believed to be close to the cavity trailing end. In fact, the peak value is found in the same area for all three blowing ratios. As discussed earlier the impact of the blowing ratio on the cooling effectiveness might be less important for the squealer tip.

Within 40% C_{ax} and 80% C_{ax}, the Plain tip offers higher averaged cooling effectiveness than the squealer tip does. The impact of the rotational speed on the film cooling effectiveness is also illustrated in Figure 10.8. It shows the pitch-wise averaged film cooling effectiveness results plotted for M=1.25. The impact of turbine rotational speeds on film cooling effectiveness can be clearly perceived from these plots.

As rpm decreases to 2000 rpm, film cooling effectiveness coverage starts earlier. For example, at 2550 rpm it starts at 30% C_{ax} and at 3000 rpm it starts at 20% C_{ax}. The highest averaged film cooling effectiveness among all the cases in Figure 10.8 appears at 2000 rpm at 85%.

Squealer tip with pressure side cooling has the same trends as plain tip with pressure side cooling. For all blowing ratios, from 50% C_{ax} to 80% C_{ax} averaged film cooling effectiveness increases slightly due to pressure side rim effectiveness. The highest value of 0.15 appears at about 90% C_{ax} where it is close to the cavity trailing end. The peak value is found in the same area for all three blowing ratios.

The area-averaged film cooling effectiveness versus the blowing ratio at the blade tip region is shown in Figure 10.9. It is shown that the overall film cooling effectiveness for

Plain tip increases monotonously as the blowing ratio is increased. This is consistent with the contour plots in Figure 10.2. Note that the overall effectiveness on the Plain tip is slightly lower than that on the squealer tip for M=0.75. With increasing blowing ratios, the situation is altered. Higher overall effectiveness is obtained on the Plain tip for both M=1.25 and 1.75.

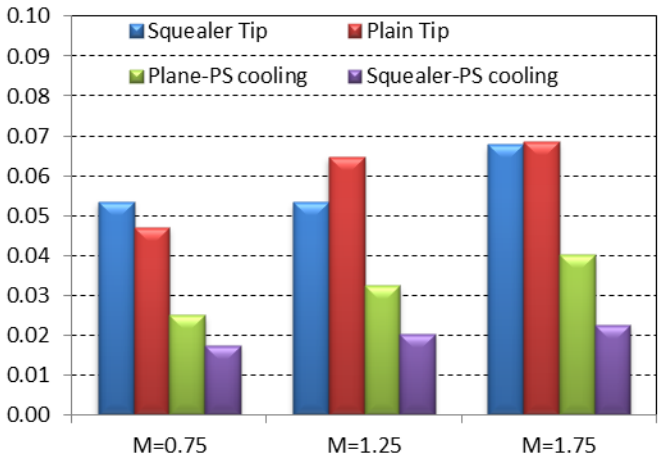

Figure 10.9: Area-averaged film cooling effectiveness versus blowing ratio at the blade tip region.

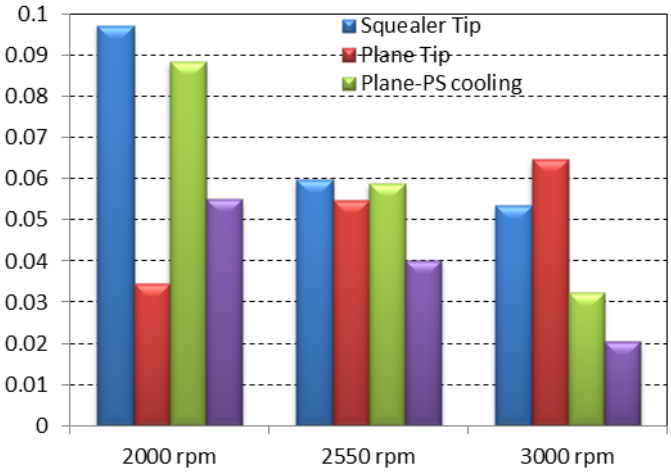

Figure 10.10: Area-averaged film cooling effectiveness versus rotational speed at the blade tip region at M=1.25.

The area-averaged film cooling effectiveness versus rotational speed at the blade tip region is shown in Figure 10.10. For all the configurations except the Plain tip by increasing the rpm, the area averaged film cooling effectiveness decreases. Squealer tip at 2000 rpm has the highest value among all the cases.

11. CONCLUSIONS FOR EACH TASK

This report deals with the specific aerodynamics and heat transfer problematic inherent to high pressure (HP) turbine sections of IGCC-gas turbines as specified in the proposal. As defined in [1], issues of primary relevance to a turbine stage operating in an IGCC-environment are: (1) decreasing the strength of the secondary flow vortices at the hub and tip regions to reduce (a), the secondary flow losses and (b), the potential for end wall deposition, erosion and corrosion due to secondary flow driven migration of gas flow particles to the hub and tip regions, (2) providing a robust film cooling technology at the hub and that sustains high cooling effectiveness less sensitive to deposition, (3) investigating the impact of blade tip geometry on film cooling effectiveness. As shown in this document, the accomplishments detailed in this report have gone far beyond those expected by achieving the objectives defined in [1]. The document includes numerical and experimental investigations. The experimental investigations were performed in the three-stage multi-purpose turbine research facility at the Turbomachinery Performance and Flow Research Laboratory (TPFL), Texas A&M University. For the numerical investigations a commercial Navier-Stokes solver was utilized. The issued treated in this report included:

1) **Decreasing the Strength of the Secondary Flow Vortices**: Major efficiency improvement has been achieved by introducing a completely **new endwall contouring technology**. In contrast to the trial and error method presented in numerous papers, the new technology is based on the controlled diffusion process which is entirely physics based. The method utilizes a prescribed deceleration of the secondary flow velocity from pressure to suction surface. By defining a target pressure and constructing the non-axisymmetric endwall contouring, it was shown that the pressure difference between the blade pressure and the suction surface on the hub can be controlled by reducing the secondary flow and thus increasing the efficiency. This method can equally be applied to HP-, IP- or LP-turbines and compressors regardless of the load coefficient, flow coefficient and degree of reaction. It is strongly physics based, very straight forward and easy to use. The method was applied to the second rotor row of the TPFL-turbine. The contouring was cut into the rotor hub of the three-stage TPFL-research turbine using CNC-machining. Efficiency measurements show for the contoured rotor a maximum efficiency of 89.9% compared to the reference non-contoured case of $\Delta\eta_{t\text{-}s} = 88.86\%$. This is an efficiency increase of $\Delta\eta = 1.04\%$, which is almost double the value obtained from the numerical simulation of $\Delta\eta = 0.51\%$ presented in the report. This new method is particularly significant for applications to power generation steam turbines. The high-, intermediate and low pressure units (HP, IP, LP) consist of many stages, with HP- and IP-units. Contouring all rotor endwalls of these units will substantially increase the unit efficiency. For a 200MW HP-unit of 16 stages, we estimate an efficiency improvement close to 5%.

2) **Robust Film Cooling at the Hub, Impact of Endwall Contouring**: The new method of endwall contouring not only has improved the turbine aerodynamic efficiency but it also has substantially improved the film cooling effectiveness of the contoured

endwall. To determine the impact of the endwall contouring on film cooling effectiveness, the new contouring technology was applied to the first rotor row. Performing an extensive RANS simulation by using the boundary conditions from the experiments, aerodynamics, performance and film cooling effectiveness studies were performed by varying the injection blowing ratio and turbine rotational speed. The film cooling experiments were carried out using pressure sensitive paint (PSP) measurement technique. Measurements were conducted for three coolant-to-mainstream mass flow ratios (MFR) of 0.5%, 1.0% and 1.5%. Film cooling data is also obtained for three rotational speeds, 3000 rpm (reference condition), 2550 rpm and 2400 rpm and they are compared with non-contoured endwall data. For 3000 rpm two more coolant to mainstream mass flow ratio of 0.75% and 1.25% are performed to have a better view of how film cooling effectiveness is changing. Comparing numerical and experimental results of the film cooling effectiveness investigations of the contoured case with the reference non-contoured case, clearly shows the improving effect of contouring on film cooling effectiveness for all cases investigated in this report.

CFD captures the trend however overpredicts the effectiveness. For a fixed coolant mass flow, the measured cooling film tends to decay in both coverage and effectiveness as the rotational speed decreases. In addition, quantitative and qualitative discrepancies between experimental and numerical results were observed in this study. Many factors can affect the accuracy of numerical simulations, which include numerical models, turbulence models, transitional models, etc. RANS is generally capable of reflecting the trend accurately and can be utilized as a useful tool for parameter studies and variation, and even for design and optimization purposes. A convincing example is that the contouring in this study is finalized according to RANS predictions. The subsequent rotating turbine experiments showed a higher efficiency gain than the one that was calculated.

3) Investigating the Impact of Blade Tip Geometry on Film Cooling Effectiveness: Detailed numerical and experimental investigations of film cooling effectiveness were conducted on the blade tips of the first rotor row pertaining to a three-stage research turbine. Four different blade tip ejection configurations were utilized to determine the impact of the hole arrangements on the film cooling effectiveness. Particular attention was paid to ensure a uniform pressure distribution within the small cavity inside the blade close to the blade tip. This required an extensive design iteration process implementing the results of solid mechanics design into the numerical simulation. The final configurations were manufactured and installed diametrically on the rotor hub to avoid rotor imbalance. The first configuration includes a pair of blades with radially arranged ejection holes positioned along the camber of the blade flat tip. The second configuration consists of a pair of blades with radially arranged holes embedded in the blade tip squealer. The third configuration has a flat tip but the ejection holes are arranged on the pressure side under given ejection angles. The fourth configuration has the same pressure side hole arrangements as the third configuration but the tip has squealer shape. Measurements were performed using pressure sensitive paint (PSP) technique. Three blowing ratios M = 0.75, 1.25 and 1.75 at three different

rotational speeds of 3000 rpm (reference condition), 2550 rpm and 2000 rpm were utilized. In a parallel effort, extensive numerical investigations of the above configurations were performed to give a better view of flow behavior. The results of the above research are summarized below:

1) The film cooling ejections on both the Plain tip and squealer tip affect the flow behaviors at the tip region. Strong interactions between the cooling jets and the leakage flow have been observed on both blade tips. However the flow characteristics on the Plain tip differ from those on the squealer tip.
2) In Plain tip, it is shown that the coolant particles tend to travel in the opposite direction of rotation, especially for the cooling jets exiting from the first two cooling holes. This phenomenon is due to the rotation and does not exist in a stationary cascade. This shows that the cascade results cannot be transferred to a rotating turbine.
3) In Plain tip, because of the movement of the injected cooling jet through vertical holes, the relative jet velocity vector has the opposite direction to the direction of rotation. This substantially reduces the effectiveness.
4) In squealer tip with hole injection, the coolant covers almost the entire tip region.
5) In case of the Plain tip with pressure side holes under rotation, the coolant covers only a small portion close to the trailing edge. In contrast, the stationary cascade shows a different film cooling effectiveness behavior. In the current rotating turbine experiments, the ejected jets move away from the blade tip, thus contributing only marginally to the blade tip cooling. In contrast, in the stationary cascade (without rotation) , the tip vortex generated by the pressure difference directly on the tip helps the ejected jets to cover larger portion of the blade tip. The comparison of rotating turbine results with the results of stationary cascades shows again that the cascade results do not represent the flow and heat transfer situation in a real turbine environment.
6) In case of squealer tip with pressure side holes under rotation, shows that, in contrast to the stationary cascade results, no noticeable film cooling is achievable with this configuration.

Necessary future work, Endwall cooling: The introduction of hub contouring improved the film cooing effectiveness due to purge flow compared to non-contoured case. The results for both cases, however, show that major portion of the hub is not covered. In both cases, the coolant is concentrated mostly on the suction side of the endwall, leaving its pressure side less covered. To accomplish a uniform coverage the geometry of the circumferential slot must be modified to account for the circumferential movement of the slot and the non-uniformity of the exiting mass flow through the slot. This issue will be extensively discussed in a new proposal that the PI of this project Dr. Schobeiri will submit to DOE. In that proposal he will reveal a method, how to solve the non-uniformity of the film cooling effectiveness.

Necessary future work, blade tip cooling: The research work presented in this document has clearly shown that in absence of rotation, no adequate results can be obtained by stationary cascades. Of particular significance is the tip ejection geometry. In order to achieve a full coverage of the blade tip at an optimum blowing ration of around unity, the ejection angles must be configured differently. This issue will be extensively discussed in a new proposal that the PI of this project Dr. Schobeiri will submit to DOE.

NOMENCLATURE

C	Oxygen concentration
C_{ax}	Axial chord length of the rotor blade (C_{ax}=4.16 cm)
C_{SKE}	Coefficient of secondary kinetic energy, $C_{SKE}=\frac{W_{sec}^2+W_{rad}^2}{W_{ref}^2}$
DR	Coolant-to-mainstream density ratio
f (P_{ratio})	Relation between intensity ratio and pressure ratio
HP, IP, LP	High, intermediate, low pressure
i	Incidence flow angle change from design point (3000 rpm) at the 1st stage rotor inlet
I	Pixel intensity for an image
$\dot{m}$	Mass flow rate
M	Average blowing ratio ($=\rho_c V_c/\rho_m W_2$)
MFR	Purge-to-mainstream mass flow ratio
MW	Molecular weight of gas
P_{O_2}	Partial pressure of oxygen
Δp	Pressure difference
R1, R2, R3	First, second and third rotors
RANS	Reynolds averaged Navier-Stokes
Re	Reynolds number, $V_2 Chord/\nu$
S1, S2, S3	First, second and third stators
SST	Shear Stress Transport turbulence model
T_c	Stator-Rotor gap Coolant temperature (°C)
T_f	Local film temperature (°C)
T_m	Mainstream temperature (°C)
U	Tangential average velocity (m/s)
u/c_o	Dimensionless performance parameter, $u/c_o=\frac{\pi n r_{mid}}{30\sqrt{\Delta H_{stage}}}$
URANS	Unsteady Reynolds Averaged Navier-Stokes
V	Average absolute velocity of mainstream air (m/s)
V_c	Avg. velocity of coolant air from the stator-rotor gap (m/s)
V_u	Tangential component of absolute velocity (m/s)
W	Relative average velocity of mainstream air (m/s)
W_{sec}	Secondary velocity in relative frame, $W_{sec}=-W_{ax}\sin\Psi_{mid}+W_{circ}\cos\Psi_{mid}$
X	Axial location

Greek

α	Absolute velocity flow angle (º)
β	Relative velocity flow angle (º)

η Local film-cooling effectiveness

$\eta_{t\text{-}s}$ Total-to-static efficiency,

$$\eta_{t\text{-}s} = \frac{1 - \frac{T_{t_{out}}}{T_{t_{in}}}}{1 - \left(\frac{p_{out}}{p_{t_{in}}}\right)^{\frac{\kappa-1}{\kappa}}}$$

η_{aw} Adiabatic film cooling effectiveness,

$$\eta_{aw} = \frac{T_{t_{aw,0}} - T_{t_{aw,f}}}{T_{t_{aw,0}} - T_{t_c}}$$

κ Heat capacity ratio

ρ_c Density of coolant air (kg/m^3)

ρ_m Density of mainstream air at 1st stage stator exit

ν Kinematic viscosity

ϕ 1st stage flow coefficient ($=V_{axial}/U_3$)

λ 1st stage load coefficient ($=\left(U_2 V_{u_2} + U_3 V_{u_3}\right)/U_3^2$)

Ψ_{mid} Mid-span turning angle,

$$\Psi_{mid} = \tan^{-1}\left(W_{circ,mid}/W_{ax,mid}\right)$$

ζ_{Ptr} Relative total pressure loss coefficient,

$$\zeta_{Ptr} = \frac{P_{tr_{in}} - P_{tr_{out}}}{\frac{1}{2}\rho W_{ref}^2}$$

Subscripts

0 Without film cooling (MFR=0%)

1 At 1st stage stator inlet

2 At 1st stage stator exit (rotor inlet)

3 At 1st stage rotor exit

air Mainstream air along with air as coolant

aw Adiabatic wall

ax Axial

blk Image without illumination (black)

c Coolant

circ Circumferential

f With film cooling

in Inlet

m Mainstream

mid Mid-span

mix Mainstream air along with nitrogen as coolant

out Outlet

r Relative

rad Radial

ref	Reference image with no mainstream and coolant flow
sec	Secondary
SKE	Secondary kinetic energy
t	Total or stagnation value
t-s	Total-to-static

Superscript

*	At lower rotating speeds than design point (3000 rpm)

LIST OF FIGURES

LIST OF TABLES

REFERENCES

[1] Schobeiri M.T., Han, J.C., 2009, " Aerodynamics and Heat Transfer Studies of Parameters Specific to the IGCC- Requirements: Endwall Contouring, Leading Edge Filleting and Blade Tip Ejection under Rotating Turbine Conditions, Submitted to: US-Department of Energy.

[2] Dennis, R.A., and Harp, R., 2007, "Overview of the U.S. Department of Energy's Office of Fossil Energy Advanced Turbine Program for Coal Based Power Systems with Carbon Capture ," Proceedings of GT2007 ASME Turbo Expo 2007: Power for Land, Sea and Air May 14-17, 2007, Montreal, Canada GT2007-28338.

[3] Wenglarz, R.A., and Fox, R.G. Jr., 1990, "Physical Aspects of Deposition From Coal_Water Fuels Under Gas Turbine Conditions," Journal of Engineering for Gas Turbines and Power, Jan 1990, pp9-14.

[4] Schobeiri, M.T., 2005, "Turbomachinery Flow Physics and Dynamic Performance,"first edition , by Springer-Verlag, Heidelberg, New York, Toronto, ISBN 3-540-22368-1, Second Edition 2012, ISBN 978-3-642-24674-6.

[5] Traupel, W., "Thermische Turbomaschinen," Bd.I, 1977, Springer_Verlag, Berlin.

[6] Denton, J.D., "Loss Mechanisms in Turbomachines," ASME Journal of Turbomachinery, Vol.115, pp. 621-656 (1993).

[7] Sieverding C.H., 1985," Recent Progress in the Understanding of Basic Aspects of Secondary Flows in Turbine," Blade Passages. ASME Transactions, Journal of Engineering for Gas Turbines and Power, Vol. 107, pp. 248-257 (April 1985).

[8] Langston, L.S., 2001, " Secondary Flows in Axial Turbines-A Review," Annals of the New York Academy of Sciences, Vol. 934, pp. 11-26.

[9] Schobeiri, M.T., Gilarranz, J., and Johansen, E., "Final Report on: Efficiency, Performance, and Interstage Flow Field Measurement of Siemens-Westinghouse HP-Turbine Blade Series 9600 and 5600," September, 1999.

[10] Schobeiri M.T., Gillaranz, J. L., and Johansen E.S., 2000, "Aerodynamic and Performance Studies of a Three Stage High Pressure Research Turbine with 3-D Blades, Design Point and Off-Design Experimental Investigations," Proceedings of ASME Turbo Expo 2000, 2000-GT-484.

[11] Schobeiri, M.T., Suryanaryanan, A., Jerman, C., and Neuenschwander, T., 2004, "A Comparative Aerodynamic and performance study of a three-stage high pressure turbine with 3-D bowed blades and cylindrical blades," Proceedings of ASME Turbo Expo 2004 Power of Land Air and Sea, June 14 - 17, 2004, Vienna, Austria, paper GT2004-53650.

[12] Treiber, M., Abhari, R.S., and Sell, M., 2002, "Flow Physics and Vortex Evolution in Annular Turbine Cascades," ASME, GT-2002-30540, Proceedings of ASME TURBO EXPO 2002 June 3-6, 2002, Amsterdam, The Netherlands.

[13] Hartland, J., and Gregory-Smith, D., 2002, "A Design Method for the Profiling of End Walls In Turbines," ASME, GT-2002-30433, Proceedings of ASME Turbo Expo 2002, June 3–6, 2002, Amsterdam, The Netherlands.

[14] Ingram, G., Gregory-Smith, D.G., Rose, M., Harvey, N., and Brennan, G., 2002, "The Effect of End-Wall Profiling on Secondary Flow and Loss Development in a Turbine Cascade," Proceedings of ASME Turbo Expo 2002, 2002-GT-30339.

[15] Boncinelli, P., Maceli, N., Arnone, A., and Rossi, E., "Geometrical Effects and Coolant Injection Impact on the Performance of an Hp Transonic Heavy-duty Turbine Stage," Proceedings of ASME Turbo Expo 2004, 2004-GT-54178.

[16] Becz, S., Majewski, M.S., and Langston, L.S., 2003, "Leading Edge Modification Effects on Turbine Cascade Endwall Loss," Proceedings of ASME Turbo Expo 2003, 2003-GT-38898.

[17] Zess, G.A., and Thole, K.A., 2002, "Computational Design and Experimental Evaluation of Using a Leading Edge Fillet on a Gas Turbine Vane," ASME Journal of Turbomachinery, Vol. 124, pp. 167 –175.

[18] Eymann, S., Reinmöller, U., and Niehuis, R., 2002, "Improving 3d Flow Characteristics in a Multistage Lp Turbine by Means of Endwall Contouring and Airfoil Design Modification –Part 1:

Design and Experimental Investigation," Proceedings of IGTI'02 ASME Turbo Expo 2002, 2002-GT-30352.
[19] Shih, T.I-P., and Lin, Y.-L., "Controlling Secondary-Flow Structure by Leading-Edge Airfoil Fillet and Inlet Swirl to Reduce Aerodynamic Loss and Surface Heat Transfer," Proceedings of ASME Turbo Expo 2002, 2002-GT-30529.
[20] Lethander, A.T., Thole, K.A., Zess, G., and Wagner, J., 2003, "Optimizing the Vane-Endwall Junction to Reduce Adiabatic Wall Temperatures in a Turbine Vane Passage," Proceedings of ASME Turbo Expo 2003, 2003-GT38939.
[21] Sauer, H., Müller, R., and Vogeler, K., 2000, "Reduction of Secondary Flow Losses in Turbine Cascades by Leading Edge Modifications at the Endwall," May 8-11, 2000, Munich Germany, 2000-GT-0473.
[22] Gustafson,R., Mahmood, G., and Acharya, 2007, "Aerodynamic Measurements in a Linear Turbine Blade Passage with Three_Dimensional Endwall Contouring, ASME-IGTI-Paper GT2007_28073.
[23] Schobeiri M.T. and Han, J.C., 2001 "Aerodynamics and Heat Transfer Studies of Parameters Specific to the IGCC-Requirements: Endwall Contouring, Leading Edge Filleting and Blade Tip Ejection under Rotating Turbine Conditions, A Proposal Submitted in Response to U. S. Department of Energy National Energy Technology LaboratoryUniversity Turbine Systems Research Program Funding Opportunity Number: DE_FOA_0000031 Announcement Type: Initial CFDA Number: 81.089 Fossil Energy Research and Development Topic: Aero/Heat Transfer.
[24] Ahn, J.Y., Schobeiri, M.T., Han, J.C., and Moon, H.K., "Film Cooling Effectiveness on the Leading Edge Region of a Rotating Turbine Blade with Two Rows of Film Cooling Holes Using Pressure Sensitive Paint," ASME Journal of Heat Transfer, Vol. 128, September 2006, pp. 879_888.
[25] Ahn, J.Y., Schobeiri, M.T., Han, J.C., and Moon, H.K., "Film Cooling Effectiveness on the Leading Edge of a Rotating Blade Using Pressure Sensitive Paint," International Journal of Heat and Mass Transfer, Vol. 50, January 2007, pp. 15_25.
[26] Suryanarayanan, A., Mhetras, S., Schobeiri, M.T. and Han, J.C, 2006, "Film-cooling Effectiveness on a Rotating Endwall," ASME Paper, GT-2006-90034, in press to appear in the ASME transactions, Journal of Turbomachiery.
[27] Suryanarayanan, A, Özturk, B., Schobeiri, M.T. and Han, J.C, 2007, " Film-cooling Effectiveness on a Rotating Turbine Platform Using Pressure Sensitive Paint Technique, ASME-Paper GT-27122, recommended for the publication in the ASME transactions, Journal of Turbomachiery.
[28] Schobeiri, M.T., John, J., and Pappu, K., 1996, "Development of Two-Dimensional Wakes within Curved Channels, Theoretical Framework and Experimental Investigation," ASME Journal of Turbomachinery, Vol. 118, PP. 506-518.
[29] Schobeiri, M.T., and Pappu, K., 1999, "Optimization of Trailing Edge Ejection Mixing Losses Downstream of Cooled Turbine Blades: A Theoretical and Experimental Study," ASME Journal of Fluids Engineering, Vol. 121, PP. 118-125.
[30] Schobeiri, M.T., and Chakka, P., 2002, "Prediction of Turbine Blade Heat Transfer and Aerodynamics Using Unsteady Boundary Layer Transition Model," International Journal of Heat and Mass Transfer, Vol. 45, PP. 815-829.
[31] Schobeiri, M.T., and Radke, R.E., 1994, "Effects of Periodic Unsteady Wake Flow and Pressure Gradient on Boundary Layer Transition along the Concave Surface of a Curved Plate,"ASME Paper 94_GT_327, presented at the International Gas Turbine and Aero-Engine Congress and Exposition, Hague, Niederlands, June 13-16, 1994.
[32] Schobeiri, M.T., Read, K., and Lewalle, J., 2003, "Effect of Unsteady Wake Passing Frequency on Boundary Layer Transition, Experimental Investigation and Wavelet Analysis," Journal of Fluids Engineering, Vol. 125, pp 251-266, a combined two-part paper, this paper received the ASME-2004 FED-Best Paper Award.
[33] Wright, L., Schobeiri, M. T., 1999, "The Effect of Periodic Unsteady Flow on Boundary Layer and Heat Transfer on a Curved Surface," ASME Transactions, Journal of Heat Transfer, November 1998, Vol. 120, pp. 22-33.

[34] Schobeiri, M. T., Öztürk, B., and Ashpis, D., 2003, "On the Physics of the Flow Separation Along a Low Pressure Turbine Blade Under Unsteady Flow Conditions," ASME 2003-GT-38917, presented at International Gas Turbine and Aero-Engine Congress and Exposition, Atlanta, Georgia, June 16-19, 2003, also published in ASME Transactions, Journal of Fluid Engineering , May 2005, Vol. 127, pp. 503-513.

[35] Schobeiri, M.T.and Öztürk, B., 2004, "Experimental Study of the Effect of the Periodic Unsteady Wake Flow on Boundary Layer development, Separation, and Re-attachment Along the Surface of a Low Pressure Turbine Blade," ASME 2004-GT-53929, presented at International Gas Turbine and Aero-Engine Congress and Exposition, Vienna, Austria, June 14-17, 2004, also published in the ASME Transactions, Journal of Turbomachinery, Vol. 126, Issue 4, pp. 663-676.

[36] Schobeiri, M.T., Öztürk, B. and Ashpis, D., 2005, "Effect of Reynolds Number and Periodic Unsteady Wake Flow Condition on Boundary Layer Development, Separation, and Re-attachment along the Suction Surface of a Low Pressure Turbine Blade," ASME Paper GT2005-68600.

[37] Schobeiri, M.T., Öztürk, B. and Ashpis, D., 2005, "Intermittent Behavior of the Separated Boundary Layer along the Suction Surface of a Low Pressure Turbine Blade under Periodic Unsteady Flow Conditions," ASME Paper GT2005-68603.

[38] Öztürk, B. and Schobeiri, M.T., 2006, "Effect of Turbulence Intensity and Periodic Unsteady Wake Flow Condition on Boundary Layer Development, Separation, and Re-attachment over the Separation Bubble along the Suction Surface of a Low Pressure Turbine Blade," ASME, GT2006-91293.

[39] Abdelfattah, S., Chibli, H., and Schobeiri, M.T., 2009, "Experimental and Numerical Study of the Performance of a Three_Stage Turbine at Design and Off_design Operating Conditions," ASME, GT-2009-5933.

[40] Chibli, H., Sherif A., and M.T. Schobeiri, 2009, "An Experimental and Numerical Study of the Effects of Flow Incidence Angles on the Performance of A Stator Blade Cascade of A High Pressure Steam Turbine," Proceedings of ASME Turbo Expo 2009 June 18-12, Orlando Florida, GT-2009-59131.

[41] Sauer, H., Wolf, H., "The Influence of the Inlet Boundary Layers on the Secondary Losses of Turbine Stages," AGARD-Conference Proceedings537, Montreal, Canada Oct.1993.

[42] Sauer, H., Wolf, H., "Influencing the Secondary Flow in Turbine Cascades by the Modification of the Blade Leading Edge," European Conference on Turbomachinery, Antwerpen 1997.

[43] Ingram, G., Gregory-Smith, D.,Rose, M., N. Harvey, N. and Brennan, G., 2002, "The Effect of End-Wall Profiling on Secondary Flow and Loss Development in a Turbine Cascade," Proceedings of ASME Turbo Expo 2002, GT-2002-30339.

[44] Ingram, G. Gregory-Smith, D. and Harvey, N., "Investigation of a Novel Secondary Flow Feature in a Turbine Cascade with End Wall Profiling," Proceedings of ASME Turbo Expo 2004, GT2004-53589.

[45] Saha, A.K., and Acharya, S., 2006, "Computations of Turbulent Flow and Heat Transfer through a Three-Dimensional Non-Axisymmetric Blade Passage," Proceedings of ASME Turbo Expo 2006, GT2006-90390.

[46] Praisner, T. J., Allen-Bradley, E., Grover, D. C. Knezevici and Sjolander, S. A., 2007, "Application of Non-Axisymmetric Endwall Contouring to Conventional and High-Lift Turbine Airfoils," Proceedings of ASME Turbo Expo 2007, GT2007-27579.

[47] Harvey, N. W., Rose, M. G. , Taylor, M. D.S. Shahpar, J., Harland and D. G. Gregory-Smith, 2000, "Nonaxisymmetic Turbine End Wall Design: Part I: Three-Dimensional Linear Design System," J TURBOMACH, Vol. 122, pp 278-285.

[48] Harland, J.C., Gregory-Smith, D.G., Harvey, N.W. and Rose, M.G., 2000, "Nonaxisymmetic Turbine End Wall Design: Part II – Experimental Validation," J TURBOMACH, Vol. 122, pp 286-293.

[49] Brennan, G.N., Harvey, W., Rose, M.G., Fomison, N. and Taylor, M.D., 2001, "Improving The Efficiency of The Trent 500 HP Turbine Using Non-Axisymmetric End Walls: Part 1 Turbine Design," Proceedings of ASME Turbo Expo 2001, 2001-GT-0444.
[50] Harvey, N.W., Rose, M.G., Brennan, G. and Newman, D.A. 2002, "Improving Turbine Efficiency Using Non-Axisymmetric End Walls: Validation in The Multi-Row Environment and with Low Aspect Ratio Blading," Proceedings of ASME Turbo Expo 2002, GT-2002- 30337.
[51] Germain, T., Nagel, M. Raab, I., Schuepbach, P.R., Abhari, S. and Rose, M., 2008, "Improving Efficiency of a High Work Turbine Using Non-Axisymmetric End Walls Part I: Endwall Design and Performance," Proceedings of ASME Turbo Expo 2008, GT2008-50469.
[52] Snedden, G., Dunn, D., Ingram, G. and Gregory-Smith, D., 2009, "The Application of Non-Axisymmetric Endwall Contouring in a Single Stage, Rotating Turbine," Proceedings of ASME Turbo Expo 2009, GT2009-59169.
[53] Snedden, G., Dunn, D., Ingram, G. and Gregory-Smith, D., 2010, "The Performance of a Generic Non-Axisymmetric End Wall in a Single Stage, Rotating Turbine at On and Off-Design Conditions," Proceedings of ASME Turbo Expo 2010, GT2010-22006.
[54] Schobeiri, M.T., 2010, "Fluid Mechanics for Engineers," A Graduate Textbook, Springer Verlag, ISBN978-3-642-11593-6.
[55] Schobeiri, M.T. 1979, " Theoretische und experimentelle Untersuchungen laminarer und Turbulenter Strömungen in Diffusoren, Dissertation, Technische Hochschule Darmstadt, D17.
[56] Menter, F., 1994. "Two-Equation Eddy-Viscosity Turbulence Models for Engineering Applications". AIAA Journal, 32, pp. 1598-1605.
[57] Menter, F., 1994. "Two-Equation Eddy-Viscosity Turbulence Models for Engineering Applications". AIAA Journal, 32, pp. 1598-1605.
[58] Abdelfattah, S.A. and Schobeiri, M.T., 2010, "Experimental and Numerical Investigations of Aerodynamic Behavior of a Three-Stage HP-Turbine at Different Operating Conditions," Proceedings of ASME TURBO EXPO 2010, GT2010-23564.
[59] Schobeiri, M.T. and Lu, K., 2011, Endwall Contouring Using Continuous Diffusion, a Breakthrough Method and its Application to a Three-stage High Pressure Turbine, ASME Paper, GT2011-45931.
[60] Schobeiri, M.T., Lu, K. and Han, J.C., "Effect of Purge Flow on Aerodynamics Performance and Film Cooling Effectiveness on a Rotating Turbine with Non-Axisymmetric Endwall Contouring", Proceedings of ASME Turbo Expo 2012, GT2012-69069.
[61] Abdelfattah, S.A., 2013, "Numerical and Experimental Analysis of Multi-Stage Axial Turbine Performance at Design and Off-Design Conditions," Dissertation, Texas A&M University.
[62] Ahn, J., Schobeiri, M.T., Han, J.C., and Moon, H.K., 2004, "Film Cooling Effectiveness on the Leading Edge of a Rotating Turbine Blade," IMECE 2004-59852.
[63] Suryanarayanan, A., Özturk, B., Schobeiri, M.T and J.C. Han, 2010, " Film-cooling Effectiveness on a Rotating Turbine Platform Using Pressure Sensitive Paint Technique", ASME Transaction, Journal of Turbomachinery, Vol. 132, Issue 4, pp. 041001-13.
[64] Suryanarayanan, A., Mhetras, S.P. Schobeiri, M.T and Han, J.C , 2009, "Film-cooling effectiveness on a Rotating Blade Platform", ASME Transaction, Journal of Turbomachinery, Vol. 131, Issue 1, pp. 011014-12.
[65] Schuepbach, P., Abhari, R. S., Rose, M. G., and Gier, J., 2009. "Influence of Rim Seal Purge Flow on Performance of an Endwall profiled axial turbine, ASME-paper, GT2009-59653.
[66] Jenny, P. Abhari, R.S., Rose, M.G., Brettschneider, M., and Gier, J., 2012, "A Low Pressure Turbine with Profiled EndWalls and Purge Flow Operating with a Pressure Side Bubble," ASME Journal of Turbomachinery, 134, 061038.
[67] Dr. F. Menter, CFX, Germany, Private communications relative to the CFX-transition model, April, 2008.
[68] Langtry, R.B., and Menter, F.R., "Transition Modeling for General CFD Applications in Aeronuatics", AIAA paper 2005-522, 2005.

[69] Schobeiri, M. T., 1999, "Efficiency, Performance and Flow Measurement of Siemens-Westinghouse HP-Turbine Blades," Series 9600 and 5600, Final Report.
[70] Schobeiri, M. T., Gilarranz, J.L, Johansen, E.S., 2000, "Aerodynamic and Performance Studies of a Three Stage High Pressure Research Turbine with 3-D Blades, Design Points and Off-Design Experimental Investigations," 2000-GT-484.
[71] Schobeiri, M.T., Suryanarayanan A., Jermann, C., and Neuenschwander, T., 2004,"A Comparative Aerodynamic and Performance Study of a Three-Stage High Pressure Turbine with 3-D Bowed Blades and Cylindrical Blades," GT-2004-53650.
[72]Schobeiri, M. T., 1989, "Optimum Trailing Edge Ejection for Cooled Gas Turbine Blades," ASME J. of Turbomachinery, 111 (4), pp.510-514.
[73] McLachlan, B., and Bell, J., 1995, "Pressure-Sensitive Paint in Aerodynamic Testing," Exp. Therm. Fluid Sci., 10, pp. 470–485.
[74] Wright, L.M., Gao, Z., Varvel, T.A., and Han, J.C., 2005, "Assessment of Steady State PSP, TSP and IR Measurement Techniques for Flat Plate Film Cooling," ASME HT-2005-72363.
[75] Rallabandi, A. P., Grizzle, J., and Han, J. C., 2011, "Effect of upstream step on flat plate film cooling effectiveness using psp," ASME Journal of Turbomachinery, 133, p. 041024.
[76] Coleman, H.W., and Steele, W.G., 1989, Experimentation and Uncertainty Analysis for Engineers, John Wiley & Sons, New York.
[77] Holman. J. P., 2000, Experimental Methods for Engineers, McGraw Hill, New York.
[78] Narzary, D.P., Liu, K.C, and Han, J.C., 2009, "Influence of coolant density on turbine blade platform film-cooling," Proceedings of ASME Turbo Expo 2009, GT2009-59342.
[79] Lu, K., Schobeiri, M.T. and Han, J.C., "Numerical Simulations of Film Cooling on Rotating Blade Tips within a High-Pressure Turbine", Proceedings of ASME TURBO EXPO 2013, GT2013-94806.
[80] M.R Khajavi, M.H Shariat, Failure of first stage gas turbine blades, Engineering Failure Analysis, Volume 11, Issue 4, August 2004, Pages 589-597.
[81] Metzger, D.E., Bunker, R.S. and Chyu, M.K., 1989, "Cavity Heat Transfer on a Transverse Grooved Wall in a Narrow Flow Channel," J. Heat Transfer, Vol. 111, pp. 73-79.
[82] Bunker, R.S., "A Review of Turbine Blade Tip Heat Transfer," Heat Transfer in Gas Turbine Systems, Annals of the New York Academy of Sciences, 934, May 2001, pp. 64-79.
[83] Azad, G.S., Han, J.C. and Teng, S., 2000, "Heat Transfer and Pressure Distributions on a Gas Turbine Blade Tip," ASME Paper 2000-GT-194.
[84] Azad, G.S., Han, J.C. and Boyle, R.J., 2000, "Heat Transfer and Flow on the Squealer Tip of a Gas Turbine Blade," ASME Paper 2000-GT-195.
[85] Bunker, R.S., Ameri, A.A. and Bailey, J.C., 2000, "Heat Transfer and Flow on the First-Stage Blade Tip of a Power Generation Gas Turbine: Part 1-Experimental Results," J. TURBOMACH, Vol. 122, pp. 263-271.
[86] Ameri, A.A. and Bunker, R.S., 2000, "Heat Transfer and Flow on the First-Stage Blade Tip of a Power Generation Gas Turbine: Part 2-Simulation Results," J. TURBOMACH, Vol. 122, pp. 272-277.
[87] Kim, Y.W. and Metzger, D.E., 1995, "Heat Transfer and Effectiveness on Film Cooled Turbine Blade Tip Models," J. TURBOMACH, Vol. 117, pp. 12-21.
[88] Kim, Y.W, et al, 1995, "A Summary of the Cooled Turbine Blade Tip Heat Transfer and Film Effectiveness Investigations Performed by Dr. D. E. Metzger," J. TURBOMACH, Vol. 117, pp. 1-11.
[89] Kwak, J.S. and Han, J.C., 2002, "Heat Transfer Coefficient and Film-Cooling Effectiveness on a Gas Turbine Blade Tip," ASME Paper GT2002-30194.
[90] Kwak, J.S. and Han, J.C., 2002, "Heat Transfer Coefficient and Film-Cooling Effectiveness on the Squealer Tip of a Gas Turbine Blade," ASME Paper GT2002-30555.
[91] Acharya, S., Yang, H., et al, 2002, "Numerical Simulation of Film Cooling on the Tip of a Gas Turbine Blade," ASME Paper GT-2002-30553.

[92] Christophel, J.R., Thole, K.A. and Cunha, F.J., 2004, "Cooling the Tip of a Turbine Blade Using Pressure Side Holes - Part 1: Adiabatic Effectiveness Measurements," ASME Paper GT2004-53251.
[93] Yang, H., Chen, H.C. and Han, J.C., 2004, "Numerical Prediction of Film Cooling and Heat Transfer with Diffenrent Film-Hole Arrangements on the Plain and Squealer Tip of a Gas Turbine Blade," ASME Paper GT2004-53199.
[94] Nasir, H., Ekkad, S.V., Bunker, R., and Prakash, C., 2004, "Effects of Tip Gap Film Injection from Plain and Squealer Blade Tips," ASME Paper GT2004-53455.
[95] Gao, Z., Narzary, D., Mhetras, S. and Han, J.C., 2009, "Effect of Inlet Flow Angle on Gas Turbine Blade Tip Film Cooling," J. TURBOMACH, Vol. 131, pp. 1-12.
[96] Park, J.S., Lee, D.H., Rhee, D.H., Cho, H.H., and Kang, S.H., 2010, "Heat Transfer and Effectiveness on the Film Cooled Tip and Inner Surface of a Turbine Blade," ASME Paper GT2010-23203.
[97] Achary, S., Kramer, G., Moreaux, L. and Nakamata, C., 2010, "Squealer Tip Heat Transfer with Film Cooling," ASME Paper GT2010-23688.
[98] Naik, S., Georgakis, C., Hofer, T. and Lengani, D., 2012, "Heat Transfer and Film Cooling of Blade Tips and Endwalls," J. TURBOMACH, Vol. 134, pp. 1-11.
[99] Metzger, D.E., Dunn, M.G., and Hah, C., 1991, "Turbine Tip and Shroud Heat Transfer," ASME J. TURBOMACH, Vol. 113, pp. 502-507.
[100] Dunn, M.G. and Haldeman, C.W., 2000, "Time-Averaged Heat Flux for a Recessed Tip, Lip, and Platform of a Transonic Turbine Blade," ASME J. TURBOMACH, Vol. 122, pp. 692-697.
[101] Srinivasan, V. and Goldstein, R.J., 2003, "Effect of Endwall Motion on Blade Tip Heat Transfer," J. TURBOMACH, Vol. 125, pp. 267-273.
[102] Zhou, C., Hodson, H.P., Tibbott, I., and Stokes, M., 2011, "Effects of Endwall Motion on the Aero-Thermal Performance of a Winglet Tip in a HP Turbine," 2011, ASME Paper GT2011-46373.
[103] Acharya, S., and Moreaux, L., 2012, "Numerical Study of the Flow Past a Turbine Blade Tip: Effect of Relative Motion between Blade and Shroud," ASME Paper GT2012-69192.
[104] Yang, D., Yu, X. and Feng, Z., 2008, "Investigation of Leakage Flow and Heat Transfer in a Gas Turbine Blade Tip with Emphasis on the Effect of Rotation," ASME Paper GT2008-51215.
[105] Zhang, D.H., Zeng, M. and Wang, Q.W., 2009, "The Influence of Rotating Speed on Film Cooling Characteristics on GE-E3 Blade Tip with Different Tip Configurations," ASME Paper GT2009-60295.
[106] Dring, R., Blair, M., and Joslyn, H., 1980, "An Experimental Investigation of Film Cooling on a Turbine Rotor Blade," ASME J. Eng. Power, 102(1), pp. 81–87.
[107] Takeishi, K., Aoki, S., Sato, T., and Tsukagoshi, K., 1992, "Film Cooling on a Gas Turbine Rotor Blade," ASME J. Turbomach., 114(4), pp. 828–834.
[108] Abhari, R., and Epstein, A., 1994, "An Experimental Study of Film Cooling in a Rotating Transonic Turbine," ASME J. Turbomach., 116(1), pp. 63–70.
[109] Ahn, J.Y., Schobeiri, M.T., Han, J.C., and Moon, H.K., 2007 "Effect of rotation on leading edge region film cooling of a gas turbine blade with three rows of film cooling holes," International Journal of Heat and Mass Transfer, Volume 50, Issues 1-2, pp. 15-25.
[110] Ahn, J.Y., Schobeiri, M.T., Han, J.C., and Moon, H.K., 2006, "Film Cooling Effectiveness on the Leading Edge Region of a Rotating Turbine Blade With Two Rows of Film Cooling Holes Using Pressure Sensitive Paint," J. Heat Transfer. 2006; 128(9):879-888.
[111] Suryanarayanan, A., Özturk, B., Schobeiri, M.T and J.C. Han, 2010, "Film-cooling Effectiveness on a Rotating Turbine Platform Using Pressure Sensitive Paint Technique," ASME Transaction, J. TURBOMACH, Vol. 132, pp. 041001-12.
[112] Suryanarayanan, A., Mhetras, S.P. Schobeiri, M.T and Han, J.C, 2009, "Film-cooling effectiveness on a Rotating Blade Platform" in print to be published in the ASME Transactions, J. TURBOMACH.